

# Image processing on reconfigurable hardware for continuous monitoring of fluorescent biomarkers in cell cultures

THÈSE N° 6652 (2015)

PRÉSENTÉE LE 30 JUIN 2015

À LA FACULTÉ INFORMATIQUE ET COMMUNICATIONS  
LABORATOIRE DES SYSTÈMES INTÉGRÉS (IC/STI)  
PROGRAMME DOCTORAL EN GÉNIE ÉLECTRIQUE

ÉCOLE POLYTECHNIQUE FÉDÉRALE DE LAUSANNE

POUR L'OBTENTION DU GRADE DE DOCTEUR ÈS SCIENCES

PAR

**Julien Michel GHAYE**

acceptée sur proposition du jury:

Prof. D. Atienza Alonso, président du jury  
Dr S. Carrara, Prof. G. De Micheli, directeurs de thèse  
Dr P. Colpo, rapporteur  
Prof. D. Demarchi, rapporteur  
Prof. D. Atienza Alonso, rapporteur



ÉCOLE POLYTECHNIQUE  
FÉDÉRALE DE LAUSANNE

Suisse  
2015



# Acknowledgements

This thesis crystallizes the work I have performed here at the Swiss Federal Institute of Technology in Lausanne over the course of four years and a half. It would not have materialized if it wasn't for the interaction, help and cooperation of many people and I seize this opportunity to express them my gratitude. First and foremost, I would like to thank my advisor Dr. Sandro Carrara and co-advisor Prof. Giovanni De Micheli for giving me the opportunity to pursue my research within the Integrated Systems Laboratory (LSI). In particular, I would like to thank Dr. Sandro Carrara for the constant exchanges, fruitful advices and discussions throughout the course of this research, without forgetting the trust he put in me from the beginning, including during my pre-doctoral internship.

Furthermore, I am grateful to the various members of my thesis committee; Prof. David Atienza Alonso, Prof. Jean-Philippe Thiran, Dr. Pascal Colpo and Prof. Danilo Demarchi for the time and effort they have put in reading and evaluating this thesis, along with providing constructive feedbacks. In particular, I would like to thank Dr. Pascal Colpo for providing expertise and man-hours for part of the biological side of this thesis. Of course, I extend this to the members of his group at the Institute for Health and Consumer Protection at the Joint Research Center in Ispra, Italy, who I collaborated with: Sinan Muldur, Patricia Urbán-López and Agnieszka Kinsner-Ovaskainen.

I thank my colleagues and collaborators of the NutriChip project that constituted a major part of my research work and focus; Prof. Martin Gijis, Prof. Richard Hurrell, Dr. Guy Vergères, Prof. Jeremy Ramsden and Dr. Sandro Carrara for their proposal and management of the NutriChip project throughout more than three years; Qasem Ramadan, Paolo Silacci, Gözen Köklu, Flurina Schwander and Katrin Kopf-Bolanz for the exchanges and discussions we had on this common project.

I also would like to thank present and past members of the LSI: Alena Simalatsar, Andrea Cavallini, Aya Ibrahim, Camilla Baj Rossi, Cristina Boero, Federico Angiolini, Francesca Stradolini, Giovanni Resta, Gözen Köklü, Hassan Ghasemzadeh, Hu Xu, Ioulia Tzouvadaki, Irene Taurino, Jaume Joven, Jian Zhang, Luca Amarù, Maxime Thammasack, Nima Aliakbarinodehi, Pierre-Emmanuel Gaillardon, Sara Ghoreishizadeh, Somayyeh Rahimian, Vasilis Pavlidis, Wenqi You Dubout, Winston Haaswijk, Xifan Tang. I would also like to thank my former office mate Shashi Bobba for the countless unexpected discussions about pretty much any topics. I am also grateful to my current office mates; Michele De Marchi for sharing his passion about

## Acknowledgements

---

mountaineering, sports climbing and about pretty much anything else that interests him, and Francesca Puppo for her joyful presence and letting me know I am unknowingly thinking out loud when working. I need not to forget the master students who collaborated with me: Madhura Avinash Kamat and Chiara Succa. And finally, I must acknowledge the whole administrative team; Christina Govoni, the forceful secretary of LSI, for her ever cheering and helping predisposition; Rodolphe Buret for his IT support and his supply chain management; Anil Leblebici for her coordination and support regarding the organization of various scientific events.

I have a very special thought for my partner, Eleni Palla, who I met early on as a collaborator in LSI and who have been supporting me daily since. Especially, I need to thank her for her continuous input about my research, including her valuable comments on all manuscripts I wrote throughout these years, and also for her motivational support during the final part of my thesis.

And last but not least, I am indebted to my parents. I cannot thank them enough for the tremendous efforts they have done (and continue to do) in providing uninterrupted love, care, support and presence. Furthermore, they have always been supportive, yet critical, of all my choices, letting me do trials-and-errors over and over again on pretty much anything.

*Lausanne, March 2015*

J. G.



# Abstract

Fluorescence microscopy is a wonderful widespread tool in biological research. It is the primary modality for bioimaging and empowers the study and analysis of multitudes of biological processes. It can be applied to fixed biosamples, that is samples with frozen biological features by mean of chemical linkers, or *in situ* live biosamples providing useful insights on the spatio-temporal behavior of fluorescently stained biomarkers. Current fluorescent microscopy techniques use digital image sensors which are used to leverage quantitative studies instead qualitative outcomes. However, state-of-the-art techniques are not suitable for integration in small, contained and (semi-)autonomous systems. They remain costly, bulky and rather quantitatively inefficient methods for monitoring fluorescent biomarkers, which is not on par with the design constraints found in modern Lab-on-a-Chip or Point-of-Use systems requiring the use of miniaturized and integrated fluorescence microscopy.

In this thesis, I summarize my research and engineering efforts in bringing an embedded image processing system capable of monitoring fluorescent biomarkers in cell cultures in a continuous and real-time manner. Three main areas related to the problem at hand were explored in the course of this work: *simulation*, *segmentation algorithms* and *embedded image processing*.

In the area of *simulation*, a novel approach for generating synthetic fluorescent 2D images of cell cultures is presented. This approach is dichotomized in a first part focusing on the modeling and generation of synthetic populations of cells (i.e. cell cultures) at the level of single fluorescent biomarkers and in a second part simulating the imaging process occurring in a traditional digital epi-fluorescent microscope to produce realistic images of the synthetic cell cultures. The objective of the proposed approach aims at providing synthetic data at will in order to test and validate image processing systems and algorithms.

Various image *segmentation algorithms* are considered and compared for the purpose of segmenting fluorescent spots in microscopic images. The study presented in this thesis includes a novel image thresholding technique for spot extraction along with three well-known spot segmentation techniques. The comparison is undertaken on two aspects. The segmentation masks provided by the methods are used to extract further metrics related to the fluorescent signals in order to (i) evaluate how well the segmentation masks can provide data for classifying real fluorescent biological samples from negative control samples and (ii)

## Acknowledgements

---

quantitatively compare the segmentations masks based on simulated data from the previously stated simulation tool.

Finally, the design of an *embedded image processing* system based on FPGA technologies is showcased. A semi-autonomous smart camera is conceived for the continuous monitoring of fluorescent biomarkers based on one of the segmentation methods incorporated in the previously stated comparison. Keeping the focus on the need for integration in fluorescence microscopy, the image processing core at the heart of the smart camera results from the use of a novel image processing suite; a suite of IP cores developed under the constraints dictated by the bioimaging needs of fluorescence microscopy for use in FPGA and System-on-Chip technologies. As a proof of concept, the smart camera is applied to the monitoring and extraction of the kinetics of the uptake of fluorescent silica nano-particles in cell cultures.

Key words: smart camera, FPGA, image processing, HDL, CMOS sensor, spot extraction, adaptive thresholding, fluorescence microscopy, embedded system, nutrition, cellular uptake, nano-particles, Caco-2 cell line, A549 cell line, silica nano-particles.

# Résumé

La microscopie par fluorescence est un outil merveilleux répandu dans la recherche biologique. Il est un des outils principaux dans le domaine de l'imagerie biologique et offre la possibilité d'étudier et d'analyser une multitude de processus biologiques. Il peut être appliqué à des échantillons biologiques qui ont été fixés, c'est-à-dire à des cultures de cellules qui ont été immobilisées par un procédé chimique, ou à des échantillons biologiques vivants de manière à récolter des informations sur le comportement spatio-temporels de différents biomarqueurs colorés avec des molécules fluorescentes. Les techniques modernes de microscopie par fluorescence utilisent des capteurs d'images numériques de manière à réaliser des études quantitatives au lieu d'obtenir des résultats qualitatifs. Cependant, ces techniques de microscopie ne sont pas adaptées pour l'intégration dans les petits systèmes (semi-)autonomes. Ce sont des méthodes coûteuses, volumineuses et relativement lentes à utiliser pour l'observation de biomarqueurs fluorescents. Elles ne correspondent pas aux besoins requis pour la conception de systèmes intégrés désirant utiliser ces techniques d'imagerie.

Dans cette thèse, je résume mes différents efforts de recherches et ingénieries qui ont eu pour but de concevoir un système de traitement d'images embarqué visant à l'observation et l'analyse de biomarqueurs fluorescents dans des cultures cellulaires en temps-réel. Trois domaines ont été explorés dans le courant de ce travail de thèse : *simulation*, *technique de seuillage* et *traitement d'images embarqué*.

Dans le domaine de la *simulation*, une nouvelle approche est proposée pour la génération d'images synthétiques de cultures cellulaires virtuelles. Cette approche est divisée en deux parties. Une première partie s'occupe de la construction de cultures cellulaires virtuelles en simulant la présence individuelle de chaque biomarqueur fluorescent. La seconde partie simule l'optique et le capteur d'image utilisés dans un microscope par épi-fluorescence afin de générer des images réalistes. L'objectif de cette approche vise à générer des données synthétiques à volonté afin de pouvoir tester et valider différents systèmes ou algorithmes de traitement d'images.

Différentes *techniques de seuillage* sont prises en compte dans une étude comparative. L'étude présentée dans cette thèse fournit une comparaison quantitative de ces techniques basée sur leur capacité à segmenter des spots fluorescents dans des images microscopiques. L'étude se focalise sur trois techniques de seuillage couramment utilisées dans la littérature. Elle

## Acknowledgements

---

intègre aussi une nouvelle technique de seuillage spécialement conçue pour la détection de spots fluorescents. La comparaison est effectuée sur deux aspects via les masques de seuillage fournis par les différentes méthodes. Premièrement, ceux-ci sont utilisés pour extraire différentes caractéristiques de classifications d'images et sont évalués en fonction de leur capacité à entraîner un classificateur de Bayes naïf. Deuxièmement, les masques de seuillage sont évalués de manière quantitative grâce à l'outil de simulation mentionné ci-dessus sur base de leur capacité à segmenter les biomarqueurs fluorescents.

Enfin, la conception d'un système de traitement d'images embarqué sur FPGA est présentée. Une caméra intelligente semi-autonome est conçue pour la surveillance continue de biomarqueurs fluorescents. L'une des techniques de seuillage incluse dans l'étude mentionnée ci-dessus est en son cœur. La conception a été dirigée par les besoins de miniaturisation et d'intégration de la microscopie par fluorescence, ce qui a donné naissance à une suite d'IP visant à l'intégration de techniques de traitement d'images spécifiques sur FPGA ou *systems-on-chip*. Comme une preuve de concept, la caméra intelligente est appliquée à l'observation et à l'extraction de la cinétique de l'absorption de nano-particules fluorescentes dans des cultures cellulaires.

Mots clefs : Caméra intelligente, FPGA, traitement d'images, HDL, capteur CMOS, techniques de seuillages, microscopie par fluorescence, système embarqué, nutrition, absorption cellulaire, nano-particule, lignée de cellules Caco-2, lignée de cellule A549.

# Contents

<b>Acknowledgements</b>	<b>i</b>
<b>Abstract (English/Français)</b>	<b>iii</b>
<b>Contents</b>	<b>ix</b>
<b>List of Figures</b>	<b>xi</b>
<b>List of Tables</b>	<b>xiii</b>
<b>List of Symbols</b>	<b>xv</b>
<b>I Thesis Motivation and Overview</b>	<b>1</b>
<b>1 Motivation and Overview</b>	<b>3</b>
1.1 Quantification in Fluorescence Bioimaging . . . . .	3
1.2 Integration and Embedded Processing Challenges . . . . .	6
1.3 Research Contributions . . . . .	8
1.4 Organization of the Thesis . . . . .	9
1.5 General Comments . . . . .	11
<b>II Digital Fluorescence Bioimaging: Introduction and Considerations</b>	<b>13</b>
<b>2 Fluorescence Bioimaging</b>	<b>15</b>
2.1 Fluorescent Biomarkers . . . . .	16
2.1.1 Fluorescence Phenomenon . . . . .	16
2.1.2 Nanoscale Fluorescent Probes . . . . .	18
2.1.3 Fluorescence and Biosamples . . . . .	20
2.2 Widefield Fluorescence Microscopy . . . . .	23
2.2.1 Microscope . . . . .	23
2.2.2 Image Formation . . . . .	25
2.2.3 Optical Limit and Resolution . . . . .	28
2.3 Chapter Summary . . . . .	29
	vii

<b>3</b>	<b>Image Sensor Technologies</b>	<b>31</b>
3.1	Principle of Operation . . . . .	32
3.1.1	Solid-State Photosensing . . . . .	32
3.1.2	Photodiodes . . . . .	32
3.1.3	Photogates . . . . .	34
3.2	CMOS Sensor Architecture . . . . .	35
3.2.1	Passive Pixel Sensors . . . . .	35
3.2.2	Active Pixel Sensors . . . . .	36
3.3	CCD Sensor Architecture . . . . .	36
3.4	Sensor Characteristics . . . . .	40
3.4.1	Spatial Resolution . . . . .	40
3.4.2	Sensitivity . . . . .	41
3.4.3	Fill Factor and Full-Well Capacity . . . . .	42
3.4.4	Noise Sources . . . . .	42
3.5	Chapter Summary . . . . .	44
 <b>III Fluorescent Biomarker Monitoring: From Synthetic Samples to Smart Camera Based System</b>		 <b>47</b>
<b>4</b>	<b>Simulated Biological Cells and Synthetic Image Generation</b>	<b>49</b>
4.1	Synthetic Image Generation Tool . . . . .	50
4.1.1	Simulation and Emulation Strategy . . . . .	50
4.1.2	Cell Population Simulation . . . . .	51
4.1.3	Cell Population Imaging . . . . .	57
4.2	Tool Performance and Validation . . . . .	64
4.2.1	Computational Cost . . . . .	64
4.2.2	Signal-to-Noise Characteristics . . . . .	66
4.3	Chapter Summary and Contributions . . . . .	67
<b>5</b>	<b>Image Thresholding Methods For Fluorescent Biomarkers</b>	<b>69</b>
5.1	Segmentation Methods for Spot Extraction . . . . .	70
5.1.1	Image Preprocessing . . . . .	71
5.1.2	Segmentation of Biomarkers . . . . .	73
5.2	Comparison Frameworks for Spot Segmentation Methods . . . . .	79
5.2.1	Comparison Framework For Image Classification . . . . .	79
5.2.2	Comparison Framework For Biomarker Localization . . . . .	82
5.3	Biosample Classification Performances . . . . .	85
5.4	Localization Performance of Biomarkers on Synthetic Images . . . . .	90
5.5	Chapter Summary and Contributions . . . . .	96

<b>6 Embedded Image Processing System</b>	<b>99</b>
6.1 Target Operation . . . . .	100
6.1.1 Segmentation Method . . . . .	100
6.1.2 Outputs . . . . .	102
6.1.3 Calibration . . . . .	103
6.2 Stream Processor Concept . . . . .	103
6.2.1 Stream Protocol . . . . .	105
6.2.2 Interfacing Stream Processors . . . . .	107
6.3 Hardware Architecture . . . . .	108
6.3.1 Image Sensor . . . . .	108
6.3.2 Top-Level Design and FPGA Platform . . . . .	108
6.4 Hardware Digital Image Processing . . . . .	111
6.4.1 Stream Processing Blocks . . . . .	111
6.4.2 Histogram Processing Accelerator . . . . .	123
6.5 System Validation . . . . .	131
6.6 Chapter Summary and Contributions . . . . .	135
<b>IV Applications and Thesis Outlook</b>	<b>137</b>
<b>7 Applications</b>	<b>139</b>
7.1 Nutrition Analysis and NutriChip Project . . . . .	140
7.1.1 Biological Model and Lab-on-a-Chip Integration . . . . .	141
7.1.2 Induced Toll-Like Receptors Monitoring . . . . .	142
7.1.3 Application Concluding Remark . . . . .	148
7.2 Silica Nano-particles . . . . .	149
7.2.1 Industrial Applications of Nano-particles and Related Concerns . . . . .	149
7.2.2 Fluorescent Nano-particles Uptake Monitoring . . . . .	150
7.2.3 Application Concluding Remark . . . . .	154
7.3 Chapter Summary and Contributions . . . . .	155
<b>8 Conclusions and Outlook</b>	<b>157</b>
8.1 Thesis Summary and Contributions . . . . .	158
8.2 Future Perspectives . . . . .	159
<b>A Appendix</b>	<b>161</b>
<b>Bibliography</b>	<b>176</b>
<b>Curriculum Vitae</b>	<b>177</b>





# List of Figures

1.1	Timeline . . . . .	4
1.2	Example of miniaturized integrated fluorescence microscope . . . . .	6
1.3	Example of smart camera prototype processing fluorescent images . . . . .	7
1.4	Image processing pyramid . . . . .	11
2.1	Typical fluorophore excitation and emission spectra . . . . .	16
2.2	Fluorescent phenomenon . . . . .	18
2.3	Common fluorescent probes . . . . .	18
2.4	Direct and indirect immunofluorescence . . . . .	21
2.5	Fluorescence microscope schematic . . . . .	23
2.6	Cross-section of a typical sample setup for epi-fluorescence microscopy . . . . .	24
2.7	Aberration free point spread function . . . . .	27
3.1	Photodiode cross-section and I-V characteristics . . . . .	33
3.2	Photogate cross-section . . . . .	34
3.3	CMOS image sensor architecture . . . . .	35
3.4	Passive and active pixel architecture for CMOS sensors . . . . .	36
3.5	Three phase clocking scheme for charge transfer in CCDs . . . . .	38
3.6	CCD image sensor architecture . . . . .	39
3.7	Examples of CCD and CMOS spectral sensitivity . . . . .	41
4.1	Examples of fluorescent Caco-2 human cells . . . . .	50
4.2	Cell population example . . . . .	52
4.3	Detailed cell population example . . . . .	56
4.4	Vignetting in synthetic images . . . . .	59
4.5	Examples of synthetic images with various magnification . . . . .	61
4.6	Synthetic image of three cells . . . . .	62
4.7	Side-by-side comparison of synthetic and real fluorescent clusters . . . . .	62
4.8	Synthetic image generator computational cost . . . . .	65
4.9	Signal-to-Noise ratio versus exposure time of synthetic images . . . . .	66
5.1	T-point algorithm concept . . . . .	74
5.2	Otsu's algorithm concept . . . . .	75
5.3	GLT algorithm flowchart . . . . .	77

## List of Figures

---

5.4	Examples of Caco-2 cells expressing TLR2 receptors . . . . .	80
5.5	Sample segmentation masks from the segmentation methods . . . . .	84
5.6	Amount of fluorescent pixel based effect-size and AUC . . . . .	88
5.7	Amount of fluorescent pixel based effect-size and AUC . . . . .	88
5.8	Sample segmentation masks of a synthetic cell . . . . .	91
5.9	Parameter exploration for global thresholding on TH filtered images . . . . .	92
5.10	Parameter exploration for Sauvola's thresholding technique . . . . .	93
5.11	Parameter exploration for the GLT method . . . . .	94
6.1	Generic view of a basic image stream processor . . . . .	104
6.2	Image stream processing branching using stream (de-)multiplexers . . . . .	105
6.3	Image stream processing splitting using dedicated stream splitter . . . . .	105
6.4	Image stream protocol timing diagrams . . . . .	106
6.5	Structural architecture of the smart camera for biomarker monitoring . . . . .	109
6.6	Structural view of the preprocessing stream processor . . . . .	110
6.7	Structural view of the segmenting stream processor . . . . .	111
6.8	Structural view of stream processing blocks performing basic operations . . . . .	112
6.9	Structural view of the image adder and accumulator . . . . .	114
6.10	Structural view of the Exponential moving average block . . . . .	116
6.11	Structural view of a generic rank filter block . . . . .	118
6.12	Control and data path of the window extractor . . . . .	119
6.13	Control and data path of the rank selector . . . . .	120
6.14	Sorting network examples . . . . .	121
6.15	Structural view of the Top-Hat filter block . . . . .	122
6.16	Structural architecture of the histogram processing accelerator . . . . .	124
6.17	Control and datapath of the cumulative moment builder . . . . .	125
6.18	Structural architecture of the cumulative moment processing block. . . . .	127
6.19	Generic structural view of the implementation of scheduled sequencing graphs	128
6.20	Scheduled sequencing graph used for measurements metric computation . . . . .	129
6.21	Scheduled sequencing graph used in Otsu's hardware implementation . . . . .	130
6.22	Picture of the smart camera prototype <i>in situ</i> . . . . .	132
6.23	Denoised images of microbeads . . . . .	133
6.24	Linearity measurements using microbeads . . . . .	134
6.25	Photobleaching measurements of microbeads . . . . .	135
7.1	Biological model of the gastrointestinal tract . . . . .	141
7.2	Technological platform for the NutriChip project . . . . .	143
7.3	Caco-2 with expressed TLR2 using a CMOS image sensor . . . . .	145
7.4	Kinetics of TLR2 expression measured using fluorescence bioimaging . . . . .	146
7.5	Kinetics of TLR2 expression measured using RT-PCR . . . . .	148
7.6	A549 with internalized fluorescent nano-particles imaged a CMOS imager . . . . .	150
7.7	Kinetics of silica nano-particles uptake measured using the smart camera . . . . .	151
7.8	Effect size distributions between groups with various time of exposure to NPs . . . . .	153

# List of Tables

2.1	Spatial resolution for various objectives at various wavelengths . . . . .	29
3.1	Maximal pixel pitch for image sensors based on various microscope objectives	40
4.1	User-defined input parameters for the generation of cell populations . . . . .	51
4.2	User-defined input parameters for the simulation of imaging process . . . . .	58
5.1	Segmentation methods included in the comparative study . . . . .	71
5.2	Comparative table based on the amount of fluorescent pixels . . . . .	87
5.3	Comparative table based on the mean fluorescent pixel intensity . . . . .	87
6.1	Characteristics of the CMOS sensor used for the smart camera design . . . . .	108
6.2	CMOS image sensor configuration for microbeads samples . . . . .	133
7.1	Pearson and Spearman correlation coefficients with RT-PCR . . . . .	147
7.2	Cohen's <i>d</i> effect sizes between groups with various time of exposure to NPs . .	152
7.3	GMM's components for the effect size distributions in Fig. 7.8 . . . . .	154



# List of Symbols

2D	2-Dimensional
3D	3-Dimensional
ADC	Analog-to-Digital Converter
ASIC	Application Specific Integrated Circuit
APS	Active Pixel Sensor
AUC	Area Under Curve
BIC	Bayesian Information Criterion
Caco-2	Human Colon Adenocarcinoma
C-Elegan	Caenorhabditis Elegan
CC	Connected Component
CCD	Charge Coupled Device
CMOS	Complementary Metal Oxide Semiconductor
CPU	Central Processing Unit
DDR2	Double Data Rate
DMA	Direct Memory Access
DNA	Deoxyribonucleic Acid
DSNU	Dark Signal Non-Uniformity
DSP	Digital Signal Processor
E-Coli	Escherichia Coli
EMA	Exponential Moving Average
FB	Frame Buffer

## List of Symbols

---

FIONA	Fluorescence Imaging with One-Nanometer Accuracy
FITC	Fluorescein Isothiocyanate
FLIM	Fluorescence Life-Time Imaging
FPGA	Field Programmable Gate Array
FPN	Fixed-Pattern Noise
GIT	Gastrointestinal Tract
GMM	Gaussian Mixture Model
GFP	Green Fluorescent Protein
HDL	Hardware Description Language
IIR	Infinite Impulse Response
IP	Intellectual Property
LED	Light Emitting Diode
LPS	Lipopolysaccharide
LoC	Lab-on-a-Chip
LSNR	Local Signal-to-Noise Ratio
LTI	Linear Translation Invariant
MOS	Metal-Oxide-Semiconductor
mRNA	Messenger RNA
MM	Mathematical Morphology
NA	Numerical Aperture
NCG	Negative Control Group
ND	Neutral Density
NP	Nano-particle
PALM	Photoactivated Localization Microscopy
PBS	Phosphate Buffered Saline
PCC	Pearson's Correlation Coefficient
PoC	Point-of-Care

PPS	Passive Pixel Sensor
PRNU	Pixel Response Non-Uniformity
PSF	Point-Spread Function
QD	Quantun Dot
RT	Room Temperature
RT-PCR	Reverse Transcription Polymerase Chain Reaction
ROC	Receiver Operating Characteristics
SDRAM	Synchronous Dynamic Random Access Memory
SE	Standard Error
SG	Stimulated Group
SNR	Signal-to-Noise Ratio
SoC	System-on-a-Chip
SPAD	Single Photon Avalanche Diode
SRCC	Spearman's Ranked Correlation Coefficient
STORM	Stochastic Optical Reconstruction Microscopy
TH	Top-Hat
TIRF	Total Internal Reflection Fluorescence
TLR	Toll-Like Receptor
TLR2	Toll-Like Receptor 2
TLR4	Toll-Like Receptor 4
TRITC	Rhodamine Isothiocyanate
UART	Universal Asynchronous Receiver/Transmitter
$\mu$ GIT	Miniaturized Gastrointestinal Tract
USB	Universal Serial Bus





# **Thesis Motivation and Overview** **Part I**



# 1 Motivation and Overview

## 1.1 Quantification in Fluorescence Bioimaging

Fluorescence microscopy is a wonderful widespread tool in biological research. It is the primary modality for bioimaging and empowers the study and analysis of multitudes of biological processes. It can be applied to fixed biosamples, that is samples with *frozen* biological features by mean of chemical linkers, or *in situ* live biosamples providing useful insights on the spatio-temporal behavior of fluorescently stained targets. It is the development of digital electronics in the 1990s and the advent of digital cameras with sufficient resolution combined with the abundant availability of computing power that brought quantitative capabilities to fluorescence microscopy.

The combined development of the field of optics and biochemistry, highlighted in Fig. 1.1, brought fluorescence microscopy to the level of resolution we enjoy today. Their combined improvements in optical techniques and specialized fluorescent probes were instrumental in this endeavor. The advent of *fluorescein* that was first synthesized in 1871 by Adolph Von Baeyer [4], as well as the derivation of thousands of other fluorescent compounds over the last century such as *Fluorescein Isothiocyanate* (FITC) or *Rhodamine Isothiocyanate* (TRITC) enabled the fluorescent staining of different intracellular structures. Other development landmarks are the invention of the optical fluorescent microscope in 1911 by Otto Heimstädt and Heinrich Lehmann [58], quickly followed in 1914 by the research of Stanislaus Von Prowazek showcasing the first usage of this microscope technique to study dye binding to living cells. Another revolution in fluorescence techniques started in 1942 with the work of Albert Coon *et al.*, which marked the beginning of immunofluorescence [18]. This technique harnesses the power of immunological reactions by linking these synthetic organic dyes to antibodies, thus enabling the visualization of specific antigens in fixed cells.

Next to the synthetic organic dyes, a new revolution for live cell imaging started in the early 1960s with the discovery of the *Green Fluorescent Protein* (GFP) in a jellyfish species by Osamu Shimomura [122]. It is only about thirty years later, in 1993, that the GFP was successfully expressed in a living organism for the first time; Martin Chalfie used novel gene cloning

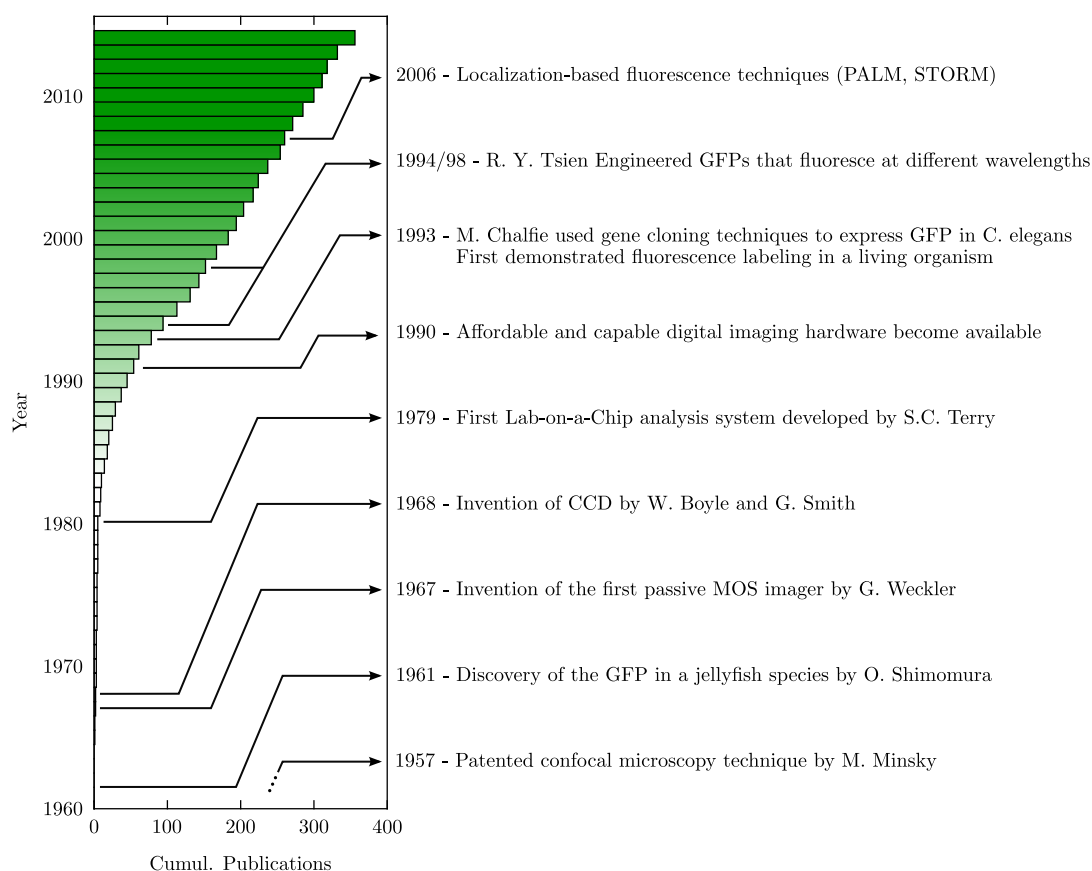


Figure 1.1 – Cumulative number of publications referenced on WebOfScience for "quantitative fluorescence imaging".

techniques and managed to express it in *Escherichia Coli* (E-Coli) and in *Caenorhabditis Elegan* (C-Elegan) [15]. It is however the work of Roger Tsien, who lead the research on GFP after that, that resulted in a whole palette of biological fluorophores featuring increased intensity and different colors with respect to the wild type GFP [119].

In recent years, novel fluorescent probes are emerging from nano-technologies such as *Quantun Dots* (QDs) [77, 109] and *Nano-particles* (NPs) [112, 130]. The development of these new fluorophores are all products of the quest aiming at the selection of a suitable [109] fluorescent label for a given application. That is aiming for brightness increase and photo-stability increase while insuring bio-compatibility and minimal interference with the sample.

In the field of optics, efforts were focused on improving the optical resolution. Indeed, there is one fundamental physical barrier that limits our ability to directly observe biological processes occurring on the sub-cellular scale. The actual resolution of any optical microscope, including

that of fluorescence microscopes and all its derivatives, is limited due to the diffraction barrier [10] in classical optics. This limit was defined by Abbe as

$$d = \frac{\lambda}{2N_A} \quad (1.1)$$

where  $\lambda$  is the imaging wavelength, that is the wavelength at which the probes fluoresce, and  $N_A$  is the numerical aperture (i.e. a measure of the light gathering capabilities) of the imaging optics. This brings the limit to around 200nm for a high-end fluorescent system fitted with an oil-immersion objective. This barrier fostered the development of new imaging techniques beside classical wide-field microscopy such as *Total Internal Reflection Fluorescence* (TIRF) microscopy whose concept dates back to 1956 [3], confocal microscopy in 1957 [79], and multi-photon microscopy initiated by two-photon microscopy experiments in 1990 [23]. These techniques only partially improved the spatial resolution, they however provide major improvement in the sample sectioning by limiting the depth span within which the fluorescent probes are stimulated. This leads to significant improvements in the *Signal-to-Noise Ratio* (SNR) of observed samples compared to the wide-field microscopy technique.

Digital image sensors are the real enabler to quantification in fluorescence microscopy. The sensors we have available today, whether based on the *Charge Coupled Device* (CCD) or *Complementary Metal Oxide Semiconductor* (CMOS) technology, replace efficiently the eye of the observer and offer objectivity where early fluorescence microscopy was mostly subjective. An image sensor is essentially an array of photosensitive devices acting as photon accumulators that produces digital images of the focused sample. Furthermore, these images can then be processed by various image processing techniques depending on the target application.

It is however the amazing evolution of digital electronics that provided sensors with high enough sensitivity and low noise characteristics. It enabled image processing techniques to yield quantitative results on fluorescent microscope systems. Indeed, the early CMOS sensors as developed by Gene Weckler in 1967 [142] or the first CCD sensor as designed by Willard Boyles and George Smith a year later [11] had limited sensitivity, significant noise, and relatively big photosensors or pixels.

These sensors combined with signal processing techniques offered leads to a major revolution in the field of fluorescence microscopy. Thanks to them, super-resolution techniques [52] such as *Photoactivated Localization Microscopy* (PALM) [6], *Stochastic Optical Reconstruction Microscopy* (STORM) [9] or *Fluorescence Imaging with One-Nanometer Accuracy* (FIONA) [148] are now available to us, offering spatial resolution of fluorescent molecules comparable to that of electron microscopy. Deconvolution techniques [140] also became available to better increase the SNR and resolution of the images. Digital image sensors also enabled the creation of high-throughput fluorescence microscopes that can now provide new insights about the cell dynamics by enabling the localization and tracking of fluorescently tagged proteins.

All these evolutions in the fields of optics, biochemistry and electronics yielded to the birth of

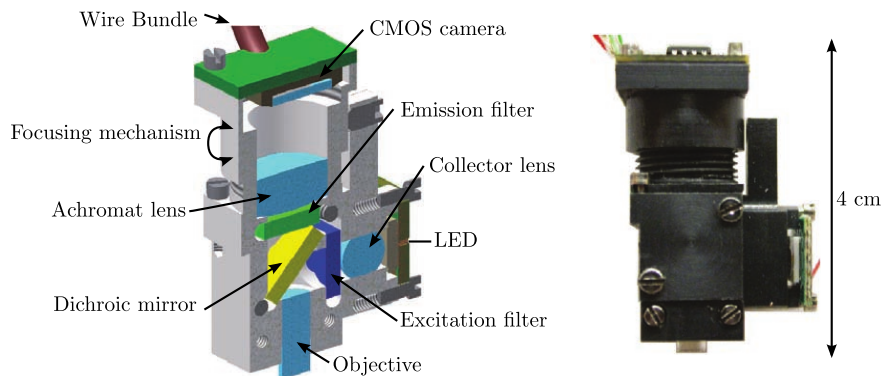


Figure 1.2 – Example of miniaturized integrated fluorescence microscope with discrete optics. Reprinted from [38].

quantitative fluorescent microscopy in 1990s (Fig. 1.1) along with all the research activities centered around it.

### 1.2 Integration and Embedded Processing Challenges

Quantitative fluorescence microscopy as described previously remains a costly, bulky and a rather quantitatively inefficient method for bio-assays and biological research in general. The current commercial fluorescence microscope cost range is in the order of \$10,000 for the lower end models right up to the order of \$100,000 and above. These optical systems can weigh tens of kilos and present fragile pieces of equipment. They usually require proper training to operate in order to maximize their capabilities. Moreover, fluorescence microscopy has some overhead. First, the preparation of the assay or samples is time consuming and more often than not costly. The biologists are limited in the amount of experiments they can prepare daily. Second, the data acquisition, or images in this case, is also time demanding. Providing provably significant results requires the acquisition of numerous data points within a controlled and objective framework. One can easily imagine that acquiring images for hours is not really in accordance with this requirement. Finally, the actual processing of the data is not a trivial step either. Whether it is for simple denoising, image segmentation and analysis or specific processing (e.g. post processing for super-resolution techniques), some processing power, resources and expertise need to be allocated in order to have access to the final results of any experiment.

However, these downsides can be mitigated through integration. It is again the revolution behind integrated circuit technologies and the idea of miniaturization that currently lead the way to cost efficient and automated bio-assays in cell analysis. This integration is highly beneficial for numerous applications. For example high-content screening applications such as drug discovery [39, 88, 126] and food testing [105] rely on extensive investigations and studies of a given compound. Beside them, classical single cell experiments are nowadays

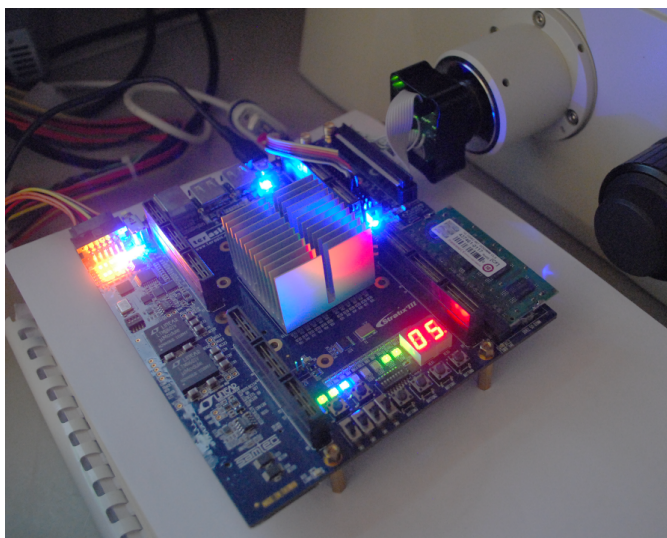


Figure 1.3 – Example of smart camera prototype featuring a FPGA processing board. The image elaboration is performed right at the source while the image sensor collects image from the fluorescence microscope.

attempted on a larger scale [44] thus leading to the same requirement as high-screening applications. The development of a high-throughput, cost effective integrated system able to handle a large number of samples and able to parallelize the experiments is a necessity in these fields as they rely on statistically relevant data sets for their analysis.

Microfluidic technologies or, more generally, *Lab-on-a-Chip* (LoC) technologies are a major vector for integrated fluorescence detection [100, 143]. They offer the possibility of multiplexed assays and limit the amount of analyte required for a single experiment. Compared to slide based or macro-assay based experiments, LoCs offer an unprecedented level of scaling. A ten-fold reduction in size obviously lead to a 100-fold improvement in the number of samples per surface area. On top of this, it also leads to an additional 100-fold decrease of sample time preparation due to Fick's law of molecular diffusion [14].

The imaging of such LoCs is commonly done using traditional fluorescence microscopes. There are however research efforts done towards the integration of the optics and light illumination. Miniaturized integrated fluorescence microscope have already been manufactured as proof-of-concept [38, 83, 94]. They feature *Light Emitting Diode* (LED) technologies for fluorophore excitation, miniaturized discrete optics and either a photosensitive diode [94] or a CMOS image sensor [38] for data collection. An example of such integrated optics is shown in Fig. 1.2. Other research efforts towards imaging integration focus on micro-fabrication of Fresnel zone plates directly on LoC devices or contact imaging [7, 42, 56, 123], which suppresses the need for discrete focusing optics.

The last step for quantitative fluorescent microscope integration is related to signal and image processing. Embedding signal processing techniques within the miniaturized system

offers a direct feedback during the imaging process, which is key for repeated experiments and the automation of the system. Furthermore, high-throughput systems are such that a huge amount of data is generated in a short amount of time. Terabytes of information, often redundant, can be generated by the image sensors. This in turn puts a heavy load on temporary storage solutions both in speed and capacity which is a bottleneck for today's systems. Integrating the signal processing and data elaboration right at the source, that is by processing images on the fly, in real-time, avoids unnecessary data storage and provides a feedback channel for experimental control.

There are multiple ways of providing embedded image processing capabilities to fluorescence microscopy through the use of smart cameras. Broadly speaking, the term smart camera can be defined as "an embedded vision system that is capable of extracting application-specific information from the captured images" [8]. Such systems can be implemented in multiple ways using modern digital electronic technologies. General purpose embedded processors, *Digital Signal Processors (DSPs)*, *Field Programmable Gate Arrays (FPGAs)* or even *Application Specific Integrated Circuits (ASICs)* can be employed. The choice of technology heavily depends on the final application and is a trade-off between numerous factors. Examples include, but are not limited to: (i) physical constraints such as power consumption or physical size; (ii) design constraints including engineering cost, ease of integration and flexibility; (iii) computational power and capabilities required by the target application; (iv) flexibility required for the system. Nowadays, a popular choice for embedded image processing is the FPGA technology [5], including for microscopy applications [31, 38]. It offers both the inherent parallelism of digital hardware and the flexibility of software through reprogramming capabilities. Furthermore modern FPGA devices feature enough resources and embedded memory to be viable solutions for embedded image processing. Combined with their ease of use and reprogrammability, they make ideal research and testing platforms.

### 1.3 Research Contributions

This thesis includes both research oriented work and engineering oriented implementations. On the research side, multiple existing algorithms and a novel one are compared and reviewed for biomarker monitoring and cytometry purposes. On the implementation side, a novel method for generating synthetic fluorescent images and a fully featured smart camera system have been developed for the continuous monitoring of fluorescent biomarkers. All the output contributions done during the course of this thesis are published in [32–37].

The five main contributions to the field by this thesis are as follow

- Image simulation and generation tools are essential for testing and validating image processing algorithms, especially considering that the generation of image datasets of real samples is a time-consuming process. They provide an objective way of testing, validating and comparing algorithms designed for a given purpose. In this thesis, the



interest lies in the detection and extraction of fluorescent spots in microscopic images of cell samples. Current image generation tools and methods are limited to the generation of synthetic fluorescent images where the fluorescent signal is merely emulated using parametric texture generators [66, 67, 127]. The image meta-data provided by these tools only gather cell population level information (e.g. cell sizes, average fluorescent intensity, number or cells). We built on top of these and propose a simulation approach that is able to generate images based on the contribution of each fluorophore present in a synthetic cell population [33]. The generated meta-data features intra-cellular detail, i.e. the number of fluorophores present in each cell and their location in space. This provides an advantage in testing and validating image processing algorithms for fluorescent spot extraction used in the context of quantitative fluorescence microscopy.

- *2-Dimensional (2D)* and *3-Dimensional (3D)* fluorescent spot extraction algorithms are already presented in the literature [40, 60, 87, 96, 101, 103, 151]. Based on existing techniques, low level image operations and techniques are gathered and compared using both real fluorescent images and synthetic images. The presented comparison provides qualitative and quantitative comparison results as well as a new view on these algorithms for fluorescent biomarker extraction.
- A novel local thresholding method, the *GLT* method, is also explained and proposed in aforementioned study. This technique is specifically designed for the segmentation of fluorescent spots in microscopic images and offers improved segmentation data when compared to the other segmentation methods.
- A novel image processing suite for FPGAs has been developed and tested for the implementation of biomarker monitoring algorithms. Existing processing suites [2, 75, 144] are at the base of this development. They are however not suitable for microscopic applications as their focus is mainly on high-speed, high-framerate video processing. The novel suite features a fully reconfigurable stream processing architecture that can implement a number of image processing algorithms. The proper usage of this suite of *Intellectual Property (IP)* cores is demonstrated by implementing a selected fluorescent spot extraction algorithm from the comparative study for on-line monitoring of biomarkers.
- The developed techniques are applied on images acquired with a low-cost mid-range CMOS image sensor proving that biomarker monitoring and cytometry does not necessarily requires the use of scientific grade CCD sensors. The monitoring of the inflammatory response of Caco-2 cells as well and the measurement of NPs uptake in A549 cells are successfully performed.

## 1.4 Organization of the Thesis

Beside the conclusion, the remaining chapters of this thesis are organized in three parts: (i) Chapters 2 and 3 provide some background in digital fluorescence bioimaging; (ii) Chapters

## Chapter 1. Motivation and Overview

---

4 to 6 are the core of this thesis and present techniques ranging from the simulation of fluorescent biomarkers to the design of a smart camera for real-time biomarker monitoring; (iii) Chapter 7 presents applications of the core techniques on real biosamples.

**Chapter 2** provides the background required in fluorescence bioimaging. More specifically, it explains the fluorescence phenomenon and its applications in life-sciences for bioimaging. In a second part, a description of epi-fluorescence microscopy is provided as all the images dealt with in this thesis are acquired using this technique. This description also includes a mathematical description of the imaging process.

**Chapter 3** presents the different technologies usually used for producing image sensors employed in bioimaging. The basic principle of operation is explained for both CMOS and CCD light sensing technologies. This includes an overall comparison of the performance of the two technologies. In particular, the focus is put on the various limitations induced by the image sensor for fluorescence imaging.

**Chapter 4** deals with the topic of realistic fluorescent image generation. The developed new tool presented in this chapter uses a parametric model of a fluorescently stained cell population. The generated cell population features a distribution of generic fluorescent stained biomarkers. It builds upon the concepts introduced in Chapter 2 and 3 in order to properly simulate the imaging process of fluorescent molecules and generate realistic images by simulating the sampling action of an image sensor.

**Chapter 5** presents a study of various segmentation algorithms for the extraction of fluorescent spots in microscopic images. Multiple low to mid-level segmentation algorithms for fluorescent spot extractions are compared, including the novel *GLT* algorithm. This comparison is handled both with real fluorescent images and synthetic images. Real images of stained *Human Colon Adenocarcinoma (Caco-2)* cells, a type of cell usually used as an *in vitro* model for the human small intestinal mucosa, are used to qualitatively evaluate the performance of the algorithms. Synthetic images generated by the tool presented in Chapter 4 are also used to quantitatively evaluate the algorithms and identify which are best to evaluate the level of stimulation of the cells.

**Chapter 6** details the smart camera architecture developed to monitor fluorescent biomarkers. Based on the results of the comparison in Chapter 5, a single image processing algorithm is implemented using a hardware description language. This chapter focuses on the development of a general purpose image processing suite for FPGA devices. A collection of self contained IP cores that are able to inter-operate in order to implement selected algorithms.

**Chapter 7** presents experimental measurements provided by the techniques and tools detailed in the two previous chapters. A first application is the monitoring of *Toll-Like Receptor 2 (TLR2)* in stimulated Caco-2 cells. An inflammatory response is induced in the cells and monitored by a subset of the algorithms presented in Chapter 5. A correlation between the elaborated data and measured *Messenger RNA (mRNA)* is shown.

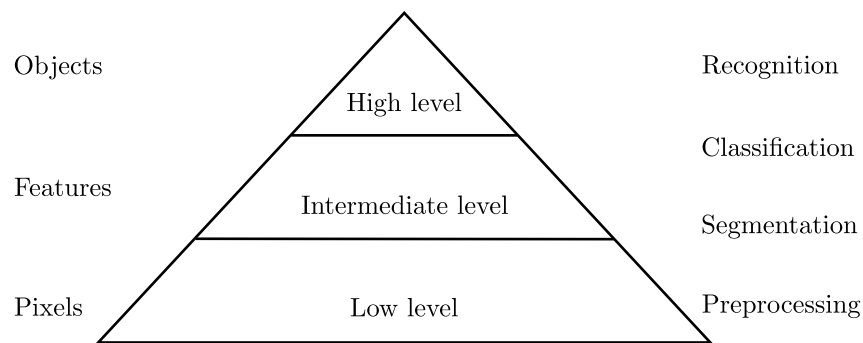


Figure 1.4 – Image processing pyramid. Adapted from [5].

A second application shows the monitoring of fluorescent NPs uptake in A549 cells, adenocarcinomic human alveolar basal epithelial cells, using the smart camera system of Chapter 6.

**Chapter 8** concludes this thesis. It gives an overall view of the contributions made and summarizes the work done. Finally, possible extensions of this work are discussed and perspectives are given with respect to the developed tools and methods.

## 1.5 General Comments

The goal of this thesis is the development of an embedded monitoring system for fluorescent biomarkers. It is important to detail the scope and context within which the work has been conducted.

First, the system was developed as part of a LoC system or a table top diagnostic system for which cost is a primary parameter in the production constraints. This forced the use of CCD image sensors to be ruled out in favor of inexpensive mid-performance CMOS light sensing technologies. The challenge this entails is to prove that fluorescent biomarker monitoring can be done with a general purpose CMOS image sensor and does not necessarily require the use of high-end scientific grade CCD sensor arrays. As a result the smart camera presented in Chapter 6 uses a low cost CMOS sensor and all the experimental results and images presented in the application chapter of this thesis (Chapter 7) were acquired using it.

Second, for flexibility reasons, the smart camera was implemented using the FPGA technology. This constrained the choice of segmentation algorithms that are selected for the comparative study presented in Chapter 5. The focus is put on low-level image processing operations as defined by the image processing pyramid in Fig. 1.4. Intermediate to high-level techniques such as watershed segmentation [40], snake segmentation [41] or wavelet transform based techniques [96] were ruled out in order to retain the ability to provide a hardware version for modern FPGA devices.

## Chapter 1. Motivation and Overview

---

Finally, as we mentioned in the previous introductory sections, quantitative fluorescence microscopy can be applied to numerous applications and used on many types of sample. Two types of sample are used throughout the following chapters. They are selected based on the two applications that fostered and supported this thesis.

The first application is related to field of food and nutrition sciences. A major part of this thesis fits within the scope of the NutriChip project [138]. This project proposes to investigate the effects of food ingestion by humans through the use of a LoC platform. It aims at the development of analytical strategies enabling food screening, in particular for dairy products. Within the scope of that project, the Caco-2 cell line is used as an *in vitro* model for the for the human small intestinal mucosa. TLR2 are fluorescently monitored as markers relating the cellular immune reactions to the nutrients.

The second application deals with the cytotoxicity of silica NPs. These NPs are found in a wide range of industrial sectors producing goods destined for human use. As part of their safety assessment, the study of their uptake in *in vitro* cell cultures is required. Practically, the A549 cell line is used and the uptake of fluorescent silica NPs is monitored.

More details about these two applications are found in the final chapter of this thesis. After the main core chapters (Chapter 4 to 6), the Chapter 7 offers a final view on the work done in the thesis by demonstrating its impact on the two aforementioned applications.

# **Digital Fluorescence Bioimaging** **Part II**

## **Introduction and Considerations**



## 2 Fluorescence Bioimaging

Research in life-sciences heavily depends on direct observations. It is the primary mode of discovery for extending our knowledge about biological processes, cellular functions, structures and mechanisms. It is no surprise that the discovery of nanometer-sized fluorescent probes combined with high-resolution microscopy techniques lead to the revolution we observed during the last century in bioimaging. We are today able to capture images of *in vivo* and sometimes *in situ* specimen thanks to the combined evolution of optics, biochemistry and system engineering.

The interest in fluorescence microscopy originates from the desire to observe intra-cellular structures and the various processes that take place in the cellular environment. A major hurdle before the advent of fluorescent probes was the inability to distinguish specific proteins within cells with respect to others. The cellular environment is filled with numerous proteins and is naturally transparent, rendering the process of optically identifying a given type of protein nearly impossible. A solution to this was brought in the form of fluorescent molecules. They are usually referred to as *fluorescent dyes, markers, probes* or *fluorescent labels* and are used to tag one or many biological processes of interest thus rendering them visible. Countless fluorescent probes have been developed over the last two decades for an equally big amount of targets. One of the major advantages of these fluorescent markers is that they are bio-compatible, whether inherently or by design, and do not interfere with the proper function of the cells, enabling the study of cell populations *in vivo*.

This chapter offers an introduction to bioimaging by highlighting various key elements required for the proper understanding of the various techniques presented in this thesis. First, an explanation on the concept of fluorescence is given along with a couple of fluorescent staining techniques used in practical bioimaging applications. A second section then recalls the basics of epi-fluorescence microscopy by presenting the optics and image formation process in a classical widefield fluorescent microscope.

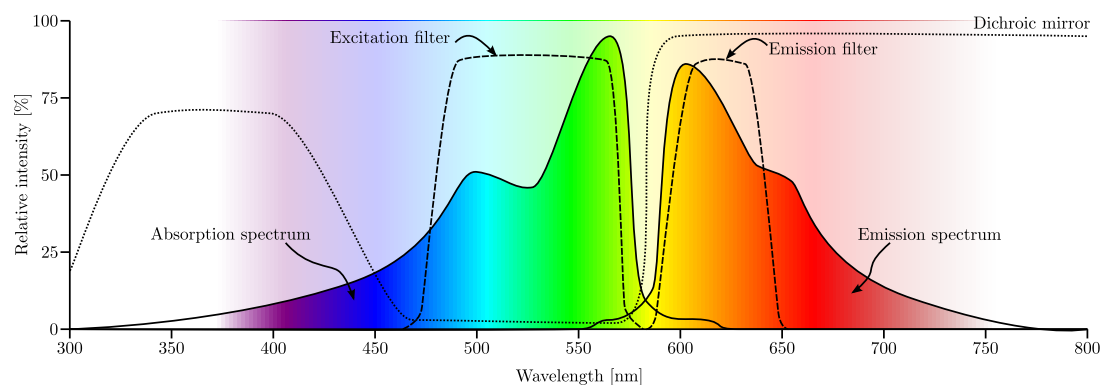


Figure 2.1 – Representation of the excitation and emission spectra of a typical fluorescent material used in bioimaging. The profiles of the *excitation filter*, the *emission filter* and the *dichroic mirror* show how they match the emission and excitation spectra in order to extract the fluorescent signal as described in Section 2.2.1.

## 2.1 Fluorescent Biomarkers

Fluorescent probes have different forms and their size vary between 1nm to 100nm. One common element is the presence of one or many fluorescent molecules which have to be stimulated in order to fluoresce. This section first explains the physical principles behind the fluorescence phenomenon. It then introduces the main types of fluorescent probes currently in use in life-sciences. The last part details a couple of staining techniques by which fluorescent molecules are bound to specific targets relevant to the work presented in this thesis.

### 2.1.1 Fluorescence Phenomenon

In the context of fluorescence microscopy, a fluorescent molecule is often referred to as a *fluorophore* or *fluorochrome*. It is brought in its excited state using an excitation light at a specific wavelength and typically re-emits light at a longer wavelength. A given fluorophore is characterized by an excitation spectrum and an emission spectrum. These two spectra are distinct from each other; a representation of typical spectra for a fluorophore is given in Fig. 2.1. Practically, the peak intensity locations of the spectra are used to refer to a specific fluorophore. For example, the natural *Green Fluorescent Protein* (GFP) is characterized by excitation/emission peaks at 395/509nm and fluorescein is characterized by peaks at 494/521nm.

Along with phosphorescence, fluorescence is a subtype of luminescence [43]. Luminescence is conveniently defined as the radiation emitted by an excited molecule relaxing into its ground state. This phenomenon takes its root in the fact that a molecule can exist in a variety of distinct energetic or electronic states ( $S_1$ ,  $S_2$ , ...) beside their relaxed ground state ( $S_0$ ). The basic process by which a fluorophore fluoresce is depicted in the partial energy diagram in Fig. 2.2. The fluorescence occurs at the third step of a four-steps process:



1. From the ground state  $S_0$ , the fluorophore can absorb a quantum of energy in the form of an excitation photon ( $E_{ex} = h\nu_{ex} = hc/\lambda_{ex}$ ) moving it into an excited state  $S_1$ . One should note that each electronic state has multiple vibrational states due to the ability of the molecule to absorb a small quantity of vibrational energy. The energy of an exciting photon required to trigger this jump between the ground state and any excited state is equal to the energy difference between these two states. Taking into consideration the vibrational states, there exists a range of wavelengths within which photons are able to excite a given fluorophore. This explains the breadth of the absorption spectrum as presented in Fig. 2.1.
2. After absorption of a photon, the fluorophore undergoes vibrational relaxation. That is, excess energy that was absorbed above the base level of the excited state, resulting in a vibrationally excited fluorophore, is lost and converted to heat.
3. The third step is the actual fluorescence. After undergoing vibrational relaxation, the fluorophore is at the lowest vibration state of the excited state. Fluorescence is the loss of energy ( $E_{em} = h\nu_{em} = hc/\lambda_{em}$ ) through the emission of a photon when the fluorophore returns to its ground state.
4. The last step is a second vibrational relaxation, but this time at the ground state, which dissipates any excess vibrational energy remaining after the photon emission. Again the multiple possible vibrational states of the ground state explain that there exists a range of possible wavelengths for the emitted photon, also explaining the breadth of the emission spectrum.

This process is such that, due to the vibrational relaxations happening both after the absorption and emission steps, the energy of the absorbed photon is greater than the energy of the emitted photon ( $E_{ex} \geq E_{em}$ ). Practically this loss of energy translates in a shift towards longer wavelengths between the absorption and the emission spectrum. This shift is known as the Stoke's shift.

There are however other relaxation processes a fluorophore can undergo to return to its ground state. Radiationless processes can occur either through internal conversion where the all the absorbed energy is heat dissipated, or through any fluorescence quenching mechanisms [121] (e.g. collisional process). All the electronic states mentioned thus far only involve what is known as singlet states. There is also another type of electronic states, the triplet states, involved in intersystem crossing processes such as phosphorescence and delayed fluorescence [43].

Beside the excitation and emission peak wavelengths, the notion of quantum yield is also used to characterize a given fluorophore type. It is defined as

$$Q_e = \frac{\text{number of emitted photons through fluorescence}}{\text{number of absorbed photons}} \quad (2.1)$$

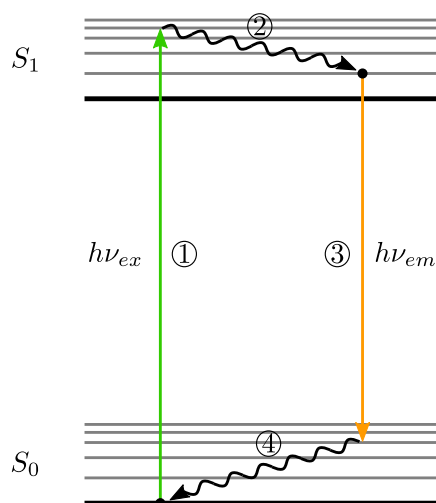


Figure 2.2 – Jablonski diagram of the fluorescence process as described in Section 2.1.1. (1) Absorption of an exciting photon. (2) Vibrational relaxation on the excited singlet state  $S_1$ . (3) Emission of a photon by fluorescence. (4) Vibrational relaxation on the ground state  $S_0$ .

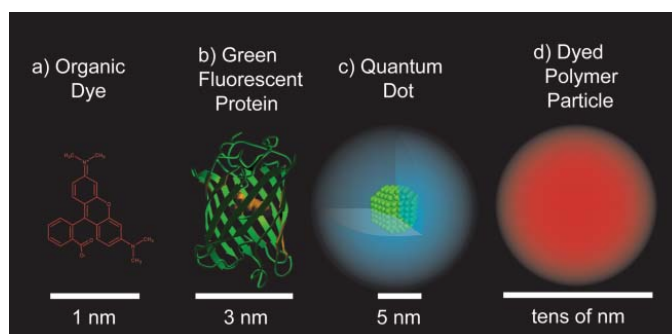


Figure 2.3 – Several common fluorescent probes. Reprinted from [12].

Finally it is important to mention that the fluorescence process can only be repeated a finite amount of time for a given fluorophore. The amount of cycles is typically in the order the hundreds of thousand [135] before the fluorophore is not anymore able to respond to excitation photons due to chemical damages. This process, known as photobleaching, is heavily dependent on the environment within which the fluorophore is excited.

### 2.1.2 Nanoscale Fluorescent Probes

There is currently an increasing number of available fluorescent probes. A fluorescent probe can be defined as the range of fluorescent nanomaterials that can be functionalized for a given application, such as biotechnology. In its simplest form a fluorescent probe is embodied by a single fluorophore. On the other end, a fluorescent probe can take the form of a complex

nanostructure carrying multiple fluorophores.

Regardless of the application, one can easily extract the two main issues that novel probes are trying to address: brightness and photostability. The brightness issue is addressed by improving various aspects of fluorescent probes. This includes multiplying the amount of fluorescent molecules per probes and using fluorescent molecules with higher quantum yields, higher excitation and higher emission peaks. The photostability issue is due to interactions between the fluorescent molecules and the external environment where they are used. This implies shielding them from solvent molecules and other reactive species present in solution in order to improve their stability.

The fluorescent nanomaterials used for probes can be classified in four broad categories (Fig. 2.3): *Organic fluorophores*, *Biological fluorophores*, *Quantum dots* and *Nano-particles*. Each of them has its own advantages and disadvantages for bioimaging applications.

### **Organic Fluorophores**

Organic fluorophores or organic dyes are the earliest class of fluorescent nanomaterials. They are single molecule dyes and as a result are the smallest, on the order of 1nm. Common types of such fluorophores are *fluorescein* (e.g. FITC), *rhodamine* (e.g. TRITC, Texas Red), *cyanide* (e.g. Cy3, Cy5) and *Alexa fluor* dyes. An advantage of these fluorescent molecules is their small size which inherently reduces the interaction they may have with the biological sample under investigation. This small size however can also be considered as a limitation in some applications, leading to non-specific binding and diffusion within the target generating a high background signal [12]. This is why these fluorescent molecules are typically conjugated to biological compounds such as proteins or any amino-acid chain containing molecules [50] leading to techniques like immunofluorescence staining. In spite of their drawbacks such as short Stoke's shift, broad spectrum profiles and susceptibility to photobleaching, these organic fluorophores are widely in use today due to their widespread availability and ease of use. Available commercial kits provide ready made conjugated fluorophores with absorption and emission wavelengths ranging from the near infrared to ultra-violet light.

### **Biological Fluorophores**

Biological fluorophores, also called fluorescent proteins, are of great interest for the study of *in vivo* cells. The most popular fluorescent protein is the *Green Fluorescent Protein (GFP)*. The main particularity of these fluorescent proteins is that their genes can be added to the host genome using genetic engineering techniques. As a result, the genetically modified living cells are expressing specific proteins tagged with fluorophores without affecting their biological function. This leads to numerous applications for quantifying protein expressions, protein interactions or analyzing their dynamics [141]. Based on the wild type GFP, a multitude of related fluorescent proteins have been generated via mutagenesis [21] with increased

fluorescence intensity and a range of fluorescent emission wavelengths covering most of the visible spectrum. Optical properties of fluorescent proteins are very similar to the organic fluorophores and exhibit similar behaviors regarding photostability and intersystem crossing processes [134].

### Quantum Dots

With respect to the organic and biological fluorophores, the quantum dots are a very recent class of fluorescent nanomaterial [77]. They consist of a nanometer sized (2-50 nm) semiconductor crystal and often a protective shell required to render them bio-compatible [24, 51]. They are an appealing class of fluorescent material as they typically provide a better quantum yield and are less sensitive to photobleaching. Furthermore, they feature a wide absorption spectrum, large Stoke's shift and a narrow emission band resulting in brighter fluorescence [74]. Quantum dots are however susceptible to stochastic blinking, effectively leading a significant amount of them to exhibit dark states [147]. As a result, quantum dots are considered as complementary to classical organic and biological fluorophores.

### Fluorescent Nano-particles

A major shortcoming of the organic fluorophores is their photostability. The direct contact they experience with their environment leads to photobleaching. This results in a fast decrease in fluorescence intensity and limits the sample usefulness over time. In order to solve this issue, researchers have developed *Nano-particles* (NPs) [12] which act as vehicles encapsulating thousands of organic fluorophores [152, 153]. There exists three types of NPs: polymer-based, metal-based and silica-based. The size of these NPs typically ranges between 10 to 100nm. Recently, silica NPs have attracted a lot of attention as this material is hydrophilic, making it ideal for biological applications. It is furthermore an ideal surface for functionalization since various biological compounds can be conjugated on the silica surface [141]. Encapsulating many fluorophores in such manner renders the whole system robust against stochastic blinking and increases the brightness simply due to the sheer amount of fluorescent molecules present within. Furthermore, the silica material shields the fluorophores against the environment reducing their tendency to photobleach. However, fluorescent NPs still follow the limitations of organic fluorophores by design. That is, they are still characterized by a broad emission spectrum and a short Stoke's shift.

#### 2.1.3 Fluorescence and Biosamples

Fluorescent nanomaterials need to be functionalized to bind and report on specific biological targets. There exists numerous techniques available depending what type of fluorescent nanomaterial is used and what biological functions are targeted. This section focuses on two techniques: immunofluorescence staining [29] and NPs delivery [111].

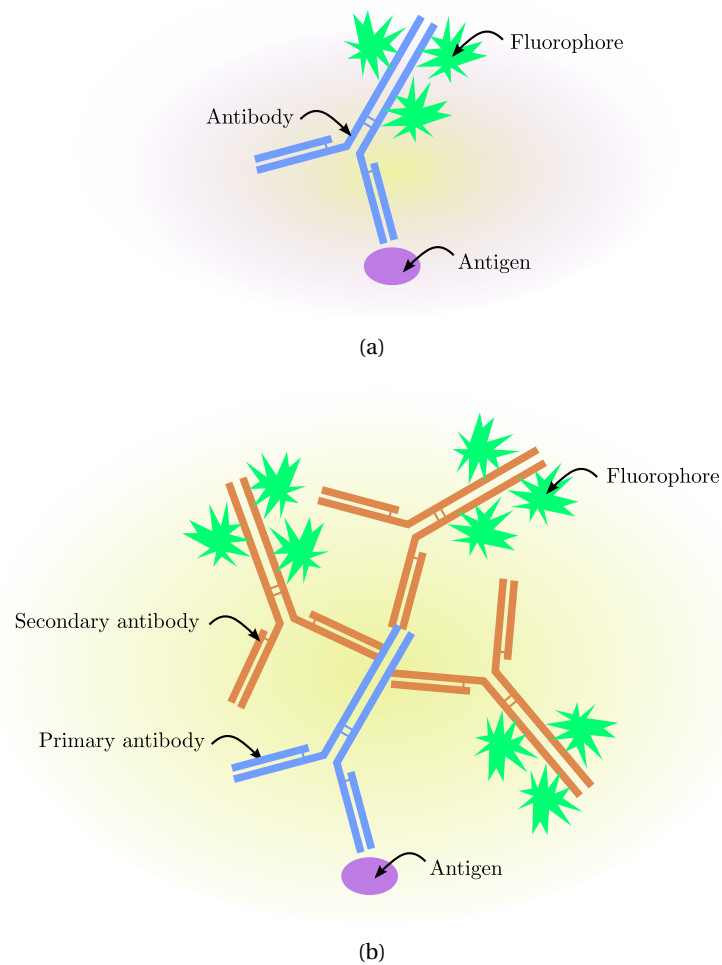


Figure 2.4 – (a) Direct and (b) indirect immunofluorescence staining concept.

### Immunofluorescence Staining

Immunofluorescence staining is a common technique employed for binding fluorophores to specific targets. It uses the high selectivity of antibodies for their antigens, typically proteins. An antibody is itself a protein complex whose basic structure resembles the letter Y. A cartoon of an antibody is depicted in Fig. 2.4(a). An antibody features two distinct regions called the *Fab region* and the *Fc region*. The *Fab region* (the two arms of the Y) features the antigen binding sites. The *Fc region* (the tail of the Y) is an identifier for other antibodies or cell receptors to recognize. While this process is naturally involved with the immune system, immunofluorescence staining uses it to couple fluorophores with antigens. There are two existing variations of this technique : *direct immunostaining* and *indirect immunostaining*.

*Direct immunostaining* is the simplest most obvious form of immunofluorescence staining. It involves a single type of antibody whose *Fc region* is populated with one or multiple fluorophores. The *direct* adjective indicates that the fluorescently-tagged antibodies directly bind

to the target antigen. It is presented in Fig. 2.4(a). This approach is typically used to detect, and eventually quantify, the presence of the target antigen. However, the limited amount of fluorophores that get bound to a single antigen is limited. This limits the sensitivity of the technique.

*Indirect immunostaining* uses a two-steps approach involving a primary non-fluorescent antibody and a secondary fluorescently-tagged antibody. The concept of this technique is depicted in Fig. 2.4(b). The first step uses a primary antibody that is specific to the target antigen. The *Fc region* of this primary antibody becomes the target for secondary fluorescently-tagged polyclonal antibodies. Polyclonal antibodies are secreted by different animals and thus recognize different epitomes on the *Fc region* of the primary antibodies. Compared to the *direct immunostaining* approach, this approach increases the sensitivity because multiple secondary polyclonal antibodies can bind to a single primary antibody (i.e. indirectly to a single antigen). As a result the average amount of fluorophores attached to a single antigen is increased, thus amplifying the fluorescent signal. The drawback of this technique is its complexity. It is time consuming and requires two incubation periods. Furthermore since the success of the second step depends on the success of the first, the quality of the antibodies and careful execution of staining protocols are predominant.

### Nano-particles Delivery

Three main strategies are in use today for intracellular NP delivery [111]: *passive*, *facilitated* and *active* delivery.

*Passive delivery* is the simplest approach. It relies on the natural cellular endocytosis process of unmodified fluorescent NPs. It simply involves incubating the cells with the desired NPs for a given amount of time. This passive technique is commonly used to report on the natural cellular uptake rates of NPs of various sizes. Its main advantage is that the NP surface does not need to be functionalized with a particular targeting agent. This advantage is also its drawback as the intra-cellular targeting capabilities are inherently limited.

*Facilitated delivery* leverages the endocytosis process by using exogenous agents. These can either be added to the extracellular environment or conjugated with the NP surface. For example, a peptide sequence can be added to the NP surface in order to facilitate their internalization by cells. Another technique, conceptually similar to the immunostaining technique, involves the use of proteins on the NP surface. This provides selective binding to specific antigens.

Finally, *active delivery* relies on physically acting on the cellular barrier in order to deliver the NPs within the cytoplasm without using the natural endocytosis process. Such techniques involve micro-injections [27], electroporation [73] or the use of gene guns [132].

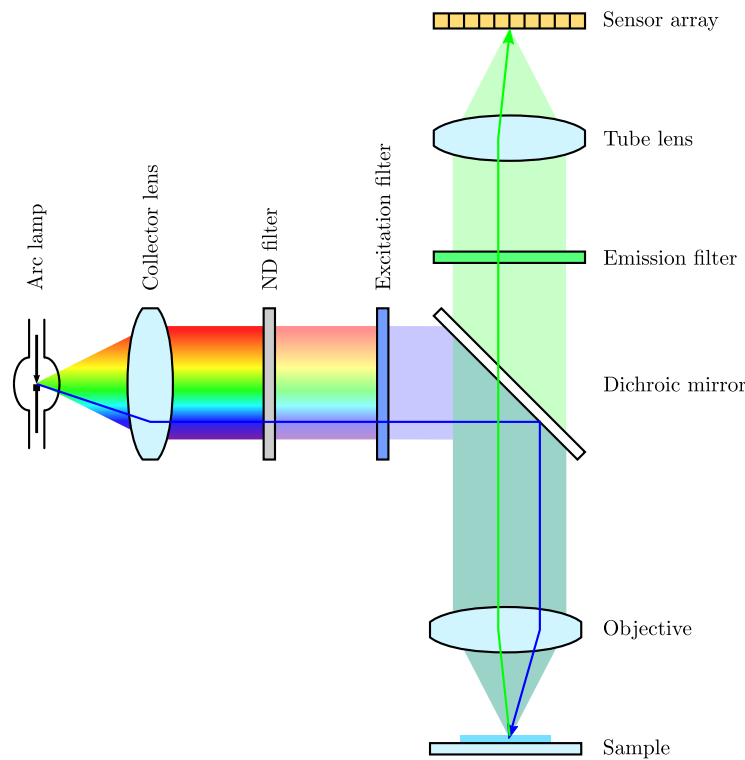


Figure 2.5 – Schematic of an epi-fluorescence microscope

## 2.2 Widefield Fluorescence Microscopy

Widefield fluorescent microscopy is the most common and used microscopy technique for imaging fluorescent samples. The focus of this section is first set on describing the concept of this microscopy technique along with its main components. Second a mathematical description of how the image is formed is provided before commenting and defining the optical resolution.

### 2.2.1 Microscope

By breaking down the concept of fluorescence microscopy in its simplest form, one can identify the two goals that this technique has to achieve: (i) deliver energy in order to excite the fluorescent probes and (ii) recover the fluorescent signal emitted by the sample. Figure 2.5 shows how these are achieved in a classical widefield fluorescence microscope. Current widefield microscopes implement the Köhler illumination. This technique ensures that the specimen under observation is illuminated with a high degree of uniformity. In turn, it means that every fluorophores under illumination have an equal probability of absorbing an exciting photon.

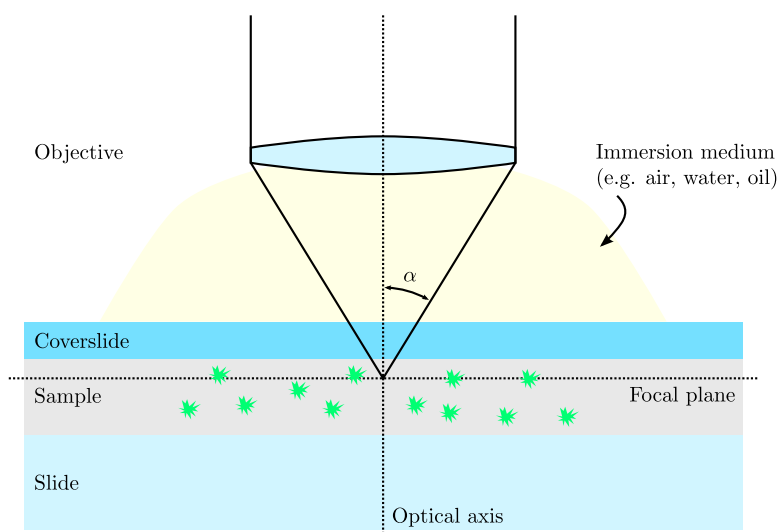


Figure 2.6 – Cross-section of a typical sample setup for epi-fluorescence microscopy.

Each fluorophore within the sample is considered as a point of light emitting photons that may get captured by the objective (Fig. 2.6). According to geometrical optics, the optical setup is such that each ray of light emitted by a fluorophore on the focal plane and captured by the objective will travel into the microscope tube and will get focused on the image plane, where the image sensor array is located. The image that is formed on the sensor is the integrated contributions of every fluorophore at a given time.

Based on how fluorescence works the sample must be illuminated within a specific range of wavelengths defined by the excitation spectrum and re-emits light within a lower range of wavelengths as defined emission spectrum. In order to achieve this in a practical setup, fluorescence microscopes make use various light filters; the *Neutral Density* (ND) filter, the *excitation filter*, the *emission filter* and the *dichroic mirror* are typically organized as shown in Fig. 2.5.

First, the *Neutral Density* (ND) filter is used to reduce the illumination intensity of the lamp. It is characterized by the fact that it reduces the intensity equally over all the wavelengths of the spectrum. This filter is practically changed on a regular basis by the user to adapt the excitation light intensity on the sample, usually as a countermeasure against the photobleaching of the fluorescent probes.

The *excitation filter* is typically a bandpass filter matching the excitation spectrum of the fluorophores. It is used to filter the white light originally produced by the lamp. The two common types of lamp used in fluorescent microscope setups are mercury or xenon arc lamps. These light sources emit light covering the whole visible spectrum, including ultra-violet and infrared wavelengths, and characterized by distinct peaks at specific wavelengths.



Down the line, the *dichroic mirror* is used as a high-pass light filter. In the ideal case, this mirror reflects the excitation wavelengths of the fluorophores and is transparent to the emission wavelengths. The light filtered by the *excitation filter* thus gets reflected and focused onto the sample via the objective. The objective here acts also as the condenser, which is what defines an epi-illumination system.

After excitation, the fluorescent signal is collected by the objective, then goes through the *dichroic mirror* unaltered and is finally filtered by the *emission filter*. The latter is also a bandpass filter, ideally matching the emission spectrum of the fluorophore type and ensures that only fluorescent emissions get transferred to the image sensor.

Typical filter profiles for the *excitation filter*, the *emission filter* and the *dichroic mirror* are shown on Fig. 2.1. This figure also shows that they work as a whole and are specific to one type of fluorophore profile. The various cut-off frequencies are tuned in order to maximize the excitation light intensity and maximize the amount of photons that gets focused on the sensor, while disregarding the wavelengths within the excitation/emission spectra overlap.

### 2.2.2 Image Formation

A widely used approach to model a fluorescent microscope and the image formation is through a *Linear Translation Invariant* (LTI) system. This is based on the fact that the photons emitted by the fluorescent samples are emitted randomly, which translate into an emitted light that can be considered as incoherent. As a result each point in the sample contributes independently to the final image.

A LTI system is characterized by its impulse response [97]. In the case of microscopy, the impulse response is also known as the 3D intensity *Point-Spread Function* (PSF)  $g_{psf}(x, y, z)$  or incoherent PSF. By definition, the PSF represents the image that is produced by an ideal point source in the object space modeled by a 3D Dirac impulse. For an ideal point source in the object space at position  $(u, v, w)$  the produced image  $I(x_i, y_i, z_i)$  in the image space is

$$I(x_i, y_i, z_i) = g_{psf}(x_i - u, y_i - v, z_i - w) \quad (2.2)$$

which is a linear translation of the incoherent PSF.

This however does not account for the magnification of the objective. Assuming a microscope with  $M$  times magnification and taking into consideration geometrical optics [129], the image  $I(x_i, y_i, z_i)$  produced by an ideal point source in the object space at position  $(u, v, w)$  is

$$I(x_i, y_i, z_i) \propto g_{psf}\left(\frac{x_i}{M} - u, \frac{y_i}{M} - v, \frac{z_i}{M^2} - w\right) \quad (2.3)$$

which is a linear translation of a scaled version of the incoherent PSF. Note that the lateral magnification is  $M$  while the axial (along the optical axis) magnification is  $M^2$ .

## Chapter 2. Fluorescence Bioimaging

---

Extending from an ideal point source modelled by a 3D Dirac impulse to a sample represented by an object function  $O(x, y, z)$ , the image produced in the image space is given by a convolution expression

$$I(x_i, y_i, z_i) \propto (O * g_{psf})(x_i, y_i, z_i) \quad (2.4)$$

$$\propto \int_{\mathbb{R}^3} O(x, y, z) g_{psf}\left(\frac{x_i}{M} - x, \frac{y_i}{M} - y, \frac{z_i}{M^2} - z\right) dx dy dz \quad (2.5)$$

where  $*$  is the convolution operator. The object function  $O(x, y, z)$  is characteristic of the sample. It represents the ability of the sample to fluoresce at the wavelength  $\lambda_{em}$ . It is in direct relation with the illumination intensity, the distribution of the fluorophores in the sample and all their optical characteristics (see Section 2.1).

Light can be described and treated as an electromagnetic wave and, as such, responds to Maxwell's equations. The diffraction theory of optical systems was derived from them [10] and eventually led to various models for the widefield PSF of microscopes. The incoherent PSF  $g_{psf}(x, y, z)$  as used hereabove is the intensity impulse response. It is related to the complex-valued amplitude impulse response  $h_{\lambda_{em}}(x, y, z)$ , also called coherent impulse response, of the optical system. For a widefield microscope we have [150]

$$g_{psf}(x, y, z) = |h_{\lambda_{em}}(x, y, z)|^2 \quad (2.6)$$

The fact that the light intensity (i.e. the energy per unit of time) is favored compared to the amplitude and phase of the emission light in the image formation process is linked to existing light sensing technologies. Available light detectors for microscopy (see Chapter 3) are only sensitive to the intensity of the incident light. They cannot measure directly the radiation amplitude and phase separately.

The amplitude impulse response at a given wavelength  $\lambda$  is given by the 2D Fourier transform [45]

$$h_{\lambda}(x, y, z) = \int_{\mathbb{R}^2} P(u, v) \exp\left(2\pi i \sqrt{(n/\lambda)^2 - (u^2 + v^2)}\right) \exp(2\pi i (xu + yv)) du dv \quad (2.7)$$

where  $P$  is a complex expression referred to as the pupil function of the microscope and  $n$  is the refractive index of the object medium.

Assuming the special case of aberration free optics and circular aperture, the amplitude impulse response can also be derived from the Debye diffraction integral [150]

$$h_{\lambda}(x, y, z) = C_0 \int_0^{\alpha} \sqrt{\cos\theta} J_0\left(kn\sqrt{x^2 + y^2} \sin\theta\right) \exp(-ikz \cos\theta) \sin\theta d\theta \quad (2.8)$$

where  $J_0$  is the zeroth-order Bessel function of the first kind,  $C_0$  is a complex constant,  $k = 2\pi/\lambda$

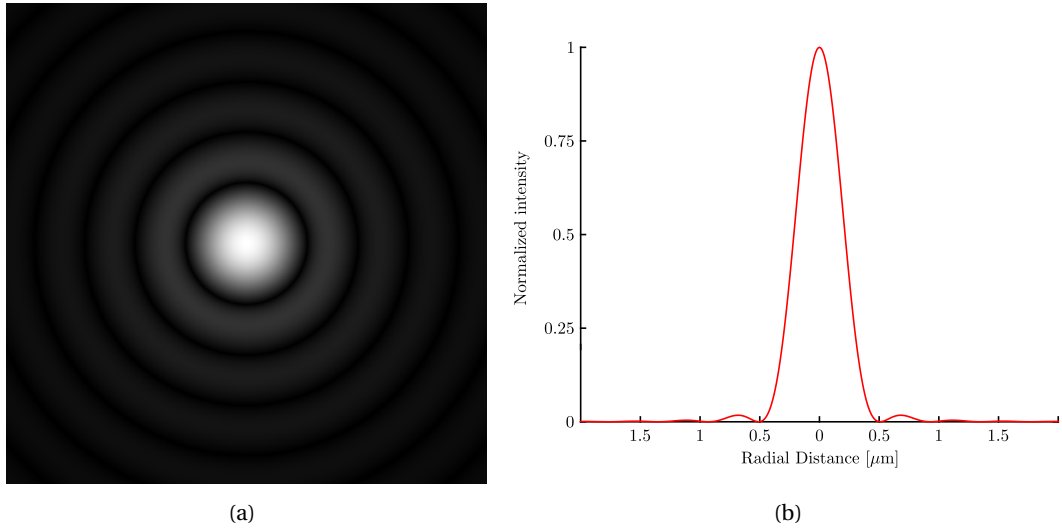


Figure 2.7 – Aberration free intensity PSF. (a) The *Airy disk* pattern is the incoherent PSF characteristic of an ideal (i.e. no aberration) in-focus diffraction-limited microscope setup. The depicted Airy pattern was generated from Eq. (2.10) with  $n = 1$ ,  $N_A = 0.6$  and  $\lambda = 500\text{nm}$ . It represents a surface of  $2\mu\text{m} \times 2\mu\text{m}$ . Note that the graylevels used were adjusted in order to visually enhance the peripheral disks. (b) Radial profile of the Airy disk in (a).

is the wavenumber and  $\alpha$  is the maximal convergence semi-angle of the objective as defined in Fig. 2.6. Under the paraxial condition ( $\sin \alpha \approx \alpha$ ), Eq. (2.8) asymptotically tends to

$$h_\lambda(x, y, z) = \alpha^2 C_0 \exp(-ikz) \int_0^1 J_0 \left( knt \sqrt{x^2 + y^2} t \sin \alpha \right) \exp \left( -\frac{ikz}{2} t^2 \sin^2 \alpha \right) t dt \quad (2.9)$$

Note that in Eq. (2.7) (2.8) and (2.8) the depth coordinate  $z$  represents the defocusing effect.

Figure 2.7 shows the intensity PSF generated by a point source on the focus plane for a widefield microscope, assuming aberration free optics and the paraxial approximation. This pattern is commonly known as the *Airy disk* pattern. It is derived by solving Eq. (2.9) by setting  $z = 0$  and injecting the resulting expression in Eq. (2.6)

$$g_{psf}(x, y, z)|_{z=0} = \left( 2 \frac{J_1(kN_A \sqrt{x^2 + y^2})}{kN_A \sqrt{x^2 + y^2}} \right)^2 \quad (2.10)$$

where  $J_1$  is the first-order Bessel function of the first kind and  $N_A = n \sin \alpha$  is the numerical aperture of the objective.

### 2.2.3 Optical Limit and Resolution

The spatial resolution of a microscope system is one of the most important parameter to be aware of. It represents the ability of the system to resolve (i.e. to distinguish) two spatially close structures within the sample. The spatial resolution is finite and is a consequence of the diffraction of light. As explained in the previous section, a point source results in a diffraction pattern, which in the ideal case is an *Airy disk* pattern.

In order to be able to resolve two point sources in the focal plane, one must be able to separate their diffraction patterns. The optical resolution of a microscope system is defined as the minimum distance by which the two point sources must be separated for them to be resolved. The optical resolution can be defined for every technique designed for separating two overlapping diffraction patterns.

There are however two criteria that are commonly used to numerically attribute a resolving power to an optical system: Abbe's limit and Rayleigh's distance. Both of them are based on the *Airy disk* pattern equation (Eq. (2.10)); more specifically, they are a function of the size of the *Airy disk*, which is impacted by the light wavelength  $\lambda$  and the numerical aperture  $N_A$  of the objective.

Abbe's limit is defined as the half-amplitude diameter of the central peak of the *Airy disk*

$$d_{Abbe} = \frac{\lambda}{2N_A} \quad (2.11)$$

and Rayleigh's distance is defined as the radius of the *Airy disk*. That is the distance between the peak of the diffraction pattern and the first zero.

$$d_{Airy} = 1.22 \frac{\lambda}{2N_A} \quad (2.12)$$

Basically, what is to retain from these two criteria is that the resolving distance is proportional to the wavelength and inversely proportional to the numerical aperture. Practically, one should select a fluorophore emitting in the short wavelengths while imaging it with a high numerical aperture objective in order to maximize the spatial resolution. This however does not take into account other essential parameters related to the image sensors that are discussed in Chapter 3.

As examples, Table 2.1 summarizes the resolving power as defined by Rayleigh's distance for a range of common objectives used in fluorescence widefield microscopy at various wavelengths ranging from ultra-violet to infrared light.

Table 2.1 – Spatial resolution for various objectives at various wavelengths according to Rayleigh’s criterion (Eq. (2.12)).

$M$	$N_A$	$\lambda = 400\text{nm}$	$\lambda = 500\text{nm}$	$\lambda = 600\text{nm}$	$\lambda = 700\text{nm}$
100×	1.4	174nm	218nm	261nm	305nm
60×	1.4	174nm	218nm	261nm	305nm
60×	1.95	257nm	321nm	385nm	449nm
40×	1	244nm	305nm	366nm	427nm
40×	0.95	257nm	321nm	385nm	449nm
20×	0.75	325nm	407nm	488nm	569nm
10×	0.45	542nm	678nm	813nm	949nm
4×	0.2	1,220nm	1,525nm	1,830nm	2,135nm
2×	0.1	2,440nm	3,050nm	2,660nm	4,270nm

## 2.3 Chapter Summary

This chapter proposes an introduction to the various techniques commonly used in fluorescence imaging. It consists of two main sections: one dedicated to the fluorescent biomarkers and the other dedicated to the description and principle of operation of a classical epi-fluorescent microscope.

The first half of the chapter provides an overview of the range of techniques used to tag biomarkers *in vitro* with a specific fluorescent probe. An initial review of the fluorescence phenomenon is given along with some of its limitations and specificities. Next, a few classes of fluorescent nanoprobe are described along with common staining techniques used to bind them to biomarkers. Given the huge amount of probes available today, only a few predominant ones are detailed. In particular, the *organic fluorophores* and *fluorescent nano-particles* are of interest within the scope of this thesis as they are used in the various experiments presented throughout.

The second half of the chapter describes the principle of operation of a classic epi-fluorescence microscope. It provides a simplified view of the various components involved in such microscopic system and highlights how they take advantage of the Stokes’ shift to isolate and image the fluorescent signal. Furthermore, a mathematical description of the imaging process occurring in a fluorescent microscope is given by modeling the optics as a *Linear Translation Invariant (LTI)* system. This lays down the foundation for the synthetic image generator tool presented in the upcoming Chapter 4.

To have a digital transduction of the fluorescent biological information, the use of image sensor arrays capturing and digitizing the fluorescent signal is required. The concept and operation of these light sensors are described in the next chapter.



## 3 Image Sensor Technologies

In Chapter 2, we have discussed the biochemistry of fluorescent nanomaterials and the required optics for filtering out the fluorescent signal. However, as we argued in Chapter 1, the quantification revolution that occurs in fluorescent bioimaging is happening thanks to the development of light sensing technologies. This chapter focuses on light sensing arrays commonly used on widefield fluorescent microscopy setups: *Complementary Metal Oxide Semiconductor* (CMOS) image sensors and *Charge Coupled Device* (CCD) image sensors.

The CCD image sensors have traditionally been used for producing high quality images. Ever since their advent, they have been dominating the market in various research areas such as microscopy. The CCD technology initially provided better *Signal-to-Noise Ratio* (SNR) and higher sensitivity than CMOS sensors. This lead researchers and equipment manufacturers to use and supply this technology. There exists an extensive literature using CCD sensors to leverage results of biological assays obtained via fluorescence microscopy. This remains a general truth today in spite of the huge research effort that went into improving CMOS processes for light sensing. However, CMOS sensors appear to overcome CCD sensors for the range of applications where low cost, low power and high level of integration are non negligible design constraints. This is the case for consumer electronics as well as for some specific research areas such as biomedical or *Lab-on-a-Chip* (LoC) applications. For example, CMOS sensors are favored for the design and fabrication of miniaturized fluorescent microscopes aiming at *in situ* tissue monitoring [38, 83] or within integrated systems such as LoCs [94, 105] or *Point-of-Care* (PoC) systems [89].

Each of these two technologies have distinct advantages and disadvantages that need to be understood in the scope of fluorescent bioimaging. This chapter aims at providing a quick review of these two technologies, detailing their principle of operation and basic pixel structures along with common sensor array architectures. Finally, various sensor characteristics and performance parameters are highlighted in order to identify the various limitations related to fluorescent microscopy, or low light imaging in generally, that need to be careful controlled when selecting an image sensor for a particular experiment.

### 3.1 Principle of Operation

A typical image sensor consists of a 2D array of photosensitive elements used for sampling the spatial distribution of an incident electromagnetic radiation. For example, the array of sensors is carefully placed at the focal plane of a microscope fluorescent setup in order to measure the intensity of the focused and magnified fluorescent radiation. When talking about the CMOS and CCD technologies, we are interested in the operation of silicon based photodetectors that are built relying on the photoconductivity effect in order to convert incident photons into a measurable electrical signal; in particular, the *photodiode* and the *photogate* are the two types of photodetectors typically used for building CMOS image sensors and CCD image sensors respectively.

#### 3.1.1 Solid-State Photosensing

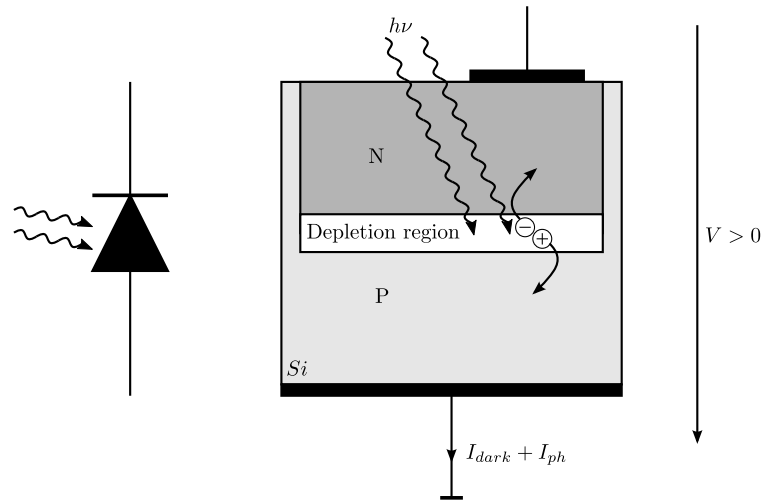
Solid-state photosensing is based on the photoconductivity phenomenon in semiconductors by which the absorption of incident photons induces the generation of electron-hole pairs. More specifically, these materials are characterized by a bandgap energy  $E_g$  that is defined as the energy difference between the highest valence band and the lowest conduction band [116]. This bandgap energy is the energy that is required to free an outer shell electron from its bounds to an atom nucleus and becomes a mobile charge carrier. It is an important parameter for using a solid as a radiation detection material as it is equal the minimum energy  $E = h\nu$  that an incident photon must carry in order to create an electron-hole pair within the material. Incidentally, this defines the maximal wavelength from which incident photons will trigger the photoconductivity phenomenon. In the case of an intrinsic silicon crystal characterized by a bandgap of  $E_g = 1.12\text{eV}$ , the maximal wavelength is about 1,107nm. This characteristic makes silicon devices ideal for visible light sensing (wavelength between 390nm to 700nm) and thus for fluorescence microscopy.

In the absence of an electric field, any electron-hole pair that is generated in the material tends to recombine after a specific amount of time and the energy that was absorbed gets re-emitted or heat dissipated. The presence of an electric field is required to separate the generated charge carriers and prevent them from recombining. As a result, they can be converted into an electric signal and perform as a radiation detector. There exists many types of photodetector performing this action [128], out of which we are interested in the *photodiode* and *photogate* constructs.

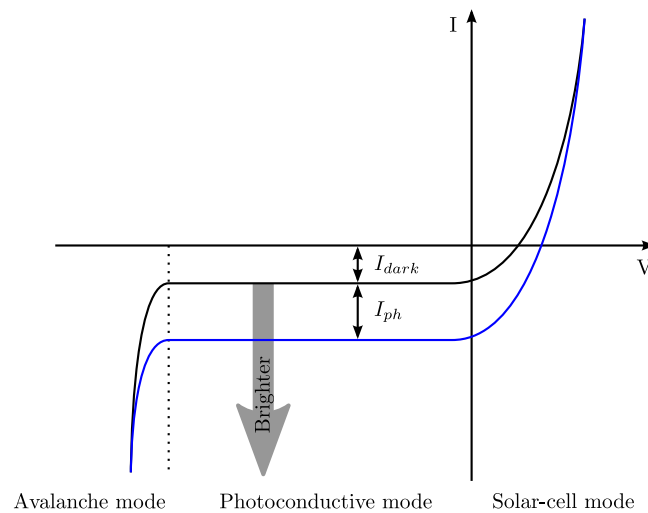
#### 3.1.2 Photodiodes

The basic light sensing element used in CMOS image sensors is the photodiode. It is based on the properties of the junction between *p*-type and *n*-type silicon semiconductors as shown in the cross-section on Fig. 3.1(a). In particular, the electric field that forms in the depletion region at the *p-n* junction is used to separate the photogenerated carriers. Whenever an





(a) Photodiode cross section



(b) Photodiode I-V curve

Figure 3.1 – (a) Basic structure of a photodiode when reversed biased for operation in the *Photoconductive mode*. (b) I-V curve of a typical photodiode. The gray arrow shows how the curve is modified when the photodiode is under illumination. Depending on the biasing, the *Avalanche mode*, the *Photoconductive mode* and the *Solar-cell mode* can be selected. A photodiode is typically operated in the *Photodiode mode* where the photocurrent current  $I_{ph}$  is proportional to the incident light intensity.

electron-hole pair is generated within the depletion layer due to an absorbed photon, the electric field forces the electron towards the *n*-type region and the hole towards the *p*-type region. In circuit, this movement of carrier induces an electrical current  $I_{ph}$  which can be

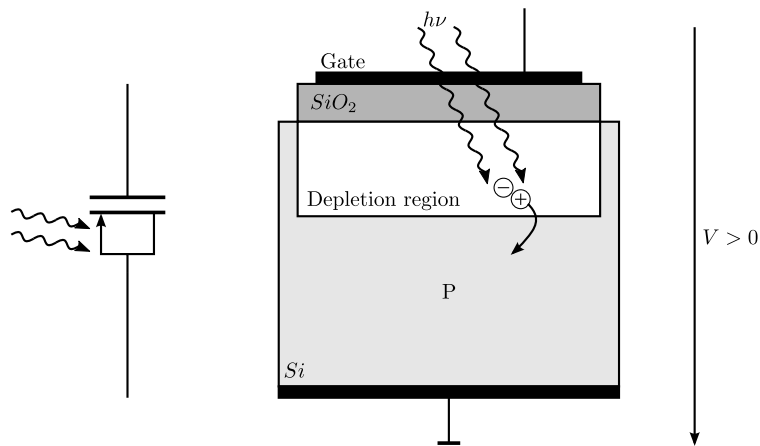


Figure 3.2 – Cross section of a photogate based on a biased MOS capacitor.

measured and quantified.

A photodiode has three modes of operation as shown on the generic I-V curve in Fig. 3.1(b). The *avalanche mode* and the *photoconductive mode* are used for photon detection and quantification. The *avalanche mode* is achieved by reverse biasing the photodiode beyond the breakdown voltage. In this mode each absorbed photon generates multiple electron-hole pairs due to the avalanche effect. This is used to create single photon detection sensors known as *Single Photon Avalanche Diodes (SPADs)* [68, 115]. However, most CMOS image sensors are operating photodiodes within the *photoconductive mode*. This mode is achieved by reverse biasing the photodiodes without reaching the breakdown voltage. It is characterized by a linear relationship between the photogenerated current  $I_{ph}$  and the incident light intensity rendering photon quantification possible.

### 3.1.3 Photogates

The photogate is the photodetector used in CCD sensors. As shown in the cross-section in Fig. 3.2, it is based on a *Metal-Oxide-Semiconductor (MOS)* capacitor. In its basic form, this device consists of a polysilicon gate isolated from the *p*-type silicon by a layer of silicon oxide. Whenever biased accordingly (Fig. 3.2), a depletion region is created under the insulator within the *p*-type silicon. Similarly to the depletion layer in the photodiode, the resulting local electric field is used to separate the photogenerated carriers. Unlike the photodiodes, which exhibit a photocurrent when exposed to light, photogates accumulate negative charges within the depleted region (i.e. on the MOS capacitor) at a rate proportional to the light intensity.

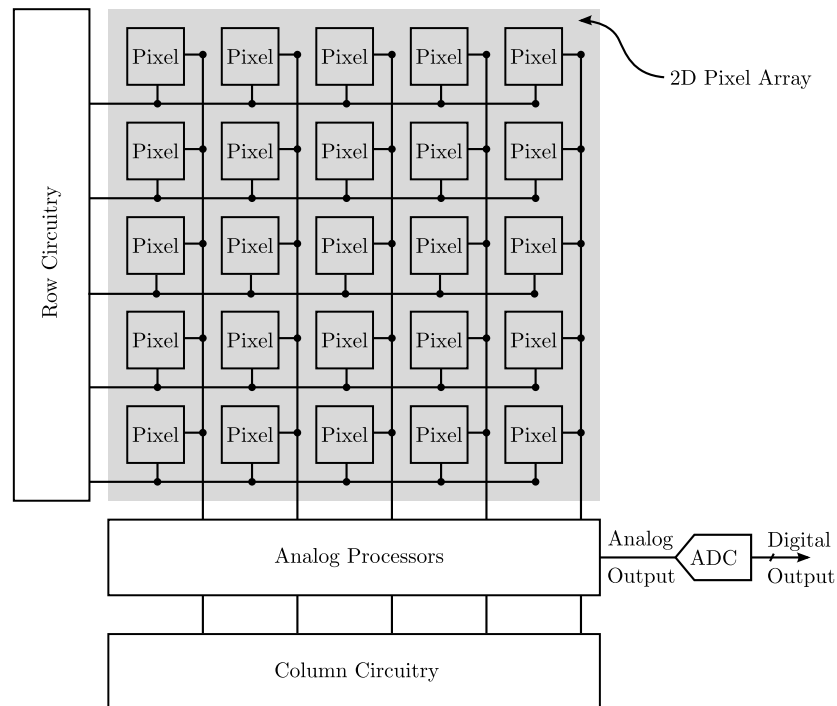


Figure 3.3 – General view of CMOS image sensors.

## 3.2 CMOS Sensor Architecture

A generic architecture for a CMOS image sensor is depicted in Fig. 3.3. It consists of an array of pixels which can be randomly accessed via dedicated column and row circuitry, much like a digital memory except that analog data is read out and buffered or amplified using row analog processors. Each pixel is a construct of a photodiode and of front-end electronics. There exist two main categories of pixels used in CMOS sensors: *Passive Pixel Sensor (PPS)* and *Active Pixel Sensor (APS)* (Fig. 3.4). The pixels are responsible for the integration of the photoconductive current  $I_{ph}$  that is continuously produced under light exposure by discharging a local capacitor. Practically, the parasitic capacitor  $C_{pd}$  of the photodiode is often used for this purpose.

### 3.2.1 Passive Pixel Sensors

The PPS architecture was at the heart of the first CMOS image sensors on the market [63, 84]. As shown in Fig.3.4(a), the pixel circuit consists of a photodiode and a single access transistor. The PPS operation has two distinct phases. The exposure phase starts with the local parasitic capacitor  $C_{pd}$  charged to a reference voltage  $v_{ref}$ . As the photodiode is exposed to light and the access transistor is off, the photocurrent discharges  $C_{pd}$ . In the second phase, the access transistor is on and connects the pixel to the column bus. Typically, each column bus has

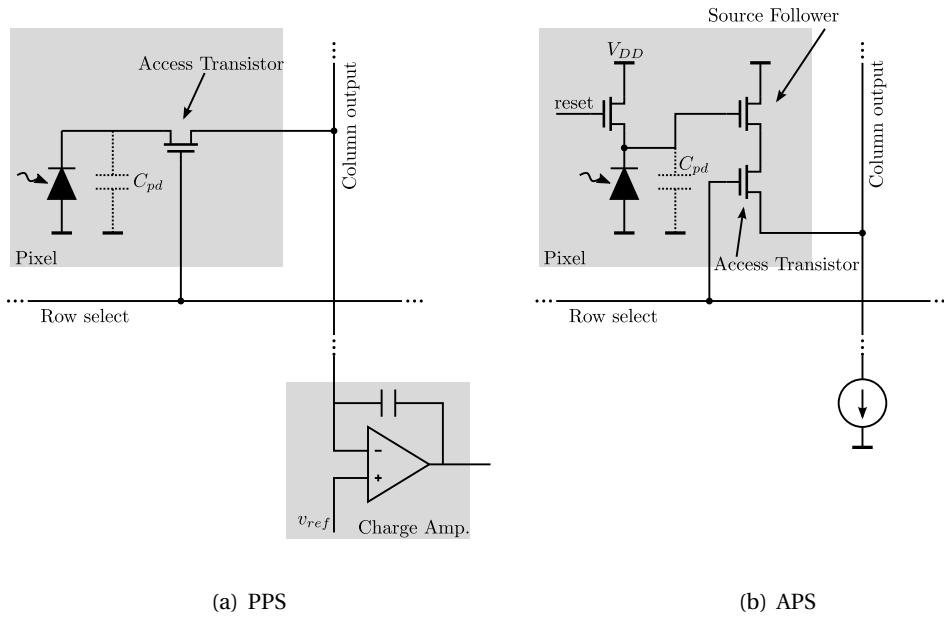


Figure 3.4 – (a) *Passive Pixel Sensor* architecture based on a single access transistor. (b) Three transistors based *Active Pixel Sensor* architecture.

a charge amplifier that integrates over time the total charges required to reset the parasitic  $C_{pd}$  to  $v_{ref}$  and produces an output voltage proportional the charges initially produced by photogeneration.

### 3.2.2 Active Pixel Sensors

With the improvement of CMOS technology, the APS pixel architecture eventually replaced the PPS architecture. Essentially, the main difference is that each APS pixel contains a local amplifier. An example of 3-transistors APS pixel design is presented in Fig. 3.4(b). The basic operation involves an initial reset of the  $C_{pd}$  local capacitor to  $V_{DD}$ , followed by the light exposure phase that discharges it with the photoconductive current. The active part comes from the added local source follower that isolates the photodetector charges from the high column capacitor when the access transistor is activated. Whenever the pixel is accessed after the light exposure, the source follower buffers the voltage across  $C_{pd}$  onto the column. In effect, a voltage proportional to the photogenerated charges is directly read out of each APS pixel.

## 3.3 CCD Sensor Architecture

As seen in Section 3.1.3, the basic CCD cell is built based on a MOS capacitor that accumulates charges locally when exposed to light. Unlike CMOS pixel architectures, a typical CCD cell

does not feature front-end electronics. The basic principle onto which an CCD image sensor array is built is the transfer of charges between close-by CCD cells, hence the given name of the technology.

In order to control the flow of charges between adjacent MOS capacitors, one needs to apply a clocking scheme to the control gates of the capacitors. Practically, there exists various clocking schemes that can be used [55]. A simplified overview of a typical clocking scheme using 3-phase clocks is presented in Fig. 3.5. In this case, a single pixel is consists of three CCD cells. The transfer of charges between adjacent MOS capacitors goes as follow. Lets assume that all the charges of a given pixel are gathered in a single MOS capacitor (Fig. 3.5(a)) which is in holding mode (i.e. high voltage on the gate). Putting the adjacent MOS capacitor in holding mode enables the charges to spread under the two gates of the two capacitors (Fig. 3.5(b)). Finally, collapsing the depletion region under the initial MOS capacitor forces all the charges to reside in the adjacent MOS capacitor (Fig. 3.5(c)). This explanation is used to highlight the underlying mechanism of charge transfer in CCD sensors. It is an simplification of what is currently used in modern CCD sensors [55] and whose details are beyond the scope of this thesis.

Architecture-wise, CCD image sensors are commonly found in three flavors: *Full-Frame* CCDs, *Inter-Line* CCDs and *Frame-Transfer* CCDs. The top level of each of these architectures is presented in Fig. 3.6 along with the specific flow of charges between CCD cells.

*Full-Frame* CCDs feature the most straightforward approach. Fig. 3.6(a) shows that every pixel in the sensor array is sensitive to light (depicted in white). Each pixel features a photogate collecting photogenerated charges during the light exposure period. After the exposure period, each row of charges gets shifted downwards until it reaches the output CCD shift register. This shift register is a row of light shielded (depicted in gray) MOS capacitors which serially shifts pixel charges out of the image sensor. The readout of the pixel charges needs to be performed fast enough so that light photogenerated charges during the readout process do not corrupt the captured image. A common way of preventing this data corruption is to add a mechanical shutter shielding the whole sensor during this readout phase. This however makes them incompatible with microscopic applications that require continuous imaging for which the uninterrupted mechanical operation of the shutter is not adapted.

*Inter-Line* CCDs are the most common CCD sensors found in microscopy setups. This architecture is depicted in Fig. 3.6(b). Each pixel features a photodiode (depicted in white) that is used to collect charges during light exposure and a shielded CCD cell (depicted in gray). After the exposure time, the charges collected by the photodiode get immediately transferred to the associated CCD cell before initiating a readout process similar to that of the *Full-Frame* architecture. The advantage of this architecture is that the built-in photodiodes allow for electronic shuttering. Furthermore, while the CCD cells are being read out, the photodiodes can be exposed to light in order to immediately start capturing the next frame. This continuous trait is what makes this architecture popular in various research areas including quantitative

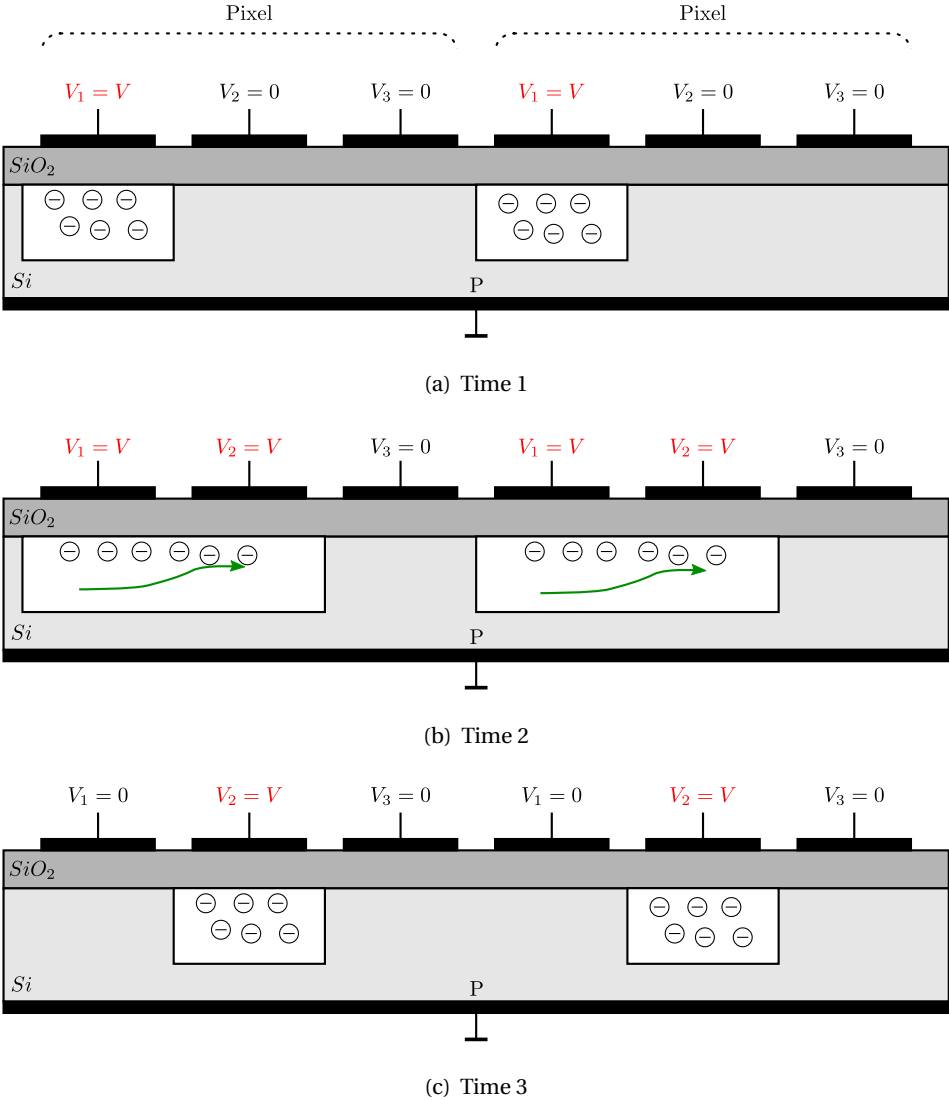
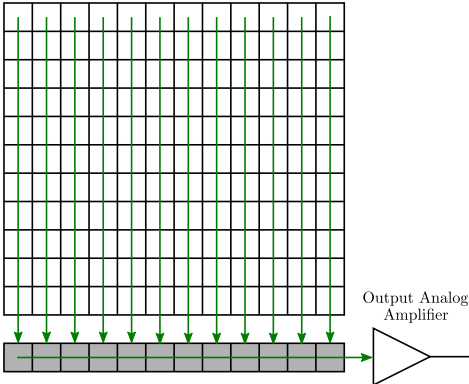
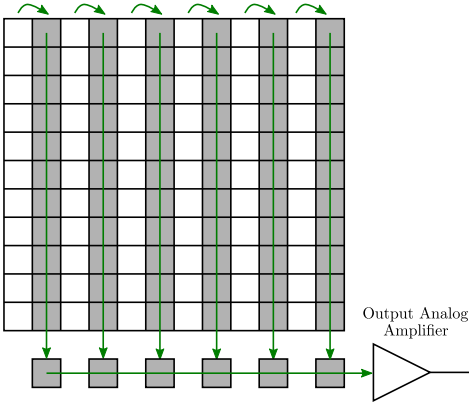


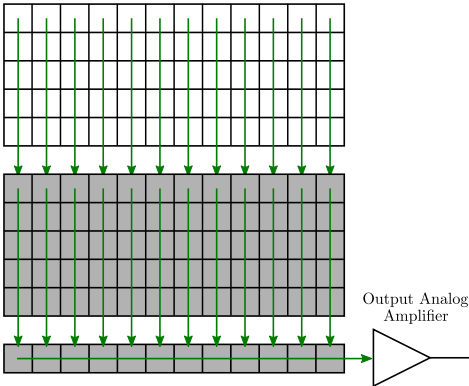
Figure 3.5 – Simplified 3-phases ( $V_1$ ,  $V_2$  and  $V_3$ ) clocking scheme for controlling charges transfer between adjacent MOS capacitors.



(a) Full-Frame



(b) Inter-Line



(c) Frame Transfer

Figure 3.6 – General view of the three common readout techniques used CCD image sensors.

## Chapter 3. Image Sensor Technologies

---

Table 3.1 – Maximal pixel pitch  $P_{max}$  for image sensors based on various microscope objectives given their lateral magnification  $M$ , numerical aperture  $N_A$  and resolution  $d_{Airy}$ . In reference to Table 2.1.

$M$	$N_A$	$d_{Airy}$ ( $\lambda = 400\text{nm}$ )	$P_{max}$
100×	1.4	174nm	8.71 $\mu\text{m}$
60×	1.4	174nm	5.23 $\mu\text{m}$
60×	1.95	257nm	7.71 $\mu\text{m}$
40×	1	244nm	4.88 $\mu\text{m}$
40×	0.95	257nm	5.14 $\mu\text{m}$
20×	0.75	325nm	3.25 $\mu\text{m}$
10×	0.45	542nm	2.71 $\mu\text{m}$
4×	0.2	1,220nm	2.44 $\mu\text{m}$
2×	0.1	2,440nm	2.44 $\mu\text{m}$

fluorescence microscopy.

The *Frame-Transfer* architecture is essentially the *Full-Frame* architecture where half of the CCD wells are shielded against light (Fig. 3.6(c)). These shielded CCD cells are used to quickly receive all the charges collected by the exposed photogates after the exposure period. Similarly to *Full-Frame* CCDs, a mechanical shutter is required to prevent corruption while transferring the charges from the photosensitive area to the shielded CCD cells. This design also allows for pipelining with an image being captured while the previous one is being readout.

### 3.4 Sensor Characteristics

#### 3.4.1 Spatial Resolution

The spatial resolution refers to the size and pitch of the pixels in the sensor array. For microscopic applications, this parameter is critical as we need to ensure that a given image sensor is able to sample the magnified image of the microscope properly.

As detailed in Section 2.2.3, a microscopic setup is a diffraction-limited optical system. The Rayleigh distance  $d_{Airy}$  from Eq. (2.12) relates the minimum distance that the microscopic setup is able to resolve at a specific wavelength for a given numerical aperture.

The maximum pixel pitch  $P_{max}$  that an image sensor can feature is given by *Nyquist's Limit Theorem* [97]

$$P_{max} = \frac{M d_{Airy}}{2} \quad (3.1)$$

where  $M$  is the lateral magnification of the optical setup.

Table 3.1 shows examples of ideal pixel pitches for various optical resolutions given by common



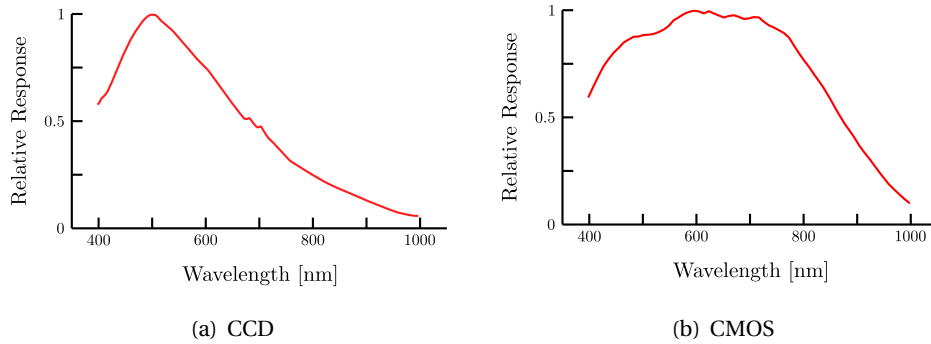


Figure 3.7 – Examples of CCD and CMOS monochromatic spectral sensitivity. (a) Sony ICX274AL CCD sensor. (b) Aptina MT9V032 CMOS sensor.

microscope objectives (see Chapter 2, Table 2.1). The maximal pitch is to be favored since it allows for maximum photosensitive area per pixel. This in turns directly affects the *Full-Well Capacity* and the *Dynamic Range* of the photodetectors (see Section 3.4.3 and 3.4.4).

### 3.4.2 Sensitivity

The *Responsivity* and *Quantum Efficiency* are two common parameters for quantifying the operation of photodetectors. They are responsible for the sensitivity of a light sensor, which incidentally is an important parameter for low light applications such as quantification fluorescence microscopy.

The *Responsivity*  $R_{ph}$  is the gain of the detector. It relates the input-output relationship of a photodetector through the ratio between the photogenerated current  $I_{ph}$  and the incident light power  $P_O$  onto the photosensitive area.

$$R_{ph} = \frac{I_{ph}}{P_O} \quad (3.2)$$

This *Responsivity* has a direct relation with the *Quantum Efficiency* of the photodetector. The *Quantum Efficiency*  $Q_e$  is defined as the probability that an impinging photon will generate a free charge carrier. Considering the number of photogenerated carriers  $N_e = TI_{ph}/q$  over a period of time T and the number of impinging photons  $N_{ph} = TP_O/h\nu$ , the *Quantum Efficiency* is defined as

$$Q_e = \frac{N_e}{N_{ph}} = \frac{\frac{TI_{ph}}{q}}{\frac{TP_O}{h\nu}} = R_{ph} \frac{h\nu}{q} \quad (3.3)$$

where  $q$  is the elementary charge and  $h\nu$  is the energy per photon at the given wavelength.

Due to its dependency to the incident light wavelength, the notion of *Quantum Efficiency* is often extended to the notion of *Spectral Sensitivity* which denotes the relative efficiency of a sensor with respect to the signal wavelength. Fig. 3.7 shows the *Spectral Sensitivity* of a CCD and a CMOS image sensor. For silicon based sensors ( $E_g = 1.12\text{eV}$ ), the *Spectral Sensitivity* typically spans from 200nm to about 1,100nm. These are the limits defined by the wavelengths at which the photoconductive phenomenon can occur (see Section 3.1.1). The *Spectral Sensitivity* of a sensor is often characterized with peak efficiencies at some given wavelengths. When applied to fluorescence microscopy, these ideally need to be matched with the peak emission wavelength of the used fluorescent materials in the biological assays.

### 3.4.3 Fill Factor and Full-Well Capacity

The *Fill Factor* of a sensor is defined as the ratio between the photosensitive area to the total area of a pixel. Due to the low amount of circuitry present in each pixel of CCD sensors, this ratio can easily reach values beyond 90%. However, this value can decrease significantly in CMOS sensors, mainly for APS pixels with large front-end electronics. Modern techniques however tend to increase the *Fill Factor* through the use of microlenses on top of the photodetectors or even by using *Back Side Illumination* where the light reaches the photosensitive areas through the bulk silicon [55, 92].

The size of the photosensitive area, and indirectly the *Fill Factor*, affects the *Full-Well Capacity* of the pixels. This parameter is defined as the total number of photogenerated electrons  $N_{sat}$  that a photodetector is able to hold. This parameter basically defines the saturation level of the photodetector and has to be taken into consideration for high intensity signals and/or prolonged exposures of the sensor to light.

### 3.4.4 Noise Sources

The identification and understanding of the various noises sources acting on image sensors are paramount to evaluate their capabilities. There are mainly two types of noise: *temporal noise* and *spatial noise*.

The *Photon Shot Noise*, the *Dark Current* and the *Read Noise* are the main components of *temporal noise*. This type of noise affects the sensor at the pixel level, has a time-dependency and is non deterministic.

On the other hand, the *spatial noise* is deterministic. Its main components are the *Fixed Pattern Noise* and other pixel level defects (e.g. hot pixels, dead pixels).

The noise generated by the sensor under given imaging conditions (sensor temperature and exposure time) defines the smallest detectable photocurrent. This current is defined as the standard deviation  $\sigma_{nf}$  of the noise floor, i.e. the sum of all detectable noises sources under dark conditions. Combined with the *Full-Well Capacity*, this defines the *Dynamic Range*, i.e.

the ability of a sensor to adequately image both low and high intensity signals.

$$DR = 20 \log_{10} \frac{N_{sat}}{\sigma_{nf}} \quad (3.4)$$

#### Photon Shot Noise

The *Photon Shot Noise* is a fundamental limitation of any photodetector. It is a basic form of statistical uncertainty associated with the quantum nature of photon streams. Any counting problem, such as the photon counting performed by photodetectors, is ruled by the Poisson process. In other words, the number of photogenerated carrier pairs  $N_e$  over a period of time  $T$  is described by the Poisson discrete probability distribution

$$\Pr(N_e = k) = \frac{\exp(-\hat{N}_e) (\hat{N}_e)^k}{k!} \quad (3.5)$$

where  $\hat{N}_e$  is the expected value of  $E(N_e)$ .

The resulting signal-to-noise ratio is the square-root of the signal  $\sqrt{N_e}$ . In other words, the stronger the signal the bigger the signal-to-noise ratio. It comes that, whenever fewer photons are collected as it can be with weak fluorescent signals in fluorescent microscopy, the *Photon Shot Noise* cannot be neglected.

#### Dark Current

As explained in Section 3.1, an electron-hole pair is generated whenever a specific quantity of energy is absorbed in a semiconductor. One way of generating this pair of carriers is with incident photons, which is the concept used by photodiodes and photogates. However, it comes to no surprise that a pair of carriers can also be generated through the thermal agitation of the matter.

Similarly to the photogenerated carriers, thermally generated carriers can get separated by the electric field in the diffusion region of the photodetector (see Section 3.1). This results in the so-called *Dark Current* which charges continuously the photodetectors over time. This *Dark Current* is mostly a function of the temperature  $T$  [116]

$$I_{dark} \propto T^{3/2} \exp\left(\frac{-E_g}{2kT}\right) w \quad (3.6)$$

where  $E_g$  is the bandgap energy of the semiconductor,  $w$  is the thickness of the depletion layer and  $k$  is Boltzmann's constant. The *Dark Current* is a constant noise that competes directly with the signal for charging the photodetectors and thus limits the *Dynamic Range*.

Similarly to the accumulation of photogenerated carriers, the accumulation of thermally generated carriers is also a counting problem. This results in the *Dark Current* also being

governed by Poisson statistics leading to what is known as the *Dark Shot Noise*.

### Fixed-Pattern Noise

Ideally, the generated photocurrent and the *Dark Current* are equal among the pixels in a sensor array under a uniform illumination and fixed temperature. However, there exist spatial variations due to the fabrication process leading to mismatches in these currents between one photodetector to another. This results in what is known as the *Fixed-Pattern Noise* (FPN) when a snapshot is taken.

The FPN is divided in two components [114]; the *Dark Signal Non-Uniformity* (DSNU) and the *Pixel Response Non-Uniformity* (PRNU). The DSNU results from the dark current variability between the individual pixels in the absence of light, while PRNU results from the variability of pixel gain under illumination of the sensor. This type of noise must be dealt with for applications that require big exposure times to the sample light, which is often the case for epi-fluorescence microscopy.

CMOS sensors are more susceptible to this noise compared to CCD sensors due to the multiplication of devices in the front-end electronics per pixel (photodiode, multiple transistors).

### Read Noise

There are many other noise sources that affect the temporal noise in image sensors. Among them, the *reset noise* is generated when resetting the photodetectors prior to light exposure and *readout noise* is added during the readout process of the pixel values. Some *quantization noise* also gets added if the analog signal generated by the sensor array has to be digitized. Environmental noise sources also have an impact and are mainly related to power supply fluctuations and circuitry coupling. The descriptions of these auxiliary noise sources are out of the scope of this chapter and have already extensively been reported in literature [55, 131].

## 3.5 Chapter Summary

This chapter mainly aims at providing an overview of the two competing solid-state light sensing technologies: CMOS and CCD. It is organized in such a way that first the basic concepts about solid-state photosensing are reviewed. These concepts lead to the description of the principle of operation of the two basic photosensors used today: the photogate and the photodiode. The following remaining sections focus on the various architectures applied to the design of CMOS and CCD image sensors. Furthermore, a section is dedicated to the various noise sources inherent to their architecture design.

In order to link back to the introductory section of this chapter, CCD image sensors are currently the *de facto* type of sensors provided with fluorescent microscopy setups despite

their high cost and the huge improvements done in CMOS light sensing. However, CMOS sensors can be a viable alternative in some fluorescent applications [64, 65]. They can be empowered by adequate image processing algorithms and become a cost efficient solution for integrated applications. This is one of the main traits this thesis aims at demonstrating, principally through the use of a low cost and mid-performance CMOS sensor when applied to fluorescent biomarker monitoring.



**Fluorescent Biomarker Monitoring **Part III****  
**From Synthetic Samples to  
Smart Camera Based System**





## 4 Simulated Biological Cells and Synthetic Image Generation

The various techniques employed in quantification fluorescence microscopy rely on the values provided by the image sensors. Signal processing is essential in order to analyze and extract data from microscopic images. The development of image processing algorithms and other image handling systems have to be tested and validated before they can be entrusted into automated or semi-automated systems. The tedious, classical approach is heuristic with algorithms being refined incrementally based on real biological fluorescent images. While this step is still required for a full practical validation, early development cycles and image processing technique comparisons and evaluations can be efficiently performed on simulated data [66, 127].

The use of simulated data for the development, validation and testing of image processing techniques is relevant in the field of bioimaging. The creation of biological samples represents an investment in time and money. Distinct biological samples created using the same protocol will not yield identical images simply due to the inherent intractable number of experimental parameters influencing them. Furthermore, the development and evaluation of image processing techniques applied to imaged ill-understood biological processes is hindered by the fact that the desired output is unknown. Synthetic image simulators can help in the process by providing synthetic data along with a well defined framework.

In this chapter, a synthetic image generation tool is presented. This tool uses a parametric model to emulate a fluorescently stained population of cells. This population gets imaged at the level of single fluorophore by simulating the image formation process of an epi-fluorescence widefield microscope (Chapter 2) and by the sampling action of an image sensor array (Chapter 3). Existing synthetic image generators for fluorescence bioimaging only simulate biological samples at the cellular level (cells or cell organelles) [66, 67, 127]. The approach used to generate synthetic images presented in this chapter is an extension of the work that was originally published in [33].

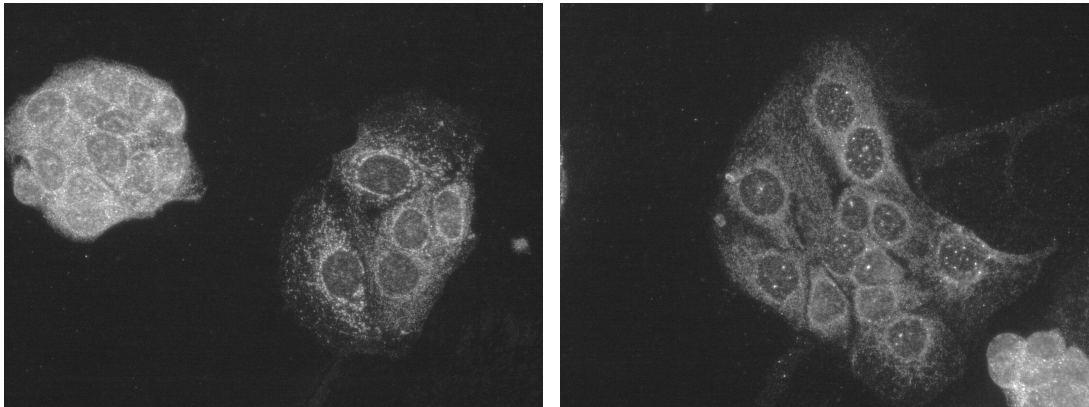


Figure 4.1 – Real images acquired from Caco-2 human cells with fluorescently stained TRL2 receptors.

### 4.1 Synthetic Image Generation Tool

#### 4.1.1 Simulation and Emulation Strategy

The overall strategy for generating realistic images is to model the imaging system as a whole and match an actual epi-fluorescence microscopy setup as detailed in Section 2.2.1. That is we need to consider the fluorescent stained sample on one hand and the optical setup on the other.

First, we need to solve the problem of emulating a fluorescent sample. Fluorescence microscopy uses various dyes in order to label biological structures or molecules of interest. In other words, one can abstract a fluorescent sample by a cloud of fluorescent molecules with a specific distribution in space dictated by the geometry of the cells and their inner distribution of the biological targets. Section 2.1.3 highlights various fluorescence staining techniques that practically attach multiple fluorophores to a single biological target. Additionally, multiple targets can be clustered together in a region typically smaller than the optical resolution. This leads our simulation strategy to consider and define clusters of fluorophores. A cluster of fluorophores is the smallest element to deal with and has a defined position in space matching the location of a single biological target. Emulating a fluorescent biological sample requires to use a model of the biological target distribution and associate a cluster of fluorophores with each one. Arguably, biological samples always contain multiple cells, often clustered together as shown in Fig. 4.1. Thus, the synthetic image generation tool must provide the possibility of generating a population of cells. This lead to a hierarchical concept where a sample is a population of cells, a population of cells is a collection of clusters of cells, a cluster of cells is a collection of fluorescent clusters and a fluorescent cluster is a group of one or many fluorophores.

Second, given this cloud of fluorescent clusters, the synthetic image generation tool needs

Table 4.1 – User-defined input parameters for the generation of cell populations.

Parameter	Unit	Description
$w \times h$	$\mu\text{m} \times \mu\text{m}$	Sample area
$N_{cc}$	ADU	Desired amount of cell clusters
$[N_{min} \cdot \cdot N_{max}]$	ADU	Range of desired number of cells per cell cluster
$\sigma_c$	$\mu\text{m}$	$\sigma$ for randomizing cell centers around cell cluster centers
$r_c$	$\mu\text{m}$	Cell radius
$r_n$	$\mu\text{m}$	Nucleus radius
$k$	ADU	Number of Spline knots for modeling cell nuclei and cytoplasm
$[-\alpha, \alpha]$	$\mu\text{m}$	Range for randomizing knots polar coordinates (radial)
$[-\beta, \beta]$	rad	Range for randomizing knots polar coordinates (angular)
$D$	$1/\mu\text{m}^2$	Density of fluorescent clusters
$[n_{min} \cdot \cdot n_{max}]$	ADU	Range of desired amount of fluorophores per fluorescent cluster
$[-d, d]$	$\mu\text{m}$	Depth range for out-of-focus fluorescent clusters
$o_{max}$	ADU	Maximal allowed overlap between cells

to simulate the imaging process. Each fluorophore cluster is considered to be a single point in space emitting photons at a given rate and at a certain wavelength. The tool simulates the optical properties of a widefield epi-fluorescent microscope by considering the PSF of the optical system. A proper model of the PSF is used to generate a diffraction pattern of the fluorescent clusters. Finally the behavior of an image sensor is simulated by sampling the diffraction pattern, which results in the desired synthetic image of the cell population.

#### 4.1.2 Cell Population Simulation

The primary task of the synthetic image generation tool is the generation of a cloud of fluorescent clusters in the object space. The methodology applied to achieve this goal is hierarchical. First, a population of cells is generated. Each cell location is randomly generated and the cell shapes are based on a parametric model [66] [67]. Second, a random distribution of fluorescent clusters is assigned to each cell. This population generation is driven by a set of user-defined input parameters. Table 4.1 provides an overview of these parameters.

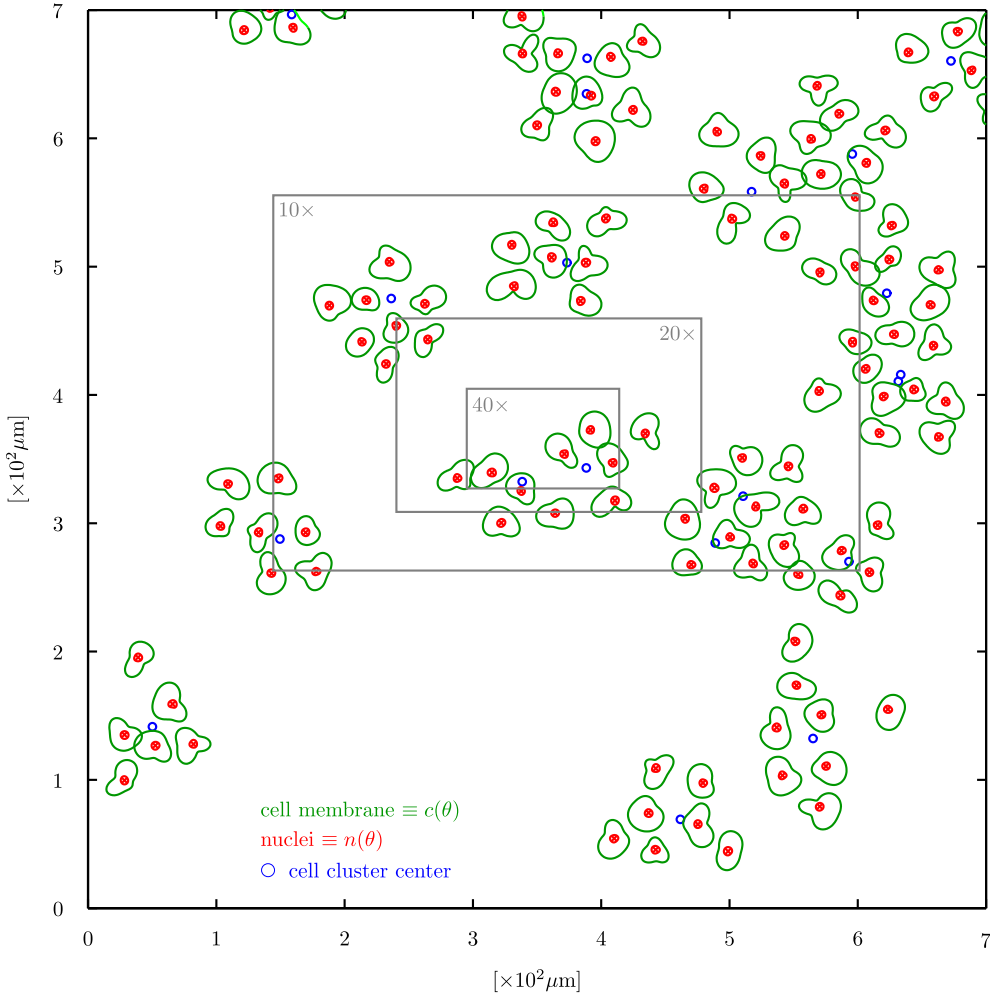


Figure 4.2 – Example of cell population.

### Cell Population

In order to generate a cell population, we first define a rectangular sample area where the cells are distributed. Let us define it as a subset of  $\mathbb{R}^2$  such that

$$\mathbf{S} = \left\{ (x, y) \in \mathbb{R}^2 : -\frac{w}{2} \leq x \leq \frac{w}{2}, -\frac{h}{2} \leq y \leq \frac{h}{2} \right\} \quad (4.1)$$

where  $w$  and  $h$  are the width and height of the sample area. These are user specified parameters and are typically in the order of hundreds of micrometers.

Let us assume we want to distribute  $N_{cc}$  cell clusters on this sample area. We start by defining the finite set of cell cluster centers  $\mathbf{CC}$  such that  $\mathbf{CC} \subset \mathbf{S}$  and its cardinality is  $|\mathbf{CC}| = N_{cc}$ . Each element of  $\mathbf{CC}$  is randomly selected from the bivariate uniform distribution  $\mathcal{U}_2$  defined on  $\mathbf{S}$

$$\mathbf{CC} = \left\{ \mathbf{cc}_i \in \mathbf{S} : i \in [1 \dots N_{cc}] \right\} \quad (4.2)$$

$$\mathbf{cc}_i \sim \mathcal{U}_2 \left( \left[ \begin{array}{c} -w/2 \\ -h/2 \end{array} \right], \left[ \begin{array}{cc} w/2 & \\ & h/2 \end{array} \right] \right) \quad (4.3)$$

The elements of  $\mathbf{CC}$ , noted  $\mathbf{cc}_i$ , are ordered pairs representing the Cartesian coordinates of the cell cluster indexed by  $i$ . The notation  $\sim$  indicates that the  $\mathbf{cc}_i$  are random variables selected based on the specified distribution, a bivariate uniform distribution  $\mathcal{U}_2$  in this case.

The next step is to define the number of cells within each cluster and their location. The number of cells  $N_i$  for the  $i^{th}$  cluster is randomly selected based on uniform distribution  $\mathcal{U}$  defined within the user-defined integer range  $[N_{min} \dots N_{max}]$ , that is  $N_i \sim \mathcal{U}([N_{min} \dots N_{max}])$ .

As for their location, the cell centers are distributed randomly around the cell cluster center using a bivariate normal distribution  $\mathcal{N}_2$ . With this we can define the set of all cell centers forming the cell population  $\mathbf{P}$

$$\mathbf{P} = \left\{ \mathbf{p}_k \in \mathbb{R}^2 : k \in \left[ 1 \dots \sum_{i=1}^{N_{cc}} N_i \right] \right\} = \bigcup_{i=1}^{N_{cc}} \mathbf{C}_i \quad (4.4)$$

where  $|\mathbf{P}| = \sum_{i=1}^{N_{cc}} N_i$  is the total number of cells in the population and  $\mathbf{C}_i$  is the set of cell centers for the  $i^{th}$  cell cluster with  $|\mathbf{C}_i| = N_i$ . The family of sets  $\mathbf{C}_i$  is defined using

$$\mathbf{C}_i = \left\{ \mathbf{cc}_i + \mathbf{c}_{ij} \in \mathbb{R}^2 : j \in [0 \dots N_i - 1] \right\} \quad (4.5)$$

$$\mathbf{c}_{ij} \sim \mathcal{N}_2 \left( \left[ \begin{array}{c} 0 \\ 0 \end{array} \right], \left[ \begin{array}{cc} \sigma_c^2 & 0 \\ 0 & \sigma_c^2 \end{array} \right] \right) \quad (4.6)$$

such that the  $\mathbf{c}_{ij}$  are ordered pairs randomized based on a symmetric bivariate normal distribution  $\mathcal{N}_2$  of mean  $[0, 0]^T$  and of standard deviation  $\sigma_c$ . The  $\mathbf{c}_{ij}$  represent the Cartesian coordinates of the cell indexed by  $j$  with respect to the center  $\mathbf{cc}_i$  of the cell cluster indexed by  $i$ .

### Single Cell

With the central location of each cell known and accounted for in  $\mathbf{P}$ , we then need to define the shape of the nucleus and of the cytoplasm for each cell. That is, we aim at generating two polar equations  $n(\theta)$  and  $c(\theta)$  defining closed shapes for each cell, one modeling nucleus boundary and the other modeling the cell boundary. Furthermore, we also have the constraint

$$\max(n(\theta)) < \min(c(\theta)) \quad , \quad \forall \theta \in [0, 2\pi] \quad (4.7)$$

ensuring that the nucleus remains within the cytoplasm.

An existing parametric shape model [66] [67], which is described hereafter, is used to generate such shapes. It is based on randomly displacing the vertices of a regular polygon prior to interpolating them with a closed spline.

Let us assume we want to generate a closed shape  $r(\theta)$ . We start with a regular polygon with  $k$  edges having a circumradius of  $r$ . The polar coordinates of each vertex defining such a polygon are

$$\begin{bmatrix} r_l \\ \theta_l \end{bmatrix} = \begin{bmatrix} r \\ \frac{2\pi l}{k} \end{bmatrix} \quad , \quad l \in [1 \dots k] \quad (4.8)$$

where  $i$  is the vertex index. The vertices coordinates are then uniformly randomized following

$$\begin{bmatrix} r_l \\ \theta_l \end{bmatrix} \rightarrow \begin{bmatrix} r_l + R \\ \theta_l + \Theta \end{bmatrix} \quad , \quad l \in [1 \dots k] \quad (4.9)$$

where  $R \sim \mathcal{U}([- \alpha, \alpha])$  and  $\Theta \sim \mathcal{U}([- \beta, \beta])$  such that  $\alpha < R$  and  $\beta < \frac{\pi l}{k}$ . The target function  $r(\theta)$  can be obtained by performing a cubic spline interpolation using the randomized vertices coordinates as the spline knots. This technique is applied for defining  $n(\theta)$  and  $c(\theta)$  for each cell in the population. The user specifies the circumradius of the cytoplasm and nucleus giving control over the cell size and the  $k, \alpha, \beta$  user-defined parameters are used to tweak the shape in order to generate more or less intricate nuclei and cell shape designs. Examples of generated cytoplasmic and nucleic shapes are depicted in Fig. 4.3.

Providing shapes for the cells is not enough, one need to consider the overlapping between cells and mitigate it. The goal is to prevent adding a new cell to the final population if it would overlap extensively with any other present cell. To this end, the generation tool associates a cell radius  $R$  with each newly generated cell.

$$R = \max(c(\theta)) \quad (4.10)$$

and then compares it to the radius of the previously generated cells using an overlapping

metric defined by

$$o_{i,j,u,v} = \frac{\|\mathbf{x}_k - \mathbf{x}_l\|}{R_k + R_l} \quad (4.11)$$

where  $\mathbf{x}_k$  and  $\mathbf{x}_l$  are the cell center coordinates and  $R_k$  and  $R_l$  are the associated cell radii. When a new cell is generated, it only is committed to the final cell population  $\mathbf{P}_f$  if its overlap with all the cells already in the final population is below a certain threshold  $o_{max}$ . Incidentally, the value of this threshold has a direct impact on the sparsity of the cells in the population. In the end the final population is such that  $\mathbf{P}_f \subseteq \mathbf{P}$ .

### Fluorescent Target Clusters

The generation of the cloud of fluorescent clusters is the final step for the cell population simulation. Based on the assumption that biomarkers are located within the cytoplasm, the tool randomly distributes fluorescent clusters within the cytoplasm of each cell within  $\mathbf{P}_f$ . That is, the location of each fluorescent cluster around a given cell center is selected by generating random cylindrical coordinates

$$\begin{bmatrix} r_f \\ \theta_f \\ z_f \end{bmatrix} = \begin{bmatrix} \text{crop}(n(\theta_f) + |R_f|, c(\theta_f)) \\ \Theta_f \\ Z_f \end{bmatrix} \quad (4.12)$$

where  $n(\theta)$  and  $c(\theta)$  are the nucleic and cytoplasmic shapes as defined earlier,  $R_f$ ,  $\Theta_f$  and  $Z_f$  are random variables.  $R_f$  follows a normal distribution  $R_f \sim \mathcal{N}(0, \sigma_f)$ ,  $\Theta_f$  follows a uniform distribution  $\Theta_f \sim \mathcal{U}([0, 2\pi])$  and  $Z_f$  also follows a uniform distribution  $Z_{th} \sim \mathcal{U}([-d, d])$ . In particular, a z-axis coordinate is generated randomly for each fluorescent cluster with the  $[-d, d]$  depth range. This depth range is used to emulate the fact that real fluorescent samples always present out-of-focus fluorescent clusters. Finally, the function  $\text{crop}(f_1(x), f_2(x))$  is defined as

$$\text{crop}(f_1(x), f_2(x)) = \begin{cases} f_1(x) & \text{if } f_1(x) < f_2(x) \\ f_2(x) & \text{otherwise} \end{cases} \quad (4.13)$$

and used within Eq. (4.12) in order to ensure that no fluorescent cluster is generated outside the cytoplasm by forcing such clusters on the cell boundary.

The number of fluorescent clusters that are generated for a given cell using this method is based on a desired density. For a given population of cells, the user defines  $D$ , the average amount of fluorescent clusters per  $\mu\text{m}^2$  within the cytoplasm. The number of fluorescent clusters for a cell  $\mathbf{p}_k \in \mathbf{P}_f$  is

$$M_k = D \int_0^{2\pi} \int_{n_k(\theta)}^{c_k(\theta)} r \, dr \, d\theta \quad (4.14)$$

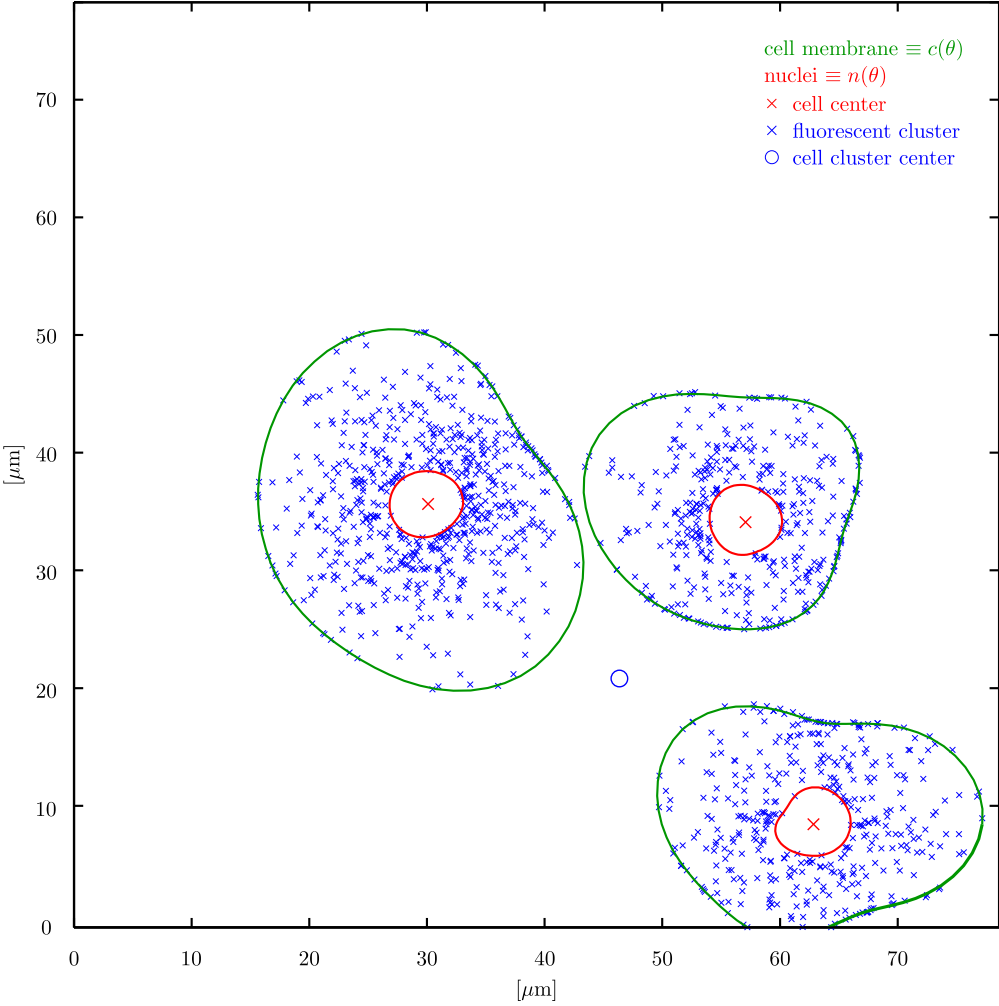


Figure 4.3 – Example of simulated population with 3 cells. Each cross represents the location of a fluorescent cluster.



Finally, we can define the set  $F_f$  of all fluorescent cluster locations that is generated by the tool after looping through all cells within  $P_f$  and generating fluorescent clusters as defined just above. We have

$$F_f = \left\{ \mathbf{f}_m \in \mathbb{R}^2 : m \in \left[ 1 \cdot \sum_{k=1}^{|P_f|} M_k \right] \right\} = \bigcup_{k=1}^{|P_f|} F_k \quad (4.15)$$

where  $|F_f| = \sum_{k=1}^{|P_f|} M_k$  is the total number of fluorescent clusters in the cell population and  $F_k$  is the set of fluorescent cluster locations within the cell  $\mathbf{p}_k \in P_f$ . The family of sets  $F_k$  is defined using

$$F_k = \left\{ \mathbf{p}_k + \mathbf{r}_{kl} \in \mathbb{R}^2 : l \in [1 \cdot M_k] \right\} \quad (4.16)$$

where the  $\mathbf{r}_{kl}$  are ordered triples (i.e. ordered set of three values) representing the cylindrical coordinates of the fluorescent cluster indexed by  $l$  with respect to the cell center  $\mathbf{p}_k \in P_f$  as generated using Eq. (4.12).

For the simulated sample to be complete, a random number of fluorophores is associated with each fluorescent cluster. These are accounted for in the set  $N_f$

$$N_f = \left\{ \mathbf{n}_m \in \mathbb{Z} : m \in [1 \cdot |F_f|] \right\} \quad (4.17)$$

where the number of fluorophores  $\mathbf{n}_k$  for each fluorescent cluster is randomly selected from the uniform distribution  $\mathcal{U}([n_{min} \cdot n_{max}])$  within a user-defined range.

### 4.1.3 Cell Population Imaging

With the final distribution of fluorescent clusters ( $F_f$  and  $N_f$ ) known for the generated sample, the image generation tool is ready to simulate the imaging process. Similarly to the cell population simulation, the simulation of the imaging process requires a number of user-defined input parameters. Table 4.2 provides an overview of these optics and image sensor related parameters.

The imaging process is a three-steps process starting with the light modeling which is used to simulate light irradiance exciting the various fluorescent clusters within the sample. The tool follows the image formation process described in Chapter 2 (see Section 2.2.2). It first produces an object function  $O(x, y, z)$  representing the sample in the object space. A second step then uses a sampling function based on a PSF model of the optics and other optical parameters to establish the image function  $I(x, y, z)$  in the image space and then sample it. This sampling action provides the amount of emission photons hitting each active pixel of the image sensor. Finally noise is added by various sources and a quantization step generates the final synthetic digital image  $I[x, y]$  of the cell population.

## Chapter 4. Simulated Biological Cells and Synthetic Image Generation

Table 4.2 – User-defined input parameters for the simulation of imaging process.

Parameter	Unit	Description
<b>Optics</b>		
$L_s$	W/m <sup>2</sup>	Excitation illumination irradiance
$N_A$	ADU	Numerical aperture
$M$	ADU	Lateral magnification
$t_{ND}$	%	Neutral density filter transmittance
$\lambda_{em}$	nm	Emission wavelength
$n$	ADU	Refraction index
<b>Image Sensor</b>		
$W$	ADU	Number of column in the sensor array
$H$	ADU	Number of rows in the sensor array
$d$	$\mu\text{m}$	Pixel pitch
$N$	ADU	Number of bits for the uniform quantizer
$T$	s	Exposure time
$N_{dc}$	$e^-$	Constant dark current charges
$\sigma_{ro}$	$e^-/s$	$\sigma$ of the readout noise
$N_{sat}$	$e^-$	Full-Well Capacity

### Illumination and Object Function

The object function  $O(x, y, z)$  results from the contribution of each fluorescent cluster  $\mathbf{f}_m = (x_m, y_m, z_m) \in \mathbf{F}_f$  by modeling them as single point-sources of light using the 3D Dirac distribution  $\delta(x, y, z)$ . Thus, we have the following object function

$$O(x, y, z) = L_s N_A^2 t_{ND} \sum_{m=1}^{|\mathbf{F}_f|} n_m S(x_m, y_m) \delta(x - x_m, y - y_m, z - z_m) \quad (4.18)$$

where  $t_{ND}$  is the transmittance of the ND filter,  $N_A$  is the *Numerical Aperture* (NA) of the objective and  $S(x, y)$  is a shading function.

In particular, the term  $L_s N_A^2$  denotes the irradiance of the illumination, expressed in W/m<sup>2</sup>, at the excitation wavelength and its dependency on the objective NA in epi-illumination setups [13, 72]. It is used by the tool to simulate various brightnesses for the light source. The term  $t_{ND}$  is used to decrease the light source irradiance by incorporating the effect of a ND filter in the excitation path.

The shading function  $S(x, y)$  models the uneven illumination. Ideally the Köhler illumination of the sample states that the rate of excitation photons hitting each fluorophores is spatially constant. This is however practically unachievable due to various imperfections within the illumination path and a quadratic function is used to model the distribution of excitation light

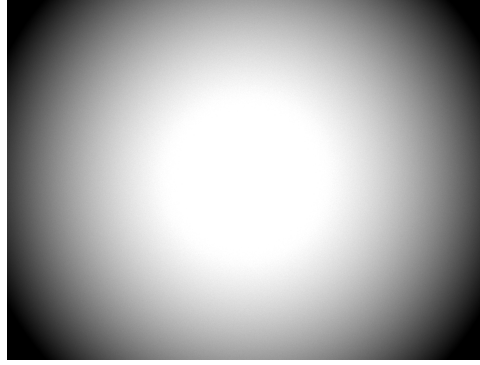


Figure 4.4 – Example of image generated images without cell population showcasing the uneven lighting distribution. The gamma of this image have been adjusted for visual purposes.

intensity [62].

$$S(x, y) = a_0 + a_1x + a_2y + a_3xy + a_4x^2 + a_5y^2 \quad (4.19)$$

This must follow the constraint that  $S(x, y)$  must stay within the range  $[0, 1]$  in the field-of-view of the image sensor. An example of shading is depicted in Fig. 4.4.

### Optics Modeling and Image Function

The optical system of any microscope, is fully characterized by its 3D PSF. As described in Section 2.2.1, the PSF is the diffraction pattern produced when the system images a single point of light. In order to benefit from it, a generic model of the object space PSF is used by the simulator in order to compute the diffraction pattern generated by each single point of light in the simulated sample (i.e. the fluorophore clusters). From the existing PSF models, the simulation tool uses a least-square Gaussian approximation of the PSF [150] as it provides a good trade-off between modeling precision and computational complexity with respect to scalar models [28]. The symmetrical 3D Gaussian function used for modeling the PSF is

$$g_{psf}(x, y, z) = \exp\left(-\frac{x^2 + y^2}{2\sigma_\rho^2} - \frac{z^2}{2\sigma_z^2}\right) \quad (4.20)$$

where  $\{\sigma_\rho, \sigma_z\}$  are the Gaussian parameters. Under the nonparaxial assumption, they can be analytically derived from known optical parameters such as the NA  $N_A$ , the emission wavelength  $\lambda_{em}$  and the medium refractive index  $n$  using

$$\sigma_\rho = \frac{1}{nk_{em}} \left( \frac{4 - 7 \cos^{7/2} \alpha + 3 \cos^{7/2} \alpha}{7(1 - \cos^{3/2} \alpha)} \right)^{-1/2} \quad (4.21)$$

$$\sigma_z = \frac{5\sqrt{7}}{\sqrt{6}nk_{em}} \left( \frac{1 - \cos^{3/2} \alpha}{(4 \cos^5 \alpha - 25 \cos^{7/2} \alpha + 42 \cos^{5/2} \alpha - 25 \cos^{3/2} \alpha + 4)^{1/2}} \right) \quad (4.22)$$

## Chapter 4. Simulated Biological Cells and Synthetic Image Generation

---

where  $\alpha$  is the maximal convergence semi-angle of the objective such that  $N_A = n \sin \alpha$  and  $k_{em} = n(2\pi/\lambda_{em})$  is the wavenumber of the emission light.

This PSF model is then used in the imaging process to produce the image function  $I(x_i, y_i, z_i)$  in the image space. Under the assumption that the simulated microscope is a *Linear Translation Invariant* (LTI) system, the object space coordinates  $(x, y, z)$  and the image space coordinates  $(x_i, y_i, z_i)$  are linearly related via the magnification

$$(x, y, z) = (Mx_i, My_i, M^2 z_i) \quad (4.23)$$

where  $M$  is the lateral magnification and  $M^2$  the longitudinal magnification. Using the image space coordinates, the image function is modeled by the convolution operation

$$I(x_i, y_i, z_i) = \frac{N_A^2}{M^2 n^2} (O * g_{psf})(x_i, y_i, z_i) \quad (4.24)$$

$$= \frac{N_A^2}{M^2 n^2} \int_{\mathbb{R}^3} O(x, y, z) g_{psf}\left(\frac{x_i}{M} - x, \frac{y_i}{M} - y, \frac{z_i}{M^2} - z\right) dx dy dz \quad (4.25)$$

The factor  $\frac{N_A^2}{M^2 n^2}$  models the light gathering capabilities of the objective, similarly to the factor  $N_A^2$  in Eq. (4.18) modeling the light condensing capabilities of the objective in epi-illumination. Injecting Eq. (4.18) in Eq. (4.24) and using the sifting property of the Dirac distribution we obtain

$$I(x_i, y_i, z_i) = L_s \frac{N_A^4}{M^2 n^2} t_{ND} \sum_{m=1}^{|Ff|} n_m S(x_m, y_m) g_{psf}\left(\frac{x_i}{M} - x_m, \frac{y_i}{M} - y_m, \frac{z_i}{M^2} - z_m\right) \quad (4.26)$$

Finally, we are interested in the image formed at the image plane (i.e.  $z_i = 0$ ) as it is the plane where the image sensor samples the image function. Thus we find

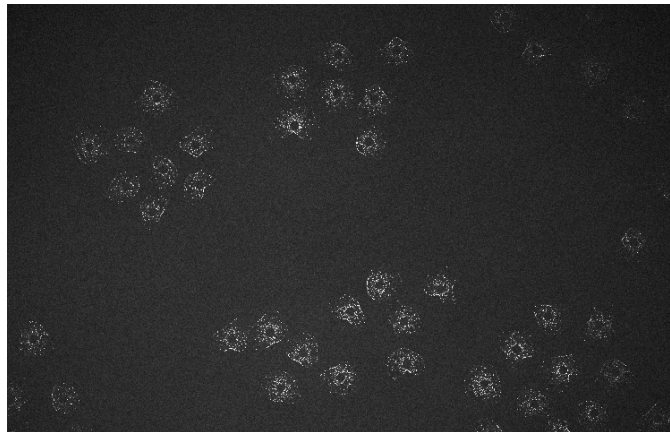
$$I(x_i, y_i) = I(x_i, y_i, 0) = L_s \frac{N_A^4}{M^2 n^2} t_{ND} \sum_{m=1}^{|Ff|} n_m S(x_m, y_m) g_{psf}\left(\frac{x_i}{M} - x_m, \frac{y_i}{M} - y_m, -z_m\right) \quad (4.27)$$

which is the irradiance of the sample on the image plane produced by fluorescence.

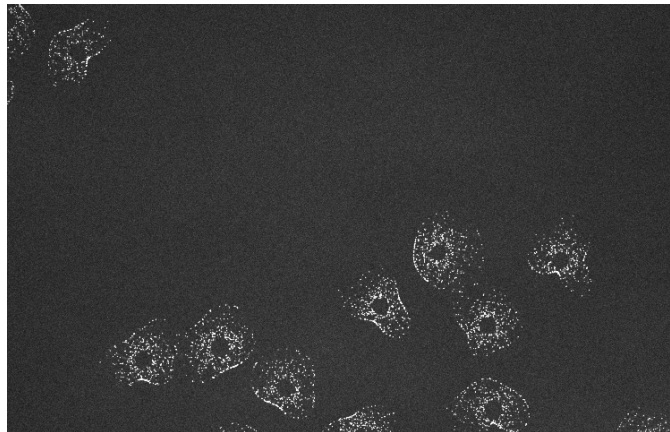
### Image Sensor and Noise Sources Modeling

Modeling the image sensor is done in two phases. First, the image  $I(x_i, y_i)$  on the focal plane is sampled and the number of photogenerated electrons per pixel is computed based on the simulated image sensor *Quantum Efficiency*. The second phase simulates *Photon Shot noise*, the *Readout Noise* and the *Dark Current* to generate the final digital output image  $I[x, y]$ .

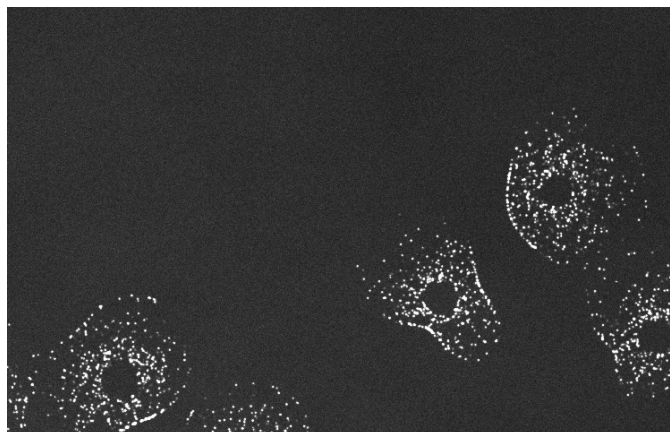
Assuming an image sensor consisting of  $W \times H$  pixels characterized by a pixel pitch of  $d$ , the



(a)



(b)



(c)

Figure 4.5 – Examples of synthetic images generated from the cell population depicted in Fig. 4.2. (a) Imaged using a 10× objective, (b) imaged using a 20× objective, (c) imaged using a 40× objective.

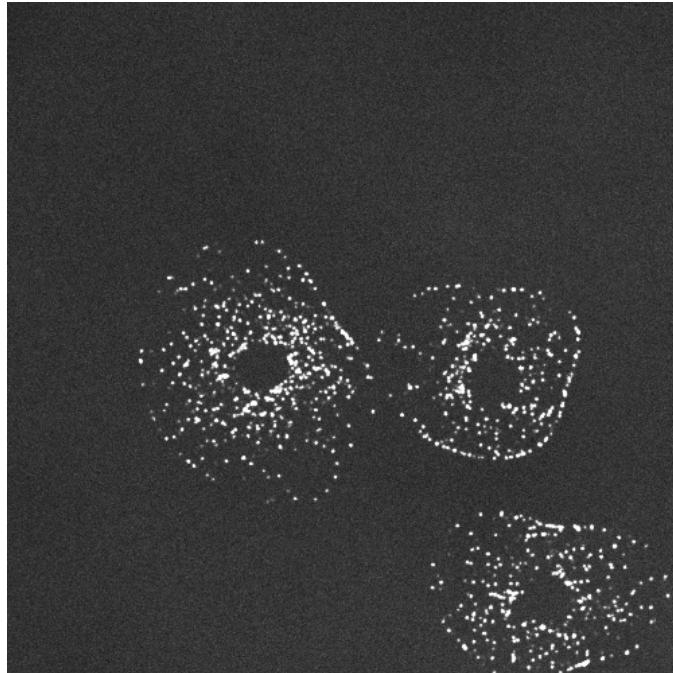


Figure 4.6 – Synthetic image of three cells associated with the cell population presented in Fig. 4.3.

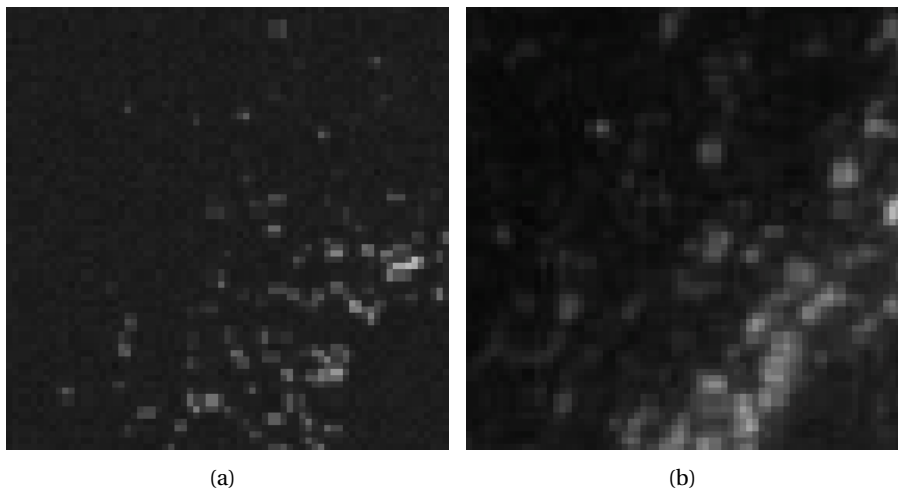


Figure 4.7 – Comparison between (a) imaged synthetic fluorescent clusters from a simulated sample and (b) real fluorescent clusters from an epi-fluorescent image. The real image is a zoomed-in portion of Fig. 4.1(a). The bottom right of the zoomed-in portion is part of a cell nuclei and the fluorescence is emitted by dyed TLR-2 surface receptors within the cytoplasm after permeabilization. The real image was captured using a  $40\times$ ,  $N_A = 0.6$  air objective and a CCD imager with  $4.4\mu\text{m}^2$  active pixels. The synthetic image generation tool was configured to match these parameters.

sampling function  $p(x, y)$  is defined by a 2D impulse train

$$p(x_i, y_i) = \sum_{n=-\frac{W}{2}}^{\frac{W}{2}-1} \sum_{m=-\frac{H}{2}}^{\frac{H}{2}-1} \delta \left( x_i - \left( d \left( n + \frac{1}{2} \right) \right), y_i - \left( d \left( m + \frac{1}{2} \right) \right) \right) \quad (4.28)$$

This sampling function is then applied to the image function in the image plane through

$$I_s(x_i, y_i) = I(x_i, y_i) p(x_i, y_i) \quad (4.29)$$

$$= L_s \frac{N_A^4}{M^2 n^2} t_{ND} \sum_{m=1}^{|Ff|} n_m S(x_m, y_m) g_{psf} \left( \frac{x_i}{M} - x_m, \frac{y_i}{M} - y_m, -z_m \right) p(x_i, y_i) \quad (4.30)$$

$$= L_s \frac{N_A^4}{M^2 n^2} t_{ND} \sum_{m=1}^{|Ff|} n_m H_s(x_i, y_i) \quad (4.31)$$

where  $H_s(x_i, y_i)$  represents the unweighted sampled diffraction pattern of a fluorophore at the location  $[x_m, y_m, z_m]$

$$H_s(x_i, y_i) = \left[ S(x_m, y_m) g_{psf} \left( \frac{x_i}{M} - x_m, \frac{y_i}{M} - y_m, -z_m \right) \right] p(x_i, y_i) \quad (4.32)$$

The number of electrons  $\hat{N}_e$  that are generated within each pixel of the sensor from the simulated fluorescent signal is obtained from  $I_s(x_i, y_i)$  by introducing the sensor *Quantum Efficiency*  $Q_e$  at the emission wavelength  $\lambda_{em}$

$$\hat{N}_e[x, y] = I_s(dx, dy) d^2 \frac{T}{h\nu_{em}} Q_e \quad (4.33)$$

where  $h\nu$  is the energy per photon at  $\lambda_{em}$ .

We can now add the *Dark Current* generated charges  $N_{dc}$ , the *Readout Noise* and  $N_{ro}$  and model the *Photon Shot Noise* using the Poisson distribution  $\mathcal{P}$  with

$$N_e[x, y] = \mathcal{P}(\hat{N}_e[x, y] + N_{dc}) + T N_{ro} \quad (4.34)$$

where the *Dark Current* is a constant, the *Readout noise* is modeled using a normal distribution  $N_{ro} \sim \mathcal{N}(0, \sigma_{ro})$  [82] and the *Photon Shot Noise* follows the Poisson distribution as defined in Chapter 3 (see Section 3.4.4).

Finally, the values of the pixels in the produced image are produced from  $N_e[x, y]$  using a  $N$  bits uniform quantizer mapped over the range  $[0 \cdot N_{sat}]$  where  $N_{sat}$  is the *Full-Well Capacity* of the simulated sensor.

In order to close this section on cell population imaging, Fig. 4.5 and 4.6 showcase some synthetic images generated with the tool. In particular, Fig. 4.5 shows three different images generated from the cell population in Fig. 4.2 based on three different simulated magnifica-

tions. Fig. 4.6 is a close up view of the synthetic image generated from the zoomed-in cell population in Fig. 4.3. A comparative point-of-view between imaged synthetic fluorescent clusters and real fluorescent clusters taken from the image in Fig. 4.1(a) is offered in Fig. 4.7.

## 4.2 Tool Performance and Validation

### 4.2.1 Computational Cost

The implementation of the synthetic image generation tool features two main procedures. A first procedure is implementing the generation of the sample and of all the accompanying meta-data, while a second procedure handles the actual image synthesis based on the set of fluorescent clusters generated by the former. Of course, these are in direct relation with the generation process of Section 4.1.2 and with the imaging process described in Section 4.1.3.

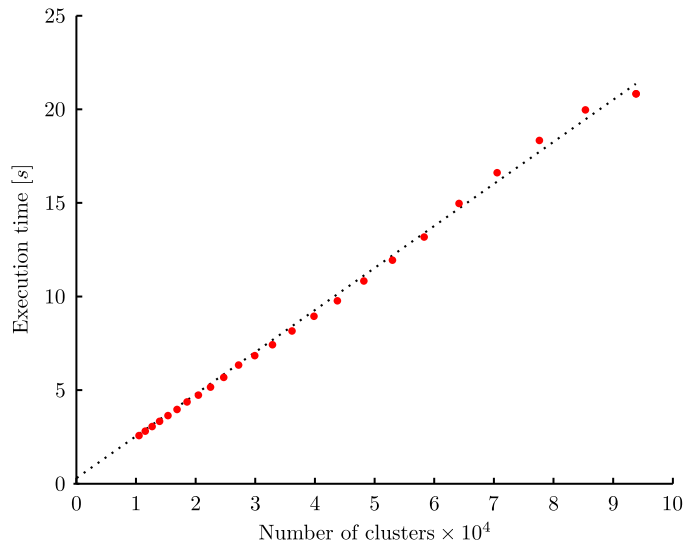
The computational effort of the procedure handling the sample generation has a linear dependency with the overall number of desired fluorescent clusters in the population. Using the big-O notation, which defines the order of the growth rate of the computational time, and based on population parameters, it runs in  $\mathcal{O}(N_{cc}N_{max}(r + \alpha)^2D)$ . As a reminder,  $N_{cc}$  is the desired number of cell clusters,  $N_{max}$  is the upper bound on the number of cells per cell cluster,  $r + \alpha$  is the maximum circumradius of any cell in the generated population and  $D$  is the fluorescent cluster density.

On the other hand, the imaging procedure has two major inputs that influence the run time: the number of fluorescent clusters within the field-of-view  $|\mathbf{P}_v|$  of the simulated image sensor and the size of the sensing active area.

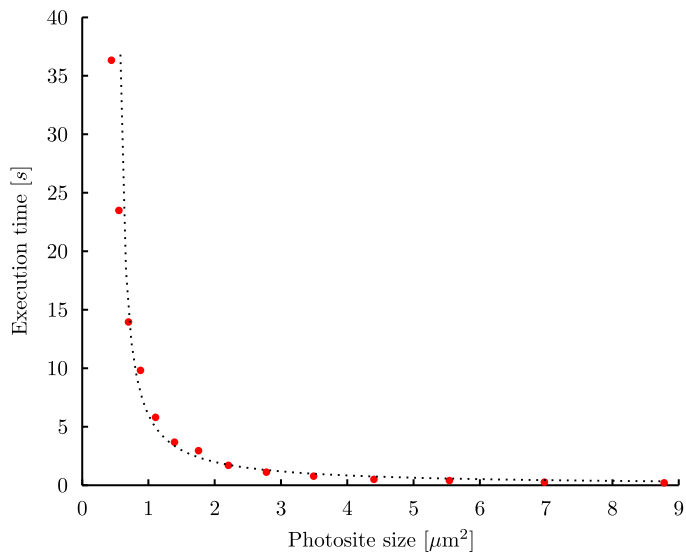
Given an image sensor characterized by a set of parameters, the imaging process evaluates the diffraction pattern of each fluorescent cluster within the field-of-view and accumulates them to the final image. This is dictated by Eq. (4.29) and results in a linear time dependency between the imaging execution time and the number of imaged fluorescent clusters  $|\mathbf{P}_v|$ . The execution time measurements are graphically depicted in Fig. 4.8(a) and exhibit this behavior. However, it is clear that the execution time will vary heavily based on which part of a generated sample is imaged. A conservative upper limit can be set assuming the field-of-view is filled with fluorescent clusters at the density  $D$ . In which case, we can write that the imaging procedure runs in  $\mathcal{O}\left(D\frac{w_i h_i}{M}\right)$  where  $D$  is the fluorescent cluster density,  $M$  is the optics magnification and  $w_i \times h_i$  is the area of the image sensor array.

On the other hand, when assuming that the sample and field-of-view stays unchanged while varying the number of active pixels in the image sensor, we obtain that the execution time of the imaging process has a quadratic dependency with the inverse of the square footage of the simulated active pixels. Fig. 4.8(b) showcases this behavior, which is dictated by the sampling pitch in Eq. (4.32) as it samples the diffraction pattern of each fluorescent cluster in the focal plane. The imaging procedure thus runs in  $\mathcal{O}((n_w n_h)^2)$ , where  $n_w \times n_h$  is the array size of the





(a)



(b)

Figure 4.8 – Execution time of the image generation tool with respect to (a) the number of fluorescent cluster in the field-of-view and (b) the total photodetector size. The data points are obtained from a single execution core of a Intel Xeon X5650 processor running at 2.66GHz by running simulation tool under Matlab R2009b (64bit).

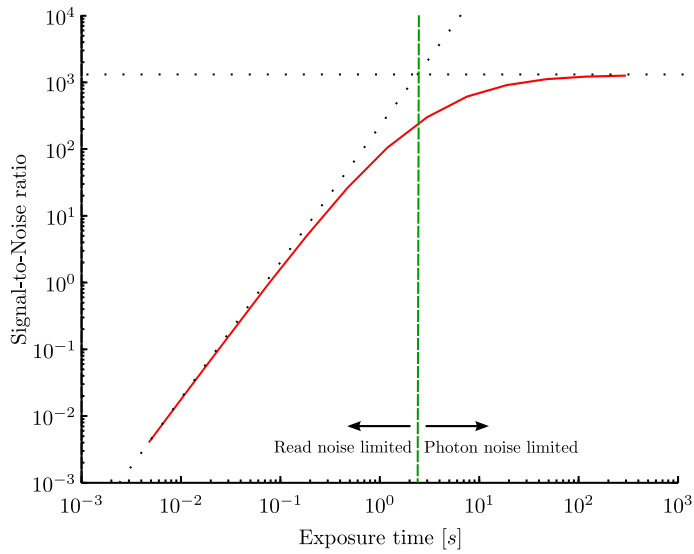


Figure 4.9 – Signal-to-Noise ratio versus exposure time of synthetic images. We can clearly identify the read-noise limited region and the photon-shot noise limited region.

image sensor.

The time required for the addition of noise in Eq. (4.34) is linearly dependent with the number of active pixels in the image sensor. As expected, it is independent from the simulated sample and is negligible with respect to the evaluation of Eq. (4.33) in the imaging process.

#### 4.2.2 Signal-to-Noise Characteristics

When acquiring a signal, such as fluorescence from a microscope, the SNR parameter is key. It is thus important to evaluate the performance of the synthetic image generation to that aspect. Depending on the image processing technique required by the application, either a short exposure time (e.g. Lucky Imaging [20] or *Fluorescence Life-Time Imaging* (FLIM) [136]) or a long exposure time (e.g. super-resolution methods [53] [52]) to the fluorescent signal is required. This results in images with a SNR that is either *read-noise limited* or *photon-noise limited*. Short time exposures of the sensor favor the influence of the *Read Noise* as the number of electrons hitting the various active pixels stays limited. On the other hand, long time exposures naturally induce that a significant number of electrons hit the active pixels of the sensor, resulting in a negligible *Read Noise* with respect to the *Photon-Shot Noise*.

It is important for the synthetic image generation tool to take into account this fact. Figure 4.9 shows the tool behavior by graphing the obtained SNR of various images with respect to the exposure time. The tool was used to generate a random cell population and a single location on that population was imaged with various exposure lengths. The expected *read-noise* limited region and *photon-shot Noise* limited region appear. The border from one to the

other is depended on user-defined parameters used to simulate the image sensor. The SNR is computed using the following definition

$$\text{SNR} = \frac{\sum_{y=1}^N \sum_{x=1}^M \hat{N}_E^2[x, y]}{\sum_{y=1}^N \sum_{x=1}^M (\hat{N}_E[x, y] - N_E[x, y])^2} \quad \text{SNR}_{dB} = 10 \log_{10}(\text{SNR}) \quad (4.35)$$

where  $\hat{N}_E[x, y]$  is the expected number of electrons gathered by the active pixel  $[x, y]$  on the image sensor as computed by the imaging process of the tool. On the other hand,  $N_E[x, y]$  represents the same value but including the electrons originating for simulated noise sources.

### 4.3 Chapter Summary and Contributions

A novel approach for generating synthetic fluorescent 2D images of cell cultures is presented in this chapter. This approach is currently implemented as a Matlab tool implementing the two described simulation engines. The first engine focuses on the modeling and generation of populations of cells. It uses parametric models to generate the cell shapes and sizes and attribute to each cell a random distribution of fluorescent clusters within the cytoplasm region, each cluster corresponding to a group of one or many fluorophores. Based on this knowledge and under the assumption that each fluorescent cluster is a single point of light, the second engine uses various user-defined parameters in order to simulate a generic digital microscope and produce synthetic images of the generated population.

The novelty included in the presented approach consists in the use of a parametric model to generate the location of tagged biomarkers in the simulated populations. This enables the tool to realistically generate images by simulating the imaging process down to each fluorescent biomarker, rather than using a procedural texture generator for the emulation of the fluorescent signal [66, 67, 127].

This tool is designed to help in the design process of image processing systems working on the extraction of fluorescent spots in bioimaging applications. It is used in the following chapter and offers quantitative comparison capabilities for the testing of various algorithms.



## 5 Image Thresholding Methods For Fluorescent Biomarkers

In this chapter, we explore global and local thresholding techniques for the monitoring of fluorescently stained biomarkers in microscopic images<sup>1</sup>. In particular, we focus this study on the segmentation of 2D fluorescent spots which are a common transduction of the signal in fluorescence bioimaging.

The segmentation techniques that are considered are built around existing image processing techniques employed in fluorescence bioimaging [26, 124, 125]. Moreover, a novel local image thresholding algorithm is presented too. They are formed around (i) a preprocessing step, (ii) and optional filtering step and (iii) a thresholding step generating a segmentation mask. In the following pages, we refer to a technique that implements these three steps as a *segmentation method*. Details about the various *segmentation methods* considered in this study are gathered in the first section of this chapter.

Two comparison frameworks are put in place to quantitatively weigh up the *segmentation methods*. The first framework focuses on their ability to classify images presenting a fluorescent signal from negative control images. This requires the use of two image datasets, a *Stimulated Group* (SG) dataset and a *Negative Control Group* (NCG) dataset. To build them, real biological samples featuring Caco-2 cells with stained TLR2 receptors as biomarkers reporting on the cellular inflammation are used. The SG dataset consists of images of Caco-2 cells that have been stimulated artificially in order for them to express TLR2 [16], while the NCG dataset consists of images of unstimulated cells. In this framework, the classification in itself is done based on features extracted from the segmentation masks.

The second comparison framework leverages the comparison of the *segmentation methods* using synthetic data and images. As opposed to the real image datasets, the meta-data provided along with the images created by the synthetic image generation tool (Chapter 4) constitutes a golden reference. This is used to evaluate the performance of the *segmentation methods* on how properly they localize and segment fluorescent spots.

---

<sup>1</sup>The study presented in this chapter was initially published in [34]. This chapter reprises and adapts part of this original work.

Through these comparisons, this study addresses the two following problems. First, the need to identify if an imaged sample presents significant fluorescence. This indicates whether a biological sample has had a specific process triggered. Second, whenever a sample is recognized as stimulated, extracting the spatial location of fluorescent spots within the images is of general interest and can, for instance, be used in quantitative co-localization analysis [133]. We are, thus, investigating the use of image thresholding and spot extraction techniques for answering these problems.

The two comparison frameworks, for classification and localization, are presented in detail within Section 5.2. The results and associated discussions are showcased in Section 5.3 and 5.4 respectively.

### 5.1 Segmentation Methods for Spot Extraction

Recent studies comparing segmentation algorithms [26], and more specifically spot detection methods [124, 125], give us a good overview of the state-of-the-art and common practices in quantitative fluorescence microscopy. Global thresholding is a common and basic technique in which a threshold value must be computed for each image. Histogram-based algorithms such as Otsu's method [98], Ridler's method or isodata [110], maximum entropy [57], and the T-point algorithm [19] are often used to extract this threshold value [87, 101, 103, 151]. When applied to fluorescent spot extraction, these algorithms often work on images filtered by signal enhancement methods [124, 125]. These signal enhancement techniques are often based on wavelets [96] and *Mathematical Morphology* (MM) operators [46, 76, 117, 137]. In particular, the MM-based *Top-Hat* (TH) filter is widely used for removing low-frequency contributions such as background fluorescence, out-of-focus fluorescence, and cytoplasm auto-fluorescence [60, 87, 103, 108]. Aside from global thresholding, local thresholding techniques are also used for the extraction of spots [91] by computing a specific threshold for each pixel based on its surroundings. Niblack's method [90] and its enhanced version by Sauvola and Pietikainen [113] belong to this category. Another popular method in cell segmentation is the watershed algorithm mainly used for separating overlapped objects of interest [40, 108, 118, 139].

In this study, a subset of these methods have been selected to segment fluorescent spots in fluorescent images. The Otsu and T-point algorithms have been selected for their ability to separate bimodal and unimodal grayscale image histograms respectively. Local thresholding approaches are represented by Sauvola's thresholding algorithm. The TH filter is also considered as a filtering step to enhance the fluorescent signal. On top of these methods, I propose a novel local thresholding technique, the *GLT* method, using the TH filter as a way to identify *Local Signal-to-Noise Ratios* (LSNRs) and extract spots below a user-defined size.

*In fine*, nine different *segmentation methods* are tested and compared. These methods are resulting from the combination of an image correction step, an optional TH filtering step and a global or local thresholding algorithm. Table 5.1 lists the names of each *segmentation method* used in this chapter and the involved processing in each step.

## 5.1. Segmentation Methods for Spot Extraction

Table 5.1 – This table collects the different *segmentation methods* involved in the study. The method name *AllPix* is considered as a reference method where only the image correction is applied.

Method	Preprocessing		Thresholding
	Correction	Filtering	
<i>AllPix</i>	Flat-field	-	All pixels
<i>T-point</i>	Flat-field	-	T-Point algorithm
<i>Otsu</i>	Flat-field	-	Otsu's algorithm
<i>Otsu(2X)</i>	Flat-field	-	Otsu's algorithm applied recursively twice
<i>Sauvola</i>	Flat-field	-	Sauvola's algorithm
<i>TH + T-point</i>	Flat-field	Top-Hat	T-Point algorithm
<i>TH + Otsu</i>	Flat-field	Top-Hat	Otsu's algorithm
<i>TH + Otsu(2X)</i>	Flat-field	Top-Hat	Otsu's algorithm applied recursively twice
<i>TH + Sauvola</i>	Flat-field	Top-Hat	Sauvola's algorithm
<i>GLT</i>	Flat-field	-	Proposed <i>GLT</i> algorithm

### 5.1.1 Image Preprocessing

The image correction and filtering as presented in the previous section are considered as the preprocessing step prior to the actual image thresholding. This study involves deterministic noise correction for all images and for some *segmentation methods*, the use of TH morphological filtering for signal enhancement. The detail of these techniques is presented hereunder.

#### Image Correction

This step deals with the removal and mitigation of deterministic noise resulting from the imaging process. The first source of such noise are all the optical aberrations of the microscopic system due to optical imperfections, uneven lighting of the sample (vignetting), undesired external light sources or even dust impeding the optical performance.

The second source of such noise is the manufacturing process which results in the *Fixed-Pattern Noise* (FPN) of the image sensor as described in Chapter 3.

In order to mitigate this noise, a flat-field correction can be applied on an image  $I$ . For a pixel at a given location  $[x, y]$ , this is applied using

$$I_C[x, y] = (I[x, y] - D[x, y]) \times \frac{\mu_F}{F[x, y]} \quad (5.1)$$

where  $I_C$  is the corrected image,  $D$  is a master dark frame,  $F$  is a master flat frame and  $\mu_F$  is a scalar equal to the average pixel value of  $F$ . A calibration step is required to compute the

master frames  $D$  and  $F$  and to evaluate  $\mu_F$ .

The master dark frame  $D$  is simply computed by averaging an arbitrary amount  $N$  of dark images  $I_{dark}$ . This constitutes an average image of the *Dark Signal Non-Uniformity* (DSNU) assuming the dark images are captured using the same imaging conditions (i.e. sensor configuration, exposure time) as for capturing the image  $I$  that needs to be corrected.

$$D = \frac{1}{N} \sum_0^{N-1} I_{dark} \quad (5.2)$$

Removing this master dark frame from every input image  $I$  thus reduces the DSNU part of the FPN.

The master flat frame  $F$  is used to compensate for the *Pixel Response Non-Uniformity* (PRNU), with the factor  $\mu_F/F[x, y]$  representing an individual correction gain factor for every pixel in the image  $I$ . The master flat frame is also computed by averaging an arbitrary amount  $N$  of flat images

$$F = \frac{1}{N} \sum_0^{N-1} (I_{flat} - D_F) \quad (5.3)$$

where  $I_{flat}$  are flat images as captured by the sensor when an even light is projected on the sensor and  $D_F$  is a master dark frame associated with the flat images  $I_F$ .

### Image Filtering

The TH morphological filter [117] is a known way of dealing with uneven background in fluorescent images [60, 87, 103, 108]. It is used to enhance the signal of objects of know size and shapes, such as fluorescent spots.

The TH filter is applied to a grayscale image  $I$  by removing its lower envelope [137]

$$Q = I - I \circ B \quad (5.4)$$

where  $B$  is a structuring element and  $\circ$  is a *Mathematical Morphology* (MM) operator. This operator is defined from the basic MM dilation operator  $\oplus$  and MM erosion operator  $\ominus$

$$I \circ B = (I \ominus B) \oplus B \quad (5.5)$$

The MM dilation operator  $\oplus$  and MM erosion operator  $\ominus$  are the two basic grayscale transformations defined by the theory of MM [46, 117]. The dilation operator replaces the value of each pixel in an image by the maximum pixel value of its neighboring pixels. It is the structuring element  $B$  that is responsible for defining where the neighboring pixels are located with respect to the current pixel. Similarly, the erosion operator replaces the current pixel



value with the minimum pixel value of the neighboring pixels. The structuring element  $B$  is typically a disk shaped element with a size similar to that of the target fluorescent spots as observed through the microscope.

Practically, the TH filter acts as a background removal tool. Features in the image that are typically smaller than the structuring element are kept after applying the filter. When processing fluorescent images with the goal of enhancing the signal emitted from fluorescent spots, we need to make sure that the structuring element size is greater than the typical spot size.

### 5.1.2 Segmentation of Biomarkers

In this section, the thresholding algorithms used for segmenting the fluorescent pixels are described. As presented previously, four thresholding algorithms are considered.

*Otsu's algorithm* and the *T-point algorithm* are two global thresholding techniques for selecting a threshold value based on the histogram  $\mathbf{H}$  of the processed image  $I$

$$\mathbf{H} = \{H[i] : i \in [0 \cdot L - 1]\}$$

$$H[i] = \sum_{x,y} \begin{cases} 1, & \text{if } I[x, y] = i \\ 0, & \text{otherwise} \end{cases} \quad (5.6)$$

where  $i$  are the histogram bin indexes and  $L$  is the number of bins.

*Sauvola's technique* and the *GLT method* are both local thresholding techniques selecting a specific threshold for each pixel in the image.

### Global Thresholding Algorithms

**T-point algorithm** The T-point algorithm [19] proposes an approach to setting thresholds for images with unimodal histograms. The proper operation of this automated method is based on two assumptions about the histogram. The background noise is the main pixel population that contributes to the single, major histogram peak in the low intensities. The remaining pixels of interest form the tail of the histogram. Such histograms can be decomposed into three parts: a steep rising slope, a steep descending slope, and a slow descending slope or tail. The goal of the T-point binarization method is to model the descending slopes using two lines, one for the steep part and one for the tail, as shown in Fig. 5.1. Considering a unimodal histogram  $\mathbf{H}$  where the peak has been identified at the bin index  $m$ . The steep and slow descending slopes are respectively located on the bin indexes  $[m \cdot k]$  and  $[k \cdot L - 1]$ , where  $k \in [m + 1 \cdot L - 1]$ . Two lines  $L_{steep}$  and  $L_{slow}$  are fitted on the histogram for the steep and the slow descending slope respectively. The T-point algorithm is searching for the optimum threshold bin index  $k^*$  such that the total error of the fittings is minimized

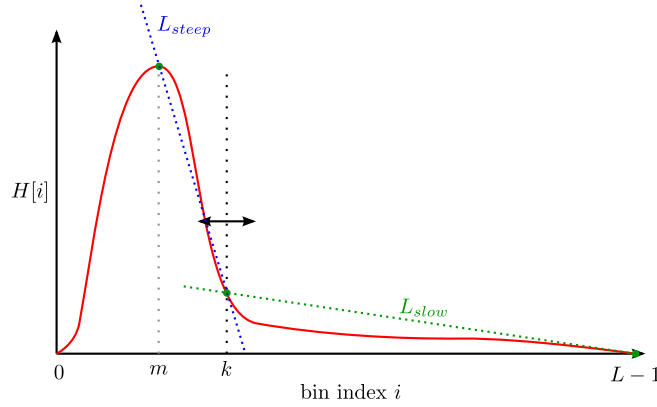


Figure 5.1 – T-point algorithm concept for the search of an optimum  $k^*$ .

$$k^* = \min_k (\epsilon(k)) \quad (5.7)$$

where the total error  $\epsilon(k)$  is the sum of the fitting errors of the lines  $L_{steep}$  and  $L_{slow}$

$$\epsilon(k) = \epsilon_{steep} + \epsilon_{slow}(k) \quad (5.8)$$

with

$$\epsilon_{steep}(k) = \sum_{i=m}^k (H[i] - \hat{H}[i])^2 \quad (5.9)$$

$$\epsilon_{slow}(k) = \sum_{i=k}^{L-1} (H[i] - \hat{H}[i])^2 \quad (5.10)$$

where  $H[i]$  is histogram value at index  $i$  and  $\hat{H}[i]$  is the estimated value of the histogram by either of the fitted lines.

**Otsu's algorithm** Otsu's algorithm [98] is an iterative process which aims at finding an optimum threshold bin index  $k^*$  in the image histogram by maximizing a criterion measure  $\sigma_B^2$  that evaluates the goodness of that index.

$$k^* = \max_k (\sigma_B^2(k)) \quad (5.11)$$

This goodness is evaluated using the intra-class variance, where the classes are defined using the threshold index  $k$ ; the class  $C_0$  consists of the histogram bins within the index range  $[k_{min} \cdot k - 1]$  and class  $C_1$  consists of the histogram bins within the index range  $[k \cdot k_{max}]$  as shown in Fig. 5.2. This intra-class variance is defined by

$$\sigma_B^2 = \omega_0 \omega_1 (\mu_1 - \mu_0)^2 \quad (5.12)$$

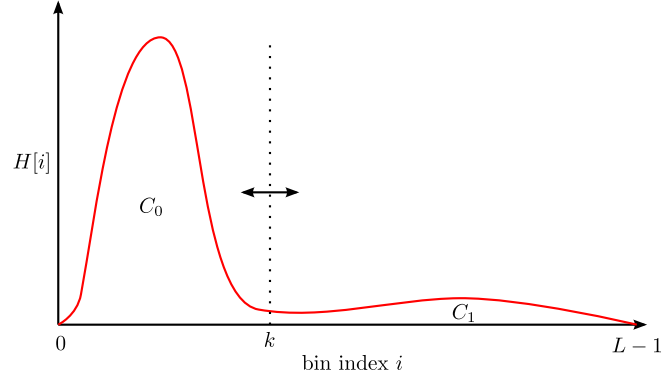


Figure 5.2 – Otsu's algorithm concept for the search of an optimum  $k^*$ .

where  $\omega_0$  and  $\omega_1$  are the probabilities of class occurrence

$$\omega_0 = Pr(C_0) = \frac{1}{N_p} \sum_{i=k_{min}}^{k-1} H[i] \quad (5.13)$$

$$\omega_1 = Pr(C_1) = \frac{1}{N_p} \sum_{i=k}^{k_{max}} H[i] \quad (5.14)$$

and  $\mu_0$  and  $\mu_1$  are the class mean level

$$\mu_0 = \frac{1}{N_p \omega_0} \sum_{i=k_{min}}^{k-1} i H[i] \quad (5.15)$$

$$\mu_1 = \frac{1}{N_p \omega_1} \sum_{i=k}^{k_{max}} i H[i] \quad (5.16)$$

with  $N_p = \sum_{i=k_{min}}^{k_{max}} H[i]$  being the total number of pixels within the considered range of histogram bins indexes  $[k_{min} \cdot k_{max}]$ .

For the *segmentation methods* called *Otsu* and *TH+Otsu* (see Table 5.1), the range of histogram bin indexes over which  $k^*$  is sought is  $[0 \cdot L - 1]$ .

For *Otsu(2X)* and *TH+Otsu(2X)*, the first iteration of Otsu's algorithm is done within the range of histogram bins  $[0 \cdot L - 1]$  leading to a first thresholding index  $k_1^*$ . The second iteration however seeks the final thresholding index  $k_2^*$  within the range of histogram indexes  $[k_1^* \cdot L - 1]$ . This recursive Otsu thresholding approach [17] is considered in order to generate segmentation masks focused on the fluorescent spots. By design, a single iteration of Otsu's algorithm will only segment the whole cell areas if enough cytoplasm auto-fluorescence is present.

### Local Thresholding Techniques

**Sauvola's thresholding technique** Sauvola's algorithm [113] acts as an edge-detection method based on a sliding window. It is targeting objects with a size similar to that of the window. Practically, the algorithm provides a threshold value for each pixel based on the mean and standard deviation of the neighboring pixel intensities. Given a pixel  $I[x, y]$  of an image  $I$ , the associated local threshold  $t[x, y]$  is a function of the local mean  $m[x, y]$  and local standard deviation  $s[x, y]$  of the pixel intensities within a square window of size  $w$  by  $w$  around  $I[x, y]$ . It is computed using

$$t[x, y] = m[x, y] + (m[x, y] - 1)k \left( \frac{s[x, y]}{R} - 1 \right) \quad (5.17)$$

where  $k$  is a positive parameter, usually within the range  $[0.2, 0.5]$ , and  $R$  is the dynamic range of  $s[x, y]$  (e.g.,  $R = 0.5$  on normalized pixel intensities and  $R = 2^{n-1}$  on  $n$ -bit images).

In Eq. (5.17), the standard deviation has a direct effect on the computed threshold value. Consider a high standard deviation among the pixels in the window, tending towards  $R$ . The computed threshold value will then tend to the mean intensity. On the contrary, the threshold of the central pixel will tend to  $m[x, y] + k(1 - m[x, y])$  for a window with pixel intensities having a low variance. In this case, the threshold is raised above the local mean of the pixel intensities, and the central pixel will more likely be classified as background.

Note that Sauvola's original binarization equation is designed for images featuring dark objects on a light background, while Eq. (5.17) is modified to account for light objects on a dark background, as fluorescence microscopy images require.

**GLT algorithm** The GLT algorithm is a novel thresholding method for the extraction and localization of fluorescent spots that deal with the limitations observed while working with other thresholding methods from the literature. Global thresholding methods using Otsu's algorithm or the T-point algorithm have a limited efficiency in extracting bright spots. First, fluorescent images principally feature unimodal histograms; this implies a trade-off when selecting a threshold value as the signal and the background histogram contributions are merged. Second, the fluorescent signal is corrupted by auto-fluorescence of the cytoplasm and out-of-focus contributions of some fluorescent probes. This results in a random and uneven background in the fluorescent images.

As a consequence, we have developed the following thresholding method by taking advantage of the background removal effect of the TH filter, drawing inspiration from the watershed segmentation approach [139].

The purpose of this new method is to extract a certain amount of pixels around local maxima (i.e., identify blobs of fluorescent pixels). The core concept lies in sweeping threshold values starting from the lowest value in the image  $I$  and searches for blobs (using *Connected Component (CC)* labeling) of a suitable size containing the local

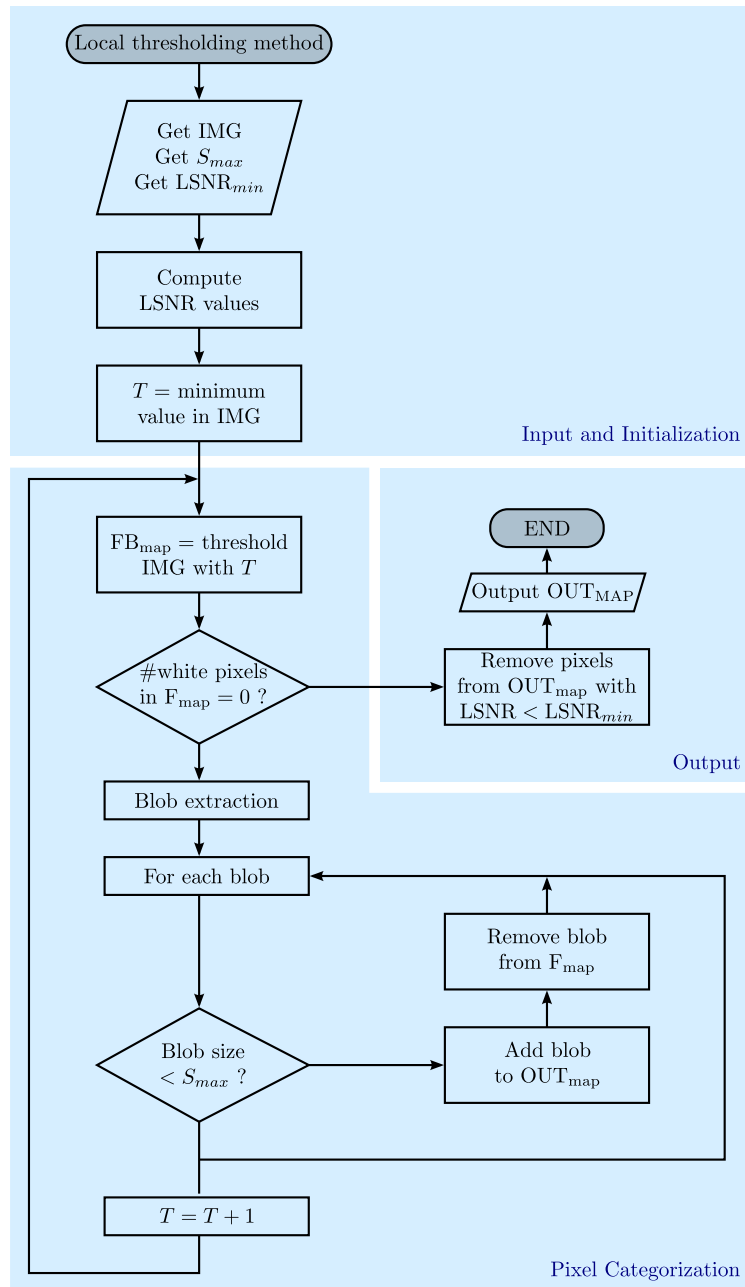


Figure 5.3 – Flowchart of the *GLT* algorithm method.

maxima of the image. The fluorescent pixels composing a given blob are characterized by an intensity value greater than a particular threshold that specific to this blob and to the local maxima it is enclosing. The user specifies a maximum size for the blobs. This indicates if a blob needs to be broken down. Details of the algorithm flow can be found in Fig. 5.3 and are explained hereunder.

1. *Input and initialization:* This method takes as input the original image  $I$  and sets a starting threshold value  $T$  equal to the lowest pixel intensity. The original image is thresholded with  $T$  and a fluorescent-background pixel map is generated, labeling the pixels either as fluorescent (white) or background (black). A maximal size  $S_{max}$  in pixels for the blob size is also input.
2. *Pixel categorization:* The pixel categorization is the core of the algorithm. It is an iterative process. Each iteration is detecting the blobs, or connected components, within the fluorescent-background pixel map. Each detected blob is analyzed and categorized depending on its size. If the amount of pixels forming the blob is lower than  $S_{max}$ , it is considered as having a suitable size and assumed to contain a local maximum. It is then removed from the pixel map and will be part of the output mask. Otherwise, it is kept in the pixel map for the next iteration. Before iterating, the threshold value  $T$  is increased. The iteration process stops once the amount of fluorescent pixels in the pixel map reaches 0.
3. *Output:* The output mask is a binary image. It contains only blobs of fluorescent pixels with a pixel count inferior to  $S_{max}$  each containing at least one local maximum. The output map locates the bright fluorescent spots within the image and provides an approximation of their location.

The GLT algorithm takes advantage of the MM operators by using them to compute an estimation of the *Local Signal-to-Noise Ratio* (LSNR). The LSNR for a given pixel  $[x, y]$  is given using

$$\text{LSNR}[x,y] = \frac{I_{sig}[x,y]}{I_{bg}[x,y]} \quad (5.18)$$

where  $I_{bg}$  is an estimation of the background approximated by the lower envelope of an original image  $I$ , and  $I_{sig}$  is an estimation of the useful signal of  $I$  using the TH filter.

$$I_{bg} = I \circ B \quad (5.19)$$

$$I_{sig} = I - I \circ B = I - I_{bg} \quad (5.20)$$

This estimation of the LSNR is used to filter the extracted output mask. Fluorescent pixels corresponding to a LSNR inferior to a given value  $\text{LSNR}_{min}$  are trimmed out.

## 5.2 Comparison Frameworks for Spot Segmentation Methods

### 5.2.1 Comparison Framework For Image Classification

The comparison framework for classification requires to build two datasets of images from real biological samples: the *Stimulated Group* (SG) dataset and the *Negative Control Group* (NCG) dataset. The samples preparation protocol and the imaging setup used in this process are described in this section, before the actual comparison framework technicalities are explained.

#### Sample Preparation

Caco-2 cells were seeded in Lab-Tek chamber slides (Thermo Scientific Nunc) at a cell density of  $1.2 \times 10^5$  cells/cm<sup>2</sup> in DMEM/F12 medium supplemented with 10% fetal bovine serum. After 21 days, differentiated cells were stimulated over a 24 hours treatment period with *Lipopolysaccharide* (LPS) from E-Coli bacteria (L4391, Sigma-Aldrich) at a final concentration of 1  $\mu$ g/ml in order to get TLR2 expressed on the cell cytoplasm. After treatment, the cells were rinsed with *Phosphate Buffered Saline* (PBS), pH 7.4, and fixed with 4% paraformaldehyde in PBS for 10 minutes at *Room Temperature* (RT). After rinsing, the cells were permeabilized with 0.1% Triton X-100 in PBS for 3 minutes, then rinsed twice with PBS, and treated with 10% goat serum albumin in PBS for 20 minutes at RT. The cells were then labeled with an anti-TLR2 antibody (dilution 1:200, H175, Santa Cruz Biotechnology) for 1 hour at RT in 10% goat serum in PBS. The cells were then washed thrice with 0.1% Tween in PBS. After additional incubation with a FITC-conjugated goat anti-rabbit IgG (dilution 1:100, F2911) for 30 minutes at RT, the cells were mounted with Vectamount mounting medium for fluorescence (Vector Laboratories).

The cells prepared as described constitute the base to generate the SG dataset. Conversely, the NCG dataset is generated from cells prepared using the same protocol but ignoring the stimulation with LPS thus hindering the expression of TLR2 receptors.

#### Imaging Setup

The images are produced using an epi-fluorescent microscope setup. An Eclipse Ti-S inverted microscope combined with a Plan Fluor objective (40 $\times$ ,  $N_A = 0.6$ ) is used to image the samples. A 465–495nm band pass excitation filter, a 505nm dichroic mirror, and 515–555nm emission filter are used. The images are captured using a non-cooled black and white CCD image sensor (Sony ICX274AL) with a dynamic range of 12 bits. The image sensor pixels are 4.4 $\mu$ m by 4.4 $\mu$ m in size and form an array of 1,628 by 1,236 active pixels. Taking into consideration the 0.7 $\times$  magnification of the relay lens in front of the image sensor, a distance of 4.4 $\mu$ m in the image plane corresponds to  $\sim 157$ nm in the object plane. Sample images from both datasets are shown in Fig. 5.4.

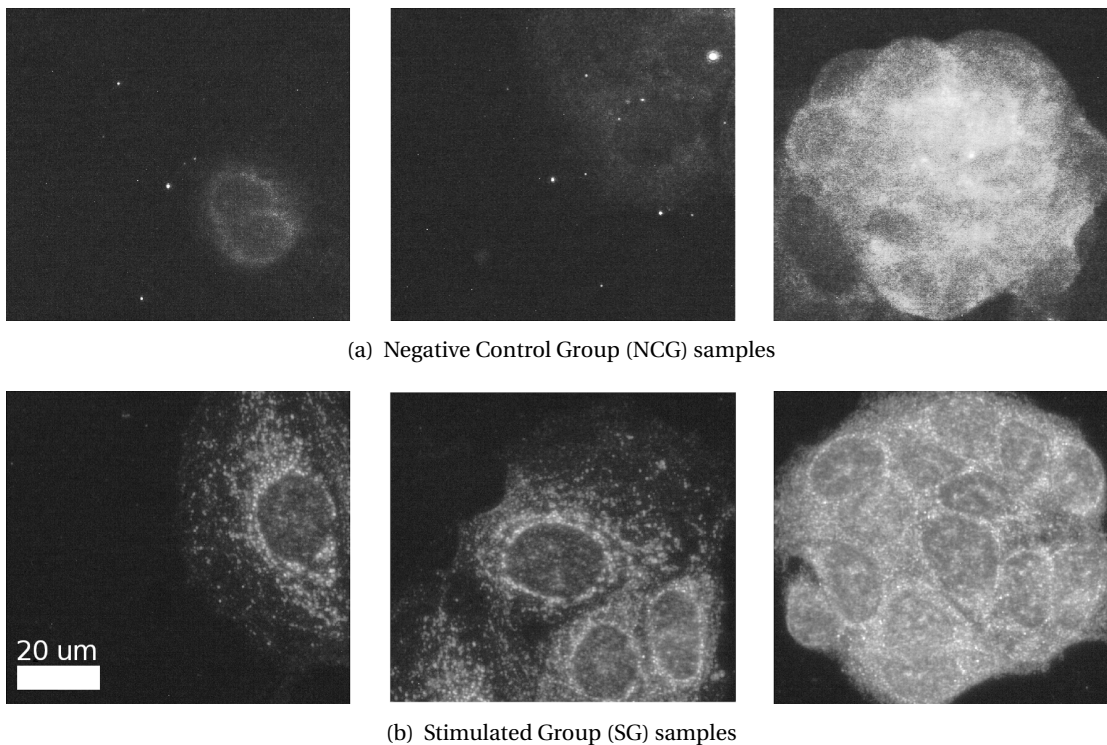


Figure 5.4 – Examples of Caco-2 cells expressing TLR2 receptors. The receptors were stained with a fluorescent dye through indirect immunostaining. (a) Sample images of cells from the NCG for which the exposure to LPS has been skipped during their preparation. (b) Sample images from the SG dataset showing cells with TLR2 expressed from LPS stimulation. Each image showcased in this Figure represents a sample area of about  $87\mu\text{m} \times 79\mu\text{m}$ . Note that the images intensity has been adapted for display purposes.

### Comparison Framework

Provided with a sample image, a *segmentation method* produces a segmentation mask and an observation  $t_l = (x_l, c_l)$  is made, where  $c_l$  is the class of the sample (i.e. either SG or NCG) and  $x_l$  is a measurement made on the image via the mask. We are considering two classification features for making the measurements: the amount of fluorescent pixels per cell and the mean pixel intensity.

**Amount of fluorescent pixels per cell** This value is the average number of fluorescent pixels per cell. In this work, the amount of cells in each image is assumed to be known. It can be measured in a preprocessing step, for example, through *Deoxyribonucleic Acid* (DNA) staining. The amount of fluorescent pixels per cell is expected to be higher for SG images than for NCG images. Ideally, a *segmentation method* processing a NCG image should not segment any pixels and discard them all as background.

**Mean pixel intensity** This value is the normalized average pixel intensity of all the fluorescent pixels.



## 5.2. Comparison Frameworks for Spot Segmentation Methods

For a given feature, we obtain a set of observations  $\mathbf{t} = \{t_l : l \in [1 \cdot N]\}$ , which is the union  $\mathbf{t} = \mathbf{t}_{SG} \cup \mathbf{t}_{NCG}$  between the set of observations made on the SG dataset

$$\mathbf{t}_{SG} = \left\{ t_i : t_i = (x_i, SG), i \in [1 \cdot N_{NCG}] \right\} \quad (5.21)$$

and the set of observations made on the NCG dataset

$$\mathbf{t}_{NCG} = \left\{ t_j : t_j = (x_j, NCG), j \in [1 \cdot N_{NCG}] \right\} \quad (5.22)$$

The first point of comparison between the *segmentation methods* is an evaluation of the effect size between the NCG and SG group using the  $d$  statistic (Hedge's  $g$ ) [85]. Practically, the effect size is evaluated using

$$d = \frac{\overline{x}_{SG} - \overline{x}_{NCG}}{\sigma_{pooled}} \quad (5.23)$$

$$\sigma_{pooled}^2 = \frac{(N_{SG} - 1)\sigma_{SG}^2 + (N_{NCG} - 1)\sigma_{NCG}^2}{N_{SG} + N_{NCG} - 2} \quad (5.24)$$

where  $\overline{x}_{SG}$  and  $\overline{x}_{NCG}$  are the sample means made on the observation sets  $\mathbf{t}_{SG}$  and  $\mathbf{t}_{NCG}$  respectively, and  $\sigma_{SG}^2$  and  $\sigma_{NCG}^2$  are their associated variance. The standard error on this  $d$  statistic is computed using [85]

$$se_d = \sqrt{\frac{N_{SG} + N_{NCG}}{N_{SG}N_{NCG}} + \frac{d^2}{2(N_{SG} + N_{NCG}) - 1}} \quad (5.25)$$

Such an effect size can be computed for each *segmentation method* based on the observations sets. As a high effect size indicates a good separation of the two classes (SG and NCG), we can identify for each feature the best performing *segmentation methods* for classifying the Caco-2 cell samples by putting the effect sizes side by side.

We are also considering *Receiver Operating Characteristics (ROC)* analysis as a comparison tool. Consider the naive Bayes classifier trained with the observation sets  $\mathbf{t}_{SG}$  and  $\mathbf{t}_{NCG}$ . A common performance metric of the resulting trained classifier is the *Area Under Curve (AUC)*. It is used in this study to compare the performance of the various Bayes classifiers trained using the observation sets generated from the segmentation results of the algorithms.

The method used to estimate the various AUC is that described in [149]. It provides a non-parametric estimator for the AUC and an estimate for its variance based on leave-pair-out bootstrap scheme, which makes it ideal for datasets with few samples. Practically,  $B$  bootstrap replications  $\mathbf{T} = \{\mathbf{t}_b^* : b \in [1 \cdot B]\}$  are obtained by re-sampling the set of observations  $\mathbf{t}$  using a balanced bootstrap mechanism [22]. Each replication  $\mathbf{t}_b^*$  is then used to train a naive Bayes classifier, effectively producing  $B$  scoring functions  $h_{\mathbf{t}_b^*}(x)$ . The procedure selects a pair of observations  $(t_i, t_j)$  — one from each class SG and NCG — and averages its contribution to

the Wilcoxon–Mann–Whintey statistics [70, 145] over all the possible bootstrap replications. Formally, we have

$$\widehat{AUC} = \frac{1}{N_{SG}N_{NCG}} \sum_{i=1}^{N_{SG}} \sum_{j=1}^{N_{NCG}} \sum_{b=1}^{N_B} \frac{I_i^b I_j^b H(h_{\mathbf{t}_b^*}(x_i) - h_{\mathbf{t}_b^*}(x_j))}{\sum_{b'=1}^B I_i^{b'} I_j^{b'}} \quad (5.26)$$

where  $H$  is the Heaviside step function and  $I_i^b I_j^b$  equals 1 unless either of the observations forming the pair  $(t_i, t_j)$  is contained in  $\mathbf{t}_b^*$ , in which case it equals 0 and voids the contribution. On the other hand, a standard error on  $\widehat{AUC}$  can be computed using

$$se_{\widehat{AUC}} = \frac{1}{N_{SG}^2} \sum_{i=1}^{N_{SG}} \hat{U}_{1_i}^2 + \frac{1}{N_{NCG}^2} \sum_{j=1}^{N_{NCG}} \hat{U}_{2_j}^2 \quad (5.27)$$

where  $\hat{U}_{1_i}^2$  and  $\hat{U}_{2_j}^2$  can be obtained from the bootstrap replications  $\mathbf{t}_b^*$ , similar to  $\widehat{AUC}$ . Details of their calculation are left out of this thesis for clarity and we refer the reader to [149] for more details.

Similar to the effect size, an estimation of the AUC can be computed for each *segmentation method*. The closer the area is to 1, the better the trained naive Bayes classifier is. In turn, for each classification feature (amount of fluorescent pixels per cell or mean pixel intensity), we can evaluate the performance of the *segmentation method* by directly comparing the effect sizes and classifier performance.

### 5.2.2 Comparison Framework For Biomarker Localization

After a sample image has been classified as SG, using the blobs of fluorescent pixels as an approximation for the fluorescent spot locations becomes of interest. Comparing the *segmentation methods* on this ground using the real SG dataset is not feasible as the location of every fluorescent biomarker is not precisely known. To overcome this, the synthetic image generation tool presented in Chapter 4 is put to use and configured to match the experimental setup and imaging conditions.

Consider a synthetic SG dataset  $\mathbf{I}_{syn} = \{I_n : n \in [1 \cdot N]\}$  built from  $N$  synthetic images. Such a dataset contains images each featuring a random number of stained cells for which the precise locations (i.e., pixel locations within the image) of each fluorescent probe is known. Overall the dataset features  $N_{cells}$ , each stained by  $N_p$  probes over  $N$  images. A *segmentation method* processing the set of images  $\mathbf{I}_{syn}$  generates a set of segmentation masks  $\mathbf{M}_s = \{M_n : n \in [1 \cdot N]\}$  that can be partitioned in  $N_{blobs}$  segmentation blobs using CC labeling. These segmentation results are analyzed and compared using the following metrics:

**Recovered probes** Consider the number of probes  $N_{rec}$  that are recovered by  $\mathbf{M}_s$  over the synthetic dataset, knowing that a probe is deemed recovered if its pixel location within the image belongs to a blob of fluorescent pixels. The recovered probes value corresponds

## 5.2. Comparison Frameworks for Spot Segmentation Methods

---

to the relative amount of recovered probes over the synthetic dataset  $N_{rec}/N_p$ .

**Blobs per cell** This value is a direct measure of the average amount of segmentation blobs per cell over the synthetic dataset  $N_{blobs}/N_{cells}$ .

**Blobs without probes** This value indicates the fraction of blobs that do not recover any probe over the synthetic dataset.

**Blob size** This is the average size in pixels of the segmentation blobs over the synthetic dataset.

**Probes per blob** Knowing the location of the probes, we can determine the average amount of probes that are recovered by a single segmentation blob.

**Chi-squared ( $\chi^2$ )** This value is the chi-squared histogram distance metric [99] used to quantify whether an image segmentation of a sample featuring fluorescent probes is relevant and contains useful information.

Consider the  $N_p$  probes and their location within each image of the set  $\mathbf{I}_{syn}$ . One can define a set of masks  $\mathbf{M}_p = \{L_n : n \in [1 \cdot N]\}$  where  $L_n$  is a mask identifying the location of the probes within  $I_n$  using

$$L_n[x, y] = \begin{cases} 1, & \text{if pixel } I_n[x, y] \text{ encloses at least one probe} \\ 0, & \text{otherwise} \end{cases} \quad (5.28)$$

where  $I_n[x, y]$  is a pixel of  $I_n$ . In other words,  $\mathbf{M}_p$  is an ideal set of segmentation masks featuring the minimum number of segmentation pixels such that the amount of recovered probes equals 100% with 0 blob without probes. From  $\mathbf{M}_p$ , one can compute the following set of images

$$\mathbf{D}_p = \{I_n * L_n : n \in [1 \cdot N]\} \quad (5.29)$$

where  $*$  is a pixel-wise multiplication between the image  $I_n$  and the location mask  $L_n$ . Finally, we obtain the intensity distribution of the pixels where the probes are located by taking the histogram  $\mathbf{H}_p$  of the non-null pixel values of  $\mathbf{D}_p$ . That is, the histogram  $\mathbf{H}_p$  represents the distribution of pixels selected by the ideal set of segmentation masks  $\mathbf{M}_p$ .

Similarly, provided with a set of segmentation masks  $\mathbf{M}_s$  generated by a *segmentation method*, one can extract the intensity histogram  $\mathbf{H}_s$  of the segmented pixels using

$$\mathbf{D}_s = \{I_n * M_n : n \in [1 \cdot N]\} \quad (5.30)$$

For our purpose, the  $\chi^2$  histogram distance value is defined as the bin-to-bin distance between the ideal histogram  $\mathbf{H}_p$  and the histogram  $\mathbf{H}_s$ . It is computed using

$$\chi^2 = \sum_i \frac{(H_s[i] - H_p[i])^2}{H_s[i] + H_p[i]} \quad (5.31)$$

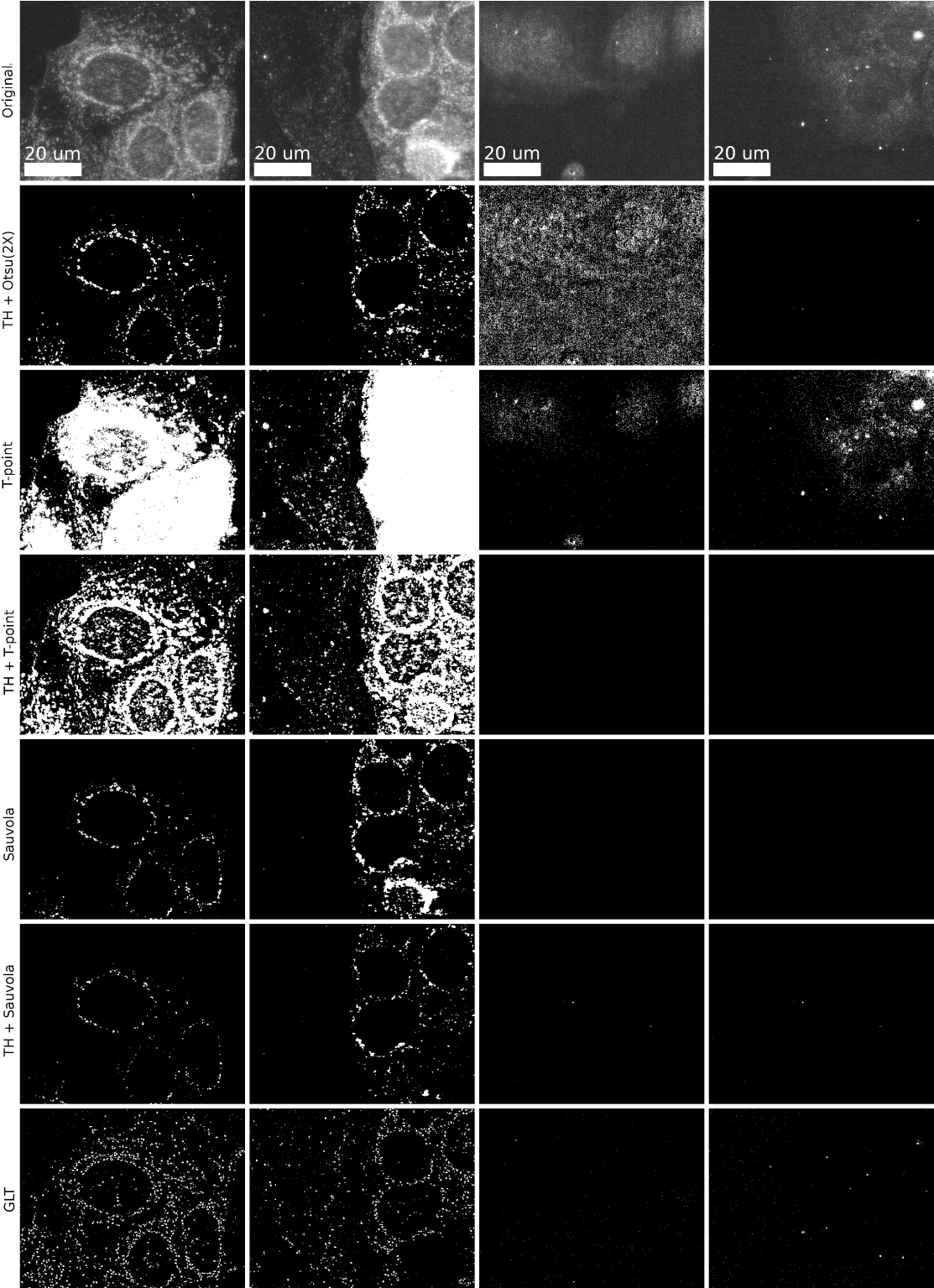


Figure 5.5 – Sample segmentation masks resulting from the application of selected *segmentation methods*. The top row depicts the unprocessed images with the two first images being representative of the SG dataset and the two last being representative of the NCG dataset. These have adapted intensity for display purposes.

where  $H_P[i]$  and  $H_S[i]$  are the frequencies reported in the  $i^{th}$  bin of  $\mathbf{H}_P$  and  $\mathbf{H}_S$ , respectively.

This  $\chi^2$  histogram distance gives us a single figure of merit to evaluate the quality of a set of segmentation masks. The less a set of segmentation masks  $\mathbf{M}_S$  is recovering basic information carried by the fluorescent probes, the greater the value of  $\chi^2$ .

Practically, we are interested in recovering as many probes as possible. Thus, the *segmentation methods* that generate the greatest recovered probe values are favored, other things being equal. However, we consider segmentation masks with small, spatially contained blobs better in localizing fluorescent spots when compared to segmentation masks featuring big, spread blobs. So, having a small average blob size, characterized by few probes per blobs is favored when compared to having a great number of recovered probes. Also, the amount of blobs without probes and  $\chi^2$  distances are monitored to ensure that the segmentation masks are not extracting irrelevant pixels.

### 5.3 Biosample Classification Performances

This section presents and analyzes the results of the comparison classification framework presented in Section 5.2.1. It is applied to two datasets, a SG dataset of 22 images and a NCG dataset of 15 images. Each image features a variable amount of imaged Caco-2 cells ranging from 1 to 20, and they all have been captured in the same experimental and imaging conditions. The first row of Fig 5.5 depicts representative sample images from both datasets.

The various algorithms used in the considered *segmentation methods* are parameterized as follow:

**Top-Hat filtering** The structuring element used for this operator is a disk of 21 pixels in diameter.

**T-point algorithm** The histograms used to set thresholds are computed using a bin width of 32, as smaller bins produce big discontinuities in the histograms frequencies, which in turn prevent proper lines fitting on the descending slopes. Since the images have a 12-bit resolution, this divides the histograms into 128 bins.

**Otsu's algorithm** The histogram bin width used is 16, resulting in histograms divided into 256 bins. The purpose of this selection is that it has no significant impact on the results when compared to a bin size of 1 while enabling the method to be less computationally intensive.

**Sauvola's thresholding technique** The algorithm parameters are set as follow; dynamic range  $R = 0.5$  (our images have normalized pixel values), window width  $w = 41$  (radius = 20) and  $k = 0.34$  (as suggested in [113]).

**GLT algorithm** The maximum size for any fluorescent blob is  $S_{max} = 15$  and only fluorescent pixels with a LSNR greater than 1.7 are kept.

Each row in Fig. 5.5 displays the resulting segmentation masks of one of the nine considered *segmentation methods*, except for the first row, which depicts the original, unprocessed images. Note that the Otsu-based methods are only represented by the second row for space consideration. When dealing with SG images, the masks produced by Otsu (not recursively)-based methods resemble the ones produced by T-point-based methods. As for the one using Otsu recursively, the masks are similar to the one presented on the second row, only the blobs of fluorescent pixels appear slightly *fatter*. The most important results on the second row are the masks of the NCG images. They are typical of all the Otsu-based methods and give an idea of how they handle images with low fluorescence and few spots.

Table 5.2 presents the average amount of fluorescent pixels recovered by each *segmentation method* over both datasets. The resulting effect sizes and performance of trained naive Bayes classifiers (AUC) are reported in Table 5.2 with a 95% confidence interval.

Similarly, Table 5.3 deals with the mean pixel intensity and related effect sizes and AUC. Finally, Fig. 5.6 and 5.7 report graphically the various computed effect sizes along with the various estimated AUC from Table 5.2 and 5.3 for an easy comparison.

The set of parameters used to configure the various *segmentation methods* was obtained empirically. For each *segmentation method*, the parametrization that is used to obtain the results presented in Table 5.2 and 5.3 are those that maximized the absolute value of the effect size computed from the mean pixel intensity. This parameter optimization was done manually and only the best results are reported here.

These results are analyzed and discussed for each thresholding algorithm in order to identify the best-performing *segmentation methods*. We discuss here the usage of the amount of pixels per cell and mean pixel intensity measurements as classification features to distinguish between SG and NCG images.

**AllPix** Using only the average pixel intensity per cell, without segmentation, as a classification feature is not reliable. Table 5.3 shows that the average pixel intensity is 0.114, which is the smallest value compared with the other methods. Fluorescent images from the SG dataset feature few bright pixels and a lot of background, low-intensity pixels. This effectively decreases the mean pixel intensity when all the pixels are segmented, and reduces the effect size between the two datasets.

**T-point based methods** On the SG dataset without TH filtering, using the threshold value computed by the T-point algorithm results in segmenting most of the cell cytoplasm. Similarly, on the NCG dataset images, clouds of segmented pixels appear where the cells are located. This can be observed in the third row of Fig. 5.5. Looking at the amount of fluorescent pixels in Table 5.2, we can observe a huge variability in the results, which limits the effect size (1.69) and the classifier performance ( $AUC = 0.925$ ) with respect to the best methods. Table 5.3, referring to the mean pixel intensity classification feature, offers the same conclusion. Only this time the relatively low mean pixel intensity (0.216)

### 5.3. Biosample Classification Performances

Table 5.2 – Amount of fluorescent pixels per cell on each dataset, related effect size, and AUC of trained naive Bayes classifiers for different *segmentation methods*.

Method	SG pixels per cell ( $\sigma$ )	NCG pixels per cell ( $\sigma$ )	Effect size ( $1.96 \times se$ )	AUC ( $1.96 \times se$ )
<i>AllPix</i>	--	--	--	--
<i>T-point</i>	28,332 (19,752)	2,626 (4,354)	1.69 (0.26)	0.925 (0.026)
<i>Otsu</i>	15,914 (9,291)	33,004 (26,254)	-0.97 (0.23)	0.753 (0.028)
<i>Otsu(2X)</i>	3,178 (1,826)	10,758 (8,939)	-1.33 (0.25)	0.839 (0.030)
<i>Sauvola</i>	819 (689)	2 (5)	1.56 (0.25)	0.987 (0.030)
<i>TH + T-point</i>	17,471 (8,556)	973 (732)	2.54 (0.31)	0.993 (0.030)
<i>TH + Otsu</i>	7,618 (3,188)	43,676 (44,449)	-1.31 (0.24)	0.925 (0.026)
<i>TH + Otsu(2X)</i>	1,244 (566)	14,260 (17,579)	-1.20 (0.24)	0.998 (0.030)
<i>TH + Sauvola</i>	327 (260)	2 (4)	1.65 (0.27)	0.985 (0.028)
<i>GLT method</i>	2,593 (1,504)	75 (118)	2.20 (0.29)	0.981 (0.028)

Table 5.3 – Mean pixel intensity (normalized) on each dataset, effect size, and AUC of trained naive Bayes classifiers for different *segmentation methods*.

Method	SG pixels intensity ( $\sigma$ )	NCG pixels intensity ( $\sigma$ )	Effect size ( $1.96 \times se$ )	AUC ( $1.96 \times se$ )
<i>AllPix</i>	0.114 (0.048)	0.059 (0.012)	1.48 (0.25)	0.938 (0.037)
<i>T-point</i>	0.216 (0.058)	0.096 (0.027)	2.55 (0.31)	0.970 (0.033)
<i>Otsu</i>	0.271 (0.087)	0.073 (0.018)	2.96 (0.35)	1.000 (0.036)
<i>Otsu(2X)</i>	0.422 (0.128)	0.105 (0.085)	2.87 (0.34)	0.964 (0.034)
<i>Sauvola</i>	0.554 (0.054)	0.806 (0.167)	-2.27 (0.29)	0.863 (0.034)
<i>TH + T-point</i>	0.242 (0.074)	0.091 (0.021)	2.62 (0.32)	0.989 (0.033)
<i>TH + Otsu</i>	0.316 (0.089)	0.092 (0.104)	2.40 (0.30)	0.955 (0.032)
<i>TH + Otsu(2X)</i>	0.490 (0.117)	0.236 (0.339)	1.12 (0.24)	0.972 (0.038)
<i>TH + Sauvola</i>	0.444 (0.036)	0.769 (0.159)	-3.18 (0.24)	0.843 (0.032)
<i>GLT method</i>	0.316 (0.094)	0.111 (0.029)	2.79 (0.33)	1.000 (0.036)

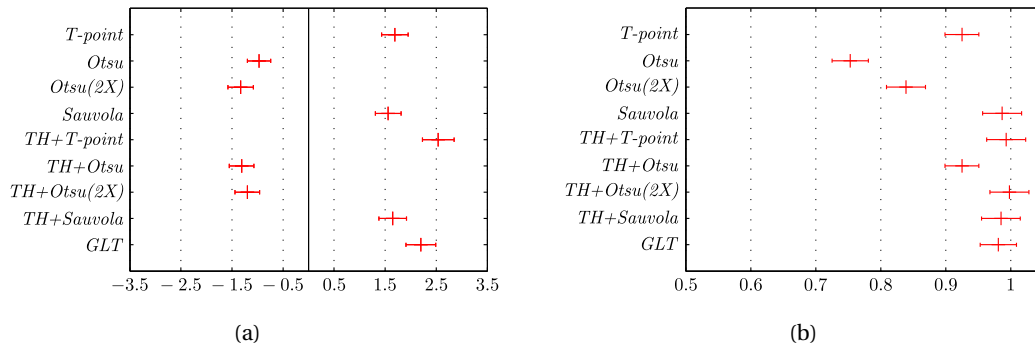


Figure 5.6 – Effect size and AUC computed from the amount of fluorescent pixels per cell measurements made by each *segmentation method* on both SG and NCG datasets. The effect size is a measure of the distance between both datasets and the AUC estimates are measures of the performance of naive Bayes classifiers trained on the measurements.

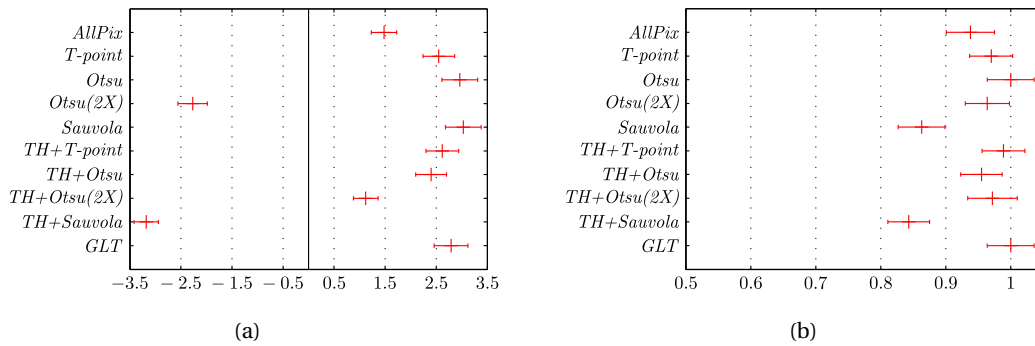


Figure 5.7 – Effect size and AUC computed from the mean pixel intensity measurements made by each segmentation scheme on both SG and NCG datasets. The effect size is a measure of the distance between both datasets and the AUC estimates are measures of the performance of naive Bayes classifiers trained on the measurements.



of the SG dataset is the cause, as the segmented areas include a lot of background pixel. Filtering the images with TH before computing the threshold value is beneficial. As the fourth row of Figure 5.5 shows, *TH+T-point* prevents the background pixels from the cell cytoplasm from being segmented in SG images. Furthermore, few pixels are segmented in NCG images compared other *segmentation methods*, which is expected behavior. In Table 5.2, we can notice the reduced variability in the amount of fluorescent pixels per cell introduced by the TH filter, by comparing both *T-point* and *TH+T-point*. This results in a higher classification performance as indicated by the increased effect size ( $1.69 < 2.54$ ) and AUC ( $0.925 < 0.993$ ). From Table 5.3, we can see that using the TH filter helps segmenting the fluorescent spots. The mean pixel intensity increases for the SG dataset, whereas it remains almost unchanged for the NCG dataset. This results in a slightly improved classification performance. Practically, the T-point algorithm is particularly well suited as most fluorescent images feature a unimodal histogram, characteristic of a lot of background pixels and few pixels of interest. The TH filter further enhances the unimodality by removing slow variations of background. Considering the amount of fluorescent pixels per cell or the mean pixel intensity classification features independently, the *TH+T-point* method is among the bests.

**Otsu based methods** Unlike the T-point algorithm, Otsu's algorithm is designed to separate the image histogram into two classes using a threshold having the highest separability. This makes it ideal for bimodal histograms. Fluorescent images feature occasionally this behavior when the amount of fluorescently stained cells is high enough to balance the background contribution to the histogram. As predicted, Otsu's algorithm is ill-suited for classification, even when applied recursively twice. While the extracted information on the SG dataset appears to be good (i.e., low amount of fluorescent pixel per cell and high mean pixel intensity), every *segmentation method* using Otsu behaves poorly when facing the NCG dataset. Table 5.2 presents negative effect sizes for these *segmentation methods* because the average amount of fluorescent pixels per cell is higher for the NCG dataset than for the SG dataset. Furthermore, the variability of the amount of fluorescent pixels per cell for the NCG dataset is considerable. The masks, example of NCG images provided in the second row of Figure 5.5, show the two typical outcomes from our NCG dataset. Either a lot of noise is segmented, or only bright macro-objects (e.g., dust particles) are segmented. The former comes from Otsu selecting a threshold somewhere in the middle of the single mode of the histogram that represents unstained cell samples and the background. The latter comes from the proper separation between the unstained cells/background mode in the low intensities and the mode added by the high-intensity unwanted objects. To sum up, Otsu-based *segmentation methods* cannot be recommended for the problem of classification. Despite the relative good classification performances obtained when using the mean pixel intensity classification feature on our datasets, these *segmentation methods* provide unwanted segmentation results for NCG images where a low (ideally null) amount of fluorescent pixel per cell is expected.

**Sauvola based methods** Unlike the previously discussed methods, Sauvola's approach provides a specific threshold value for each pixel in an image based on its immediate surroundings. This practically removes the influence of slow varying background intensity by extracting regions with a local high contrast. Compared with other methods, Sauvola's thresholding technique is extracting fewer pixels of higher intensities with a limited standard deviation when processing the SG dataset. Notably, the extracted amount of fluorescent pixels per cell on the NCG dataset is statistically null, showing that this technique can be set to exclude most of the background noise. As a result, the effect size and AUC figures presented in Table 5.2 confirm that the amount of fluorescent pixels per cell can be used to obtain a reliable classification. Conversely, a classification based on the mean pixel intensity is not reliable owing to the very low amount of extracted pixels in the NCG dataset. When the TH filter preprocessing step is used, the results and observations practically remain unchanged, which is no surprise considering that the TH filter filters out low frequencies that are already ignored in Sauvola's algorithm by design. This is confirmed by the effect sizes and AUC (Table 5.2), which show that TH filtering does not enhance the classification results. The observed drop in the amount of fluorescent pixels per cell can be reduced by increasing the size of the structuring element used in TH filtering compared with the size of the sliding window used for Sauvola's algorithm.

**GLT method** This method was specifically designed to extract fluorescent spots by searching for blobs of fluorescent pixels of limited size having intensity higher than that of their surroundings. With *Sauvola*, it is one of the two methods that segments the fewest pixels when no fluorescent signal is present in an image. Looking at the effect sizes and AUC obtained in Tables 5.2 and 5.3, this method is comparable to the global thresholding *TH+T-point* method.

After having analyzed the real images, we can already sum up a few important points for classifying fluorescent sample images. First, the simple average image intensity and Otsu-based *segmentation methods* are not reliable for classification. The best *segmentation methods* for this task are *TH+T-point*, *Sauvola*, and the *GLT method*.

### 5.4 Localization Performance of Biomarkers on Synthetic Images

This section presents and discusses the results of the comparison framework for localization presented in Section 5.2.2. It is applied on a synthetic SG dataset built from 100 images. For each considered method, a parameter space exploration is performed and used to analyze how the six comparison metrics are influenced. A segmented sample of a synthetic cell is depicted in Fig. 5.8, featuring randomly distributed fluorescent biomarkers, uneven background fluorescence, and cytoplasm autofluorescence. Similar to the real datasets, each image from the synthetic dataset features a varying amount of cells, between 1 and 10 in this case.

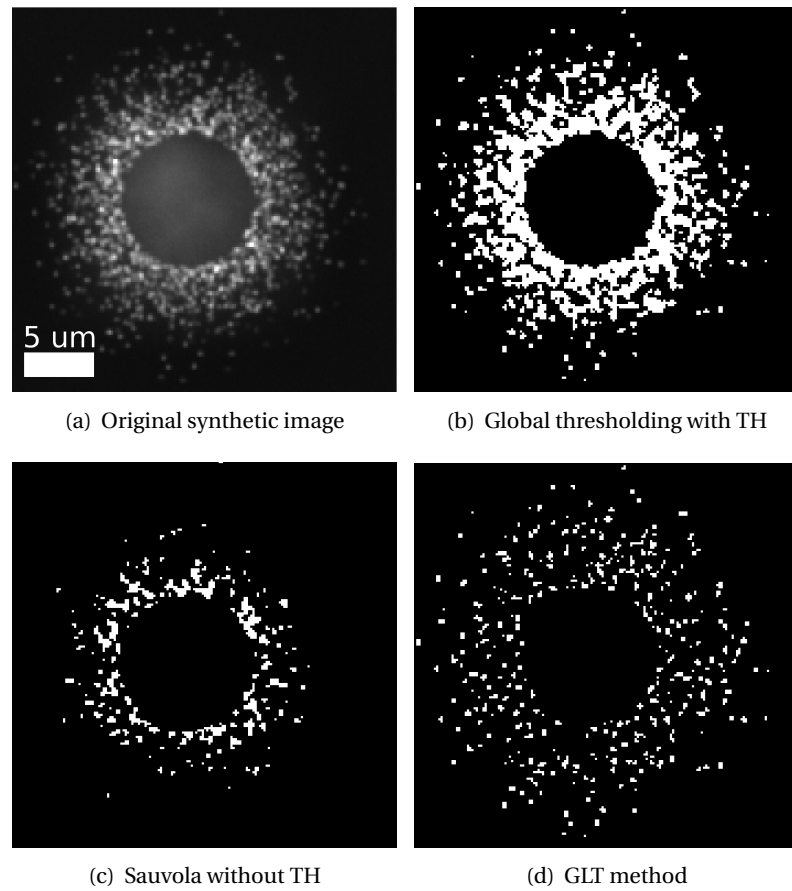


Figure 5.8 – (a) Close-up of an imaged synthetic cell. (b) Segmentation mask with a global thresholding ( $th = 0.09$ ) on the TH filtered image. (c) Segmentation mask with Sauvola's thresholding technique ( $k = 0.34$ , radius = 20). (d) Segmentation mask with the GLT algorithm ( $S_{max} = 15$ ,  $LSNR_{min} = 1.7$ ).

We are interested in comparing the segmentation quality on SG images of the best-performing *segmentation methods* for classification. Thus, the three methods we are considering here are (a) global thresholding on TH filtered images (this includes *TH+Otsu*, *TH+Otsu(2X)* and *TH+T-point*), (b) *Sauvola*, and (c) the *GLT method*. The parameter exploration results are presented in Fig. 5.9, Fig. 5.10 and Fig. 5.11, respectively. Fig. 5.9 details the behavior of the global thresholding method applied on TH filtered images by plotting the various comparison metrics with respect to the thresholding value. Similarly, Fig. 5.10 presents the response of the metrics using *Sauvola* by varying the  $k$  parameter and the window radius. Finally, Fig. 5.11 presents the response of the metrics using the *GLT method* by varying the  $S_{max}$  and  $LSNR_{min}$  parameters.

Let us now analyze and discuss the various curves plotted in Fig. 5.9, Fig. 5.10 and Fig. 5.11 to determine what method is best suited for properly segmenting fluorescent spots using synthetic images.

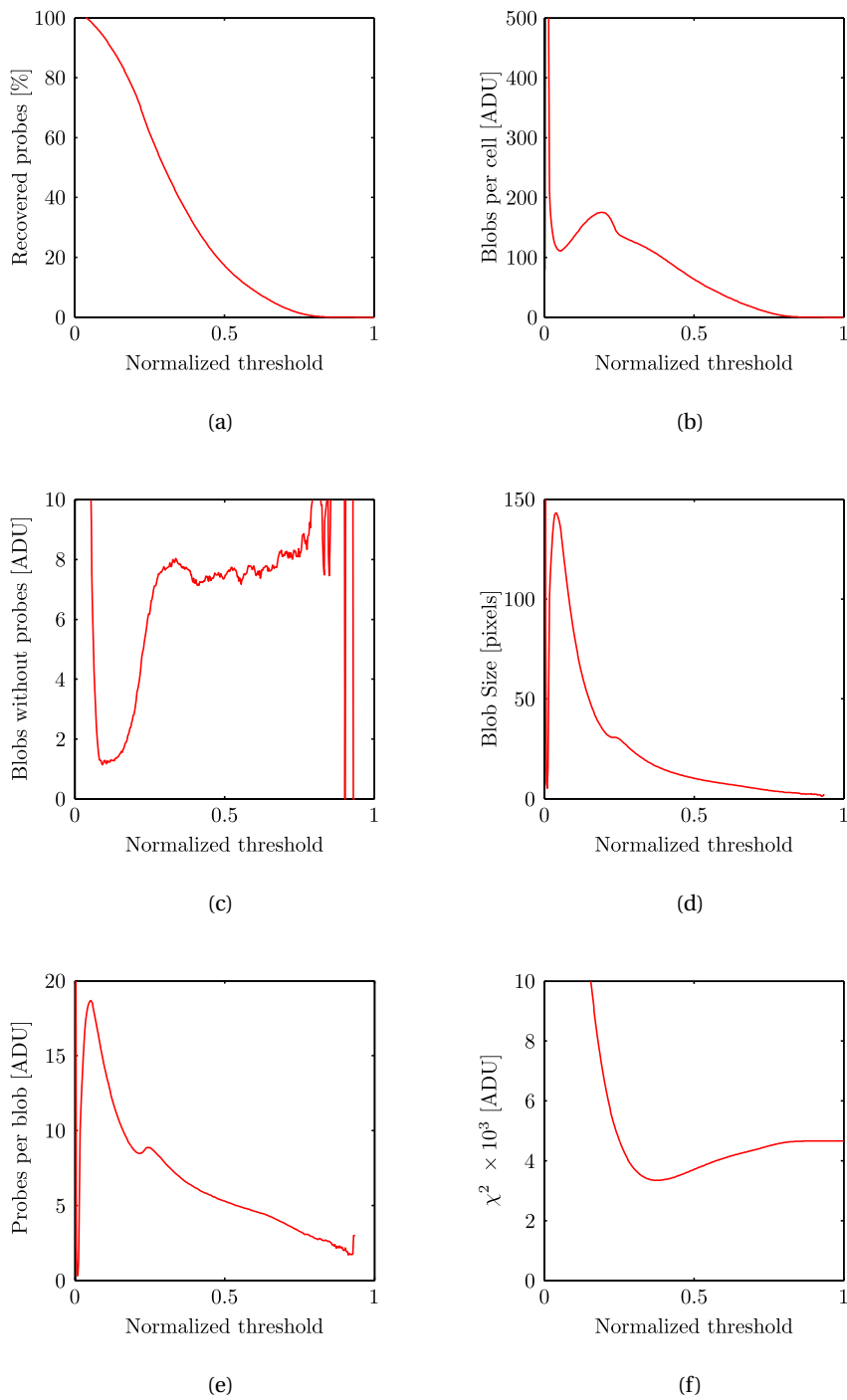


Figure 5.9 – Parameter exploration for the global thresholding technique on TH filtered images. This technique has only one parameter, the threshold value, represented on the x-axis in a normalized manner.

## 5.4. Localization Performance of Biomarkers on Synthetic Images

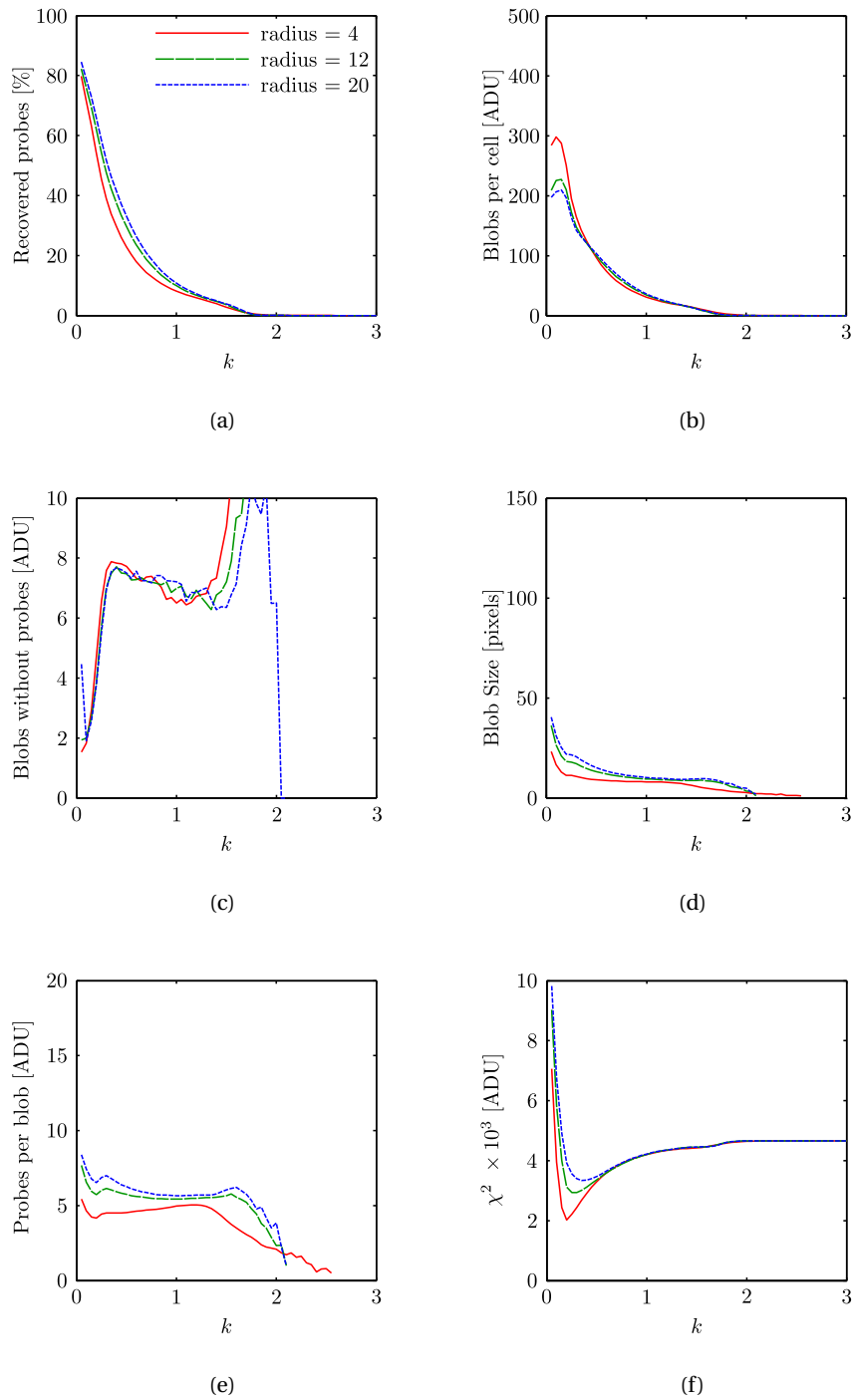


Figure 5.10 – Parameter exploration for the *Sauvola method*. The x-axis represents the  $k$  parameter ranging from 0 to 3. The red solid (radius = 4), green dashed (radius = 12), and blue dotted (radius = 20) curves show the influence of the window radius.

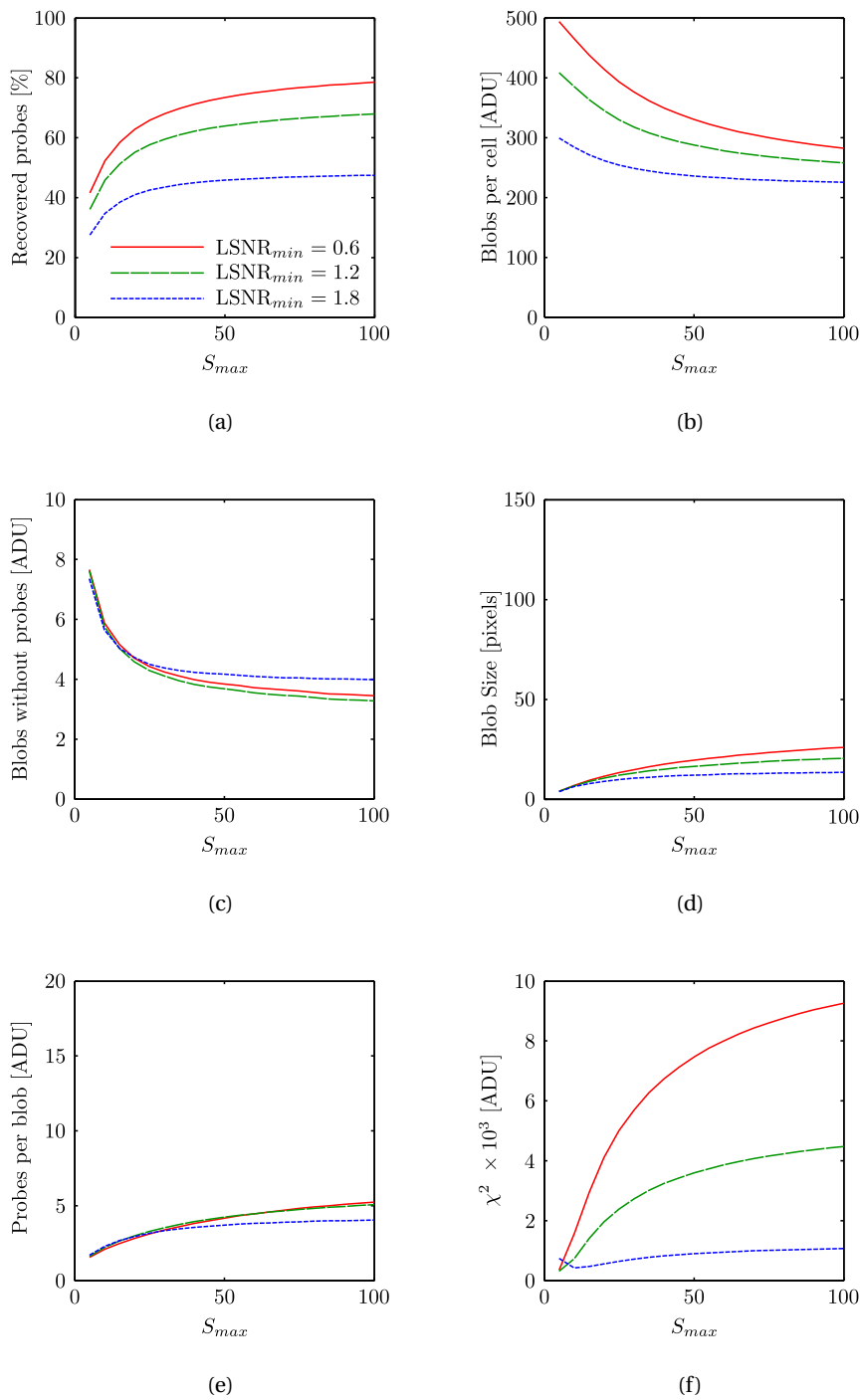


Figure 5.11 – Parameter exploration for the *GLT method*. The x-axis represents the  $S_{max}$  parameter ranging from 0 to 100. The red solid (LSNR<sub>min</sub> = 0.6), green dashed (LSNR<sub>min</sub> = 1.2), and blue dotted (LSNR<sub>min</sub> = 1.8) curves show the influence of the filtering based on the LSNR.

**Global thresholding on TH filtered images** Starting at a threshold value of 0, the whole filtered image is segmented. In this case, we have a single blob having the same size as the image enclosing all the fluorescent probes. As the threshold value increases, the average amount of blobs per cell decreases drastically (Fig. 5.9(b)) and their average size drops just above 454 pixels (Fig. 5.9(d)). In this case, many blobs just represent noise from the background. Thus, the relative amount of blobs failing to recover fluorescent probes is high (Fig. 5.9(c)). Proper fluorescent spot segmentation happens for a normalized threshold value high enough so that background noise is not segmented. In our test case, this happens for a normalized threshold value of 0.09, where the amount of blobs not recovering fluorescent probes is minimum (Fig. 5.9(c)). Further increase of the threshold will eventually trigger some blobs to be broken down into many blobs (local maximum in Fig. 5.9(b)) alongside with the amount of blobs not enclosing any probes (local maximum in Fig. 5.9(c)). This indicates that global thresholding applied on TH filtered images has an optimal threshold value which maximizes the segmentation and spot extraction efficiency. Below this optimal threshold, the segmentation masks include background noise. This situation occurs when the *TH+T-point* method is used to determine the threshold value (0.02). Above the optimal threshold, some information is lost. With an average normalized threshold value of 0.14 and 0.33 for *TH+Otsu* and *TH+Otsu(2X)* respectively, the latter appears less optimal.

**Sauvola method** A very low value of the parameter  $k$  comes down to thresholding a given pixel with the average pixel intensity within its surrounding window. This results in many blobs segmenting noise. The amount of blobs is very high (Fig. 5.10(b)), just like the amount of blobs not enclosing any fluorescent probe (Fig. 5.10(c)). By design, Sauvola's method removes segmentation noise for a high enough value of  $k$ . In our test case, this happens for a value of  $k$  greater than 0.2, independently from the radius. From this value of  $k$  and higher, which corresponds to peaks found in the average blob size (Fig. 5.10(d)), all the metrics from Fig. 5.10 are decreasing except for the blobs without probes and the  $\chi^2$  histogram distance. This means blobs are getting fewer and smaller, effectively locating fluorescent dots but leaving behind some useful information contained in the images. Looking at the influence of the window radius, we observed that the various curves seem to converge as the radius increases. Increase of the window radius seems to favor a bigger average size of the blobs, which inherently favors the amount of fluorescent probes enclosed per blob.

**GLT method** We are analyzing the effect of the maximum allowed size for a blob  $S_{max}$  (x-axis on Fig. 5.11) and of the  $LSNR_{min}$  parameter. As we can see on Fig. 5.11, a value of  $S_{max}$  smaller than the average size of a fluorescent spot cannot be considered. If  $S_{max}$  is smaller than 5 pixels, the results are meaningless. However, as we sweep  $S_{max}$  up until 100 pixels, we can observe that more fluorescent spots are segmented, while the amount of blobs not segmenting probes is decreasing and the  $\chi^2$  histogram distance is increasing. This indicates that our blobs are becoming bigger and collecting more and more probes per blob. The  $LSNR_{min}$  parameter practically reduces the average size of

the blobs as it increases. This has the exact opposite effect as the  $S_{max}$  parameter on the metrics in Fig. 5.11. Note that in our test case, a  $LSNR_{min}$  value smaller than 0.6 allowed background noise to be segmented.

Knowing that the segmentation goal is to locate the fluorescent probes, we are interested in segmenting an image so that we have as many small blobs as possible, each enclosing a minimum amount of fluorescent probes. The *GLT method* performs best in that aspect. Looking at Fig. 5.11 and within the parameter range described just above, it is able to provide 225–300 blobs per cell between 4 and 13 pixels in size enclosing from two to four fluorescent probes. In other words, we are recovering 27–47% of the probes while keeping the  $\chi^2$  histogram distance between 400 and 1 000. Sauvola’s method is able to provide similar blob sizes but the blobs are fewer per cell, between 75 and 85, extracting up to 15% of the probes only for a  $\chi^2$  distance ranging from 3 600 to 4 600. A smaller  $\chi^2$  distance could be achieved at the expense of the blob size and the amount of probes per blob. In contrast, the global thresholding of TH filtered images is not able to provide a  $\chi^2$  distance smaller than 3 350, which results in blobs of 16 pixels segmenting 35% of the probes only. A lower threshold value increases drastically the blob sizes and a smaller threshold value further reduces the accuracy. As a result, the *GLT method* is preferred as it is able to recover relevant fluorescent pixels in a greater number of smaller blobs compared with other methods, while keeping the amount of failed blob segmentations contained.

### 5.5 Chapter Summary and Contributions

In this chapter, various image segmentation algorithms are considered and compared for the purpose of segmenting fluorescent spots in microscopic images. Commonly used global thresholding algorithms (T-point and Otsu’s algorithms) and a local thresholding algorithm (Sauvola’s algorithm) combined with the mathematical morphology Top-Hat filter have been selected. These algorithms have been selected due to their wide-spread use in the field of biomarker segmentation. The presented comparison offers a new view on these algorithms as previous comparison reviews either focused on the segmentation of cells and not sub-cellular biomarkers [26] or on signal enhancement algorithms such as TH [124, 125].

The comparison further includes a novel local thresholding method, the *GLT method*, presented in this chapter. This technique was specifically designed to segment fluorescent spots in images. It was designed by setting a focus of the various local maxima representing the bright spots. With respect to the other methods, it aimed at providing blobs of controlled size around these maxima in an attempt to translate the spatial location of the biomarkers in the produced segmentation masks.

The comparison is undertaken on two aspects. The segmentation masks provided by the methods are used to extract further metrics related to the fluorescent signals in order to (i) evaluate how well the segmentation masks can provide classification features for classifying



real fluorescent biological samples from negative control samples and (ii) quantitatively compare the segmentations masks based on simulated data from the synthetic generation tool of Chapter 4.

The novel *GLT* method is proven to perform best for the classification of the fluorescent images given the two real *Stimulated Group* (SG) and NCG datasets and based on the amount and intensity of the segmented pixels. This method is then followed by *Sauvola* and *TH+T-point* method that also successfully classify unknown images in either category.

The analysis using synthetic images and meta-data as a gold reference offers two take-away messages. First, the global thresholding techniques on TH filtered images appears to be the solution for segmenting pixels in such a way that most of the stained biomarkers are within the segmented blobs. However, if the use of the blob shapes and sizes for biomarker localization and tracking is required, the *GLT* method offers the best solution by providing the best trade-off between blob size and amount of segmented biomarkers.

This high rate of biomarker segmentation in synthetic images achieved by the global thresholding techniques on TH filtered image triggered the experiment presented in the Chapter 7 (see Section 7.1) about the timely monitoring of TLR2 biomarkers in various cell cultures.



## 6 Embedded Image Processing System

Following the study of various image segmentation methods for fluorescent biomarkers in Chapter 5, and the successful results obtained with the monitoring of TLR2 receptors on Caco-2 biosamples, the development of an embedded system is envisioned here.

In this chapter, we describe the development and implementation of an FPGA based image processing system, or smart camera system, for live monitoring of fluorescent biomarkers. The system is designed with a high level of flexibility and reconfigurability such that it is not bound nor limited by the type of observed fluorescent samples.

In Section 6.1, we lay down the various requirements for the embedded system based on the target operation and function it must fulfill. The target fluorescent spot extraction algorithm is detailed in order to identify the basic functional blocks for the system. The solution to this problem passes by the design and development of an image processing suite of inter-operating *Intellectual Property (IP)*<sup>1</sup> cores based on the concept of stream processing [5] that is explained in Section 6.2. The actual smart camera design and its architecture are presented in Section 6.3 detailing the overall aspect of the hardware image processing system using this stream processing paradigm. The operation and implementation details of specific hardware processing IP cores constituting the core elements of the stream processors are gathered in Section 6.4.

This embedded system is tailored for the real-time continuous monitoring of fluorescent biomarkers with target applications in the field of quantitative microscopy and high-throughput microscopy. As such it is important to provide characterization results validating its operation. This is performed based on a fluorescent microbead calibration kit offering the point of reference required for the validation of the system. This characterization is presented in the last section of this chapter, following the implementation details.

The digital image processing suite and its components were practically developed as soft-core

---

<sup>1</sup>In this chapter, the term IP, or IP core, refers to a reusable unit of logic as defined within the field of electronic design.

**Algorithm 1** Fluorescent spots extraction algorithm

---

```

1: function SPOT_EXTRACTION( $I, D, F, \mu_F, [k_{min} \cdot k_{max}]$ )
2:    $I_C \leftarrow (I - D) \times \frac{\mu_F}{F}$                                 ▷ Image correction
3:    $I_D \leftarrow \text{MED}(I_C)$                                        ▷ 3-by-3 median filter
4:    $I_{EMA} \leftarrow \text{EMA}(I_D)$                                        ▷ Averaging filter
5:    $I_{TH} \leftarrow \text{TOPHAT}(I_{EMA})$                                    ▷ Top-Hat filtering
6:    $\mathbf{H} \leftarrow \text{HISTOGRAM}(I_{TH})$                                ▷ Get histogram
7:    $th_0 \leftarrow k_{min}$ 
8:   for  $i \leftarrow 1, i \leq 2, i \leftarrow i + 1$  do                 ▷ Perform Otsu twice
9:      $th_i \leftarrow \text{OTSU}(\mathbf{H}, [th_{i-1} \cdot k_{max}])$ 
10:  end for
11:   $I_{mask} \leftarrow I_{TH} > th_2$                                        ▷ Segmentation
12:   $N_s \leftarrow$  number of segmented pixels
13:   $\mu_s \leftarrow$  mean value of segmented pixels
14:   $\sigma_s^2 \leftarrow$  value variance of segmented pixels
15:  return ( $I_{EMA}, I_{TH}, I_{mask}, \mathbf{H}, N_s, \mu_s, \sigma_s^2$ )
16: end function

```

---

IPs for FPGA technologies. The testing and validation of the processing hardware design ideas were eased by the versatility and reconfigurability of FPGA devices. The application of the traditional FPGA work-flow to integrate and use the IP suite among a FPGA-based embedded system presents a strong case for further integration in other technologies such as *Application Specific Integrated Circuit* (ASIC). The processing suite design is such that the core concept is disjoint from technology dependent specificities. Thus its integration to *System-on-Chips* (SoCs) or the development of ASICs for fluorescence microscopy, including its co-integration on a single die with a CMOS sensor array, is open and available. Further detail on an actual practical application of the smart camera is presented in Chapter 7 (see Section 7.2) where it is used for the monitoring the endocytosis of fluorescent NPs.

## 6.1 Target Operation

### 6.1.1 Segmentation Method

Algorithm 1 is the selected fluorescent spot segmentation algorithm for implementation on the smart camera system. Essentially, it is the *TH+Otsu(2X)* method presented in Chapter 5 with an added denoising step. It has been selected because it was used successfully prior to the design of the embedded system for the monitoring of TLR2 surface receptors on Caco-2 cells [36]. More details about these results are presented in Chapter 7 (see Section 7.1). Furthermore, this selected segmentation method necessitates only a single input parameter and is, by design, much more parallelizable compared to the *GLT* method identified as the best in Chapter 5. This makes *TH+Otsu(2X)* an ideal candidate for implementation in an FPGA-based embedded system.

As a review, this method bundles four major processing steps:

**Image correction** The first step is the mandatory image correction processing. It deals with correcting uneven exposure to light of the sample through flat-fielding correction and with the removal of the fixed-pattern noise present in every raw image.

The corrected image  $I_C$  is computed from the raw input image  $I$  using calibration data represented by the master dark frame  $D$ , the master flat frame  $F$  and its average intensity  $\mu_F$  using

$$I_C[x, y] = (I[x, y] - D[x, y]) \times \frac{\mu_F}{F[x, y]} \quad (6.1)$$

This is the same image correction as featured by the *segmentation methods* in Chapter 5 (see Section 5.1.1) for the reduction of the PRNU and DSNU.

**Denoising** The denoising step takes care of speckled noise and reduces temporal noise. The speckled noise is mostly due to hot and dead pixels in the sensor array. They are many factors influencing the appearance of these pixels such as technology, temperature, aging and exposure time. In the case of fluorescence bioimaging, the latter is the most important. A long exposure time favors the appearance of hot pixels, which are pixels exceeding their linear charge capacity due to a higher than normal dark current generation or electron gain conversion, especially in CMOS photodetectors. At the opposite, stuck or dead pixels are non-responsive and their output value becomes invariable with exposure time and temperature. This type of pixel can easily be removed using a simple median filter.

$$I_D[x, y] = \text{med}(I_C[x, y], \dots, I_C[x + \Delta x, y + \Delta y]) \quad (\Delta x, \Delta y) \in \mathbf{W} \quad (6.2)$$

where  $I_D$  is the denoised image and  $\mathbf{W}$  is a 3-by-3 cross neighboring window.

The temporal noise is non deterministic and cannot be removed. It is however possible to mitigate it by averaging images over time. The *Exponential Moving Average* (EMA) is a moving average technique implemented using the following *Infinite Impulse Response* (IIR) filter

$$I_{EMA}(t) = \frac{I_D}{\alpha} + \left(1 - \frac{1}{\alpha}\right) \times I_{EMA}(t - 1) \quad (6.3)$$

where  $I_{EMA}(t)$  is the current EMA denoised image and  $I_{EMA}(t - 1)$  is the EMA denoised image computed during the previous iteration and  $\alpha$  is a coefficient between 0 and 1 representing the weight of  $I$  versus  $I_{EMA}(t - 1)$ . This technique of averaging images has the advantage that no image besides the current EMA image needs to be stored for temporal noise reduction, while a classic window averaging of  $N$  images requires to store the  $N - 1$  previous input images in order to produce an output. This makes the EMA filter valuable for embedded image processing. Finally the value of the coefficient  $\alpha$  can

be selected using

$$\alpha = \frac{2}{N+1} \quad (6.4)$$

in order to obtain a temporal noise amplitude reduction by  $\sqrt{n}$  like averaging the  $n$  most recent input images would [5].

**Filtering** Once the image is denoised, the TH morphological filter is applied in order to enhance the fluorescent signal. The *Top-Hat* (TH) filtered image is simply

$$I_{TH} = I_{EMA} - I_{EMA} \circ B \quad (6.5)$$

where  $\circ$  is the opening MM operator and  $B$  is a structuring element as defined in Chapter 5 (see Section 5.1.1).

**Thresholding** The last step uses Otsu's adaptive thresholding, whose details of operation are explained in Chapter 5 (see Section 5.1.2). Two iterations of Otsu's algorithm are performed on the histogram  $\mathbf{H}$  of the filtered image  $I_{TH}$ .

The first thresholding iteration seeks an intermediate threshold value  $th_1$  within the bin range  $[k_{min} \cdot k_{max}]$ , given the conditions that  $k_{min} > 0$  and  $k_{max} < L - 1$  with  $L$  being the number of histogram bins. The second iteration of the thresholding algorithm seeks the final threshold value  $th_2$  within the bin range  $[th_1 \cdot k_{max}]$ . This threshold is used to produced the segmentation mask  $I_{mask}$  which identifies the fluorescent pixels.

$$I_{mask}[x, y] = \begin{cases} 1, & \forall I_{TH}[x, y] \geq th_2 \\ 0, & \text{otherwise} \end{cases} \quad (6.6)$$

### 6.1.2 Outputs

One of the design driver for the smart camera system is the identification of the data that needs to be extracted. There are three types of information that get output from the smart camera: *Visual information*, the *Segmented signal* and *Measurement metrics*.

**Visual information** The visual information consists of the data that can be displayed visually and understood intuitively by the user while observing a biosample. For this purpose, the denoised image  $I_{EMA}$  is recovered along with its histogram  $\mathbf{H}$  for displaying. Furthermore, the segmentation mask  $I_{mask}$  is also recovered as it can be displayed as a binary map which offers means for the user to qualitatively evaluate the segmentation offered by the smart camera. This is simple information that offers a quick feedback for the user who can adjust various input parameters (i.e.  $k_{min}$  and  $k_{max}$ ) accordingly.

**Segmented signal** The segmented signal consists of the segmented pixels within the TH filtered image. By recovering the TH filtered image  $I_{TH}$  and the segmentation mask  $I_{mask}$ ,

we recover spatial and quantitative information about the fluorescent signal. Based on these, a simple post-processing operation is required in order to provide quantitative measurements and information about the signal. These are usually extracted in the form of numerical metrics which can be linked to the observed biological process.

**Measurement metrics** Providing numerical metrics directly as an output of the smart camera is another design constraint. Whenever performing continuous monitoring of fluorescent biomarkers, the smart camera needs to be perceived as a biosensor continuously streaming a particular measurement which can be quantitatively linked with a biological function given a calibration curves [14]. As a result, we propose that the smart camera design features the ability to output the number of segmented (i.e. fluorescent) pixels  $N_s$ , the average intensity of these pixels  $\mu_s$  and their standard deviation  $\sigma_s$ , in reference to the metrics used in the comparison study presented in Chapter 5.

Other metrics based on the pixel blobs present in the segmentation mask can also be used. This includes the number of blobs, their average intensity or size for example. However, these metrics require the use of a *Connected Component (CC)* labeling procedure which is not part of the smart camera design due to its poor parallelization propensity [61]. CC labeling is better suited for execution on a sequential processor (e.g. *Central Processing Unit (CPU)* or DSP) due to its iterative nature and use of intricate data structures. Thus, CC based metrics are not output by the smart camera and their computation is left as a post processing step which can be performed by an *ad-hoc* co-processor if required.

### 6.1.3 Calibration

Given the image correction step featured in the targeted segmentation method, a calibration procedure as described in Algorithm 2 is required. The computation of the master dark frame  $D$  and of the master flat frame  $F$  are based on the averaging of  $N$  consecutive images within given conditions (see Chapter 5, Section 5.1.1).

## 6.2 Stream Processor Concept

The developed system heavily relies on the concept of image stream processors [5] and makes use of the parallelism offered by the FPGA technology. A typical image processing algorithm as executed by a CPU is a sequential process where one or more pixels are read off the memory, processed and then finally written back to the memory. This pattern repeats as many times as required by the algorithm. Furthermore, knowing that a complete image processing system often is the combination of multiple algorithms used sequentially, as is our target processing algorithm, one can understand that a major bottleneck is the memory access.

Stream processing is used to limit memory access and offload to the main CPU to dedicated image processors. Conceptually, an image source at the beginning of a stream processor

## Chapter 6. Embedded Image Processing System

---

### Algorithm 2 Calibration procedure

---

```

1: procedure CALIBRATION
2:   Setup dark conditions (experimental configuration)
3:    $D \leftarrow \text{MASTER\_FRAME}(I, N)$ 
4:
5:   Setup dark conditions (even illumination configuration)
6:    $D_F \leftarrow \text{MASTER\_FRAME}(I, N)$ 
7:   Setup even illumination (no sample)
8:    $F \leftarrow \text{MASTER\_FRAME}(I - D_F, N)$ 
9:    $\mu_F \leftarrow \text{AVERAGE\_PIXEL}(F)$ 
10: end procedure

1: function MASTER_FRAME( $I, N$ )
2:    $M \leftarrow \emptyset$ 
3:   for  $i \leftarrow 1, i \leq N, i \leftarrow i + 1$  do                                ▷ Accumulate  $N$  images
4:      $M \leftarrow M + I$ 
5:   end for
6:    $M \leftarrow M / N$                                                     ▷ Average image
7:   return ( $M$ )
8: end function

```

---

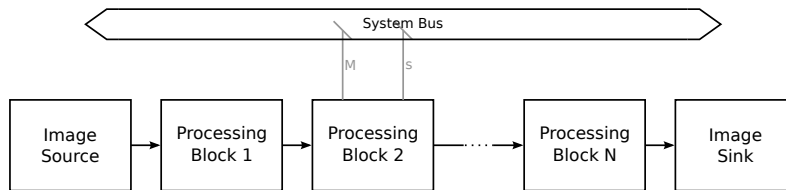


Figure 6.1 – Generic view of a basic image stream processor featuring a single image source, a single image sink and a varying amount of processing blocks. Each processing block have optional master and slave interfaces to and from the system bus. These are used for DMA operations and block configuration respectively.

accesses the image in memory, streams the pixel data through the processing pipeline using a given stream protocol, and an image sink receives the processed stream at the end of the line and writes the image back to memory. In this case, only the image source and sink require memory access and the amount of memory reads and writes stays limited thanks to the pipeline nature of such architecture.

A stream processor with a basic architecture is depicted in Fig. 6.1. It has a single image source and a single image sink with a varying number of processing blocks in between. Optionally, these blocks can have memory mapped registers for configuration purposes, or can have *Direct Memory Access* (DMA) interfaces whenever image buffering is required. Furthermore, it is possible to construct more complex stream processors such as the generic cases presented



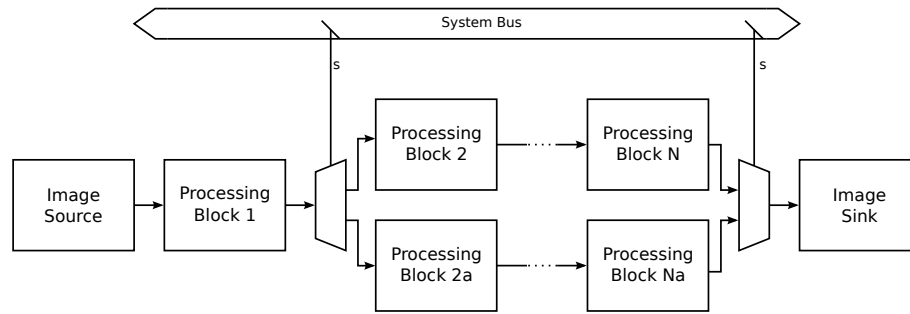


Figure 6.2 – Image stream processing branching using stream multiplexers and demultiplexers. These allow the stream to be dynamically directed towards a selected stream processing branch.

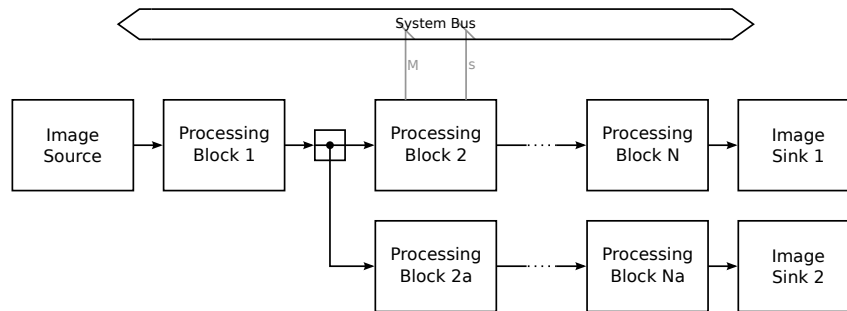


Figure 6.3 – Image stream processing splitting using dedicated stream splitter. Splitter enables for multiple stream processing branches to act in parallel.

in Fig. 6.2 and Fig. 6.3 using dedicated stream steering logic. Multiplexing and demultiplexing are put in place by allowing a dynamic selection of the blocks processing the image stream (e.g. a calibration process versus the main algorithm in a system). It is also possible to split the stream in order to feed different sets of processing blocks. This allows for multiple processing algorithms to process images in parallel at the expense of added resource usage.

### 6.2.1 Stream Protocol

In order to be able to inter-operate, the image sinks, the image sources and all the image processing blocks are implementing a common image stream protocol. On one hand, each processing block needs to be able to act a receiver and on the other hand as a sender, with the exception of image sources and image sinks that only act as sender and receiver respectively. This ensures that processing blocks can be easily re-used for different applications as their only communication with other blocks is done through a standard stream protocol interface. Fig. 6.4 shows some examples of image transfer between a sender and a receiver. The protocol

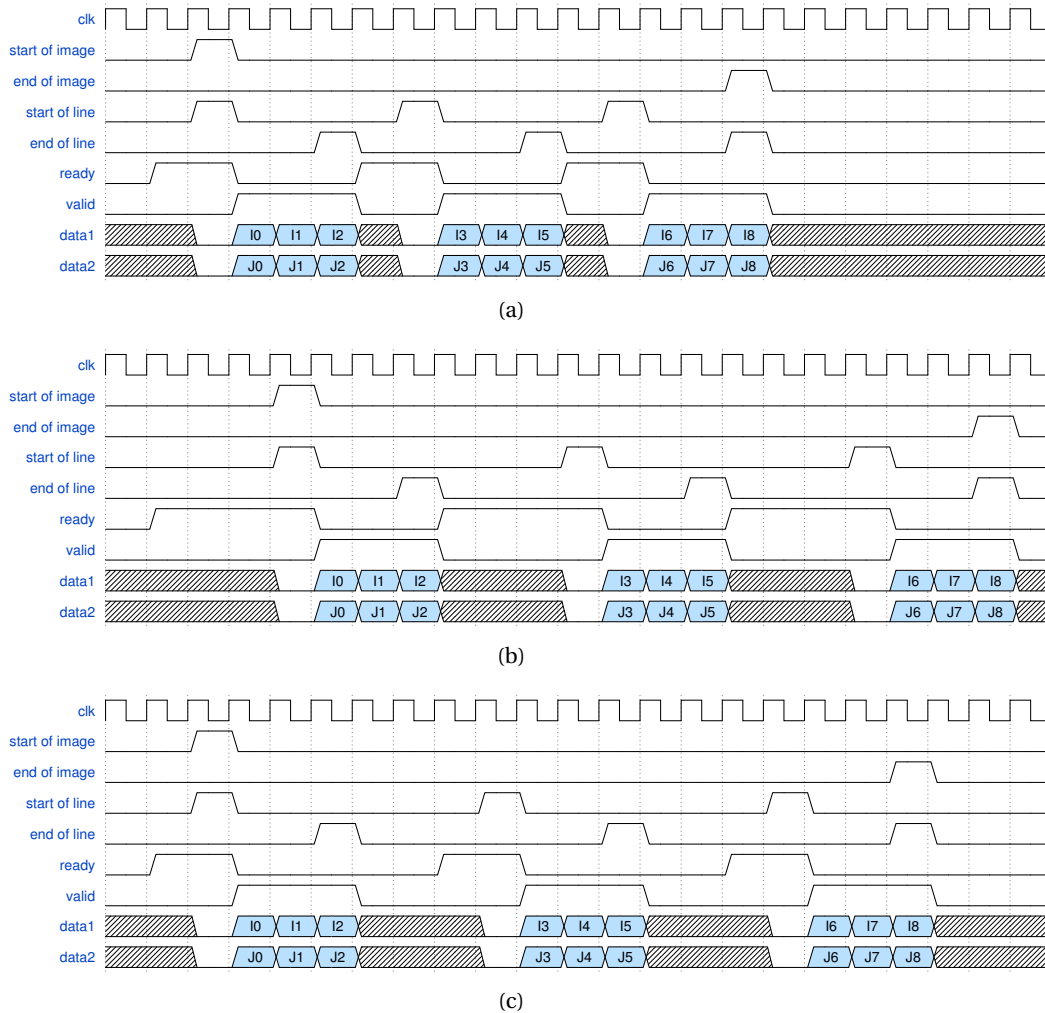


Figure 6.4 – Signal and timing diagram used by the image stream protocol. These diagrams showcase the simultaneous transfer of two  $3 \times 3$  images  $I$  and  $J$  between a sender and a receiver implementing the stream protocol. (a) The receiver asserts the ready signal as soon as possible and the sender starts streaming line of pixel data immediately. (b) The sender delays voluntarily the streaming of a line of pixel data after receiving the ready signal. (c) the receiver delays the assertion of the ready signal voluntarily after having received a full line of pixel data.

is sink-driven, with the pixel data being transferred on the data lines in a raster mode. Note that multiple data lines can be associated with a single set of control signals such that multiple images can be streamed along in a synchronized manner. For example, the data transfers showcased in Fig. 6.4 feature two data lines. The protocol specifications are as follow:

- The receiver asserts the ready signal, signaling it is ready to accept a packet of pixel data, which consists of a single image line. The image sink is responsible for initially asserting the ready signal which then travels up the pipeline until reaching the image source that can respond by sending a single image line. This ensures that every block in the image stream processor is ready to accept and process a single line of pixel data. The assertion of the ready signal can be seen as a commitment of the receiver to the sender that it is able to receive a full image line of pixel data.
- When the ready signal is asserted by the receiver, the sender can wait any given amount of clock cycles before sending data in case it has not finished processing or has not yet received data from up the stream. Once the sender has a complete line of pixels that can be transferred, it asserts the `start_of_line` signal and forces the data line to `00h`. From the next clock cycle, the sender streams the image line pixels data on the data line serially. The `end_of_line` signal is asserted by the sender when the last pixel of the image line is put on the data line.
- The `start_of_image` and `end_of_image` signals must be asserted by the sender prior to sending the first line of an image and on the last pixel of an image respectively. This ensures image synchronization between the sender and receiver.
- The `valid` signal is asserted by the sender when pixel data are put on the data line.

In the remainder of this chapter, the `start/end_of_line/image` signals are also referred to as the `sox/eox` signals.

### 6.2.2 Interfacing Stream Processors

Image sources and image sinks embody the interface that stream processors have with the rest of their environment. They are the most basic blocks upon which any stream processor is designed and built. Indeed, the simplest stream processor would only feature a single image source and a single image sink without any processing block.

In the image processing suite, image sources are responsible for generating proper image streams according to the stream protocol. The actual source of pixel data comes in two flavors. It can either be a controller specific to an image sensor or a DMA interface that is used for accessing pixel data at a given memory location.

Conversely, image sinks are responsible for receiving image streams. There are two ways pixel data within an incoming stream are handled. Using a DMA interface, the two sink flavors

Table 6.1 – Characteristics of the CMOS sensor used for the smart camera design.

Designation	MT9V032
Sensing technology	CMOS
Optical format [inch]	1/3
Pixel size [ $\mu\text{m} \times \mu\text{m}$ ]	6.0 $\times$ 6.0
Pixel array size ( $H \times V$ )	752 $\times$ 480
Pixel resolution	10bits
Dynamic range	55dB
Quantum efficiency @515nm	45%
Shutter	Electronic/Global

either directly save pixel data to a given memory location or use a histogram accumulator prior to saving the histogram data in memory.

Another existing interface for the stream processor are *Frame Buffers* (FBs). FBs are hybrid units based on an image source and an image sink. They are used by various processing blocks that require to hold frames between two executions of the stream processor.

### 6.3 Hardware Architecture

Fig. 6.5 presents a block diagram of the entire hardware architecture and of the various IP cores instantiated within the FPGA. The specifics and implementation details of the image processing blocks used by stream processors for the implementation of the spot extraction algorithm are reported in Section 6.4.

#### 6.3.1 Image Sensor

The sensor embedded in the camera head is a mid-performance CMOS image sensor (Aptina, MT9V032). This particular image sensor contains 752 $\times$ 480 active pixels, is black and white and has 10 bits resolution *Analog-to-Digital Converter* (ADC). Table 6.1 provides a few key characteristics about this sensor. It is connected to the FPGA via a 40 pins connector which carries the control signals, a 10 bits parallel interface for image readout and an *Inter-Integrated Circuit* (I<sup>2</sup>C) bus. The latter is used for configuring internal registers of the sensor.

#### 6.3.2 Top-Level Design and FPGA Platform

The FPGA board used is a DE3 development board (Terasic). It features a Stratix III mid-range FPGA (Altera, EP3SE260). In particular, it is coupled to a 1GB *Double Data Rate* (DDR2) *Synchronous Dynamic Random Access Memory* (SDRAM) module used for memory intensive digital image processing. As shown in Fig. 6.5, there are three different clock domains instantiated in the FPGA: 13MHz, 200MHz and 5MHz. All the IP cores instantiated in each domain

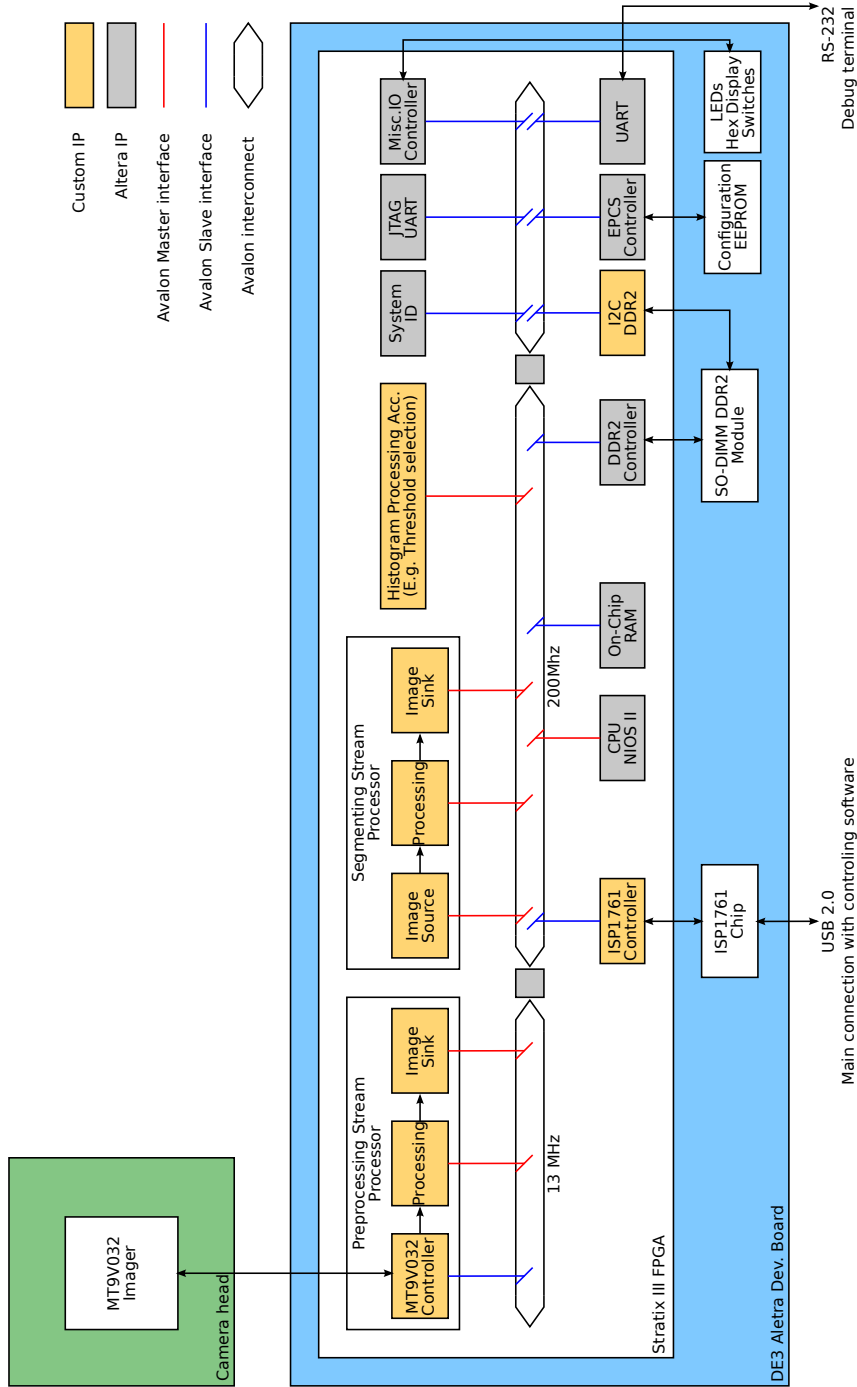


Figure 6.5 – Structural architecture of the smart camera hardware depicting the camera head and the FPGA development board. The system uses a SO-DIMM DDR2 module at the main memory and a USB 2.0 interface for communication with the controlling software. In particular, the *preprocessing stream processor*, the *segmenting stream processor* and the *histogram processing accelerator* are the specialized image processor cores built using the developed image processing suite. The main conductor is the Nios II CPU soft-core handling data communication with the software and orchestrate the execution of the processing core.

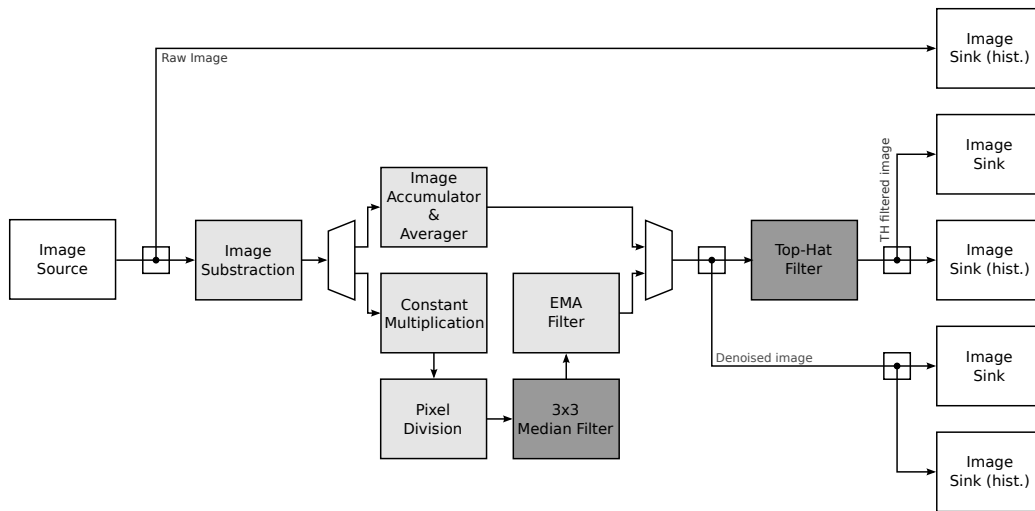


Figure 6.6 – Structural view of the *preprocessing stream processor*. It which embeds image correction (Image subtraction and division, constant multiplication), image denoising (exponential moving average filter,  $3 \times 3$  median filter) and Top-Hat filtering.

are interconnected using a common system bus (Altera Avalon bus).

The 13MHz clock domain is dedicated to the image sensor and is synchronized with its pixel clock. It features the *preprocessing stream processor* which collects, preprocesses and saves images in the main memory via DMA. The 13MHz clock has been selected as it is the slowest clock frequency that the MT9V032 CMOS image sensor is able to operate at. The goal is to use the slowest clock possible in order to limit unnecessary generation of *Thermal Noise* on the photosensors. In this configuration, the image sensor is able to provide up to 30 frames per seconds at full-resolution. Considering that the fastest biological changes typically observed on a fluorescent microscopy setup is on the order of 0.1Hz of less, Nyquist's sampling theorem is respected and a 13MHz clock on the image preprocessing domain is adapted for the application.

The 200MHz clock domain is the main clock domain in the system. This is where is located the CPU (Altera, Nios II soft-core), on-chip RAM for firmware execution, the required controller for using the *Universal Serial Bus (USB)* communication and the DDR2 controller to access to main memory. Along with the 13Mhz clock domain, it features image and data processing IP cores. It contains the *segmenting stream processor* producing the final segmenting mask and the *histogram processing accelerator*, offloading the main CPU from image histogram handling.

The 5MHz clock domain is reserved for various non critical slave IP cores such as the I<sup>2</sup>C controller, the *Universal Asynchronous Receiver/Transmitter (UART)* controller and flash memory controller, which are all required for the proper operation of the whole system.

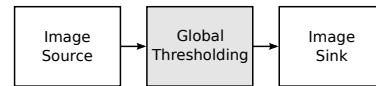


Figure 6.7 – Structural view of the *segmenting stream processor*.

## 6.4 Hardware Digital Image Processing

In this section, selected implementation details of hardware image processing IP cores are presented. In the presented image processing suite, there are currently two types of IP: *Stream processing blocks* and *Specific accelerators*.

**Stream processing blocks** The stream processing blocks are detailed in Section 6.4.1. As explained previously, they are used to build image stream processors for a particular purpose. In the smart camera design, they are used to build the *preprocessing stream processor* and the *segmenting stream processor* as shown in Fig. 6.5.

The proposed architecture for the *preprocessing stream processor* is shown in Fig. 6.6. In reference to the target operation and algorithm of Section 6.1, it is responsible for the image correction, denoising and filtering along with supporting the image correction calibration procedure.

On the other hand, the *segmenting stream processor* architecture (Fig. 6.7) is minimalist as its sole purpose is to generate a segmentation mask under the form of a binary image given the TH filtered image and a threshold value.

**Specific accelerators** Specific accelerators are not image stream processors. They are specifically tailored for a given purpose with the aim of offloading the CPU. The presented image processing suite only features a single specific accelerator dedicated to histogram manipulations and processing. Details about this accelerator are given in Section 6.4.2.

### 6.4.1 Stream Processing Blocks

In the following sections,  $I$  is defined as the image carried by the input stream to a processing block, and  $Q$  is defined as the output image carried by any output stream of a processing block.

#### Point Operations

Point operations are pixel wise operations done on the image stream. There are two slight variations of point operations, either based on a single image or on multiple images. Using a single image point operation means that the output value of a pixel at the position  $[x, y]$  is a

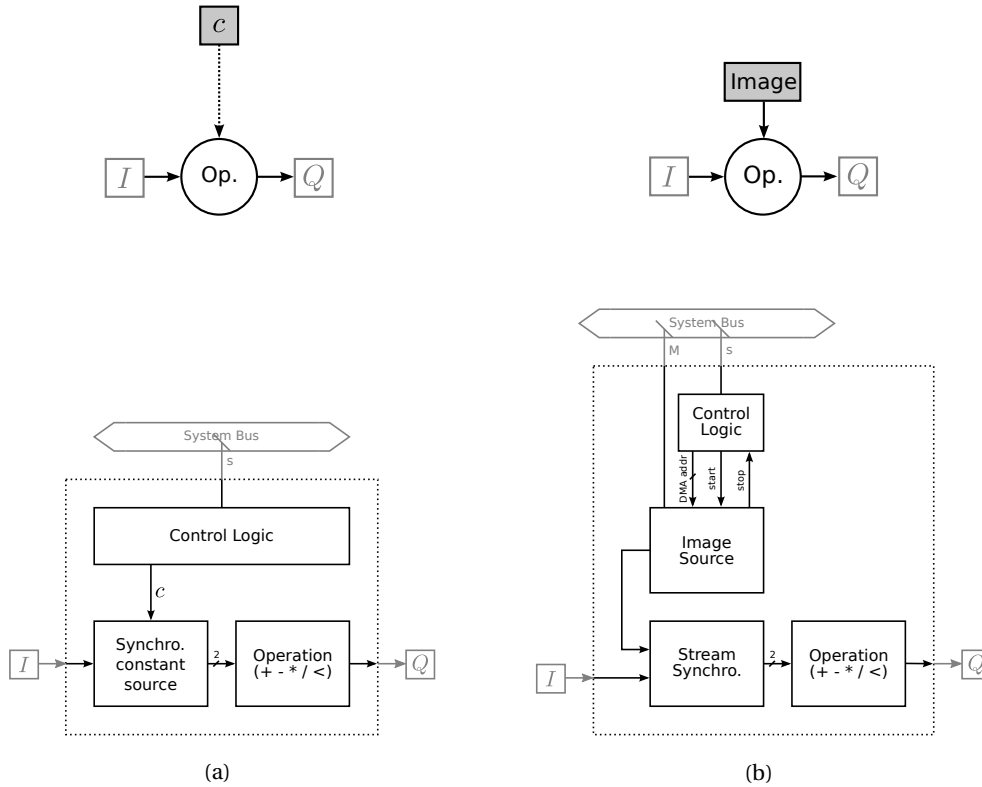


Figure 6.8 – Structural view of stream processing blocks performing basic operations (addition, difference, multiplication, division, comparison) with the pixels  $I[x, y]$  of an inputs image and (a) a constant or (b) pixels from another image in memory.

function the corresponding pixel in the input image only.

$$Q[x, y] = f(I[x, y]) \tag{6.7}$$

where  $f$  is an arbitrary function. Similarly, there is also multi-images point operations

$$Q[x, y] = f(I_1[x, y], I_2[x, y], \dots, I_n[x, y]) \tag{6.8}$$

This is used to implement the *global thresholding* block of the *segmenting stream processor* in Fig. 6.7, where the thresholding is done by a single image point operation

$$Q[x, y] = \begin{cases} 1, & \forall I[x, y] \geq th \\ 0, & otherwise \end{cases} \tag{6.9}$$

The generic implementation of a single image point operation processing block is depicted in Fig. 6.8(a). The control logic integrates memory mapped registers allowing for the dynamic



programming of the constant threshold value  $th$ . This constant is in turn used by the synchronous constant source. This constant source inputs an image stream with a single data line carrying the input image pixels  $I[x, y]$  and adds a second data line synchronous with the first one. This forms a single stream carrying two images: the input image  $I$  and a uniform image containing only pixels of value  $th$ . Finally the comparison operator is applied on the two data lines and the resulting output stream is generated.

Regarding the *preprocessing stream processor* in Fig. 6.6, only the processing blocks that are highlighted in light grey are implementation of point operations. This is the case of the image correction and correction calibration as reported in Section 6.1.1 and Section 6.1.3. These use four blocks for their implementation: The *image subtraction*, the *pixel division*, the *constant multiplication* and the *image accumulator & averager*.

Starting with the *constant multiplication* by  $\mu_F$ , this operation is implemented by a single image point operation described by the equation

$$Q[x, y] = \mu_F I[x, y] \quad (6.10)$$

It is implemented in the exact same way as the *global thresholding* block described just above. The only differences are that the constant is  $\mu_F$  and that the operation is an integer multiplication.

The image correction equation also requires two multi-image point operations. The *image subtraction* and an *pixel division*

$$Q[x, y] = I[x, y] - D[x, y] \quad (6.11)$$

$$Q[x, y] = \frac{I[x, y]}{F[x, y]} \quad (6.12)$$

The generic implementation of a multi-image point operation processing block is depicted in Fig. 6.8(b). Similarly, the control logic integrates memory mapped registers used to program the address in memory where the second image is located. An internal image source uses this address to access the image through DMA and generates a new internal image stream carrying either the master dark frame  $D$  or the master flat frame  $F$ . This new stream is synchronized with the input image stream using a stream synchronizer. From two incoming streams, this synchronizer generates a single stream with two data lines such that the pixels are synchronized. Finally either the subtraction or the division operator is applied on the two data lines and the resulting output stream is generated. This block is instantiated two times in the *preprocessing stream processor*, once for each operation.

The calibration for the image correction requires to generate the master dark frame  $D$  and the master flat frame  $F$  by averaging a given amount  $N$  of input images. The job is handled by the *image accumulator & averager* block. Details of this processing block are shown in Fig. 6.9. A noticeable difference with the previous processing block is the use of a *Frame Buffer (FB)*,

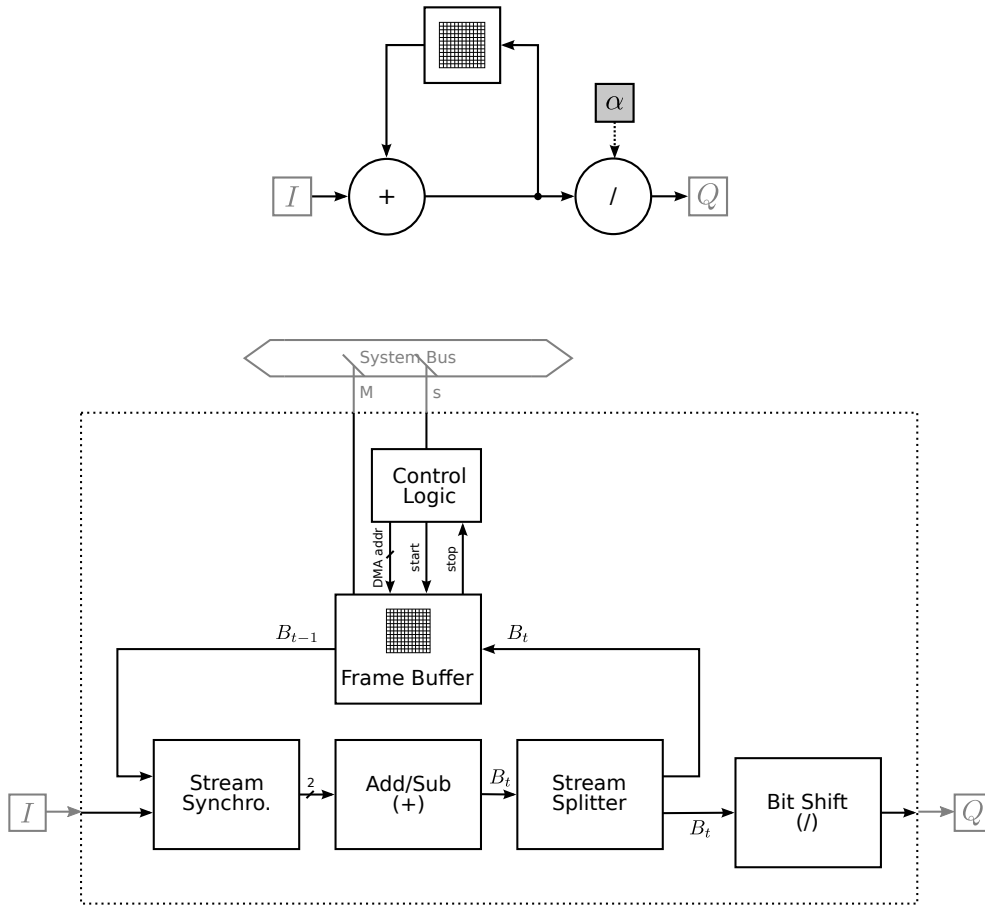


Figure 6.9 – Structural view of the image adder and accumulator. The frame buffer is used to accumulate multiple images in memory and the final dividing bit-shifting blocks produces the desired average image.

which is used to hold an intermediate image. Whenever a FB is used, the new image  $B_t$  to be held by the FB is a function of the previously held image  $B_{t-1}$  and of the input image  $I$  of the processing block. This is a multi-images point operation for which the loop equation is defined.

$$B_t[x, y] = f_{loop}(I[x, y], B_{t-1}[x, y]) \tag{6.13}$$

Similarly, the output image  $Q_t$  is also a function  $f_{output}$  of  $B_{t-1}$  and of the input image  $I$  from which the output equation is defined

$$Q_t[x, y] = f_{output}(I[x, y], B_{t-1}[x, y]) \tag{6.14}$$

Streamwise, a FB acts both as an image source and as an image sink at the same time. Com-

bined with a couple of line buffers, the image source side loads a single pixel line in a line buffer from the main memory via DMA and send it out whenever it receives a ready signal. At the same time, the image sink fills up the second line buffer and writes it back to the main memory via DMA after receiving a whole pixel line. Similarly to other blocks, the buffer address is provided by the memory mapped registers of the control logic.

The loop and output equations for the *image accumulator & averager* are

$$B_t[x, y] = I[x, y] + B_{t-1}[x, y] \quad (6.15)$$

$$Q_t[x, y] = \frac{B_t[x, y]}{N} \quad (6.16)$$

The loop equation embodies the fact that incoming images  $I$  are accumulated in the FB. Its implementation is the feedback loop in Fig. 6.9. The source side of the FB produces a stream carrying  $B_{t-1}$  which gets synchronized with the incoming stream. The images are added up and the resulting stream carrying  $B_t$  is split up to both the sink side of the FB and the output of the block. The output equation simply divides the  $B_t$  image by the constant  $N$ . This final division is implemented using bit-shifting. It saves FPGA resources but limits the value  $N$  to powers of two.

Note that this block requires the FB to be initialized to a black image, that is  $B_0[x, y] = 0$  for all pixels. Also, the output  $Q_t$  will be the desired average image only for  $t = N + 1$ . In other words  $N + 1$  images must go through the *image accumulator & averager* for the output to be valid. For our application a value of  $N = 2^4 = 16$  was selected. With the input stream carrying 10 bits of pixel data, the FB has to be fitted to receive and produce streams with 13 bits of pixel data. The final bit-shifting block brings the stream carrying  $B_t$  from 13 to 10 bits, where the 3 least significant bits are trashed away to produce the 10 bits output stream carrying  $Q_t$ .

The last processing block implemented as a point operation is the EMA *filter* block. Similarly to the previous block, it uses various pixel wise operations, image stream synchronizers and splitters and a FB in its design. It implements

$$Q_t = \frac{I_t - Q_{t-1}}{\alpha} + Q_{t-1} \quad (6.17)$$

which is re-written version of the EMA IIR filter equation (see Eq.(6.3), Section 6.1.1). This equation reduces the number of division operations to one, which is implemented using bit-shifting, to a single addition and to a single subtraction operation. Implementation details are presented in Fig. 6.10.

In this case the loop and output equations are the same

$$Q_t[x, y] = B_t[x, y] = \frac{I[x, y] - B_{t-1}[x, y]}{\alpha} + B_{t-1}[x, y] \quad (6.18)$$

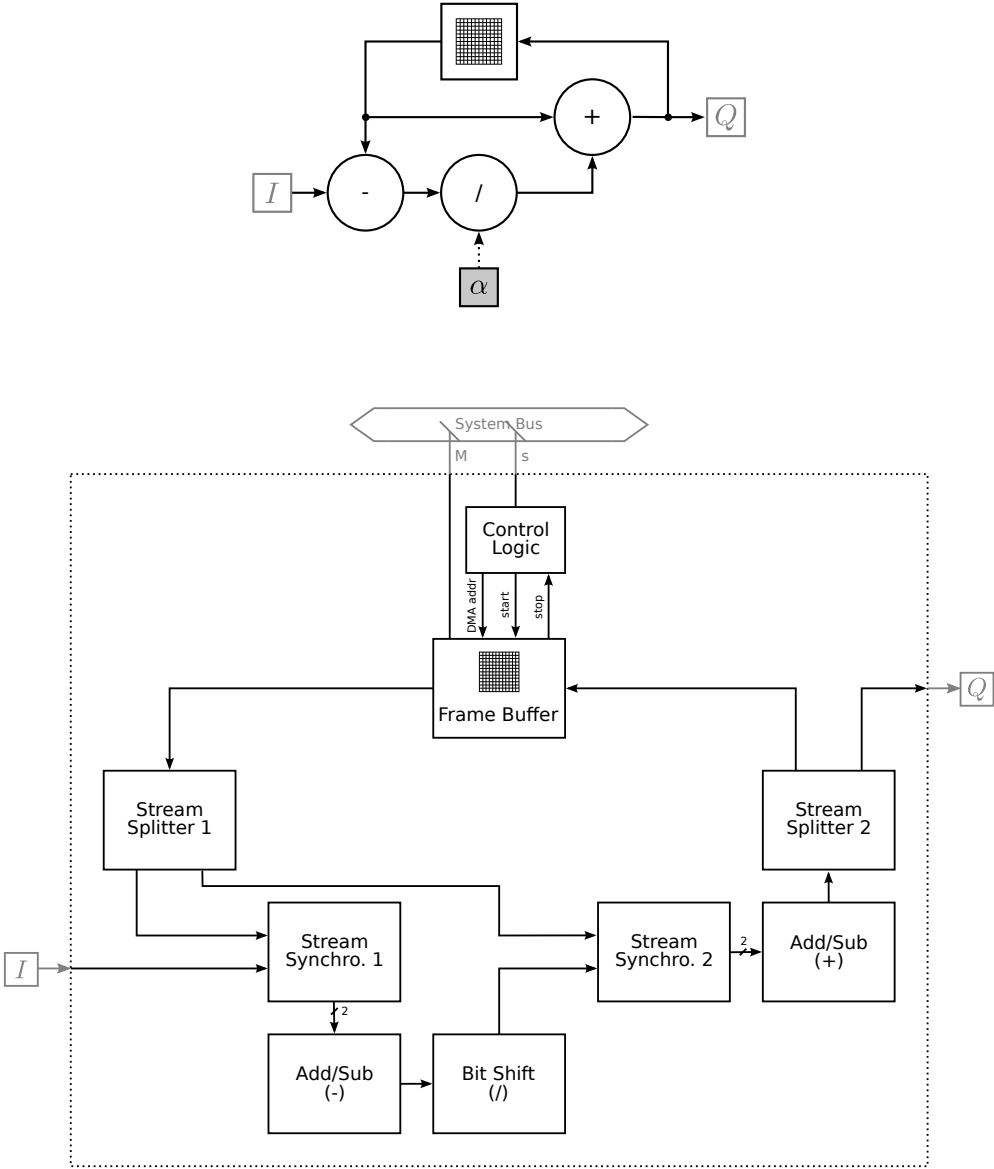


Figure 6.10 – Structural view of the EMA filter block.

Since the integer division is implemented using bit-shifting, the coefficient  $\alpha$  is limited to powers of two. Also, guard bits for the data line are introduced at the input stream and removed at the output stream. This helps suppressing the quantization noise introduced by the integer division because it is performed before the addition operation. The subtraction operation is implemented such that negative values are cropped to 0, thus preventing underflows. For our application  $\alpha$  is set to 2 and a single guard bit is used.

### Rank Filters

For the purpose of this work, we assume that local filters are extended single image point operations where the output value of a pixel at the position  $[x, y]$  is a function of multiple pixels within the neighborhood of the corresponding pixel in the input image

$$Q[x, y] = f(I[x, y], \dots, I[x + \Delta x, y + \Delta y]) \quad (\Delta x, \Delta y) \in \mathbf{W} \quad (6.19)$$

where  $\mathbf{W}$  is a neighboring window of any required shape. The median filter and the TH filter are two instances of local filters.

Rank filters [47, 48] are a subclass of local filters. They sort, or rank, the pixel values in the considered neighboring window  $\mathbf{W}$  and use as output a pixel value corresponding to a desired rank. Considering the neighboring window  $\mathbf{W}$  regroups  $N_W$  pixels, a minimum filter is a rank 0 filter, a maximum filter is a rank  $N_W - 1$  filter and a median filter is a rank  $\frac{N_W}{2} + 1$  filter. The minimum filter and maximum filter implement the erosion and dilation mathematical morphology operators respectively, which are core operators for the TH filter.

As a result, the *3-by-3 median filter* block of the *preprocessing stream processor* is implemented using a generic rank filter block. A rank filter block has two main constituents, a window extractor and a rank selector, as presented in Fig. 6.11.

The implementation detail for the window extractors and the rank selectors are gathered in Fig. 6.12 and 6.13 respectively.

The window extractor uses pixel caching [5] in order to extract a square window of size  $W \times W$  around the current output streamed pixel. This is done with the help of  $W - 1$  line buffers implemented using shift registers with  $W - 1$  uniformly spread output taps. Dedicated logic enables for row switching between the window rows and pixel switching within each window row such that border effects are taken into account. This allows the local pixel cache registers to continuously have consistent values even when the center pixel is on the border of the image by enabling mirroring of the border pixels. Finally only the  $N_W$  pixels of the neighboring window  $\mathbf{W}$  are extracted out of the square window cache. Practically, the window extractor inputs an image stream carrying a single image over one data line and generates an image stream carrying the neighboring window  $\mathbf{W}$  over  $N_W$  data lines.

On the other hand, the rank selector inputs this image stream carrying the neighboring window

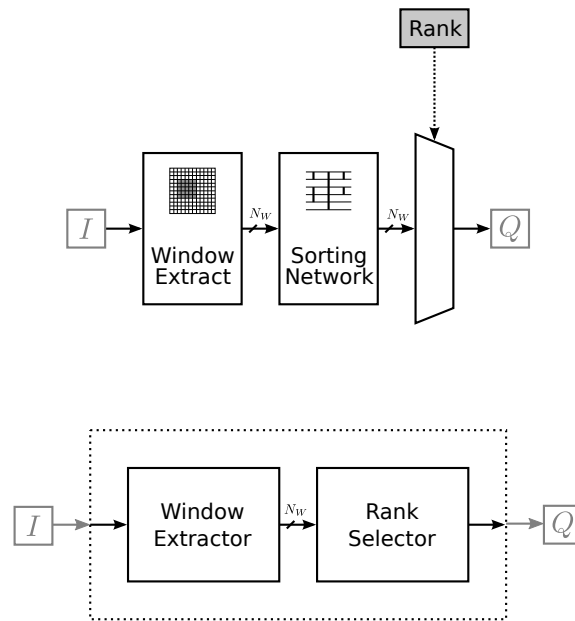


Figure 6.11 – Structural view of a generic rank filter block. It is used to implement median, minimum (grayscale erosion) and maximum (grayscale dilation) filters.

pixels and must sort the  $N_W$  pixel values of the window before finally selecting only a single value based on its ordered position. For this, a pipelined bitonic sorting network is used [81]. Examples of such sorting networks with 5 and 9 inputs are presented in Fig. 6.14 where each arrow represents a basic 2-inputs and 2-outputs sorting network implemented using a single integer comparator and two 2:1 multiplexers.

### Mathematical Morphology Operations

The *Top-Hat filter* block also uses window extractors and rank selectors in order to implement the erosion and the dilation operators. Fig. 6.15 shows the internals of the *Top-Hat filter* block implementing Eq. (5.4). The input stream is split in two. The lower path applies successively the erosion then the dilation operator, effectively producing an image stream carrying the lower envelope  $I \circ B$  defined in Eq. (5.5). The upper path simply delays the input stream carrying  $I$  using line buffers in order to match the line delay induced by the lower path. The two streams are then synchronized and the subtraction operator is applied.

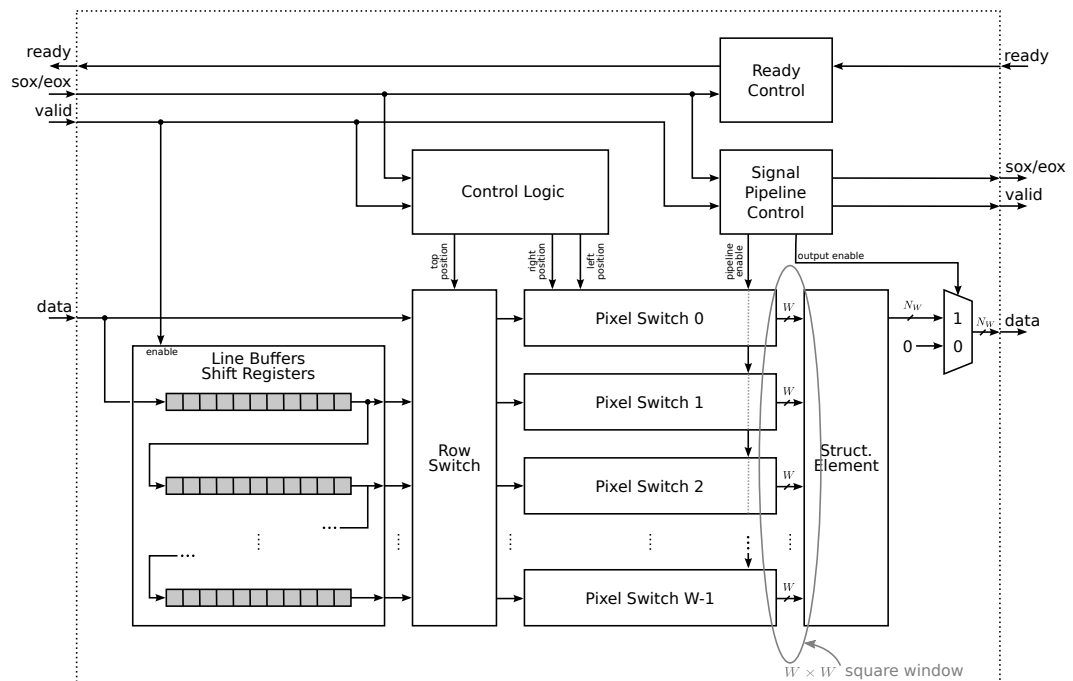


Figure 6.12 – Control and data path of the window extractor. First a  $W \times W$  square window is extracted then a structuring element defines which  $N_W$  pixels of the desired neighborhood are routed out. The window row switching and window pixel switching logic ensures that border effects are taken into account by duplicating the appropriate row and/or pixels.

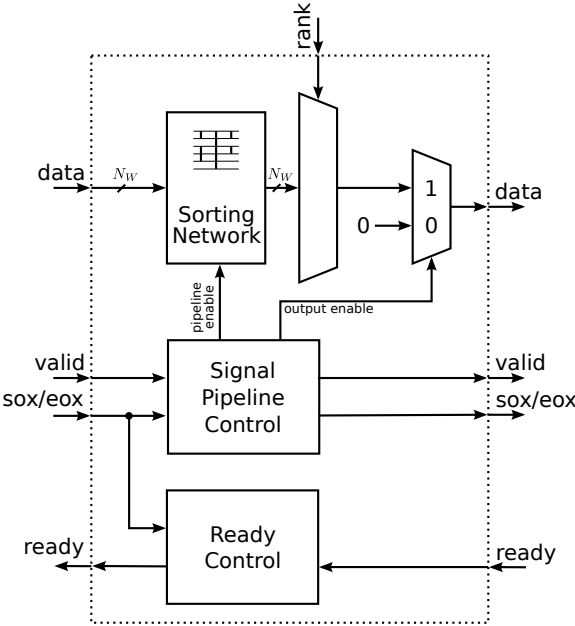


Figure 6.13 – Control and data path of the rank selector. The data path receives  $N_W$  inputs data lines that are sorted by a sorting network. A multiplexer is used to output the appropriate rank.



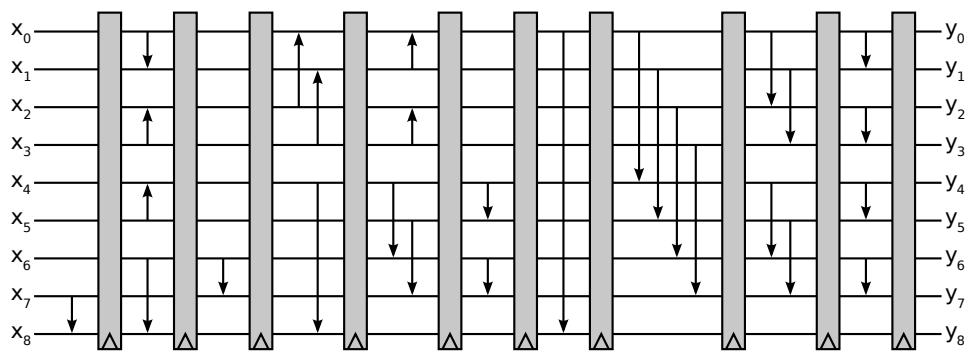
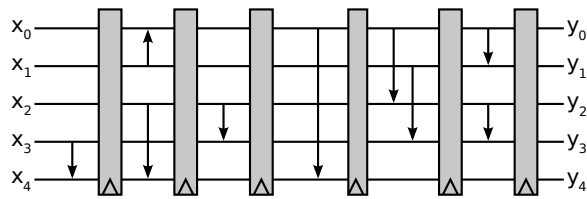
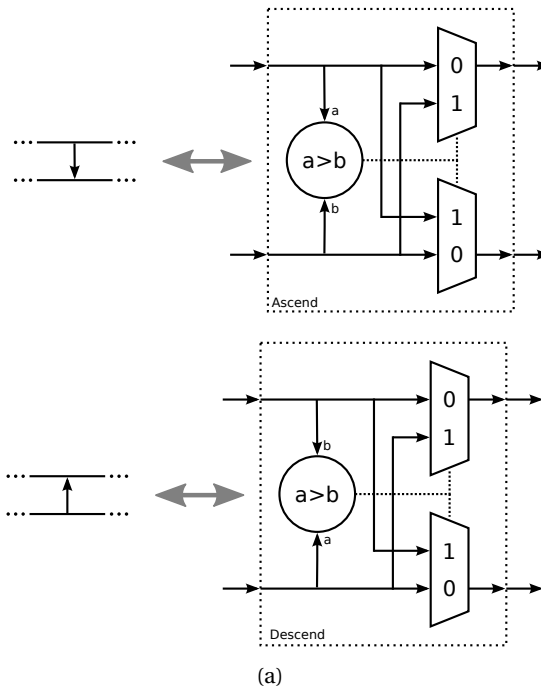


Figure 6.14 – (a)Basis and arrow convention used by the sorting networks.(b) Example of sorting network with 5 integer inputs. (c) Example of sorting network with 9 integer inputs

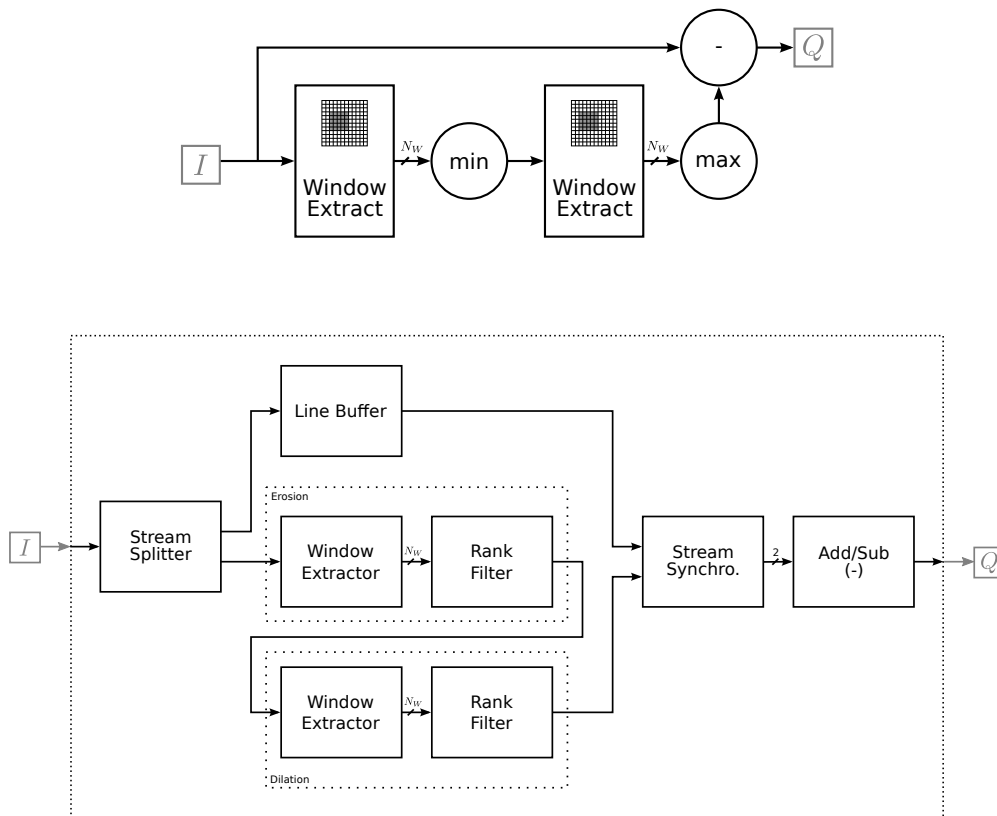


Figure 6.15 – Structural view of the Top-Hat filter block featuring the erosion and dilation operator implemented using the configurable rank filter block in Fig. 6.11. The neighborhood of  $N_W$  pixels extracted by the window extractors is the same for the erosion and dilation filter.

### 6.4.2 Histogram Processing Accelerator

The *histogram processing accelerator* is used to compute metrics based on an image histogram  $\mathbf{H}$  that was saved in the main memory by a dedicated image sink. In our system, it is used for:

- computing Otsu's threshold histogram index  $k^*$  within the index range  $[k_{min} \cdot k_{max}]$ . (see Chapter 5, Section 5.1.2);
- counting the number of pixels having values falling in a given histogram index range. That is, to extract the number of segmented or fluorescent pixels once the final threshold index is computed;
- evaluating the mean pixel  $\mu_s$  value and variance  $\sigma_s^2$  of these segmented pixels.

These three objectives are fulfilled by processing the histogram cumulative moments.

$$\begin{aligned} \mathbf{S}_r \mathbf{H} &= \{S_r H[j] : j \in [0 \cdot L - 1]\} \\ S_r H[j] &= \sum_{i=0}^j i^r H[i] \end{aligned} \quad (6.20)$$

where  $j$  is the index of the histogram cumulative moments and  $r \in \mathbb{N}$  is the moment order. In particular,  $\mathbf{S}_0 \mathbf{H}$  is the so called image cumulative histogram.

From this, we can find simple mathematical expressions that can be easily implemented using FPGA resources to compute the required values.

Computing Otsu's threshold index  $k^*$  is in direct relation with the computation of the intra-class variance  $\sigma_B^2$  as defined by Eq. (5.12). Practically, only an expression that is proportional  $\sigma_B^2$  is required to find  $k^*$ .

$$\sigma_B^2(k) \propto \frac{(M_p N_{C_0} - N_p M_{C_0})^2}{N_{C_0} (N_p - N_{C_0})} \quad (6.21)$$

with

$$\begin{aligned} N_p &= S_0 H[k_{max}] - S_0 H[k_{min} - 1] \\ M_p &= S_1 H[k_{max}] - S_1 H[k_{min} - 1] \\ N_{C_0} &= S_0 H[k - 1] - S_0 H[k_{min} - 1] \\ M_{C_0} &= S_1 H[k - 1] - S_1 H[k_{min} - 1] \end{aligned} \quad (6.22)$$

This expression is only a function of cumulative histogram moments. Its mathematical derivation is found in Appendix A.

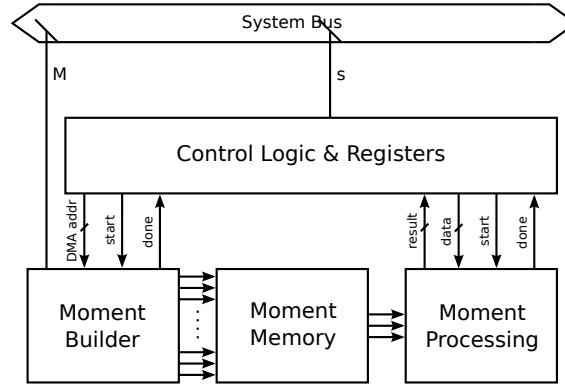


Figure 6.16 – Structural architecture of the *histogram processing accelerator*.

Finally, counting the number of pixels within a histogram index range  $s = [i_{min} \cdot i_{max}]$  and calculating their mean value and variance is also directly done using the cumulative moments

$$N_s = S_0 H[i_{max}] - S_0 H[i_{min} - 1] \quad (6.23)$$

$$\mu_s = \frac{S_1 H[i_{max}] - S_1 H[i_{min} - 1]}{S_0 H[i_{max}] - S_0 H[i_{min} - 1]} \quad (6.24)$$

$$\sigma_s^2 = \frac{S_2 H[i_{max}] - S_2 H[i_{min} - 1]}{S_0 H[i_{max}] - S_0 H[i_{min} - 1]} - \mu_s^2 \quad (6.25)$$

The architecture of the *histogram processing accelerator* is depicted in Fig. 6.16. It is logically decomposed in a histogram cumulative *moment builder*, which saves the  $S_r H$  in a local memory, and a *moment processing* block for the implementation of Eq. (6.21) (6.23) (6.24) and (6.25)

### Moment Builder

The moment builder is responsible for retrieving a histogram  $H$  from the main memory via a DMA controller, computing a desired amount of cumulative moments and saving them in a local memory for further use. Its internal construction is shown in Fig. 6.17.

The histogram bin values  $H[i]$  are saved in the main memory by the image sink in a contiguous location. This allows the DMA controller used by the *moment builder* to read multiple histogram bin values per system bus transaction and make efficient use of the system bus data width. Consider  $S_j$  the set of  $M$  histogram bin values read by the DMA controller in a single

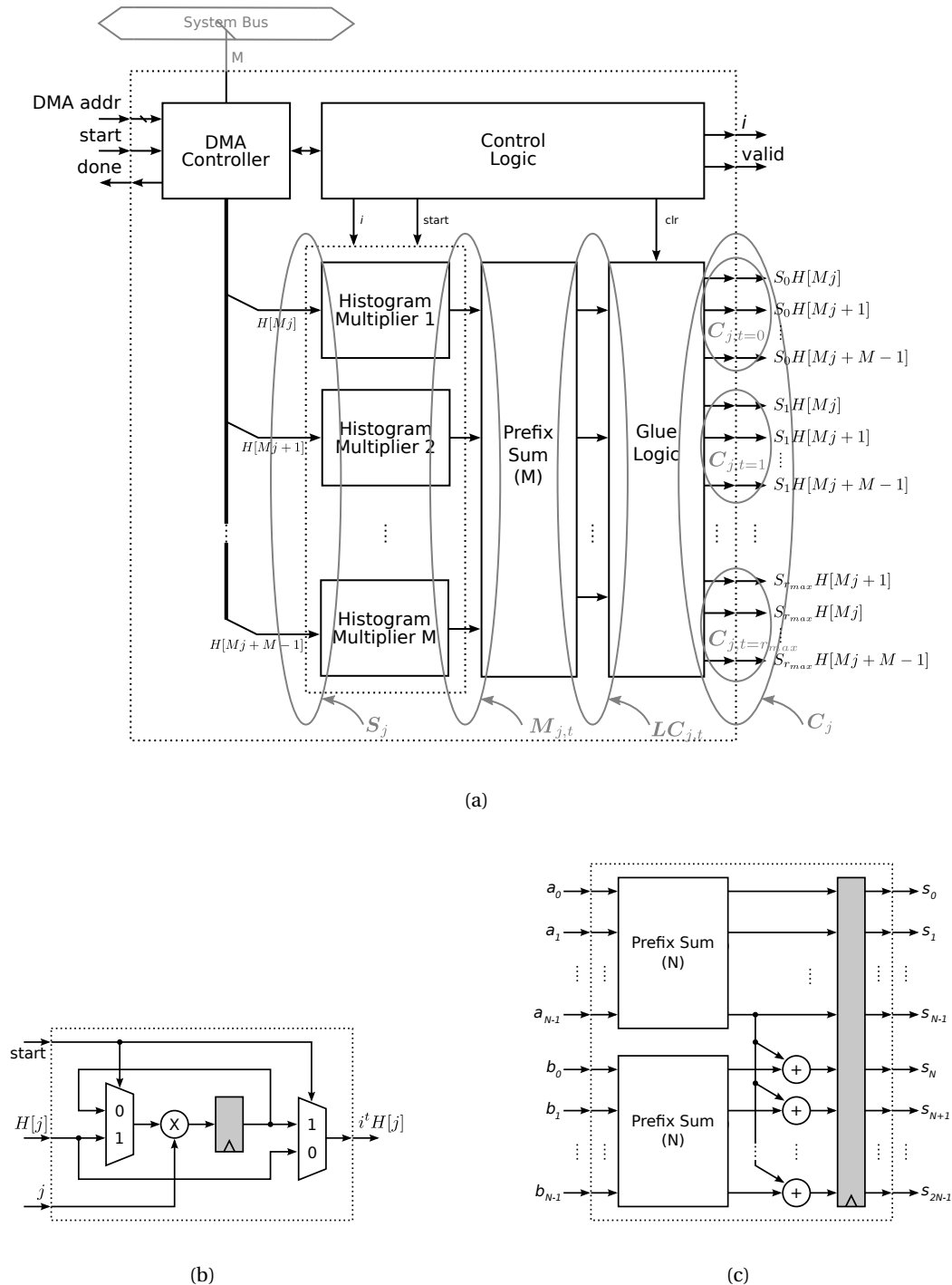


Figure 6.17 – (a) Control and data path of the cumulative *moment builder*. (b) Histogram multiplier architecture iteratively multiplying a histogram bin value  $H[i]$  with its index  $i$  at each clock cycle. (c) Recursive definition of the prefix sum of  $2N$  input integers as used by the cumulative moment builder.

bus transaction

$$\mathbf{S}_j = \{H[Mj + m] : m \in [0 \cdot M - 1]\} \quad (6.26)$$

where  $M$  is a power of two and such that the histogram  $\mathbf{H}$  is

$$\mathbf{H} = \bigcup_{j=0}^{\frac{L}{M}-1} \mathbf{S}_j = \{H[i] : i \in [0 \cdot L - 1]\} \quad (6.27)$$

These sets of  $M$  histogram bin values are distributed to the processing pipeline which handles them in parallel. The first stage of the pipeline is made of  $M$  *histogram multipliers*. They register the input histogram bin values in  $\mathbf{S}_j$  and produce successively non-cumulative histogram moments  $\mathbf{M}_{j,t}$ , one order higher at each clock cycle. The values produced by the *histogram multipliers* over time are as follow

$$\mathbf{M}_{j,t} = \{(Mj + m)^t H[Mj + m] : m \in [0 \cdot M - 1]\} \quad (6.28)$$

where  $t$  represents the clock ticks.

The second step in the pipeline is the prefix sum network. It consists of registers and adders as depicted in Fig. 6.17. Its goal is to generate local cumulative  $\mathbf{LC}_{j,t}$  moments by computing the cumulative sum of the histogram moments produced by the *histogram multipliers*

$$\mathbf{LC}_{j,t} = \left\{ \sum_{n=0}^m (Mj + m)^t H[Mj + m] : m \in [0 \cdot M - 1] \right\} \quad (6.29)$$

Finally, the third step of the pipeline deserializes the  $\mathbf{LC}_{j,t}$  and computes the final histogram cumulative moments which are saved in a local memory for further processing. The output of the pipeline is thus

$$\mathbf{C}_j = \{\mathbf{C}_{j,t} : t \in [0 \cdot t_{max}]\} \quad (6.30)$$

with

$$\mathbf{C}_{j,t} = \left\{ \mathbf{LC}_{j,t}[M-1] \sum_{n=0}^m (Mj + m)^t H[Mj + m] : m \in [0 \cdot M - 1] \right\} \quad (6.31)$$

such that the histogram cumulative moments are

$$\mathbf{S}_r \mathbf{H} = \bigcup_{j=0}^{\frac{L}{M}-1} \mathbf{C}_{j,t=r} = \{S_r H[j] : j \in [0 \cdot L - 1]\} \quad (6.32)$$

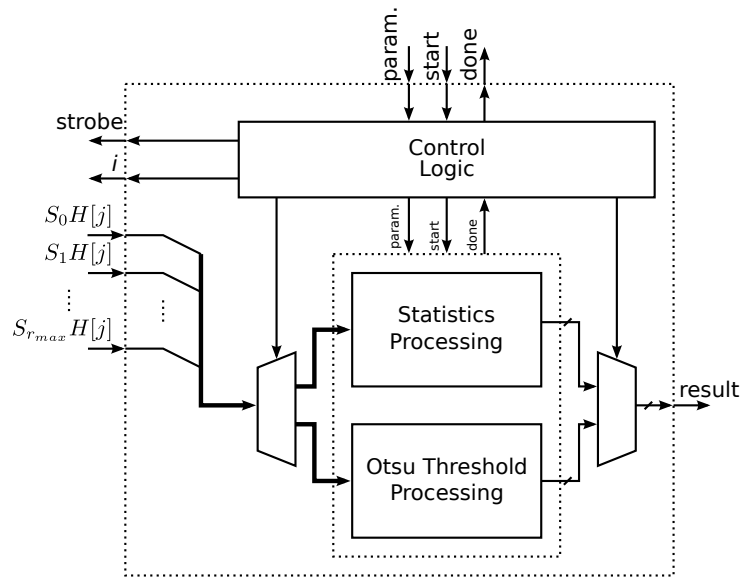


Figure 6.18 – Structural architecture of the cumulative *moment processing* block.

### Moment Processing

The *moment processing* structural architecture is shown in Fig. 6.18. It is a straightforward structure where cumulative moments  $S_r H[j]$  are read off the local memory and provided to either the *statistics processing* or *Otsu's threshold processing* block.

The *statistics processing* block handles the computation of  $N_s$ ,  $\mu_s$  and  $\sigma_s^2$  using Eq. (6.23) (6.24) and (6.25). The generic implementation used to compute these values is shown in Fig. 6.19, which implements the dedicated scheduled sequencing graph [78] of Fig. 6.20.

Similarly, the *Otsu threshold processing* block computes the threshold histogram index  $k^*$  using the dedicated scheduled sequencing graph in Fig. 6.21 which evaluates the  $\sigma_B^2$  as defined in Eq. (6.21). The control logic in this case goes through all the possible histogram indexes  $k$  within  $[k_{min} \cdot k_{max}]$ , triggers each time the evaluation of Eq. (6.21) in order to solve Otsu's optimization problem as defined in Eq. (5.11).

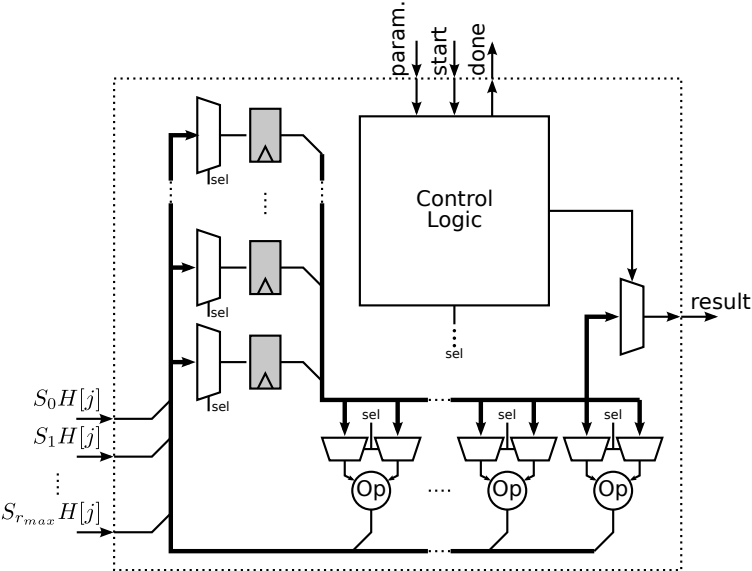


Figure 6.19 – Generic structural view of the implementation of scheduled sequencing graphs. This structure is used for both the *statistics processing* and the evaluation of (6.21) for *Otsu’s threshold processing* blocks.



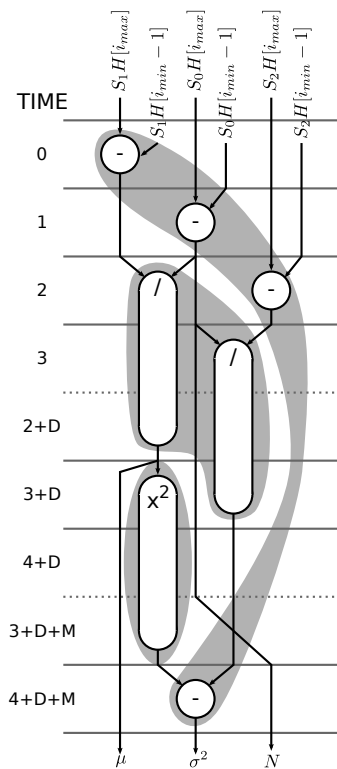


Figure 6.20 – Scheduled sequencing graph used for the computation of  $N_s$ ,  $\mu_s$  and  $\sigma_s^2$ . The gray areas represent the resource usage.

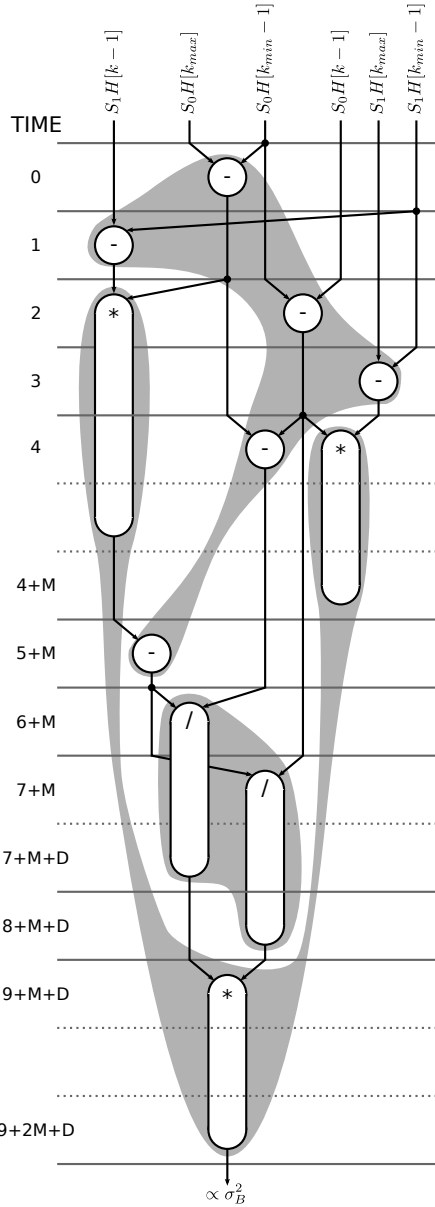


Figure 6.21 – Scheduled sequencing graph used for the evaluation of (6.21). The gray areas represent the resource usage.

## 6.5 System Validation

The final prototype of the smart camera *in situ* and a screenshot of the controlling software are shown in Fig. 6.22. A microscope image intensity calibration kit is used to measure the linearity characteristics of the smart camera system. It consists of fluorescent microbeads of various intensities covering the range of light intensities to be expected in fluorescence microscopy. The calibration kit (InSpeck Green, Life Technologies) features  $6\mu\text{m}$  diameter polystyrene microspheres with excitation and emission fluorescence frequencies of 505nm and 515nm respectively. It includes microbeads with various fluorescent relative intensities, of which the relative intensities of 1%, 10% and 100% are used.

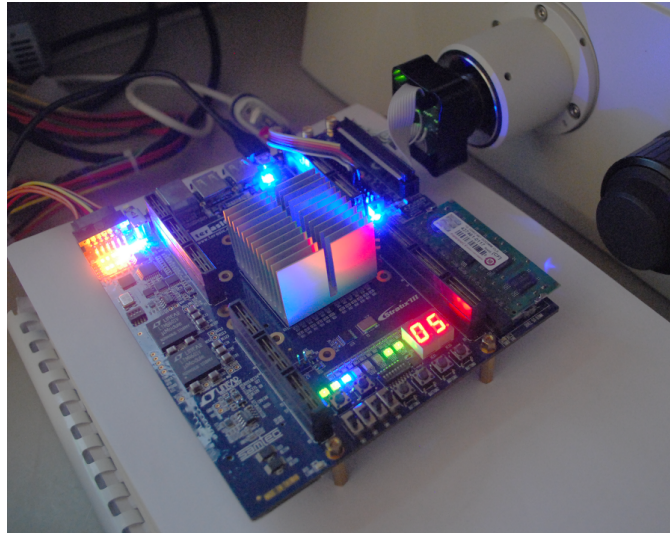
The imaging setup is depicted in Fig. 6.22(a). The developed smart camera system is mounted on the C-mount compatible optical port of an Eclipse Ti-S inverted microscope (Nikon) via a  $0.7\times$  relay lens. The objective is a Plan Fluor ( $4\times$  magnification,  $N_A = 0.13$ ), the light filtering is handled by a standard FITC filter block and the excitation light source is an Intensilight C-HGFI with a 130W Hg lamp (Nikon).

The relatively low  $4\times$  magnification objective is used to have the fluorescent microbeads appear small on the images. The  $6\mu\text{m}$  beads appear on the images as disks having an average diameter of 2.8 pixels considering the magnification in the optical path and the CMOS sensing pixel size (Table 6.1). This effectively mimics fluorescent spots as observed on real biosamples. Zoomed in denoised (i.e. before TH filtering) images of 100% relative intensity microbeads are presented in Fig. 6.23.

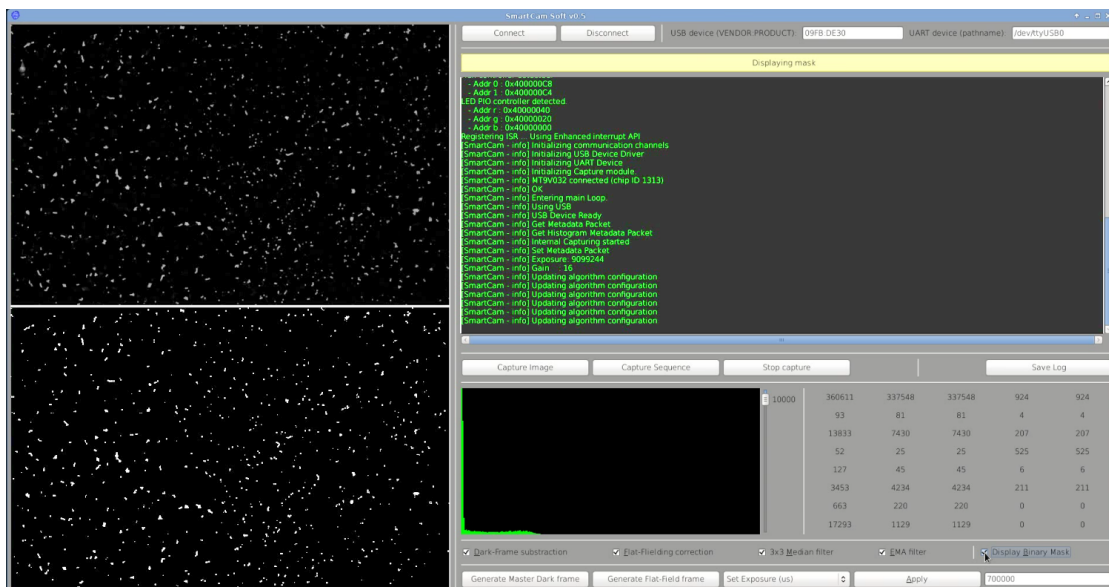
The *preprocessing stream processor* in Fig. 6.6 requires some static configuration prior to usage. The TH filter is configured with a 7-by-7 pixels, disk shaped, structuring element and the EMA filter is configured with an  $\alpha$  coefficient of 2.

The dynamic calibration of the system for image correction from Section 6.1.3 involves three steps:

- The generation of the master dark frame  $D_F$  is dynamically handled by by-passing the image subtraction and the TH filter blocks of the pre-processing stream processor and routing the image stream through the top path via the image accumulator to produce an average dark frame. The sensor was configured with a  $30\text{ms}$  exposure time and no analog gain.
- The image subtraction is activated in order to remove the master dark frame  $D_F$  from the input flat frames  $I_F$ . Again the image accumulator is used to produce the master flat frame  $F$ , and the average pixels  $\mu_F$  value from  $F$  is recovered from the final image sink. The exposure and analog gain are kept the same as in the previous step.
- Finally, the master dark frame  $D$  is generated just like  $D_F$  is generated in the first step. However, the sensor exposure and analog gain must be set to match the sensor configuration used to image the microbead sample (Table 6.2).



(a)



(b)

Figure 6.22 – (a) Picture of the smart camera *in situ*, featuring the Altera DE3 development board, a 1GB DDR2 SO-DIMM module and a custom camera head with the  $752 \times 480$  MT9V032 CMOS black and white 10 bits image sensors. (b) Screenshot of the controlling software while observing fluorescent microbeads

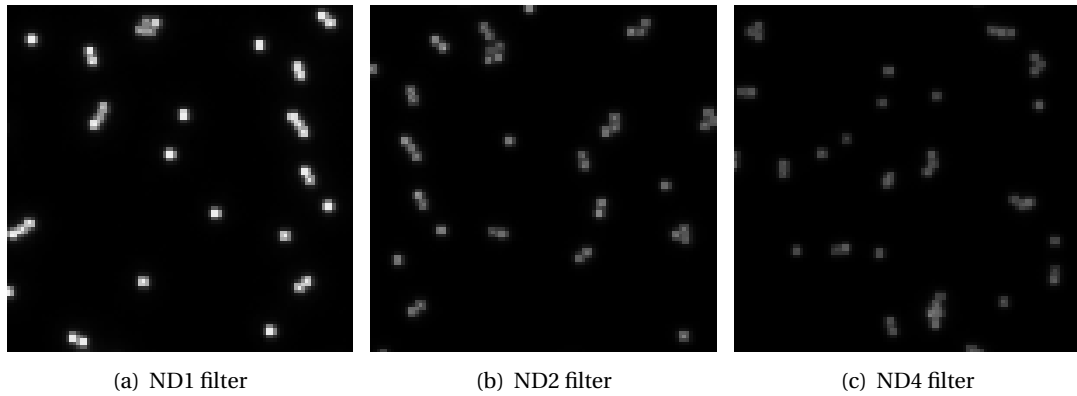


Figure 6.23 – Denoised images of 100% relative intensity microbeads with various ND filters in the excitation path of the fluorescence microscope. Each images covers a sample area of  $214\mu\text{m} \times 214\mu\text{m}$ . Each microbead is has a diameter of  $\approx 6\mu\text{m}$  which corresponds to about 2.8 pixels on these images.

Table 6.2 – CMOS image sensor configuration for microbeads samples.

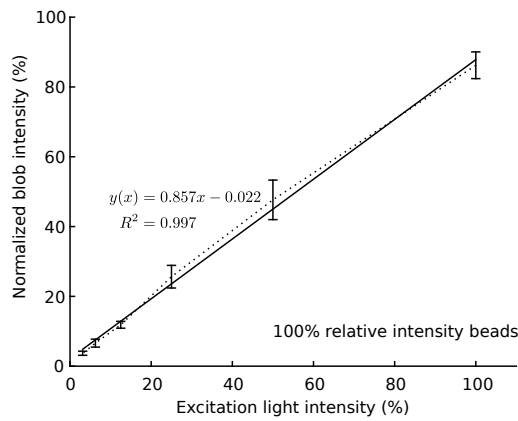
Rel. intensity	Exposure (ms)	Analog gain
100%	80 ms	1×
10%	700 ms	1×
1%	4000 ms	1×

For each step, the image accumulator is configured to accumulate 16 images before providing the average image.

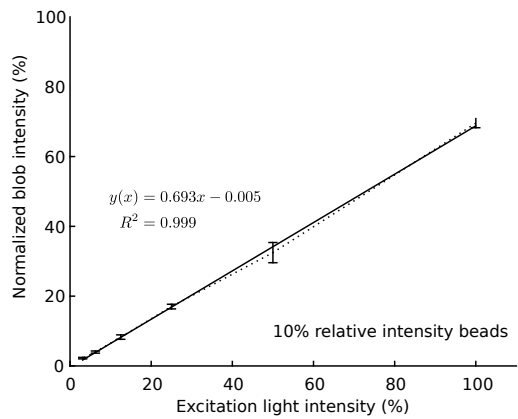
The range  $[k_{min} \cdot k_{max}]$  over which the threshold index is sought by Otsu’s algorithm is kept as wide as possible. With a 10 bits image sensor and the histogram accumulators generating histogram with bin widths of 1, it is set to  $[k_{min} \cdot k_{max}] = [0 \cdot 2^{10} - 1]$ .

In order to measure the linearity of the results provided by the camera, various ND filters are used to vary the excitation light intensity. The set of ND filters is ND1, ND2, ND4, ND8, ND16 and ND32 which respectively have a light transmittance of 100%, 50%, 25%, 12.5%, 6.25% and 3.125%. The graphs in Fig. 6.24 report the measured normalized blob intensity with respect to the emission light intensity. We can observe a high linearity between these two making the system a usable measurement tool for quantifying fluorescent biosamples given a calibration curve. Note that the normalized blob intensity is computed by performing CC labeling on the TH filtered images provided by the preprocessing stream processor and using the threshold value computed by the specific *histogram processing accelerator*. Also, no value is provided on Fig. 6.24(c) for the ND16 and ND32 filters on 1% relative intensity beads because the signal-to-noise ratio in the images is too low for the system to provide any results.

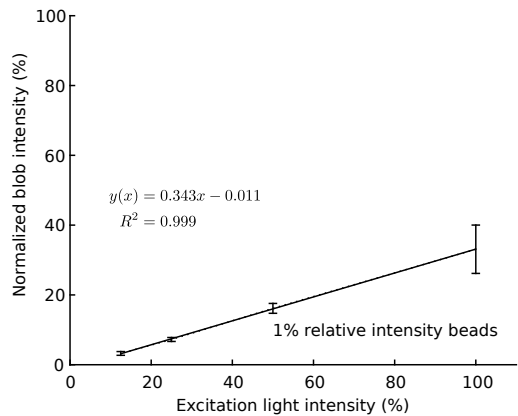
With the linearity of the system established, a single location on the 100% relative intensity



(a)



(b)



(c)

Figure 6.24 – Measured blob intensity of (a) 100%, (b) 10% and (c) 1% relative intensity microbeads with respect to various excitation light intensities. The blob intensities are normalized over the 10 bits CMOS sensor range and the excitation light intensities are normalized using the brightest excitation light provided by the Intensilight light source. Each data point results from 20 processed images and the error bars are  $1\sigma$ .

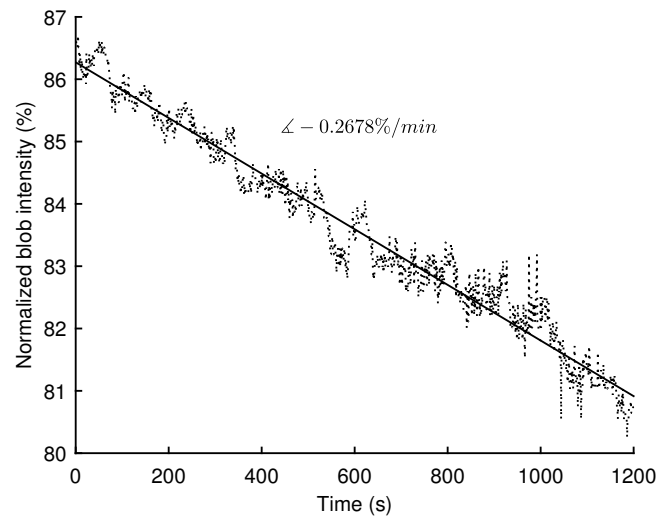


Figure 6.25 – Continuous monitoring of the 100% relative intensity microbead sample over a period of 20 minutes using the ND1 filter.

beads sample has been constantly exposed to excitation light and imaged every second for 20 minutes. With this, it is possible to capture the photobleaching characteristics of the microbeads over long periods of time. The measurements are reported on Fig. 6.25 where a decrease of the blob intensity of 0.27% per minute is observed while applying a constant excitation light using the ND1 filter.

The current smart camera prototype is able to process up to 10 frames per second. The existing bottleneck is the current USB 2.0 driver used to handle the communication on the FPGA via the ISP1762 chip (see Figure 6.5). However, since the fastest biological changes that are observed on a fluorescent microscopy setup is about 0.1Hz or less, the current system is adapted for the continuous monitoring of fluorescently stained biosamples as Nyquist's sampling theorem is still respected.

## 6.6 Chapter Summary and Contributions

This chapter presents the various aspects of the smart camera design which was conceived for the continuous monitoring of fluorescent biomarkers. The smart camera prototype is based on a FPGA platform. It implements the *TH+Otsu(2X)* segmentation method initially described in the previous chapter by means of a custom image processing suite.

This image processing suite consists of an array of custom inter-operable IP cores designed for the handling and processing of image streams. These IP cores are combined into an image stream processor in order to implement a desired processing function. This is used to implement the preprocessing operations as specified by the *TH+Otsu(2X)* segmentation method. Other cores are specialized in the processing of more specific data, such as the

## Chapter 6. Embedded Image Processing System

---

histogram data. These are hardware accelerators and in this case are used to implement Otsu's threshold selection technique. This image processing suite is by no mean linked or reserved for the *TH+Otsu(2X)* segmentation method. Its design is such that existing IP cores, or even future IP cores, can be combined in a multitude of image stream processors targeted for various applications.

The IP cores at the heart of the image processing suite were designed using a *Hardware Description Language* (HDL) by avoiding the integration of technology dependent features. It results that, even though its current usage is within the FPGA device at the core of smart camera prototype, it can be ported other design flows such as the ones used in SoC design with minor changes. This makes it ideal for future expansions of this project considering the perspective of implementing dedicated processing hardware along with an image sensor on a common CMOS die.

The smart camera prototype was tested and validated by using a microscope calibration kit featuring microbeads with various relative fluorescent intensities. A further application of the developed prototype is presented in Chapter 7 (see Section 7.2) where it is used to extract the kinetics of the uptake of fluorescent *Nano-particles* (NPs) in cell cultures.



# **Applications and Thesis Outlook** **Part IV**



## 7 Applications

This chapter focuses on two bioimaging applications for which the monitoring of fluorescent biomarkers is key and that can benefit from the integration of image processing techniques.

The first application centers around the field of nutrition. More specifically, it is part of a multidisciplinary project, the NutriChip project, whose focus is on the immunomodulatory properties of dairy products[138]. This application and the related project are described in Section 7.1. Without entering into details here, a core concept of that project is the development of a *Lab-on-a-Chip* (LoC) within which the immune response of intestinal cells to a nutrient is monitored via indirect immunofluorescence staining.

For this application, the three segmentation methods presented previously in Chapter 5 based on the global thresholding of *Top-Hat* (TH) filtered image are tested. Within the scope of this thesis, these segmentation methods are applied on Caco-2 cells in order to monitor the fluorescence emitted by stained surface receptors related to their innate immune system. This has two objectives; first confirming that such segmentation methods can be successfully used to monitor low fluorescent-light intensity signals as emitted by the biomarkers while using a mid-range CMOS image sensor; second validating the best segmentation technique which would be part of the smart camera design that is presented in Chapter 6.

The second application, presented in Section 7.2, leverages the monitoring of a different kind of biomarker using the smart camera system. The focus is around the uptake of silica *SiO<sub>2</sub> Nano-particles* (NPs) in cell cultures and their potential toxicity as they are used in a wide range of commercially available goods. Specifically for this thesis, an experiment with fluorescent silica NPs and their uptake kinetics within cultures of the A549 cell line is presented. Given the fluorescent spots that such samples present, it constitutes an ideal test for validating the smart camera design and demonstrate its ability to detect the uptake of potentially toxic agents by monitoring biomarker concentration changes in real-time.

### 7.1 Nutrition Analysis and NutriChip Project

The fields of food and nutrition sciences are increasingly important in modern societies. It comes to no surprise that nutrition plays a predominant role in the development and maintenance of health. However, questions are raised about the impact and potential risks that various food products have, especially when considering the significant increase in transformed and processed food products availability. Food products essentially expose consumers to a broad range of bioactive nutrients whose physiological properties should ideally be understood prior to entering the marketplace. Therefore, specialized tools need to be developed in order to render food product screening efficient, available and affordable. Solutions to this societal concern typically have a multidisciplinary scope that often features an engineering dimension.

The NutriChip project [138] offers one solution by aiming at the development of analytical strategies enabling food screening. In particular, this project focuses on what is known as postprandial stress [71] and its potential effects on chronic inflammatory diseases (e.g. obesity or cancer). Postprandial stress refers to the side effects caused by the cellular metabolism of nutrients occurring after food ingestion. Besides the obvious synthesis of biochemical energy, each meal provokes a kind of inflammatory response. This postprandial inflammatory response is nominally low and limited in time. However, unhealthy diets and/or food disrupt this response by lengthening and amplifying it, which in turn is thought to contribute to the genesis of chronic inflammatory diseases.

The quantitative measurements of nutritionally relevant parameters or biomarkers are key to the understanding of this metabolic concept. In order to characterize food interaction with the human organism, the NutriChip project is organized around two axis: *in vitro* food screening and nutritional studies.

**Nutritional studies** The postprandial inflammatory stress of lean and obese subjects is monitored and compared using blood as a source of biomarkers in order to assess the impact of different meals. High-fat meals are used to induce and exacerbate the postprandial rise of pro-inflammatory cytokines [71] while dairy products are used to reduce this inflammatory response [54]. It is worth mentioning that milk is of particular interest as it appears to have immunomodulatory properties. Combined with the vast possibilities of transforming technologies, dairy products appear to be a strategic vector to deliver immunomodulatory nutrients and improve the human metabolic health.

Even though human intervention studies are considered a gold standard in nutrition sciences [80], they have obvious logistic limitations. Screening food products on a large scale is impractical, and even struck by an ethic *conundrum* for various potentially unsafe goods. Nutritional studies however serve an important purpose in the NutriChip project as they validate the technologies developed for the *in vitro* food screening.

**In vitro screening** *In vitro* screening of food products using cell cultures is required for testing

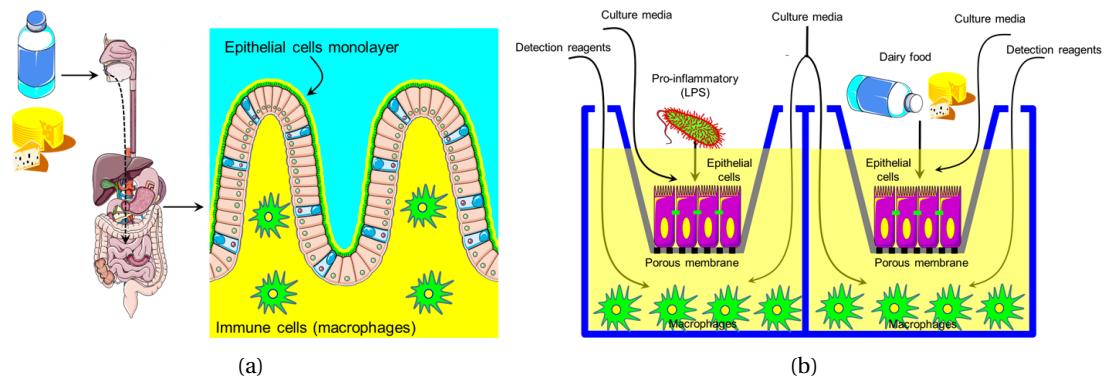


Figure 7.1 – (a) Simplified view of the human gastrointestinal wall consisting of a confluent layer of epithelial cells underlined by immune cells. (b). Schematic view of a co-culture Transwell system commonly used to mimic the gastrointestinal tract biological function *in vitro*. Reprinted from [105].

a wide range of products efficiently. By design, they offer a much more controllable and predictable environment, they are cost effective and speed-up the screening process compared to clinical studies. This is achieved through the used of a biological model, a human *in vitro* cell culture which acts as a surrogate for the human *Gastrointestinal Tract (GIT)*.

The NutriChip project proposes a LoC platform onto which an artificial and disposable *Miniaturized Gastrointestinal Tract ( $\mu$ GIT)* is used for screening digested food [104, 105]. The development of this platform is the engineering dimension of the NutriChip project, combining microfluidics for the design of the  $\mu$ GIT and a combination of optics and electronics for monitoring selected biomarkers within the cell culture through fluorescence biomimaging.

### 7.1.1 Biological Model and Lab-on-a-Chip Integration

Whenever ingested, food products undergo complex processes involving *adsorption, distribution, metabolism* and *excretion* (ADME) for which the GIT plays a central role. In particular, the gastrointestinal wall implements the necessary barrier controlling the uptake of nutrients and rejection of harmful pathogens. The surface of the GIT consists of a layer of epithelial cells forming the intestinal epithelium [30]. This epithelial layer is at the front line of the absorption process and is underlined by a secondary layer of immune cells that act as a local immune system. On one side, this biological construct is tasked with transferring nutrients from the mucosal side to the serosal side while maintaining certain tolerances. On the other side, the local immune system needs to trigger an inflammatory response against the entry of pathogenic organisms. A simplified view of this process is shown in Fig. 7.1(a).

The communication between the epithelial cells and the immune cells is thus essential. In

the scope of the NutriChip project, spying off this communication by monitoring biomarkers related to the local immune system activation is key to unveiling the immunomodulatory properties of dairy products. This objective is achieved by modeling the previously described biological construct where (i) a confluent layer of epithelial cells is cultured on a porous semi-permeable membrane and (ii) this layer is brought in contact with a secondary culture of immune cells. This co-culture model is often implemented using a Transwell device as shown in Fig. 7.1(b). Digested food can be applied on the apical side of the epithelial cell layer, which in turn communicates with the immune cells through the porous membrane on the basolateral side.

The NutriChip platform, whose concept is depicted in Fig. 7.2, features a microfluidic device reproducing the Transwell system on a miniaturized scale. The benefits are a reduction of the liquid volumes within the cell culture chamber, the ability to control the fluid flow rates and a custom access for light detection systems such as microscopes. This of course offers an improved and controlled system within which the GIT environment can better be mimicked and the monitoring of biomarkers of live cell cultures using fluorescence bioimaging techniques is possible.

### 7.1.2 Induced Toll-Like Receptors Monitoring

*Toll-Like Receptor 2* (TLR2) and *Toll-Like Receptor 4* (TLR4) are cell surface receptors that play a central role in the cellular innate immune system. These proteins are characterized by their ability to activate the inflammatory cells, making them target biomarkers for the NutriChip platform.

The goal in this application<sup>1</sup> is to apply selected techniques presented in the Chapter 5 in order to monitor the expression of TLR2 in Caco-2 cells given various degrees of stimulation of the innate immune system. The interest lies in confirming that image thresholding techniques can be used on images captured by a CMOS sensor to detect the up-regulation or down-regulation of TLR2 biomarkers. The current state-of-the-art for quantifying gene expressions are techniques based on *Reverse Transcription Polymerase Chain Reaction* (RT-PCR), which can be applied only with the extraction, amplification and quantification of mRNA coding the expression of TLR2 in Caco-2 cells. This means the cell destruction is required and, therefore, this method is not suitable for continuous monitoring. However, it is often considered as a gold standard in relative mRNA quantifications [93].

#### Cell Samples

For our experiment, human colon adenocarcinoma Caco-2 cells (Sigma) are cultured in vitro (DMEM high glucose 4500mg/ml with fetal bovine serum 10%, L-Glutamine 4mM, Pen/Strep

---

<sup>1</sup>Part of the results and discussions presented in this section were originally published in [36] and are reproduced here.

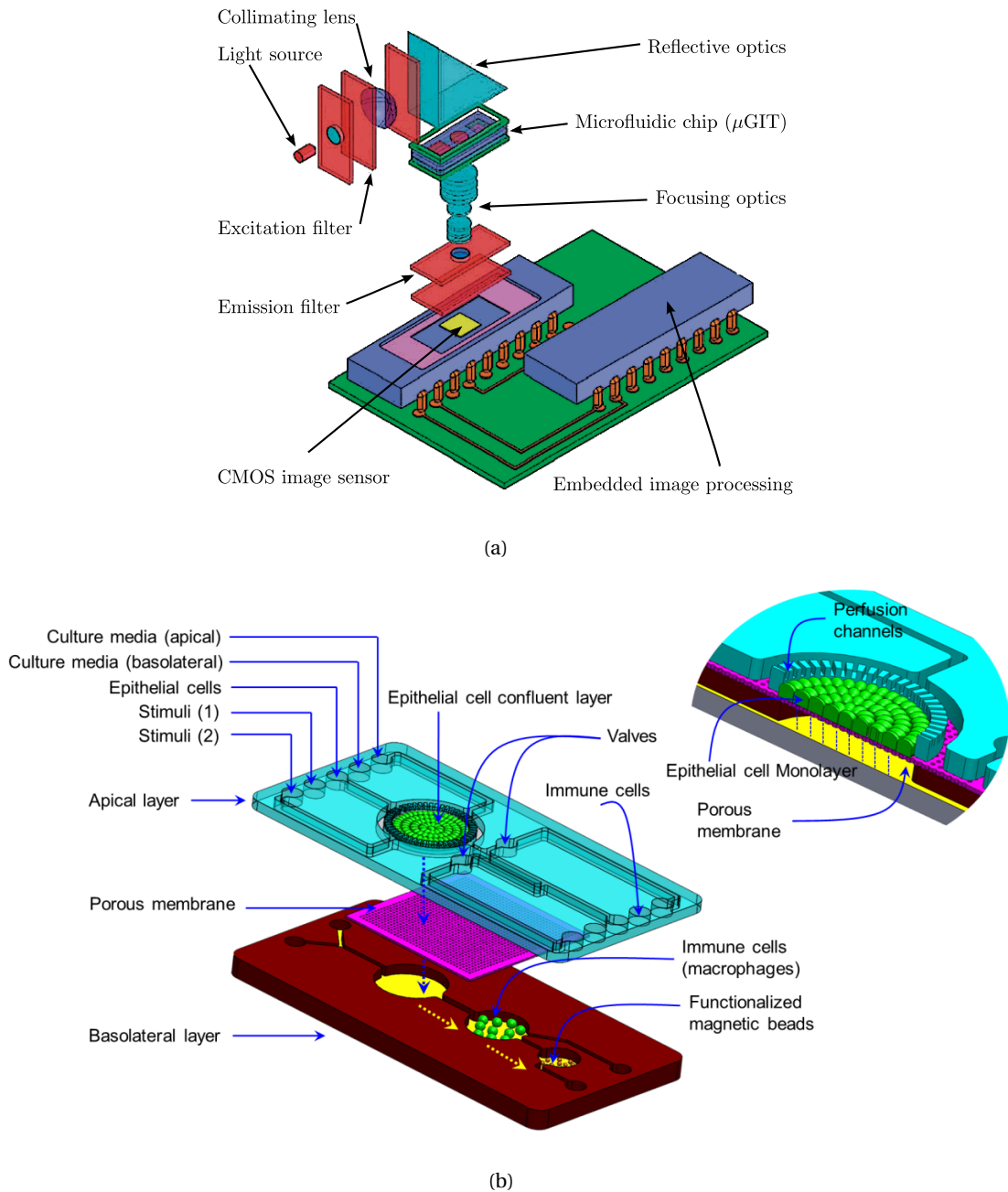


Figure 7.2 – (a) Breakout of the various modules defining the NutriChip platform. Adapted from [138]. (b) Structure of the microfluidic chip forming the miniaturized gastrointestinal tract. Reprinted from [105].

## Chapter 7. Applications

---

1%, non-essential amino acids 1%). The cells are then exposed to a concentration of 10ng/ml of *Lipopolysaccharide* (LPS).

LPS is an endotoxin found on the outer membrane of Gram-positive bacteria such as *Escherichia Coli* (E-Coli). It is known to be a powerful activator of the innate immune system of cells [102]. This includes Caco-2 cell whose TLR2 expression gets up-regulated whenever in contact with LPS [16].

The cells destined to have their TLR2 mRNA quantified through RT-PCR are treated with LPS for 1, 6 and 24 hours. On the other hand, cells destined to be imaged are treated for 2, 4, 6, 12 and 24 hours. After stimulation the cells are fixed with 3.7% formaldehyde, permeabilized with Triton-X 0.25% for 15 minutes, blocked with BSA 3%, incubated with primary antibodies (anti-TLR2 rabbit polyclonal IgG) for 2 hours and with fluorescently marked secondary antibodies (goat anti-rabbit IgG Texas Red) for 1 hour.

A couple of negative control samples for which the LPS treatment is omitted are realized for the RT-PCR and indirect immunofluorescence techniques, confirming a proper stimulation of the other cell samples by LPS.

### Imaging Setup

The optical fluorescence microscope used for imaging the Caco-2 cell samples is an Eclipse Ti-S inverted microscope. The objective is a Plan Fluor (40× magnification,  $NA = 0.6$ ), the filter set is designed for Texas Red compatible dyes (542 – 576nm band pass excitation filter, 595 – 664nm pass emission filter, 533 – 580nm reflective band and 595 – 800nm transparent band dichroic mirror) and a 0.7× relay lens projects the image on the sensor. The image sensor is the same CMOS sensor as used in the smart camera prototype in Chapter 6.

### Segmentation Methods

The considered segmentation methods are the three global thresholding methods applied on TH filtered image (see Chapter 5, Section 5.1): *TH+Otsu*, *TH+Otsu(2X)* and *TH+T-point*. These segmentation methods have been selected in spite of the others since they offer only a single configuration parameter, the diameter of the structuring element used for the TH filter. A choice is made here to favor segmentation methods with fewer parameters as the target application is embedded. Sample images of stained Caco-2 cells and related segmentation masks are collect in Fig 7.4.

### Blob Intensity

A total of 18 image datasets are considered, each consisting of 10 images taken from a single cell sample. More specifically, each set of images is characterized by:



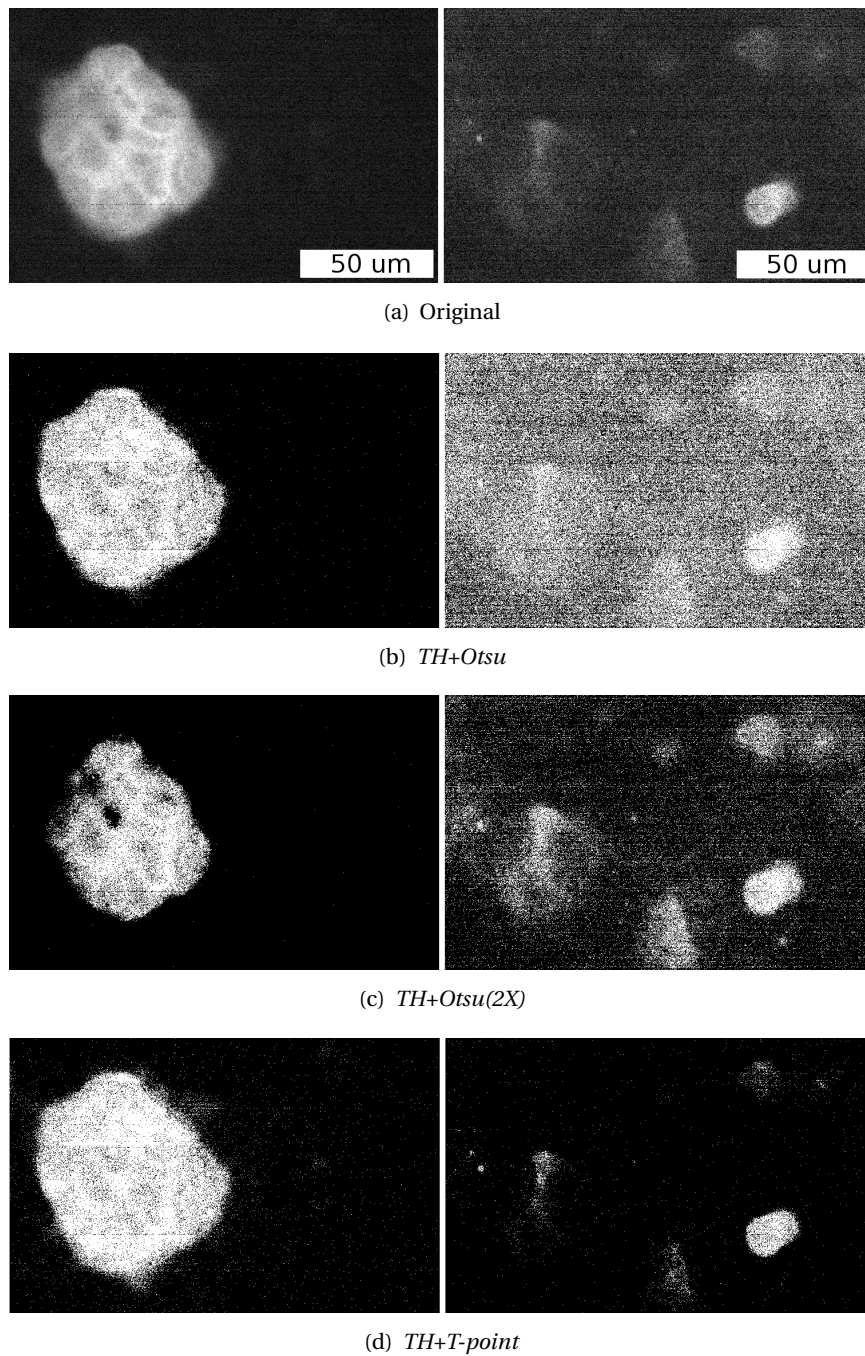


Figure 7.3 – (a) Sample CMOS images of Caco-2 cells with stained TLR2 via indirect immunofluorescence. These two images are flat field and FPN corrected and the contrast has been adapted for display purposes. They represent packed groups of Caco-2 cells stimulated with LPS for 24 hours (left) and 2 hours (right). (b) Segmentation mask obtained with the *TH+Otsu* method. (c) Segmentation mask obtained with the *TH+Otsu(2X)* method. (d) Segmentation mask obtained with the *TH+T-point* method.

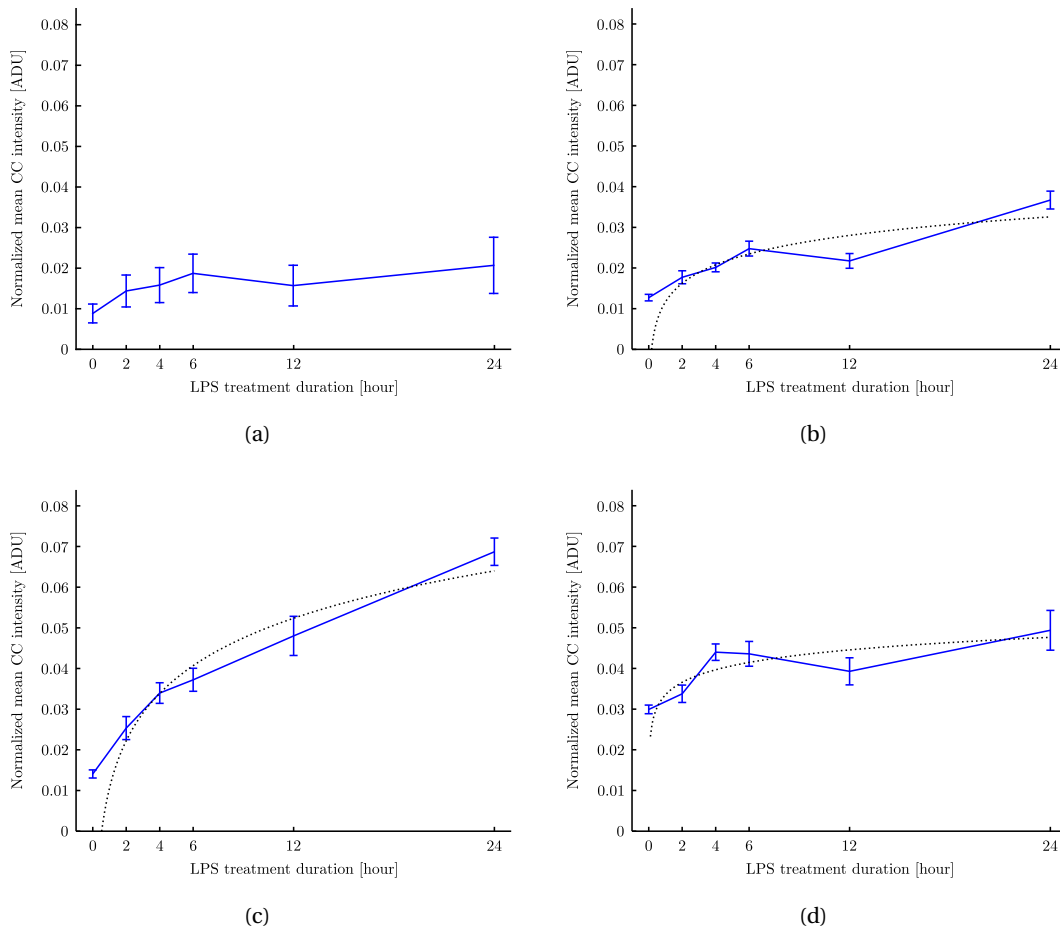


Figure 7.4 – Kinetics of TLR2 expression in Caco-2 cells as reported in ADU (Arbitrary unit) using (a) no segmentation method (b) the *TH+Otsu* method (c) the *TH+Otsu(2X)* method or (d) the *TH+T-point* method.

- the employed segmentation method,
- the treatment duration of the cell sample with LPS, either 0 (negative control), 2, 4, 6, 12 or 24 hours.

After processing, the segmentation mask of every image is labeled using CC labeling in order to stay consistent with the comparison frameworks of Chapter 5 (see Section 5.2). Based on the mean pixel intensity of each CC, the mean CC intensity of a particular image dataset is computed. These extracted mean CC intensities are then plotted with respect to the LPS treatment duration and compared to the mRNA fold change as measured by the relative RT-PCR technique compared to the control sample.

The goal of this experiment is to show that measured mean CC intensities can be successfully correlated with measured relative mRNA concentrations. That is, show that these classic

image segmentation methods can capture the up-regulation of the TLR2 in the cells as the LPS treatment lasts longer. For this reason *Pearson's Correlation Coefficients (PCCs)* and *Spearman's Ranked Correlation Coefficients (SRCCs)* [49] are used as figures of merit in order to quantify the correlation of the measurements obtained from either of the segmentation methods with the ones obtained using RT-PCR.

For reference, the PCC between two sets of measurements  $\mathbf{x} = \{x_i : i \in [1 \cdot n]\}$  and  $\mathbf{y} = \{y_i : i \in [1 \cdot n]\}$  is obtained using

$$\rho_P = \frac{\sum_{i=1}^n (x_i - \bar{x})(y_i - \bar{y})}{\sqrt{\left[\sum_{i=1}^n (x_i - \bar{x})^2\right] \left[\sum_{i=1}^n (y_i - \bar{y})^2\right]}} \quad (7.1)$$

where  $\bar{x}$  and  $\bar{y}$  are the mean measurements of each set, and the SRCC is obtained using

$$\rho_S = 1 - 6 \frac{\sum_{i=1}^n d_i^2}{n(n^2 - 1)} \quad (7.2)$$

where  $d_i$  is difference in paired ranks [49].

The core of the results are presented in the various graphs gathered in Fig. 7.4 and 7.5. The computed correlation coefficients are gathered in Table 7.1. All the relative fold changes of TLR2 mRNA expression (Fig. 7.5, green curve) or mean intensities (Fig. 7.4) are given plus or minus the *Standard Error (SE)*.

Fig. 7.5 reports the results obtained by RT-PCR where, as expected, we clearly observe an increase of the TLR2 mRNA concentration as the stimulation time by LPS increases. A logarithmic regression was performed ( $R^2 = 0.965$ ) on the three data points for LPS treatment durations of 1, 6 and 24 hours.

Fig. 7.4(b), 7.4(c) and 7.4(d) presents the mean CC intensities obtained by processing the CMOS images using *TH+Otsu*, *TH+Otsu(2X)* and *TH+T-point* after they have been corrected for the FPN. Each data point in these graphs represents the mean CC intensity computed over a data set of 10 images. As we can observe, the considered segmentation methods are able to capture the evolution trend of the amount of TLR2 in the Caco-2 cells with respect to the LPS treatment duration. Table 7.1 is using the PCCs and SRCC as figures of merit to quantify this correlation. In particular, *TH+Otsu(2X)* appears to provide CC intensities that are

Table 7.1 – Pearson and Spearman correlation coefficients between the three considered methods and RT-PCR.

	AllPix	TH+Otsu	TH+Otsu(2X)	TH+T-point
<b>Pearson</b> ( $\rho_P$ )	0.813	0.905	<b>0.989</b>	0.805
<b>Spearman</b> ( $\rho_S$ )	0.829	0.943	<b>1.000</b>	0.771

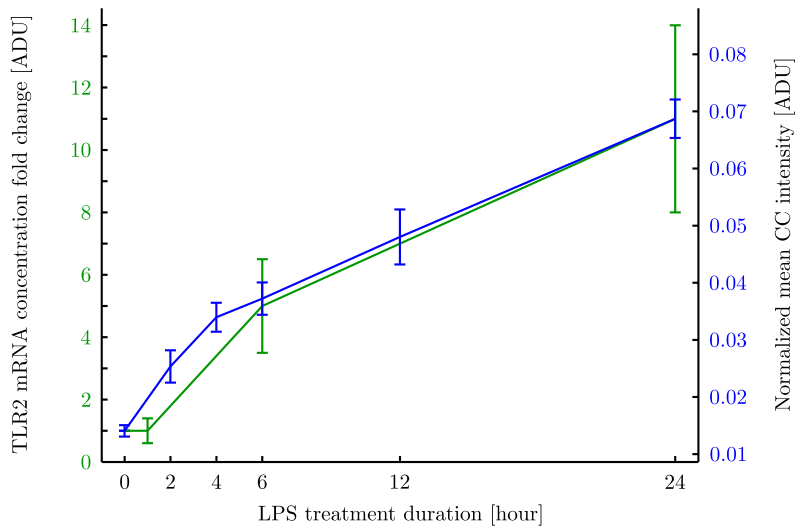


Figure 7.5 – Superposition of the fold change in TLR2 mRNA expression as measured by relative RT-PCR (green) and the mean CC intensity obtained using the *TH+Otsu(2X)* method (blue).

highly correlated with the relative mRNA fold changes ( $\rho_P = 0.989$ ;  $\rho_S = 1.000$ ). This result is highlighted in Fig. 7.5 where the measurements obtained by both methods are overlapped in order to give an intuitive idea of the correlation. Another observation we can make is the relatively high correlation obtained using the average image intensity (Fig. 7.4(a)), which is the equivalent to any other cytometry technique measuring the overall fluorescence of a sample. However, the SE on the average image intensity is largely greater than that of the CC intensities using any segmentation method. As a result, the former is not recommended. The *TH+T-point* method provides somewhat reduced performance ( $\rho_P = 0.805$ ;  $\rho_S = 0.771$ ), which comes from the limited performance of the CMOS image sensor. Notably, the low fluorescence emitted by our samples combined with the lower bit resolution and higher noise of the CMOS sensor leveled the fluorescence intensity of details from intracellular structures. The sensor is in fact acting as a spatial averaging filter, favoring the generation of images with bimodal over unimodal histograms, in turn favoring an Otsu based segmentation method.

### 7.1.3 Application Concluding Remark

Within the scope of this thesis, this application of bioimaging to the NutriChip project is twofold. First, it served the purpose of demonstrating that a correct quantification of the up-regulation of biomarkers over time is possible using common image segmentation techniques based on CMOS images in low light conditions. The use of time-consuming and costly techniques such as relative RT-PCR are not always required.

Second, the use of CMOS image sensing technology in this case is important as we can show that it is a realistic alternative to the traditional CCD technology used in commercial

bioimaging applications. The CMOS technology can be used to track and monitor a biological function using fluorescence microscopy. Its low cost characteristic, ease of manufacturability and integration capabilities with respect to the CCD technology demonstrates that affordable embedded systems such as envisioned by the NutriChip project are viable solutions. The monitoring approach applied to the TLR2 is done in the classical way. That is, by first capturing the 18 image datasets from the fixed samples, then by processing them in a second time with segmentation methods to extract measurements.

The smart camera prototype presented in Chapter 6 is not used in this case. As stated before, the segmentation method it implements (i.e. *TH+Otsu(2X)*) is a result of this experiment on TLR2 monitoring in Caco-2 cell samples. However, it has to be mentioned that since the results as presented in Fig. 7.5 are independent from the implementation of the method, the use of the smart camera would have resulted in the same outcome and conclusions. Meanwhile providing the further benefit that no lengthy post processing of the image datasets is required.

## 7.2 Silica Nano-particles

### 7.2.1 Industrial Applications of Nano-particles and Related Concerns

Engineered *Nano-particles* (NPs) have become a commodity in various industries and in medicine. Nanomaterials can be found in a wide variety of products and goods human interact with every day. In particular  $SiO_2$  silica NPs are extensively used in a range of sectors including, but not limited to, cosmetology [107], food and agriculture [25, 59], and pharmaceutical [69, 146]. As we can see, their usage goes beyond the bioimaging application as fluorescent probes presented in Chapter 2. The relatively simple synthetic process, the ability to functionalize their surface or core, combined with the fact that they benefit from a FDA-approval for use in humans explains this widespread industrial use.

Silica NPs are usually considered safe and non-toxic. However, *in vitro* studies conducted on various cell lines exposed to these NPs show that their cytotoxicity is an existing fact [95, 106]. The actual physical dimensions of the NPs, their surface functionalization and charge [86] appear to be important parameters affecting how they interact with biological systems. This raises questions about their safety due to their widespread usage in everyday products.

The safety assessment of silica NPs is thus underway. In particular, it involves the study of their cellular uptake via endocytosis. More specifically, *in vitro* studies show that silica NPs first tend to get in proximity to the cellular membrane within the first hours of exposure prior to their uptake leading the NPs to be found in the perinuclear region (i.e. close to the cell nucleus) [1, 95, 120]. Specifics about the kinetics of the uptake and the various impacting factors is however still unknown and open of research.

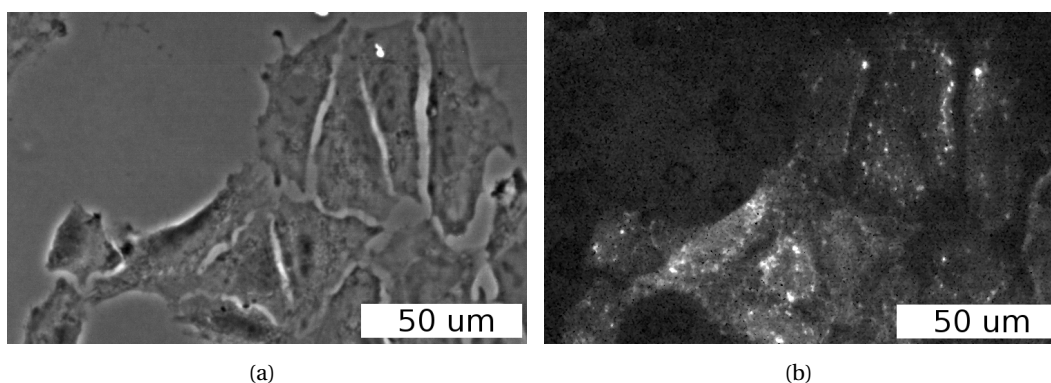


Figure 7.6 – (a) Wide-field images of A549 cells as captured by the CMOS image sensor of the smart camera, after flat-field and FPN correction. (b) Corresponding fluorescent image, after image correction for flat field and FPN, highlighting the internalized fluorescent nanoparticles after an exposure of 24 hours. This fluorescent image has been altered for display purposes.

### 7.2.2 Fluorescent Nano-particles Uptake Monitoring

Within this context, the smart camera prototype presented in Chapter 6 is used to measure the uptake over time of fluorescently stained silica NPs. A 24 hours time frame is considered for the exposure of adenocarcinomic human alveolar basal epithelial A549 cell cultures to silica NPs characterized by an 85nm diameter. This time frame is considered based on the results and observations done by studies on the kinetics of silica NPs uptake [1, 95, 120]. The data extraction and measurements performed by the smart camera should match these observation in the sense that an increase in the fluorescence intensity emitted by internalized NPs should be detected.

#### Cell Samples

Adenocarcinomic human alveolar basal epithelial cells (A549) are cultured in 75cm<sup>2</sup> flasks (Corning) in HAM-F12 + Glutamax<sup>TM</sup>-I medium (Life Technologies) supplemented with 10% heat-inactivated foetal bovine serum (Life Technologies), 10000U Penicillin/Streptomycin (Life Technologies) and 0.5% (v/v) Hepes (Life Technologies) under normal cell culture conditions (37° C; 5% CO<sub>2</sub>; 95% humidity).

For the test experiment, A549 cells are seeded onto cell culture-treated glass slides and after 48 hours the cells were exposed to 85nm silica NPs labeled with the fluorochrome *Tris(2,2'-bipyridyl)-dichlororuthenium(II) hexahydrate* ( $Ru(bpy)_3Cl_2$ ) (excitation wavelength  $\lambda_{ex} = 460\text{nm}$ , emission wavelength  $\lambda_{em} = 595\text{nm}$ ). After exposure for 3 hours, 6 hours, 9 hours and 24 hours to the NPs, the cells are washed with PBS three times in order to remove non internalized NPs from the inter-cellular medium.

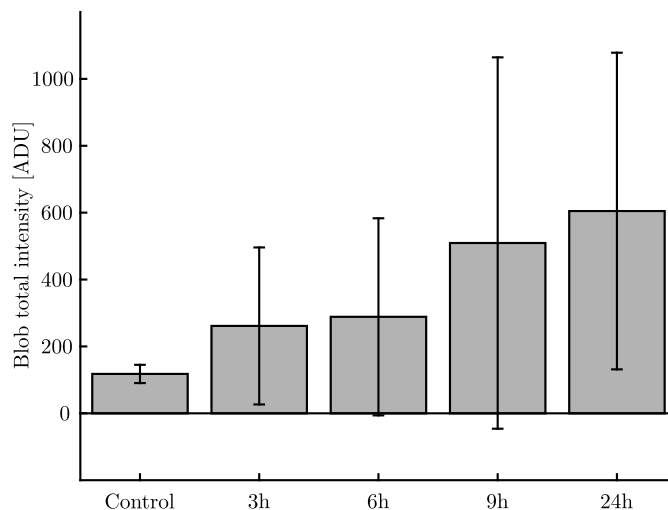


Figure 7.7 – Average total intensity per blob for each sample group. Each data point was generated using the corresponding set of 60 images. The displayed error bars are  $1\sigma$ .

The cells are then fixed with 3.7% formaldehyde (Sigma) for 15 minutes at room temperature. After a second washing step, the nuclei are stained with Hoechst (Sigma) 1 : 2000 in PBS for 45 minutes at  $37^{\circ}\text{C}$ . A third washing step is performed prior to mounting the cells and keeping at  $4^{\circ}\text{C}$  before observation.

### Imaging Setup

The imaging setup is the same as in Section 7.1, with the exception of the filter block whose filtering properties match that of the fluorescent silica NPs (465 – 495nm band pass excitation filter, 577 – 633nm band pass emission filter, 505nm dichroic mirror).

### Smart Camera Configuration

The smart camera configuration and calibration is the same as used for the camera validation (see Chapter 6, Section 6.5), with the exception of the range  $[k_{min} \cdot k_{max}]$  over which the threshold index is sought by the *TH+Otsu(2X)* segmentation method. It has been set to  $[k_{min} \cdot k_{max}] = [30 \cdot 300]$ . The lower bound is set to be slightly higher than the average pixel value of the master dark frame  $D$ . This prevents Otsu's algorithm to fail when processing images presenting no fluorescent signal as ascertained within the study in Chapter 5 (see Section 5.3). The high bound is set lower than the maximal value in order to prevent Otsu's algorithm to be influenced by highly fluorescent foreign particles (e.g. dust). Fig. 7.6 shows a group of A549 cells that have internalized fluorescent silica NPs as imaged by the smart camera.

Table 7.2 – Cohen’s  $d$  effect sizes between groups with various time of exposure to NPs.

Control & 3h	3h & 6h	6h & 9h	9h & 24h
0.866	0.103	0.501	0.187

**Blob Total Intensity**

While the linearity measurements done for validating the smart camera (see Chapter 6, Section 6.5) are looking at the blob average intensity from the CC labels, we are here looking at the blob total intensity. The measurements obtained from the control group and the four groups with cells exposed to silica NPs are presented in the bar graph in Fig. 7.7. The associated effect sizes between the groups are gathered in Table 7.2. They are calculated using Cohen’s  $d$  value

$$d = \frac{\bar{i}_1 - \bar{i}_2}{\sigma_{pooled}} \tag{7.3}$$

$$\sigma_{pooled}^2 = \frac{(N_1 - 1)\sigma_1^2 + (N_2 - 1)\sigma_2^2}{N_1 + N_2 - 2} \tag{7.4}$$

where  $\bar{i}_1, \bar{i}_2$  are the mean blob total intensities of two groups,  $\sigma_1^2, \sigma_2^2$  their standard deviations and  $N_1, N_2$  are the number of measurements made in each group.

As a result, there is a clear distinction between the control group and any other group where the cells were exposed to NPs. There is no clear distinction between 3 hours and 6 hours of exposure to NPs. A statistically significant increase in fluorescence seems measured between the 6 hours and 9 hours groups. Finally, there is no clear distinction between 9 hours and 24 hours of exposure to NPs either.

In a second step, for each group, 5 images are randomly picked from the 60 available images. The effect sizes between the groups are computed, this time with 5 images in each group. This process was randomly repeated 200,000 times. The resulting distributions of Cohen’s  $d$  effect size are reported in Fig. 7.8.

By this process, categories of images within each set of 60 images can be highlighted. These categories are extracted by fitting a *Gaussian Mixture Model (GMM)* on the effect size distributions (solid curves in Fig. 7.8). The number of Gaussian components used for the fitting is selected by minimizing the *Bayesian Information Criterion (BIC)*. The extracted Gaussian components are reported in Table 7.3, within which the components with a non negligible weight (> 10%) are highlighted.

By examining the different Gaussian components, we can confirm the conclusions deduced from the overall effect sizes in Table 7.2.

- *Control & 3h*: All the significant components clearly have a mean greater than 1, indicating that there is a significant increase in fluorescence between the control group and



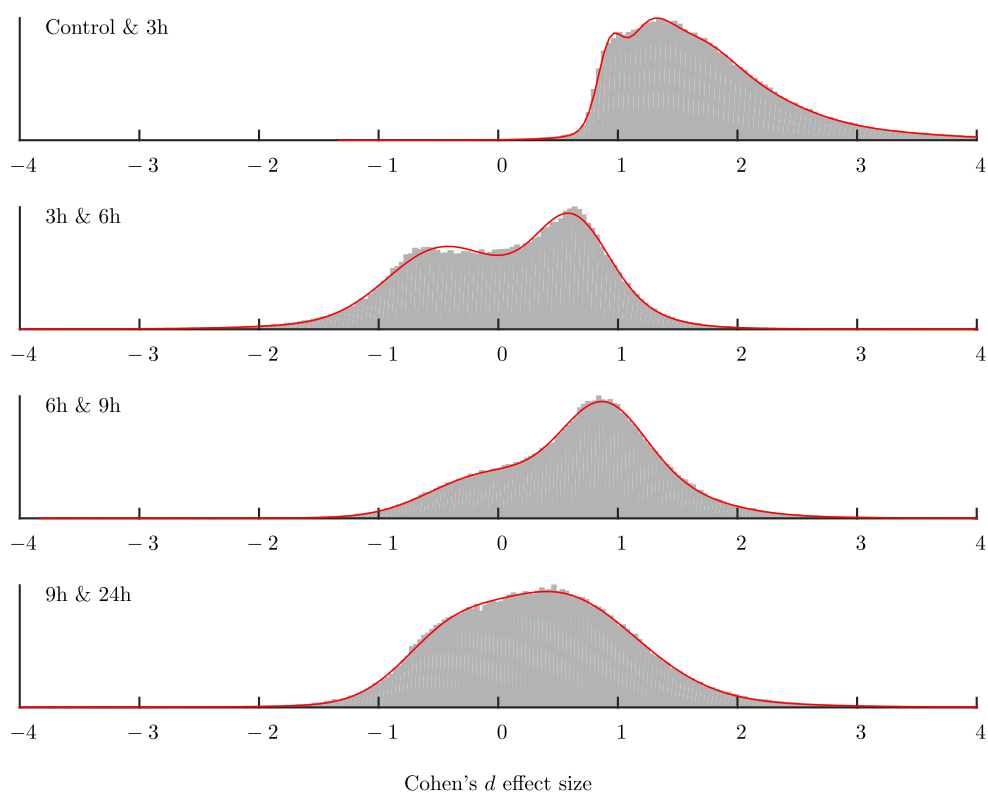


Figure 7.8 – Effect sizes distributions between groups with various time of exposure to NPs. From top to bottom: Control & 3h, 3h & 6h, 6h & 9h, 9h & 24h. The solid curves are GMM fittings. Related Gaussian components are gathered in Table 7.3.

Table 7.3 – GMM’s components for the effect size distributions in Fig. 7.8. Each Gaussian component is characterized by its mean  $\mu_i$ , standard deviation  $\sigma_i$  and weight  $w_i$  with respect to the others.

Component		1	2	3	4	5	6
<b>Control &amp; 3h</b>	$\mu_i$	3.91	1.48	1.80	0.92	1.16	2.34
	$\sigma_i$	2.72	0.07	0.22	0.01	0.03	0.70
	$w_i$	0.02	0.18	0.38	0.08	0.14	0.20
<b>3h &amp; 6h</b>	$\mu_i$	0.17	0.62	-0.23	-0.55	-	-
	$\sigma_i$	0.42	0.10	1.13	0.17	-	-
	$w_i$	0.24	0.32	0.15	0.28	-	-
<b>6h &amp; 9h</b>	$\mu_i$	0.98	-0.14	0.86	1.07	-	-
	$\sigma_i$	0.36	0.21	0.10	1.78	-	-
	$w_i$	0.40	0.24	0.32	0.04	-	-
<b>9h &amp; 24h</b>	$\mu_i$	0.48	-0.43	0.93	0.51	-	-
	$\sigma_i$	0.70	0.13	2.25	0.29	-	-
	$w_i$	0.40	0.18	0.03	0.39	-	-

the 3 hours group in all cases.

- *3h & 6h*: The components 1 and 2 hint for an increase in fluorescence between the 3 hours group and the 6 hours group for some images. However the components 3 and 4 indicate the opposite. There is no conclusive evidence of a difference between the two groups.
- *6h & 9h*: The components 1 and 3 clearly indicate an increase in fluorescence between the 6 hours group and 9 hours group for 72% of the cases.
- *9h & 24h*: The components 1 and 4 hint for an increase in fluorescence between the 9 hour group and the 24 hours group with mean of about 0.5 in for 79% of the cases. This is partly counter-balanced by component 2 showing a decrease in fluorescence in 18% of the cases.

### 7.2.3 Application Concluding Remark

In this section, we have shown the potential of embedded image processing applied to fluorescence bioimaging thanks to the smart camera design of Chapter 6.

Various fixed cell samples were successfully analyzed using the system. As described earlier, 60 different locations on each sample were analyzed automatically in order to produce the results presented in Fig. 7.7 and extract the uptake kinetics of Silica NPs in A549 cells.

The fact that the smart camera features a mid-range CMOS image sensor and is powered

by a versatile image processing suite for FPGA technologies are noteworthy once more. The continuous processing of the images by the system gives the opportunity to directly and automatically recover a stream of numerical measurements from the image processing cores. While this is used to analyze four fixed samples on the fly, it also suggests that the continuous monitoring of one single cell in a live sample subjected to NPs is within reach thanks to the real-time processing capabilities of the hardware image processor.

### 7.3 Chapter Summary and Contributions

This chapter is dedicated to the presentation of a series of experimental results obtained from the praxis of techniques and tools presented in the previous chapters. Two bioimaging applications are considered and presented; (i) the monitoring of surface receptors in immune cells applied to nutrition analysis, and (ii) the monitoring of the uptake of NPs in cell cultures applied to the study of cytotoxicity by nanomaterials.

The experiments conducted for both applications have intersecting characteristics. First, both applications target the monitoring of fluorescent biomarkers in cells. Second, the images are captured in both cases with a single CMOS image sensor, the MT9V032 sensor as used in the smart camera design. Third, the monitoring and signal extraction is done using the *TH+Otsu(2X)* segmentation method. Fourth, the analyzed fixed cell cultures present various degrees of biomarker stimulation.

The outcome of the experiment done in the scope of the Nutrichip project (see Section 7.1) can be seen as an extension of the comparison study performed on multiple image segmentation methods in Chapter 5. Here, it is however focused on a subset of these methods: the global thresholding methods on TH filtered images. This subset selection was done as this class of methods appears to segment the greatest amount of biomarkers in absolute and because they feature the lowest amount of configuring parameters.

On the other hand, the experiment conducted on the uptake of NPs in A549 cell cultures (see Section 7.2) aims at the test and validation of the smart camera operation. It demonstrates the ability of the camera to automatically recover a stream of numerical measurements from the image processing cores.

In the end, the combined outcome of both experiments contributes to the demonstration that CMOS light sensing technologies are today a viable alternative to CCD technologies for quantitative fluorescent microscopy, even in low light conditions. Furthermore, that outcome also strongly suggests that the smart camera prototype can, as it is, be used for further experiments including the monitoring of live biosamples. This would be of great interest for the *Lab-on-a-Chip* (LoC) community which aims at such results.



## 8 Conclusions and Outlook

The work presented in this dissertation is hands-on research and development on an embedded image processing system for fluorescence bioimaging applications and potentially high-throughput microscopy systems.

The main scope within which this thesis is inscribed is the NutriChip project that is presented as one of the two applications detailed in Chapter 7. Linking back to the general comments made in the introduction chapter, the research and engineering work presented throughout this thesis was practically conducted in such a way that a general view of the problem offered by the NutriChip project was kept. In other words, the focus was put on the broad problem of detecting generic fluorescent biomarkers in cell cultures rather than on the specific problem of detecting immunostained *Toll-Like Receptors* (TLRs) in immune cells within a custom microfluidic system.

This broader view was decided upon initially and led first to the design of the synthetic image generation tool of Chapter 4. This tool was a requirement for the test and validation of various the image segmentation algorithms used for biomarker detection within Chapter 5 .

Eventually, these studies evolved into the development of an embedded image processing system, the smart camera, and of a digital hardware image processing suite presented in Chapter 6. This image processing suite was developed with the needs of NutriChip in mind; particularly by following the requirement that the custom image processor needs to be closely integrated with the image sensor for the *Lab-on-a-Chip* (LoC) design. On the other hand, the smart camera design was an effort done to (i) prove the usefulness of the image processing suite and (ii) offer a system capable of analyzing different types of fluorescent images on the fly. This was eventually achieved and demonstrated by monitoring the uptake of fluorescent silica *Nano-particles* (NPs) via endocytosis in cell cultures.

### 8.1 Thesis Summary and Contributions

Chapters 1 to 3 are dedicated to the introduction and background related to problem at hand. Chapter 1 provides the required introduction to bioimaging and explains the potential advantages embedded image processing and integration technologies can bring to this field. This introduction is supported by the following two chapters of this thesis that explain in more detail the techniques and concepts behind digital fluorescence microscopy. They focus on the biological aspects used in fluorescent probing, introduce the concepts behind fluorescent microscopes and detail the technologies used for light detection.

The core part of the thesis consists of the Chapters 4 to 6. These core chapters relate the various contributions made during the research and engineering work.

In Chapter 4, a novel approach for generating synthetic fluorescent 2D images of cell cultures is presented. The resulting Matlab tool is built around a couple of simulation engines. One that focuses on the modeling and generation of populations of cells through the use of parametric models. The models are used to randomize cell shapes and sizes by procedurally distributing fluorescent clusters within the cytoplasm region. The second engine simulates the imaging process of a digital fluorescent microscope by integrating the contribution of every fluorescent cluster in a synthetic population. The novelty included in the presented approach consists in the use of a parametric model to generate the location of the fluorescent clusters in the simulated population. This allows the tool to generate images by simulating a real image acquisition process down to each fluorescent biomarker, rather than using a randomized texture generator for the emulation of the fluorescent signal as it is done by other published image generators.

In Chapter 5, a comparison between image segmentation methods for fluorescent spot extraction in microscopic images is presented. The selected methods are based on common global and local thresholding algorithms combined with the mathematical morphology Top-Hat filter, which is used as a signal enhancer. The presented comparison offers a new view on these algorithms as previous comparison reviews are either focused on the segmentation of fluorescent cells and not sub-cellular biomarkers or focused on the impact supervised and unsupervised signal enhancement algorithms have on a segmentation provided by global thresholding.

Furthermore, a novel local thresholding method, the *GLT* algorithm, is also introduced and explained in the study of Chapter 5. This technique is specifically designed to segment bright spots in images and offers improved segmentation data when compared to the other segmentation methods. While it does not recover the most biomarkers on an absolute scale, its produced segmentation masks offer the best trade-off between the recovered amount of biomarkers and the conservation of spatial distribution and information about them.

In the last core chapter of this thesis, a smart camera design is presented with the goal of offering a semi-automated tool for the continuous monitoring of fluorescent biomarkers in

microscopic applications and related integrated systems. The chapter presents a versatile image processing suite composed of various inter-operable IP cores in order to implement *TH+Otsu(2X)*, a segmentation method initially described in Chapter 5. Emphasis is made in the concluding section of that chapter that image processing suite is by no mean linked or reserved for the *TH+Otsu(2X)* segmentation method. Its design is such that existing IP cores, or even future IP cores, can be combined in a multitude of image stream processors targeted for various applications, which includes the potential design of *System-on-Chips* (SoCs) specific to microscopic biomaging applications. In the end, the smart camera prototype is validated using a microscope calibration kit featuring microbeads with various relative fluorescent intensities. These microbeads, when imaged at a low magnification, produce images featuring fluorescent spots ideal for testing. Finally, the smart camera operation is also validated within the scope of a real scenario by monitoring the uptake of fluorescent NPs in cell cultures.

Finally, Chapter 7 offers an applicative perspective of the core part of the thesis. It is dedicated to the presentation of a series of experimental results obtained from the application of techniques and tools presented in the other chapters. Two applications requiring the use of fluorescence bioimaging are gathered. A first application, related to nutrition and food ingestion by humans, seeks to monitor TLR2 inflammatory biomarkers within a biological model of a human *Gastrointestinal Tract* (GIT). It can be assimilated as an extension of the study of Chapter 5 where global thresholding methods on TH filtered CMOS images are tested for the extraction of the kinetics of TLR2 in Caco-2 cells. The second application, related to cellular cytotoxicity of nanomaterials, focuses on the validation the smart camera prototype through the monitoring of the uptake of silica NPs in A549 cell cultures.

## 8.2 Future Perspectives

The work, techniques and systems presented in this thesis have by no mean reached an end. In order to give a final note to this thesis, a handful of directions are presented which could take the output of this thesis further.

Regarding the synthetic image generator, two ideas could be pursued in order to extend the simulation approach and offer increased possibilities. First, adding the time dimension would help bring the simulation from fixed cells to live cells. With this, the tool can provide added meta-data for testing algorithms and other image processing systems by simulating the time dependency of the fluorescent signal. For example, this would enable the simulation of the photobleaching effect or of the displacement and kinetics of fluorophores. Second, extending the tool to 3D models would help better simulate out-of-focus fluorescence. This would increase significantly the required simulation time. However, given the parallelization possibilities inherent to the simulation approach, this can be mitigated with an appropriate implementation of the tool targeted for a modern parallel computing system.

In its current state, the smart camera prototype is a proof-of-concept. As it is, it successfully relates information about the fluorescence level within the field of view in a continuous

## Chapter 8. Conclusions and Outlook

---

fashion. However this capability have not been used to its fullest. The experiments performed on the uptake of silica NPs were done on fixed cell cultures. The next logical step would be to plan the monitoring of live samples using the continuous monitoring capabilities of the smart camera to highlight in real-time changes occurring in the biosamples.

From an engineering perspective, a few words need to be mentioned on the image processing suite that was developed in combination with the smart camera. As advertised before, it has been developed from the ground up in order to maximize its independence from the technology it is implemented on. However there is still the system bus interface, which is used to gain access to the main memory by various blocks (namely the image source, image sink and frame buffer), that still use the proprietary Avalon interconnect restricted to Altera FPGA devices. Extended work on the image processing suite should initially target this problem and replace it with a more widely used interconnect. Then the image processing suite can be applied on custom SoCs and the next step in integrating image processing capabilities in LoC systems can be envisioned.

Overall, I trust that this dissertation offers both global and detailed views of the research and engineering work done over the last years given the initial task of monitoring fluorescent signals for the NutriChip project.



# A Appendix

This appendix details the mathematical derivation of the expression (6.21) from Chapter 6 where re-writing the equation of the intra-class variance  $\sigma_B^2$  used by Otsu's algorithm solely as a function of cumulative histogram moments is desired.

Given the definition of the histogram  $\mathbf{H}$  of an image  $I$  (Eq. (6.9))

$$\mathbf{H} = \{H[i] : i \in [0 \cdot \cdot L - 1]\}$$
$$H[i] = \sum_{x,y} \begin{cases} 1, & \text{if } I[x, y] = i \\ 0, & \text{otherwise} \end{cases} \quad (\text{A.1})$$

where  $i$  are the histogram bin indexes and  $L$  is the number of bins, and given the histogram cumulative moments definition (Eq. (6.20))

$$\mathbf{S}_r \mathbf{H} = \{S_r H[j] : j \in [0 \cdot \cdot L - 1]\}$$
$$S_r H[j] = \sum_{i=0}^j i^r H[i] \quad (\text{A.2})$$

we have

$$S_0 H[j] = \sum_{i=0}^j H[i] \quad (\text{A.3})$$
$$S_1 H[j] = \sum_{i=0}^j i H[i]$$

which can be used to obtain the zeroth and first cumulative moments within an arbitrary

integer range  $[A \cdot \cdot B]$  such that  $B > A$

$$\begin{aligned} \sum_{i=A}^B H[i] &= \sum_{i=0}^B H[i] - \sum_{i=0}^{A-1} H[i] \\ &= S_0 H[B] - S_0 H[A-1] \end{aligned} \quad (\text{A.4})$$

$$\begin{aligned} \sum_{i=A}^B i H[i] &= \sum_{i=0}^B i H[i] - \sum_{i=0}^{A-1} i H[i] \\ &= S_1 H[B] - S_1 H[A-1] \end{aligned} \quad (\text{A.5})$$

In particular, within the range of interest  $[k_{min} \cdot \cdot k_{max}]$  for the computation of Otsu's threshold, the zeroth and first cumulative moments are

$$\begin{aligned} N_p &= S_0 H[k_{max}] - S_0 H[k_{min} - 1] \\ M_p &= S_1 H[k_{max}] - S_1 H[k_{min} - 1] \end{aligned} \quad (\text{A.6})$$

where  $N_p$  is the number of pixels and  $M_p$  is their cumulative value. Similarly, we have

$$\begin{aligned} N_{C_0} &= S_0 H[k-1] - S_0 H[k_{min} - 1] \\ M_{C_0} &= S_1 H[k-1] - S_1 H[k_{min} - 1] \end{aligned} \quad (\text{A.7})$$

for each of the two classes  $C_0$  and  $C_1$  considered by Otsu's method.

These expressions are then used to re-write the class occurrence and class mean levels from Eq. (5.13), (5.14), (5.15) and (5.16)

$$\begin{aligned} \omega_0 &= \frac{1}{N_p} \sum_{i=k_{min}}^{k-1} H[i] \\ &= \frac{1}{N_p} (S_0 H[k-1] - S_0 H[k_{min} - 1]) = \frac{N_{C_0}}{N_p} \end{aligned} \quad (\text{A.8})$$

$$\begin{aligned} \omega_1 &= \frac{1}{N_p} \sum_{i=k}^{k_{max}} H[i] \\ &= \frac{1}{N_p} (S_0 H[k_{max}] - S_0 H[k-1]) \\ &= \frac{1}{N_p} (N_p - (S_0 H[k-1] - S_0 H[k_{min} - 1])) \\ &= \frac{N_p - N_{C_0}}{N_p} \end{aligned} \quad (\text{A.9})$$

---


$$\begin{aligned}
\mu_0 &= \frac{1}{N_p \omega_0} \sum_{i=k_{min}}^{k-1} i H[i] \\
&= \frac{1}{N_p \omega_0} (S_1 H[k-1] - S_1 H[k_{min}-1]) \\
&= \frac{M_{C_0}}{N_p \omega_0} = \frac{M_{C_0}}{N_{C_0}}
\end{aligned} \tag{A.10}$$

$$\begin{aligned}
\mu_1 &= \frac{1}{N_p \omega_1} \sum_{i=k}^{k_{max}} i H[i] \\
&= \frac{1}{N_p \omega_1} (S_1 H[k_{max}] - S_1 H[k-1]) \\
&= \frac{1}{N_p \omega_1} (M_p - (S_1 H[k-1] - S_1 H[k_{min}-1])) \\
&= \frac{M_p - M_{C_0}}{N_p - N_{C_0}}
\end{aligned} \tag{A.11}$$

We can now re-write the intra-class variance expression from Eq. (5.12)

$$\begin{aligned}
\sigma_B^2 &= \omega_0 \omega_1 (\mu_1 - \mu_0)^2 \\
&= \frac{N_{C_0}}{N_p} \frac{N_p - N_{C_0}}{N_p} \left( \frac{M_p - M_{C_0}}{N_p - N_{C_0}} - \frac{M_{C_0}}{N_{C_0}} \right)^2 \\
&= \frac{1}{N_p^2} \frac{((M_p - M_{C_0})N_{C_0} - (N_p - N_{C_0})M_{C_0})^2}{N_{C_0}(N_p - N_{C_0})} \\
&= \frac{1}{N_p^2} \frac{(M_p N_{C_0} - N_p M_{C_0})^2}{N_{C_0}(N_p - N_{C_0})}
\end{aligned} \tag{A.12}$$



# Bibliography

- [1] M. Al-Rawi, S. Diabaté, and C. Weiss. Uptake and intracellular localization of submicron and nano-sized sio2 particles in hela cells. *Archives of toxicology*, 85(7):813–826, 2011.
- [2] Aletra Corporation. Video and image processing suite megacore functions. <https://www.altera.com/products/intellectual-property/all-ip/video-and-image-processing/m-alt-vipsuite.html>. Accessed: 2015-03-18.
- [3] D. Axelrod. Total internal reflection fluorescence microscopy in cell biology. *Traffic*, 2(11):764–774, 2001.
- [4] A. Baeyer. Ueber eine neue klasse von farbstoffen. *Berichte der deutschen chemischen Gesellschaft*, 4(2):555–558, 1871.
- [5] D. G. Bailey. *Design for embedded image processing on FPGAs*. John Wiley & Sons, 2011.
- [6] M. Bates, B. Huang, G. T. Dempsey, and X. Zhuang. Multicolor super-resolution imaging with photo-switchable fluorescent probes. *Science*, 317(5845):1749–1753, 2007.
- [7] M. Beiderman, T. Tam, A. Fish, G. A. Jullien, and O. Yadid-Pecht. A low-light CMOS contact imager with an emission filter for biosensing applications. *Biomedical Circuits and Systems, IEEE Transactions on*, 2(3):193–203, 2008.
- [8] A. N. Belbachir. *Smart cameras*, volume 20. Springer, 2010.
- [9] E. Betzig, G. H. Patterson, R. Sougrat, O. W. Lindwasser, S. Olenych, J. S. Bonifacino, M. W. Davidson, J. Lippincott-Schwartz, and H. F. Hess. Imaging intracellular fluorescent proteins at nanometer resolution. *Science*, 313(5793):1642–1645, 2006.
- [10] M. Born and E. Wolf. *Principles of optics: electromagnetic theory of propagation, interference and diffraction of light*. Cambridge university press, 1999.
- [11] W. S. Boyle and G. E. Smith. Charge coupled semiconductor devices. *Bell System Technical Journal*, 49(4):587–593, 1970.
- [12] A. Burns, H. Ow, and U. Wiesner. Fluorescent core-shell silica nanoparticles: towards lab on a particle architectures for nanobiotechnology. *Chemical Society Reviews*, 35(11):1028–1042, 2006.

## Bibliography

---

- [13] C. Bustamante. Direct observation and manipulation of single DNA molecules using fluorescence microscopy. *Annual review of biophysics and biophysical chemistry*, 20(1):415–446, 1991.
- [14] S. Carrara. *Bio/CMOS interfaces and co-design*. Springer Science & Business Media, 2012.
- [15] M. Chalfie, Y. Tu, G. Euskirchen, W. W. Ward, and D. C. Prasher. Green fluorescent protein as a marker for gene expression. *Science*, 263(5148):802–805, 1994.
- [16] J. Chen, J. N. Rao, T. Zou, L. Liu, B. S. Marasa, L. Xiao, X. Zeng, D. J. Turner, and J.-Y. Wang. Polyamines are required for expression of toll-like receptor 2 modulating intestinal epithelial barrier integrity. *American Journal of Physiology-Gastrointestinal and Liver Physiology*, 293(3):G568–G576, 2007.
- [17] M. Cheriet, J. N. Said, and C. Y. Suen. A recursive thresholding technique for image segmentation. *Image Processing, IEEE Transactions on*, 7(6):918–921, 1998.
- [18] A. H. Coons, H. Creech, R. Jones, and E. Berliner. The demonstration of pneumococcal antigen in tissues by the use of fluorescent antibody. *J. Immunol*, 45(3):159–70, 1942.
- [19] N. Coudray, J.-L. Buessler, and J.-P. Urban. Robust threshold estimation for images with unimodal histograms. *Pattern Recognition Letters*, 31(9):1010–1019, 2010.
- [20] B. Cronin, B. de Wet, and M. I. Wallace. Lucky imaging: Improved localization accuracy for single molecule imaging. *Biophysical journal*, 96(7):2912–2917, 2009.
- [21] A. B. Cubitt, R. Heim, S. R. Adams, A. E. Boyd, L. A. Gross, and R. Y. Tsien. Understanding, improving and using green fluorescent proteins. *Trends in biochemical sciences*, 20(11):448–455, 1995.
- [22] A. Davison, D. Hinkley, and E. Schechtman. Efficient bootstrap simulation. *Biometrika*, 73(3):555–566, 1986.
- [23] W. Denk, J. H. Strickler, and W. W. Webb. Two-photon laser scanning fluorescence microscopy. *Science*, 248(4951):73–76, 1990.
- [24] A. M. Derfus, W. C. Chan, and S. N. Bhatia. Probing the cytotoxicity of semiconductor quantum dots. *Nano letters*, 4(1):11–18, 2004.
- [25] E. Dickinson. Use of nanoparticles and microparticles in the formation and stabilization of food emulsions. *Trends in Food Science & Technology*, 24(1):4–12, 2012.
- [26] A. A. Dima, J. T. Elliott, J. J. Filliben, M. Halter, A. Peskin, J. Bernal, M. Kociolek, M. C. Brady, H. C. Tang, and A. L. Plant. Comparison of segmentation algorithms for fluorescence microscopy images of cells. *Cytometry Part A*, 79(7):545–559, 2011.

- [27] R. Freeman, T. FINDER, R. Gill, and I. Willner. Probing protein kinase (CK2) and alkaline phosphatase with CdSe/ZnS quantum dots. *Nano letters*, 10(6):2192–2196, 2010.
- [28] S. Frisken Gibson and F. Lanni. Experimental test of an analytical model of aberration in an oil-immersion objective lens used in three-dimensional light microscopy. *JOSA A*, 8(10):1601–1613, 1991.
- [29] J.-M. Fritschy and W. Härtig. Immunofluorescence. *eLS*, 2001.
- [30] J. B. Furness, W. A. Kunze, and N. Clerc. II. the intestine as a sensory organ: neural, endocrine, and immune responses. *American Journal of Physiology-Gastrointestinal and Liver Physiology*, 277(5):G922–G928, 1999.
- [31] M. Geisbauer, T. Röder, Y. Chen, A. Knoll, and R. Uhl. Adaptive platform for fluorescence microscopy-based high-content screening. In *SPIE Medical Imaging*, pages 76224D–76224D. International Society for Optics and Photonics, 2010.
- [32] J. Ghaye, G. De Micheli, and S. Carrara. Quantification of sub-resolution sized targets in cell fluorescent imaging. In *Biomedical Circuits and Systems Conference (BioCAS), 2012 IEEE*, pages 268–271, Nov 2012.
- [33] J. Ghaye, G. De Micheli, and S. Carrara. Simulated biological cells for receptor counting in fluorescence imaging. *BioNanoScience*, 2(2):94–103, 2012.
- [34] J. Ghaye, M. A. Kamat, L. Corbino-Giunta, P. Silacci, G. Vergères, G. Micheli, and S. Carrara. Image thresholding techniques for localization of sub-resolution fluorescent biomarkers. *Cytometry part a*, 83(11):1001–1016, 2013.
- [35] J. Ghaye, S. K. Muldur, P. Urbán, A. Kinsner-Ovaskainen, P. Colpo, D. Demarchi, G. De Micheli, and S. Carrara. Live demonstration: A smart camera for real-time monitoring of fluorescent cell biomarkers. In *Biomedical Circuits and Systems Conference (BioCAS), 2014 IEEE*, pages 169–169. IEEE, 2014.
- [36] J. Ghaye, C. Succa, D. Demarchi, S. K. Muldur, P. Colpo, P. Silacci, G. Vergeres, G. De Micheli, and S. Carrara. Quantitative estimation of biological cell surface receptors by segmenting conventional fluorescence microscopy images. In *Circuits and Systems (ISCAS), 2014 IEEE International Symposium on*, pages 1824–1827. IEEE, 2014.
- [37] J. Ghaye, P. Urbán, A. Kinsner-Ovaskainen, P. Colpo, D. Demarchi, G. Micheli, and S. Carrara. Smart camera system for real-time biomarker monitoring. *Biomedical Circuits and Systems, IEEE Transactions on*, 2015. submitted.
- [38] K. K. Ghosh, L. D. Burns, E. D. Cocker, A. Nimmerjahn, Y. Ziv, A. El Gamal, and M. J. Schnitzer. Miniaturized integration of a fluorescence microscope. *Nature methods*, 8(10):871–878, 2011.

## Bibliography

---

- [39] K. A. Giuliano, W. S. Cheung, D. P. Curran, B. W. Day, A. J. Kassick, J. S. Lazo, S. G. Nelson, Y. Shin, and D. L. Taylor. Systems cell biology knowledge created from high content screening. *Assay and drug development technologies*, 3(5):501–514, 2005.
- [40] T. J. Gniadek and G. Warren. WatershedCounting3D: a new method for segmenting and counting punctate structures from confocal image data. *Traffic*, 8(4):339–346, 2007.
- [41] R. Gonzalo. *Segmentation and Tracking in High-Throughput Bioimaging*. EPFL thesis no. 5657 (2013), 186 p., Swiss Federal Institute of Technology Lausanne (EPFL), March 15, 2013. 2013 research award of the Swiss Society for Biomedical Engineering.
- [42] A. Greenbaum, W. Luo, T.-W. Su, Z. Göröcs, L. Xue, S. O. Isikman, A. F. Coskun, O. Mudanyali, and A. Ozcan. Imaging without lenses: achievements and remaining challenges of wide-field on-chip microscopy. *Nature methods*, 9(9):889–895, 2012.
- [43] G. G. Guilbault. *Practical fluorescence*, volume 3. CRC Press, 1990.
- [44] S. A. Haney, P. LaPan, J. Pan, and J. Zhang. High-content screening moves to the front of the line. *Drug discovery today*, 11(19):889–894, 2006.
- [45] B. M. Hanser, M. G. Gustafsson, D. A. Agard, and J. W. Sedat. Phase retrieval for high-numerical-aperture optical systems. *Optics letters*, 28(10):801–803, 2003.
- [46] R. M. Haralick, S. R. Sternberg, and X. Zhuang. Image analysis using mathematical morphology. *Pattern Analysis and Machine Intelligence, IEEE Transactions on*, (4):532–550, 1987.
- [47] G. Heygster. Rank filters in digital image processing. *Computer Graphics and Image Processing*, 19(2):148–164, 1982.
- [48] R. Hodgson, D. Bailey, M. Naylor, A. Ng, and S. McNeill. Properties, implementations and applications of rank filters. *Image and Vision Computing*, 3(1):3–14, 1985.
- [49] M. Hollander, D. A. Wolfe, and E. Chicken. *Nonparametric statistical methods*. John Wiley & Sons, 2013.
- [50] K. L. Holmes and L. M. Lantz. Protein labeling with fluorescent probes. *Essential Cytometry Methods*, page 29, 2009.
- [51] A. Hoshino, K. Fujioka, T. Oku, M. Suga, Y. F. Sasaki, T. Ohta, M. Yasuhara, K. Suzuki, and K. Yamamoto. Physicochemical properties and cellular toxicity of nanocrystal quantum dots depend on their surface modification. *Nano Letters*, 4(11):2163–2169, 2004.
- [52] B. Huang, H. Babcock, and X. Zhuang. Breaking the diffraction barrier: super-resolution imaging of cells. *Cell*, 143(7):1047–1058, 2010.
- [53] B. Huang, M. Bates, and X. Zhuang. Super resolution fluorescence microscopy. *Annual review of biochemistry*, 78:993, 2009.



- [54] D. C. Hunter, R. Brown, T. Green, C. Thomson, M. Skeaff, S. Williams, J. M. Todd, C. E. Lister, T. McGhie, J. Zhang, et al. Changes in markers of inflammation, antioxidant capacity and oxidative stress in smokers following consumption of milk, and milk supplemented with fruit and vegetable extracts and vitamin c. *International journal of food sciences and nutrition*, 63(1):90–102, 2012.
- [55] J. R. Janesick. *Scientific charge-coupled devices*, volume 117. SPIE press Bellingham, 2001.
- [56] H. Ji, P. A. Abshire, M. Urdaneta, and E. Smela. CMOS contact imager for monitoring cultured cells. In *Circuits and Systems, 2005. ISCAS 2005. IEEE International Symposium on*, pages 3491–3494. IEEE, 2005.
- [57] J. Kapur, P. K. Sahoo, and A. K. Wong. A new method for gray-level picture thresholding using the entropy of the histogram. *Computer vision, graphics, and image processing*, 29(3):273–285, 1985.
- [58] F. H. Kasten. The origins of modern fluorescence microscopy and fluorescent probes. *Cell structure and function by microspectrofluorometry*, pages 3–50, 1989.
- [59] L. R. Khot, S. Sankaran, J. M. Maja, R. Ehsani, and E. W. Schuster. Applications of nanomaterials in agricultural production and crop protection: a review. *Crop Protection*, 35:64–70, 2012.
- [60] Y. Kimori, N. Baba, and N. Morone. Extended morphological processing: a practical method for automatic spot detection of biological markers from microscopic images. *BMC bioinformatics*, 11(1):373, 2010.
- [61] M. Klaiber, L. Rockstroh, Z. Wang, Y. Baroud, and S. Simon. A memory-efficient parallel single pass architecture for connected component labeling of streamed images. In *Field-Programmable Technology (FPT), 2012 International Conference on*, pages 159–165. IEEE, 2012.
- [62] A. Klein, R. Van Den Doel, I. T. Young, S. Ellenberger, and L. Van Vliet. Quantitative evaluation and comparison of light microscopes. *image*, 1000(1):2, 1998.
- [63] N. Koike, I. Takemoto, K. Satoh, S. Hanamura, S. Nagahara, and M. Kubo. MOS area sensor: Part I - design consideration and performance of an NPN structure 484 × 384 element color MOS imager. *Electron Devices, IEEE Transactions on*, 27(8):1676–1681, 1980.
- [64] G. Köklü, J. Ghaye, R. Beuchat, G. De Micheli, Y. Leblebici, and S. Carrara. Quantitative comparison of commercial CCD and custom-designed CMOS camera for biological applications. In *Circuits and Systems (ISCAS), 2012 IEEE International Symposium on*, pages 2063–2066. IEEE, 2012.

## Bibliography

---

- [65] G. Köklü, J. Ghaye, R. Etienne-Cummings, Y. Leblebici, G. De Micheli, and S. Carrara. Empowering low-cost CMOS cameras by image processing to reach comparable results with costly CCDs. *BioNanoScience*, 3(4):403–414, 2013.
- [66] A. Lehmußola, P. Ruusuvaori, J. Selinummi, H. Huttunen, and O. Yli-Harja. Computational framework for simulating fluorescence microscope images with cell populations. *Medical Imaging, IEEE Transactions on*, 26(7):1010–1016, 2007.
- [67] A. Lehmußola, J. Selinummi, P. Ruusuvaori, A. Niemisto, and O. Yli-Harja. Simulating fluorescent microscope images of cell populations. In *Engineering in Medicine and Biology Society, 2005. IEEE-EMBS 2005. 27th Annual International Conference of the*, pages 3153–3156. IEEE, 2006.
- [68] D.-U. Li, J. Arlt, J. Richardson, R. Walker, A. Buts, D. Stoppa, E. Charbon, and R. Henderson. Real-time fluorescence lifetime imaging system with a  $32 \times 32$   $0.13 \mu\text{m}$  CMOS low dark-count single-photon avalanche diode array. *Optics express*, 18(10):10257–10269, 2010.
- [69] V. Mamaeva, C. Sahlgren, and M. Linden. Mesoporous silica nanoparticles in medicine - recent advances. *Advanced drug delivery reviews*, 65(5):689–702, 2013.
- [70] H. B. Mann and D. R. Whitney. On a test of whether one of two random variables is stochastically larger than the other. *The annals of mathematical statistics*, pages 50–60, 1947.
- [71] A. N. Margioris. Fatty acids and postprandial inflammation. *Current Opinion in Clinical Nutrition & Metabolic Care*, 12(2):129–137, 2009.
- [72] L. C. Martin. *The theory of the microscope*, volume 1351. Blackie Glasgow, 1966.
- [73] I. L. Medintz, M. H. Stewart, S. A. Trammell, K. Susumu, J. B. Delehanty, B. C. Mei, J. S. Melinger, J. B. Blanco-Canosa, P. E. Dawson, and H. Mattoussi. Quantum-dot/dopamine bioconjugates function as redox coupled assemblies for in vitro and intracellular pH sensing. *Nature materials*, 9(8):676–684, 2010.
- [74] I. L. Medintz, H. T. Uyeda, E. R. Goldman, and H. Mattoussi. Quantum dot bioconjugates for imaging, labelling and sensing. *Nature materials*, 4(6):435–446, 2005.
- [75] Mentor Graphics Corporation. Pixel stream. <http://www.mentor.com/products/fpga/handel-c/pixelstreams/>. Accessed: 2015-03-18.
- [76] F Meyer and S. Beucher. Morphological segmentation. *Journal of visual communication and image representation*, 1(1):21–46, 1990.
- [77] X. Michalet, F. F. Pinaud, L. A. Bentolila, J. M. Tsay, S. Doose, J. J. Li, G. Sundaresan, A. M. Wu, S. S. Gambhir, and S. Weiss. Quantum dots for live cells, in vivo imaging, and diagnostics. *science*, 307(5709):538–544, 2005.

- [78] G. D. Micheli. *Synthesis and optimization of digital circuits*. McGraw-Hill Higher Education, 1994.
- [79] M. Minsky. Memoir on inventing the confocal scanning microscope. *Scanning*, 10(4):128–138, 1988.
- [80] M. M. Most, A. G. Ershow, and B. A. Clevidence. An overview of methodologies, proficiencies, and training resources for controlled feeding studies. *Journal of the American Dietetic Association*, 103(6):729–735, 2003.
- [81] R. Mueller, J. Teubner, and G. Alonso. Sorting networks on FPGAs. *The VLDB Journal—The International Journal on Very Large Data Bases*, 21(1):1–23, 2012.
- [82] J. Mullikin, L. van Vliet, H. Netten, F. Boddeke, G. Van der Feltz, and I. Young. Methods for CCD camera characterization. In *Proceedings of the SPIE Image Acquisition and Scientific Imaging Systems San Jose*, volume 2173, pages 73–84, 1994.
- [83] K. Murari, R. Etienne-Cummings, G. Cauwenberghs, and N. Thakor. An integrated imaging microscope for untethered cortical imaging in freely-moving animals. In *Conf Proc IEEE Eng Med Biol Soc*, volume 2010, pages 5795–5798, 2010.
- [84] H. Nabeyama, S. Nagahara, H. Shimizu, M. Noda, and M. Masuda. All solid state color camera with single-chip MOS imager. *Consumer Electronics, IEEE Transactions on*, (1):40–46, 1981.
- [85] S. Nakagawa and I. C. Cuthill. Effect size, confidence interval and statistical significance: a practical guide for biologists. *Biological Reviews*, 82(4):591–605, 2007.
- [86] D. Napierska, L. C. Thomassen, B. Vanaudenaerde, K. Luyts, D. Lison, J. A. Martens, B. Nemery, and P. H. Hoet. Cytokine production by co-cultures exposed to monodisperse amorphous silica nanoparticles: the role of size and surface area. *Toxicology letters*, 211(2):98–104, 2012.
- [87] H. Netten, L. J. Van Vliet, H. Vrolijk, W. C. Sloos, H. J. Tanke, and I. T. Young. Fluorescent dot counting in interphase cell nuclei. *Bioimaging*, 4(2):93–106, 1996.
- [88] P. Neuži, S. Giselbrecht, K. Länge, T. J. Huang, and A. Manz. Revisiting lab-on-a-chip technology for drug discovery. *Nature reviews Drug discovery*, 11(8):620–632, 2012.
- [89] P. Neužil, C. Campos, C. Wong, J. Soon, J. Reboud, and A. Manz. From chip-in-a-lab to lab-on-a-chip: towards a single handheld electronic system for multiple application-specific lab-on-a-chip (asloc). *Lab on a Chip*, 14(13):2168–2176, 2014.
- [90] W. Niblack. *An introduction to digital image processing*. Strandberg Publishing Company, 1985.

## Bibliography

---

- [91] B. Nielsen, F. Albregtsen, and H. E. Danielsen. Automatic segmentation of cell nuclei in feulgen-stained histological sections of prostate cancer and quantitative evaluation of segmentation results. *Cytometry Part A*, 81(7):588–601, 2012.
- [92] R. Nixon, N. Doudoumopoulos, and E. R. Fossum. Backside illumination of CMOS image sensor, Aug. 6 2002. US Patent 6,429,036.
- [93] T. Nolan, R. E. Hands, and S. A. Bustin. Quantification of mRNA using real-time RT-PCR. *Nature protocols*, 1(3):1559–1582, 2006.
- [94] L. Novak, P. Neuzil, J. Pipper, Y. Zhang, and S. Lee. An integrated fluorescence detection system for lab-on-a-chip applications. *Lab on a Chip*, 7(1):27–29, 2007.
- [95] J. S. Nowak, D. Mehn, P. Nativo, C. P. García, S. Gioria, I. Ojea-Jiménez, D. Gilliland, and F. Rossi. Silica nanoparticle uptake induces survival mechanism in A549 cells by the activation of autophagy but not apoptosis. *Toxicology letters*, 224(1):84–92, 2014.
- [96] J.-C. Olivo-Marin. Extraction of spots in biological images using multiscale products. *Pattern Recognition*, 35(9):1989–1996, 2002.
- [97] A. V. Oppenheim and A. S. Willsky. *Signals and systems*. Prentice-Hall, 1997.
- [98] N. Otsu. A threshold selection method from gray-level histograms. *IEEE Transactions on systems, Man, and Cybernetics*, 9(1):62–66, 1979.
- [99] O. Pele and M. Werman. The quadratic-chi histogram distance family. In *Computer Vision—ECCV 2010*, pages 749–762. Springer, 2010.
- [100] S. Pennathur. Improving fluorescence detection in lab on chip devices. *Lab on a Chip*, 8(5):649–652, 2008.
- [101] T. D. Pham, D. I. Crane, T. H. Tran, and T. H. Nguyen. Extraction of fluorescent cell puncta by adaptive fuzzy segmentation. *Bioinformatics*, 20(14):2189–2196, 2004.
- [102] C. R. Raetz. Bacterial endotoxins: extraordinary lipids that activate eucaryotic signal transduction. *Journal of Bacteriology*, 175(18):5745, 1993.
- [103] S. Ram, J. J. Rodríguez, and G. Bosco. Segmentation and detection of fluorescent 3D spots. *Cytometry Part A*, 81(3):198–212, 2012.
- [104] Q. Ramadan, H. Jafarpoorchehab, K. Bolanz, F. Schwander, P. Silacci, S. Carrara, J. Ramsden, G. Vergeres, and M. Gijs. Nutrichip: An integrated microfluidic system for in vitro investigation of the immunomodulatory function of dairy products. In *Proceed. of the 15th International Conference on Miniaturized Systems for Chemistry and Life Sciences,  $\mu$ TAS 2011 Conference, Seattle, USA*, pages 650–652, 2011.
- [105] Q. Ramadan, H. Jafarpoorchehab, C. Huang, P. Silacci, S. Carrara, G. Koklü, J. Ghaye, J. Ramsden, C. Ruffert, G. Vergeres, et al. Nutrichip: nutrition analysis meets microfluidics. *Lab on a Chip*, 13(2):196–203, 2013.

- [106] E. Rampazzo, R. Voltan, L. Petrizza, N. Zaccheroni, L. Prodi, F. Casciano, G. Zauli, and P. Secchiero. Proper design of silica nanoparticles combines high brightness, lack of cytotoxicity and efficient cell endocytosis. *Nanoscale*, 5(17):7897–7905, 2013.
- [107] F. Rancan, Q. Gao, C. Graf, S. Troppens, S. Hadam, S. Hackbarth, C. Kembuan, U. Blume-Peytavi, E. Ruhl, J. Lademann, et al. Skin penetration and cellular uptake of amorphous silica nanoparticles with variable size, surface functionalization, and colloidal stability. *ACS nano*, 6(8):6829–6842, 2012.
- [108] B. Reljin, M. Paskas, I. Reljin, and K. Konstany. Breast cancer evaluation by fluorescent dot detection using combined mathematical morphology and multifractal techniques. *Diagn Pathol*, 6(suppl 1):S21, 2011.
- [109] U. Resch-Genger, M. Grabolle, S. Cavaliere-Jaricot, R. Nitschke, and T. Nann. Quantum dots versus organic dyes as fluorescent labels. *Nature methods*, 5(9):763–775, 2008.
- [110] T. Ridler and S. Calvard. Picture thresholding using an iterative selection method. *IEEE transactions on Systems, Man and Cybernetics*, 8(8):630–632, 1978.
- [111] M. J. Ruedas-Rama, J. D. Walters, A. Orte, and E. A. Hall. Fluorescent nanoparticles for intracellular sensing: a review. *Analytica chimica acta*, 751:1–23, 2012.
- [112] O. V. Salata. Applications of nanoparticles in biology and medicine. *Journal of nanobiotechnology*, 2(1):3, 2004.
- [113] J. Sauvola and M. Pietikäinen. Adaptive document image binarization. *Pattern recognition*, 33(2):225–236, 2000.
- [114] M. Schöberl, C. Senel, S. Föbel, H. Bloss, and A. Kaup. Non-linear dark current fixed pattern noise compensation for variable frame rate moving picture cameras. In *Proc. 17th European Signal Processing Conference (EUSIPCO)*, pages 268–272, 2009.
- [115] D. E. Schwartz, E. Charbon, and K. L. Shepard. A single-photon avalanche diode array for fluorescence lifetime imaging microscopy. *Solid-State Circuits, IEEE Journal of*, 43(11):2546–2557, 2008.
- [116] P. Seitz. Fundamentals of noise in optoelectronics. In *Single-Photon Imaging*, pages 1–25. Springer, 2011.
- [117] J. Serra. *Image analysis and mathematical morphology, v. 1*. Academic press, 1982.
- [118] M. Sezgin et al. Survey over image thresholding techniques and quantitative performance evaluation. *Journal of Electronic imaging*, 13(1):146–168, 2004.
- [119] N. C. Shaner, G. H. Patterson, and M. W. Davidson. Advances in fluorescent protein technology. *Journal of cell science*, 120(24):4247–4260, 2007.

## Bibliography

---

- [120] K. Shapero, F. Fenaroli, I. Lynch, D. C. Cottell, A. Salvati, and K. A. Dawson. Time and space resolved uptake study of silica nanoparticles by human cells. *Molecular Biosystems*, 7(2):371–378, 2011.
- [121] V. K. Sharma, D. Mohan, and P. Sahare. Fluorescence quenching of 3-methyl 7-hydroxyl coumarin in presence of acetone. *Spectrochimica Acta Part A: Molecular and Biomolecular Spectroscopy*, 66(1):111–113, 2007.
- [122] O. Shimomura, F. H. Johnson, and Y. Saiga. Extraction, purification and properties of aequorin, a bioluminescent protein from the luminous hydromedusan, aequorea. *Journal of cellular and comparative physiology*, 59(3):223–239, 1962.
- [123] R. R. Singh, D. Ho, A. Nilchi, P. G. Gulak, P. Yau, and R. Genov. A CMOS/thin-film fluorescence contact imaging microsystem for DNA analysis. *Circuits and Systems I: Regular Papers, IEEE Transactions on*, 57(5):1029–1038, 2010.
- [124] I. Smal, M. Loog, W. Niessen, and E. Meijering. Quantitative comparison of spot detection methods in live-cell fluorescence microscopy imaging. In *Biomedical Imaging: From Nano to Macro, 2009. ISBI'09. IEEE International Symposium on*, pages 1178–1181. IEEE, 2009.
- [125] I. Smal, M. Loog, W. Niessen, and E. Meijering. Quantitative comparison of spot detection methods in fluorescence microscopy. *Medical Imaging, IEEE Transactions on*, 29(2):282–301, 2010.
- [126] V. Starkuviene and R. Pepperkok. The potential of high-content high-throughput microscopy in drug discovery. *British journal of pharmacology*, 152(1):62–71, 2007.
- [127] D. Svoboda, M. Kašík, M. Maška, J. Hubený, S. Stejskal, and M. Zimmermann. On simulating 3D fluorescent microscope images. In *Computer analysis of images and patterns*, pages 309–316. Springer, 2007.
- [128] S. M. Sze and K. K. Ng. *Physics of semiconductor devices*. John Wiley & Sons, 2006.
- [129] L. Tao and C. Nicholson. The three-dimensional point spread functions of a microscope objective in image and object space. *Journal of microscopy*, 178(3):267–271, 1995.
- [130] R. Tapeç, X. J. Zhao, and W. Tan. Development of organic dye-doped silica nanoparticles for bioanalysis and biosensors. *Journal of nanoscience and nanotechnology*, 2(3-4):405–409, 2002.
- [131] H. Tian. *Noise Analysis in CMOS image sensors*. PhD thesis, stanFord university, 2000.
- [132] E. Torney, B. G. Trewyn, V. S.-Y. Lin, and K. Wang. Mesoporous silica nanoparticles deliver DNA and chemicals into plants. *Nature Nanotechnology*, 2(5):295–300, 2007.

- [133] M. Triantafilou, M. Manukyan, A. Mackie, S. Morath, T. Hartung, H. Heine, and K. Triantafilou. Lipoteichoic acid and toll-like receptor 2 internalization and targeting to the golgi are lipid raft-dependent. *Journal of Biological Chemistry*, 279(39):40882–40889, 2004.
- [134] R. Y. Tsien. The green fluorescent protein. *Annual review of biochemistry*, 67(1):509–544, 1998.
- [135] R. Y. Tsien and A. Waggoner. Fluorophores for confocal microscopy. In *Handbook of biological confocal microscopy*, pages 267–279. Springer, 1995.
- [136] E. B. van Munster and T. W. Gadella. Fluorescence lifetime imaging microscopy (FLIM). In *Microscopy techniques*, pages 143–175. Springer, 2005.
- [137] P. Verbeek, H. Vrooman, and L. Van Vliet. Low-level image processing by max-min filters. *Signal Processing*, 15(3):249–258, 1988.
- [138] G. Vergeres, B. Bogicevic, C. Buri, S. Carrara, M. Chollet, L. Corbino-Giunta, L. Egger, D. Gille, K. Kopf-Bolanz, K. Laederach, et al. The NutriChip project—translating technology into nutritional knowledge. *British Journal of Nutrition*, 108(05):762–768, 2012.
- [139] L. Vincent and P. Soille. Watersheds in digital spaces: an efficient algorithm based on immersion simulations. *IEEE transactions on pattern analysis and machine intelligence*, 13(6):583–598, 1991.
- [140] C. Vonesch. *Fast and Automated Wavelet-Regularized Image Restoration in Fluorescence Microscopy*. EPFL thesis no. 4306 (2009), 229 p., Swiss Federal Institute of Technology Lausanne (EPFL), May 1, 2009.
- [141] F. Wang, W. B. Tan, Y. Zhang, X. Fan, and M. Wang. Luminescent nanomaterials for biological labelling. *Nanotechnology*, 17(1):R1, 2006.
- [142] G. P. Weckler. Operation of PN junction photodetectors in a photon flux integrating mode. *Solid-State Circuits, IEEE Journal of*, 2(3):65–73, 1967.
- [143] G. M. Whitesides. The origins and the future of microfluidics. *Nature*, 442(7101):368–373, 2006.
- [144] Xilinx Corporation. Video and image processing pack. <http://www.xilinx.com/products/intellectual-property/ef-di-vid-img-ip-pack.html>. Accessed: 2015-03-18.
- [145] L. Yan, R. Dodier, M. C. Mozer, and R. Wolniewicz. Optimizing classifier performance via an approximation to the Wilcoxon-Mann-Whitney statistic. In *Machine Learning, ICML-2003. International Conference on*, 2003.
- [146] P. Yang, S. Gai, and J. Lin. Functionalized mesoporous silica materials for controlled drug delivery. *Chemical Society Reviews*, 41(9):3679–3698, 2012.

## Bibliography

---

- [147] J. Yao, D. R. Larson, H. D. Vishwasrao, W. R. Zipfel, and W. W. Webb. Blinking and nonradiant dark fraction of water-soluble quantum dots in aqueous solution. *Proceedings of the National Academy of Sciences of the United States of America*, 102(40):14284–14289, 2005.
- [148] A. Yildiz and P. R. Selvin. Fluorescence imaging with one nanometer accuracy: application to molecular motors. *Accounts of chemical research*, 38(7):574–582, 2005.
- [149] W. A. Yousef, R. F. Wagner, and M. H. Loew. Estimating the uncertainty in the estimated mean area under the ROC curve of a classifier. *Pattern Recognition Letters*, 26(16):2600–2610, 2005.
- [150] B. Zhang, J. Zerubia, and J. Olivo-Marin. Gaussian approximations of fluorescence microscope point-spread function models. *Applied Optics*, 46(10):1819–1829, 2007.
- [151] G. Zhang, X. Jia, T. D. Pham, and D. I. Crane. Multistage spatial property based segmentation for quantification of fluorescence distribution in cells. In *2009 International conference on computational/Sm models for life sciences (CMLS-09)*, volume 1210, pages 3–12. AIP Publishing, 2010.
- [152] X. Zhao, R. P. Bagwe, and W. Tan. Development of organic-dye-doped silica nanoparticles in a reverse microemulsion. *Advanced Materials*, 16(2):173–176, 2004.
- [153] X. Zhou and J. Zhou. Improving the signal sensitivity and photostability of DNA hybridizations on microarrays by using dye-doped core-shell silica nanoparticles. *Analytical Chemistry*, 76(18):5302–5312, 2004.

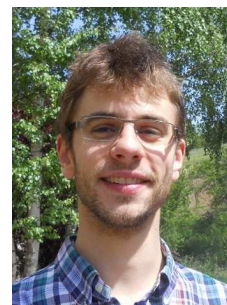


## Julien GHAYE

Ing. dipl. EPF, Electrical Engineering  
Ph.D in Electrical Engineering

Phone : +41 21 558 36 49  
Mobile : +41 78 607 67 86  
E-Mail : [julien@ghaye.net](mailto:julien@ghaye.net)  
Website : <http://julien.ghaye.net>

Belgian. 16.08.1985. Single.  
Rue de Bourg, 15  
1003 Lausanne, Switzerland



## Profile

---

Experienced in HDL design, with practical knowhow on FPGA implementation. Practiced verification methodologies of a medium sized RTL design. Structured and rigorous when approaching problems and development

## Professional Experience

---

*EPFL, Integrated Systems Laboratory. Ph.D. Candidate* (July 2010 - April 2015)

**Objectives** : Conception and development of a custom embedded image processing system dedicated to quantitative fluorescence microscopy.

**Results** :

- Comparative study of existing and novel image segmentation algorithms for microscopic images.
- Development of a synthetic image generation tool for the algorithms validation (cell and optics simulation).
- Functional FPGA based prototype processing images in real-time. (incl. firmware and software).
- Complete image processing suite of IPs compatible with Aletra design tools.
- 9 international peer-reviewed scientific publications.

*Cossilys 21, S.A. Embedded Software and Electronics Engineer* (January - Mai 2010) (20%)

French company developing and marketing video surveillance systems.

**Objectives** : development of the firmware and elimination of various electronic bugs within a USB controlled I/O electronic board.

**Results** : The updated electronic board and the embedded software have been tested and evaluated by Cossilys 21 engineers. They are currently used in Cossilys 21 products.

*Semtech, Inc. Verification Engineer* (March - June 2009)

Fabless analog and mixed-signals semiconductors provider.

**Objectives** : Application of a new verification methodology for RTL model testing and debugging.

**Results** : Working custom verification architecture based on the Open Verification Methodology. Semtech engineers evaluated and compared the new methodology with theirs.

## Education

---

Ph.D. in Electrical Engineering at **EPFL** (2010 - 2015)

*"Image processing on reconfigurable hardware for continuous monitoring of fluorescent biomarkers in cell cultures"*

M.Sc. in Electrical Engineering at **Université de Liège** (2009 - 2010)

*"Arm Gesture Recognition for Human-Computer Interaction"*

M.Sc. in Electrical Engineering at **EPFL** (2007 - 2009)

*"Implementation of an OVM Based Advanced Functional Testbench for a Mixed-Signal A/D Converter"*

B.Sc. in Computer Science and Electrical Engineering at **Université de Liège** (2003 - 2007)

## Technical Skills

---

### IT and programming

- Linux, Windows (up to 8), Mac OS X, Unix server administration, Android development.
- Languages : VHDL(-AMS), Verilog, SystemVerilog, Assembly (x86, PIC), C, C++, Java, (X)HTML, CSS, Matlab.

### Electronic design automation (EDA)

- Design, simulation and synthesis softwares : Synopsis Design Compiler, Cadence (Virtuoso, Assura, Encounter), Modelsim/Questasim, Open Verification Methodology(OVM), Altera and Xilinx design tools, Altium Designer.

## Miscellaneous

---

### Languages

- French : Native speaker
- English : Working language, proficient (C2)
- Dutch : Beginner (A2)
- German : Beginner (A0-A1)

### Hobbies

- Mountaineering
- Sports climbing
- Guitar

## Scientific Publications

---

### Journals

- **J. Ghaye**, P. Urbàn, A. Kinsner-Ovaskainen, P. Colpo, D. Demarchi, G. De Micheli, S. Carrara, "*Smart Camera System for Real-Time Biomarker Monitoring*", IEEE Transactions on BioCAS, 2015, submitted.
- G. Köklü, **J. Ghaye**, R. Etienne-Cumming, Y. Leblebici, G. De Micheli, S. Carrara, "*Empowering Low-Cost CMOS Cameras by Image Processing to reach comparable Results with Costly CCDs*", Bio-NanoScience, 2013, vol. 3, num. 4, p.403-414.
- **J. Ghaye**, M. Avinash Kamat, L. Corbino-Giunta, P. Silacci, G. Vergère, G. De Micheli, S. Carrara, "*Image thresholding techniques for localization of sub-resolution fluorescent biomarkers*", Cytometry, Part A, 2013, vol. 83, num. 11, p. 1001-1016.
- Q. Ramadan, H. Jafarpoorchehab, C. Huang, P. Silacci, S. Carrara, G. Köklü, **J. Ghaye**, J. Ramsden, C. Ruffert, G. Vergères, M. Gijs, "*NutriChip : Nutrition Analysis meets Microfluidics*", Lab-on-a-chip Journal, 2012, vol. 13, num. 2, p.196-203.
- **J. Ghaye**, G. De Micheli, S. Carrara, "*Simulated biological cells for receptor counting in fluorescence imaging*", BioNanoScience, 2012, vol. 2, num. 2, p. 94-103

### Conference proceedings

- **J. Ghaye**, C. Succa, D. Demarchi, S.K. Muldur, P. Colpo, P. Silacci, G. Vergère, G. De Micheli, S. Carrara, "*Quantitative Estimation of Biological Cell Surface Receptors by Segmenting Conventional Fluorescence Microscopy Images*", IEEE ISCAS, 2014, p. 1824-1827.
- **J. Ghaye**, G. De Micheli, S. Carrara, "*Quantification of Sub-Resolution Sized Targets in Cell Fluorescent microscopy*", IEEE BioCAS, 2012, p. 268-271.
- G. Köklü, **J. Ghaye**, R. Beuchat, G. De Micheli, Y Leblebici, S. Carrara, "*Quantitative Comparison of Commercial CCD and Custom-Designed CMOS Camera for Biological Applications*", IEEE ISCAS, 2012, p. 2063-2066.

### Demonstrations

- **J. Ghaye**, S.K. Muldur, P. Urbàn, A. Kinsner-Ovaskainen, P. Colpo, D. Demarchi, G. De Micheli, S. Carrara, "*Live Demonstration : A smart camera for real-time monitoring of fluorescent cell biomarkers*", IEEE BioCAS, 2014, p.169.